

Coupling Hydrodynamic and Biological Process Models for Wastewater Treatment

Andrew Robert Coughtrie

Submitted in accordance with the requirements for the degree of
Doctor of Philosophy

The University of Leeds
School of Civil Engineering

August 2016

Intellectual property and publication statements

The candidate confirms that the work is his own, except where work which has formed part of jointly-authored publications has been included. The contribution of the candidate and the other authors work has been explicitly indicated herein. The candidate confirms that appropriate credit has been given within the thesis where reference has been made to the work of others.

The work presented in Chapter 5 of this thesis has appeared in the following publication:

Coughtrie, A., Borman, D. and Sleigh, P. 2013. Effects of turbulence modelling on prediction of flow characteristics in a bench-scale anaerobic gas-lift digester. *Bioresource Technology*. **138** pp.297-306.

I was responsible for all modelling work including all set-up implementation and post processing of data. D. J. Borman and P. A. Sleigh contributed to the editing of the manuscript and advice on modelling methodology.

This copy has been supplied on the understanding that it is copyright material and that no quotation from the thesis may be published without proper acknowledgement.

©2016 The University of Leeds and Andrew Coughtrie.

The right of Andrew Robert Coughtrie to be identified as Author of this work has been asserted by Andrew Robert Coughtrie in accordance with the Copyright, Designs and Patents Act 1988.

Acknowledgements

I would like give my thanks first to my supervisors Dr Duncan Borman, Dr Andy Sleigh and Dr Miller Alonso Camargo-Valero for their help, advise and support throughout my Ph.D. Without their knowledge and expertise and most of all their patience this work would not have been possible. Also my thanks go to all the other members of the department who are always willing to offer advice and knowledge when asked, and making the atmosphere of the school so welcoming.

I would also like to thank my family for encouraging me to in everything I do and especially my parents for all their help over the years.

Finally I'd like to thank my friends for making me laugh and for laughing at me, life would be much less interesting without you all.

Abstract

This thesis considers the problem of modelling bioreactors with complex mixing and biokinetic growth based on both soluble nutrients and photosynthesis. From the results of investigations performed on the different modelling methods for nutrient and photosynthesis dependent biomass growth a method of coupling the two biokinetic models was proposed. This new photosynthesis-nutrient (PN) model was then investigated, validated and determined capable of predicting growth characteristics dependent on both nutrient and photosynthetic processes. Additionally an investigation into the factors which may influence the results when using computational fluid dynamics (CFD) to model the flow field within a gas-lift bioreactor was performed. It was determined that one of the main factors which must be considered when modelling bioreactors with boundary layer flow separation is the choice of turbulence model. In the case presented here it was found that the transition SST turbulence model provided the best results with the $k-\omega$ SST also performing well. Finally, a method of coupling the PN and CFD models was proposed and investigated. The photosynthesis-nutrient-hydrodynamic (PNH) model also incorporated a model for diffusion of light within the bioreactor to allow for investigations into the effects of light absorption and scattering within the bioreactor and how mixing affects the active biomass. Further investigation of this new PNH model determined that the coupling of the biokinetics and flow field provided some insight into the ability of a well-mixed bioreactor to counter low light penetration to an extent.

Contents

Acknowledgements	ii
Abstract	iii
List of Tables	viii
List of Figures	x
1 Introduction	1
1.1 Aims and objectives	4
2 Bioreactors and biological growth	6
2.1 Bioreactors and biological processes	7
2.2 Bioreactor Process Modelling	10
2.2.1 Biokinetic modelling strategies	10
2.2.1.1 Monod models	10
2.2.1.2 Cell quota (Droop) models	11
2.2.1.3 Mechanistic models	11
2.2.2 Light limited growth	12
2.2.2.1 Modelling light intensity within bioreactors	15
2.2.2.2 Modelling photosynthesis dependent growth	18
2.2.3 Hydrodynamic mixing	19
2.2.3.1 Modelling hydrodynamic mixing	20
2.3 Summary	22
3 Nutrient limited biomass growth modelling	23

3.1	Introduction	24
3.2	Numerical methods for ordinary differential equations	25
3.3	Activated sludge treatment models	26
3.3.1	Simple activated sludge biokinetic model	28
3.3.2	Bulk Biokinetic Model Reactor	33
3.3.2.1	Time Dependent Solution	33
3.3.2.2	Steady-State Solution	34
3.4	Anaerobic digestion models	35
3.5	Phytoplankton models	38
3.5.1	Monod Kinetics	38
3.5.2	Cell Quota Modelling	40
3.5.3	Multi-Nutrient modelling	41
3.6	Summary	43
4	Photosynthesis Modelling	44
4.1	Multiplicative modelling approach	46
4.1.1	Soluble nutrient model methodology	47
4.1.2	Photosynthesis modelling methodology	48
4.1.3	Nutrient uptake limiting model for low light conditions	50
4.1.4	Modelling light distribution within the culture volume	51
4.1.5	Validating the multiplicative model	52
4.2	The photosynthetic factory (PSF) model	58
4.2.1	Effects of light intensity function on the photosynthetic state of biomass	59
4.2.2	The relationship between light intensity and activated biomass in the photosynthetic factory model	63
4.3	Coupling the photosynthetic factory and cell quota models	65
4.3.1	Cell quota model with nutrient uptake limitation	66
4.3.2	Validation of PN coupled model using results from literature	70
4.3.3	Effects of varying the light intensity function on biomass growth	71

4.3.4	Effects on biomass growth of a light intensity function and the average of the function	74
4.4	Summary and conclusions	76
5	Hydrodynamic Modelling	78
5.1	Introduction	79
5.2	Computational fluid dynamics modelling	80
5.2.1	The Navier-Stokes equations	80
5.2.2	Reynolds averaged Navier-Stokes (RANS) turbulence models	83
5.2.2.1	Two equation turbulence models	84
5.2.3	Euler-Lagrange multiphase modelling	85
5.3	CFD modelling of a gas-lift bioreactor, assessing turbulence model selection and flow control	86
5.3.1	Mesh independence testing of CFD simulations	91
5.3.2	RANS turbulence model assessment	94
5.3.3	CFD solver comparison (ANSYS Fluent vs. OpenFOAM)	100
5.3.4	A comparison of different approaches for modelling the velocity induced by bubble flow in the bioreactor draft tube	102
5.4	Summary and conclusions	107
6	Coupling hydrodynamics and biokinetic growth	109
6.1	Coupled model methodology	111
6.1.1	Coupling biokinetic growth models with hydrodynamics	111
6.1.2	Modelling light distribution within a bioreactor	115
6.1.3	Steady-state CFD and mesh mapping	118
6.2	Implementation and assessment of the coupled photosynthesis-nutrient-hydrodynamic model	119
6.2.1	Solver set up	120
6.2.2	Implementation verification	122
6.2.3	Mesh mapping independence testing	123
6.2.4	Light absorption and scattering affect on biomass growth	129
6.2.5	Reynolds number scaling of a bioreactor	134

6.2.6	Effect of increasing incident light intensity on the active biomass and biomass growth	140
6.3	Summary and conclusions	142
7	Conclusions and further work	144
7.1	Conclusions	144
7.2	Implications of results	147
7.3	Further work	148
	Bibliography	149
	Appendices	162
A	Biokinetic model code	163
B	Photosynthetic model code	166
C	Coupled model source code	173

List of Tables

3.1	List of variables, units and typical values from literature	29
3.2	Petersen Matrix for processes	29
3.3	Initial conditions taken from IWA benchmark data set (IWA, 2005).	30
3.4	List of variables, units and typical values from literature	32
3.5	Petersen matrix for extended biokinetic model	32
3.6	Steady-state vs transient solution comparison	35
3.7	Constants for the multi nutrient cell quota model (Klausmeier et al., 2004)	41
4.1	Constants for multiplicative photosynthesis model obtained through experimental analysis as described by Bernard (2011)	48
4.2	Initial conditions used for the implementation of the model developed by Bernard (2011) for the periodic light variation simulation	53
4.3	Initial conditions obtained from the experimental work of Davidson et al. (1992) for use with the Bernard (2011) algal growth model implemented here as part of validating the model accuracy.	55
4.4	Constants for the photosynthetic factory model (Wu and Merchuk, 2001) .	59
4.5	Light intensity at peak x_2 for four different functions (See figure 4.8)	64
4.6	Maximum cell quota values for Nitrogen and Phosphorus	67
5.1	Solver settings for CFD simulations performed here. Any changes to these setting are described where appropriate.	89
5.2	Mesh independence densities and Y^+ values	91
5.3	Turbulence models and their respective wall treatments	95
5.4	Fluent and OpenFOAM settings comparison	100

6.1	OpenFOAM dimension system and units	120
6.2	Constants for PNH model in OpenFOAM	121
6.3	Solver settings for PNH model in OpenFOAM	122
6.4	Absorption and scattering coefficients for different test cases with their corresponding biomass concentrations	130
6.5	Dimensions and volumes for different scaled bioreactors	134

List of Figures

2.1	Absorbtion spectra for different photosynthetic pigments, chylorophyll a/b being the most common in plants	13
2.2	Structure of a typical eukaryotic algal cell Chlamydomonas; showing the main organelles including the chloroplast, mitochondrion and the thylokoid membrane.(Unknown, 2014)	14
2.3	A Schematic representation of photosynthetic response to light intensity where α the initial slope of the curve is the maximum efficiency and the point where α meets the line P_{max} is known as I_K the light saturation point. After the peak photosynthesis rate at P_{max} the curve begins to decline, this is generally refered to as photoinhibition. (Figure reproduced from Masojidek et al. (2004))	16
2.4	Schematic representation of models of algal productivity (P: rate of photosynthesis; I: light intensity; T: temperature; RD:rate of day-time respiration; μ : specific rate of photosynthesis; X: biomass cell concentration; ζ : proportionality constant; RN: night-time maintenance; λ :biomass maintenance coefficient)(Béchet et al., 2013).	19
3.1	Petersen Matrix form developed for ASM1, shows process kinetics and stoichiometry for heterotrophic bacterial growth in an aerobic environment, reproduced from (Henze et al., 2000)	27
3.2	Process diagram of reaction model	29
3.3	Function for biokinetic model	30

3.4	Plot of growth and decay of biomass and substrate usage. Line thickness variation based on specific growth rate variable increasing from a value of $\mu_m=6$ in increments of 10% upto $\mu_m=9$ where the thinnest line is the smallest value of μ_m	31
3.5	Process diagram of extended reaction model, including slowly biodegradable substrate	31
3.6	Function for extended biokinetic model	32
3.7	Plot of growth and decay of biomass and substrate usage with the addition of hydrolysis of dead biomass	33
3.8	Process diagram of bulk reactor model	34
3.9	Time dependent concentration of variables in complete mix reactor	35
3.10	ADM1 process flow diagram	37
3.11	ADM1 model flow diagram of reactions (reproduced from Batstone et al. (2002a))	37
3.12	Biomass growth under nitrogen and phosphorus limited growth	42
4.1	Photoacclimation of algae species <i>Skeletononema costatum</i> at low light ($I_L = 50 \mu\text{molm}^{-2}\text{s}^{-1}$, dark blue points and lines) and at high irradiance ($I_H = 1200 \mu\text{molm}^{-2}\text{s}^{-1}$, light blue points and lines) reproduced from (Bernard, 2011; Anning et al., 2000)	49
4.2	Comparison performed between the model of Bernard (2011), implemented here, and the dynamic experimental data of Flynn et al. (1994) for a light:dark periodic light source.	54
4.3	Comparison between solutions from the model of Bernard (2011) implemented here and the experimental results of Davidson et al. (1992) for a constant light intensity	57
4.4	Photosynthetic factory model states diagram	58
4.5	Difference in photosynthetic states for differing light intensity functions, where the subplot is the light intensity function shape. Each function has the same average value over a one day period ($266\mu\text{Mol.m}^{-2}.\text{s}^{-1}$), also depicted within the subplots.	60

4.6 The the average ratios for the different photosynthetic states under the different light intensity functions 62

4.7 A comparison between the photosynthetic states for Gaussian light functions with average values of $266\mu\text{molm}^{-2}\text{s}^{-1}$ and $500\mu\text{molm}^{-2}\text{s}^{-1}$ representing sunlight (maximum value of $2000\mu\text{molm}^{-2}\text{s}^{-1}$ representing sunlight intensity at midday.) along with a plot of diurnal light intensity and a bar chart of average biomass state 63

4.8 Comparison of light intensity functions (constant, SIN function, Gaussian function and a step function) for activated biomass vs. average light intensity ranging from 0 to $2000\mu\text{Mol.m}^{-2}\text{s}^{-1}$ (Peak direct sunlight). Figure shows the mean activated biomass fraction per day vs the mean light intensity 64

4.9 Soluble nutrient concentration under cell quota limited nutrient uptake . . . 68

4.10 Cell quota nutrient concentration and biomass for model with and without quota limited uptake 69

4.11 Biomass growth at different N:P cell ratios for two different light intensities compared to experimental work done by Rhee (1978) 70

4.12 Growth comparison between different light intensity functions 72

4.13 Growth comparison between different light intensity functions, showing plots for soluble nutrients nitrogen and phosphorus as well as their respective cell quotas. 73

4.14 Comparison between the photosynthetic states of biomass for a Gaussian light intensity function and the average intensity of the function. 75

4.15 Comparison of biomass growth for a Gaussian light intensity function and the average of that function 75

5.1 Gas-lift bioreactor geometry and experimental results as used by Karim et al. (2004) and 2-D computational geometry for CFD analysis. 90

5.2 Velocity contour and vector for mesh independence testing 92

5.3 Velocity profiles for mesh independence testing where the different mesh densities displayed in the plot are defined in table 5.2 93

5.4	Separation and reattachment points for mesh independence testing	94
5.5	Velocity contour and vector plots for different turbulence models for flow in a bench-scale bioreactor.	97
5.6	Axial velocity profiles at 0.1875m and 0.0325m from base of bioreactor for different turbulence models compared with experimental results obtained by Karim et al. (2004)	98
5.7	Axial velocity profile plots for the separation point at the outer wall of the bioreactor and the reattachment point on the drafttube wall for the different turbulence models	99
5.8	Comparison between Fluent and OpenFOAM velocity contours	101
5.9	Comparison between Fluent and OpenFOAM velocity profiles	102
5.10	Closed loop singlephase bioreactor with momentum source. Zone in which the mean average velocity force was applied in the draft tube shown in red	103
5.11	Velocity vector plots for the different methods of controlling the flow in the gas-lift bioreactor	105
5.12	Velocity vectors for the different methods of controlling the flow in the gas-lift bioreactor	107
6.1	Tanks in series model method diagram for simple loop bioreactor	112
6.2	Diagram of radiative transfer equation processes over a small distance ds . .	115
6.3	Biomass growth plot for a simple case where light intensity is set to a constant value of $266\mu Mol.m^{-2}.s^{-1}$ and the fluid velocity is at $0m.s^{-1}$. . .	123
6.4	Velocity contour plots for the velocity field when mapped from the original mesh onto courser meshes for biokinetic growth modelling.	125
6.5	Velocity profile plots for CFD solutions mapped onto coarser meshes	126
6.6	Light gradient within bioreactor (a) and light intensity profile across width of bioreactor (b)	127
6.7	Comparison of mesh independence for biomass growth in simulations using different mesh sizes with mapped velocity fields	128
6.8	Light intensity contour plots for the cases in table 6.4 under different absorption and scattering coefficients	132

6.9	Comparison of light intensity distribution along profile line 0.1875m from base of bioreactor at the different light absorption and scattering coefficients described in table 6.4.	133
6.10	Biomass growth plot comparing biomass concentration for the different absorption and scattering coefficient cases.	133
6.11	Visual comparison between different scaled bioreactors based on scaling up using Reynolds number from the bench-scale bioreactor of Karim et al. (2004). 135	135
6.12	Contour plots of velocity magnitude for different scale bioreactors	136
6.13	Contour plots of light intensity for different bioreactor sizes	137
6.14	Comparison of light intensity distribution within bioreactors at different scales using the same light absorption and scattering coefficients	137
6.15	Contour plots of photosynthetically active biomass (x_2) for different bioreactor sizes	138
6.16	Contour plots of biomass concentration for the different bioreactor sizes after 40 days of growth	139
6.17	Average concentration of biomass in the different sized bioreactors	140
6.18	Contour plots of different light intensities and their respective active biomass fractions	141
6.19	Average concentration of biomass for two different incident light intensities at the outer wall of the bioreactor; comparison with the results of the PN model.	142

Chapter 1

Introduction

Nomenclature

Abbreviations

AD	Anaerobic digestion
ADM	Anaerobic digestion model
ASM	Activated sludge model
CARPT	Computer automated radioactive particle tracking
CFD	Computational fluid dynamics
CT	Computed tomography
IAWPRC	International association on water pollution research and control
IWA	International water association
ODE	Ordinary differential equation
VFA	Volatile fatty acid
WWTP	Wastewater treatment processes

Bioreactors serve many different purposes in the modern world, from wastewater treatment and growth of microalgae, to brewing beer (Yamauchi et al., 1994) and producing drugs in the pharmaceutical industry (Fricke et al., 2013; Merchuk, 2003). As such, they are a vital part of the modern world for both environmental and health reasons. Wastewater treatment in particular is of vital importance in maintaining a clean environment in which to live. Without treatment the huge amount of wastewater produced both domestically and commercially would have a significant and detrimental affect on the environment.

To this end, experimental analysis and mathematical modelling of the flow characteristics within many different types of bioreactor have been performed. Experimental analysis

of mixing in bioreactors is inherently difficult with the need for non-invasive measuring techniques. Additionally, in situations where the reactor contents are opaque, light based measuring techniques are unusable. For example, Karim et al. (2004) used computer automated radioactive particle tracking (CARPT) and computed tomography (CT) scans to visualise the flow patterns within a gas-lift anaerobic digester with a central draft tube. The results from this work were later used to validate a computational fluid dynamics (CFD) model of the digester and develop the reactor design to improve the mixing performance (Karim et al., 2007). Due to the different reactor shapes and mixing methods around, CFD modelling of the mixing covers a wide range of reactor designs. CFD modelling work has covered many of these reactor designs and the different methods of mixing they employ, such as mechanically mixed (Aubin et al., 2004; Wu, 2010a; Joshi et al., 2011; Yu et al., 2011b; Bridgeman, 2012) and gas mixed (Mudde and Van Den Akker, 2001; Oey et al., 2003; Karim et al., 2007; Terashima et al., 2009; Wu, 2010b). CFD modelling of other aspects of fluid flow has also been done in an attempt to better understand aspects such as the effects of turbulence in reactors (Wu, 2010b, 2011; Joshi et al., 2011; Bridgeman, 2012; Coughtrie et al., 2013) and how the non-Newtonian rheology of the slurry in a reactor effects the mixing (Wu and Chen, 2008; Langner, 2009; Terashima et al., 2009; Latha et al., 2010; Wu, 2011). These models include a wide variety of fluid flow situations and with the inclusion of non-Newtonian fluid properties, the effects of biomass growth on the mixing.

In many reactor processes there is still debate as to how well mixed a reactor should be to produce the best results. Stroot et al. (2001) found that minimal mixing of an anaerobic reactor with high solids content provided stable conditions in comparison to a continuously mixed reactor. Vavilin and Angelidaki (2005) also found the preferred level of mixing to be dependent on similar conditions to Stroot et al. (2001) in that mixing was dependent upon the limiting reaction within the reactor. If methanogenesis is the rate limiting step in the reaction then a more minimal mixing is preferred in order to allow methanogenic bacteria to gather and be protected from acidogenesis. However if hydrolysis is the rate limiting step then more vigorous continuous mixing could allow for greater solid degradation and increased methane production Vavilin and Angelidaki

(2005). Turovskiy and Mathai (2006) however, suggest that due to the possible build-up of a scum layer on the surface of the slurry, preventing the biogas from escaping, mixing should be continuous.

There is a large body of work investigating biochemical reactions within AD and other wastewater treatment processes. This work has produced a number of biokinetic reaction models in the past 30 years. The first of these models and the one that set the standard in terms of format was the IWA Activated Sludge Model No.1 (ASM1) in 1987 (Henze et al., 1987). Since then there have been a number of revisions and extensions of the ASM1 model (ASM2, ASM2d, ASM3) as well as the development of the IWA Anaerobic Digestion Model No.1 (ADM1) in 2002 (Henze et al., 2000; Batstone et al., 2002b). Since their development the IWA ASM and ADM models have become the standard platform on which research into wastewater treatment processes is based. These models are complex and yet still don't fully cover all aspects of the reactions found in wastewater treatment processes. The models use Monod type kinetics for the growth and decay of biomass and substrates within a reactor but assume a bulk zero dimensional model in terms of the flow. This means that growth and decay are independent of any localised concentrations that may be found within a reactor, a situation which is not found in reality.

In algal photo-bioreactors there is also the additional issue of light penetration. As light can only reach a certain distance into the bioreactor it is important to maintain a constant exchange of biomass between the internal areas of the bioreactor and those areas where access to the necessary light is available. The efficiency of growth in a photo-bioreactor depends greatly on this light-dark cycle with the most efficient growth rate occurring when the cycle has a high frequency with a short light penetration depth (Richmond, 2004).

Although there has been some work toward creating models which couple both the fluid flow and biokinetic models they tend to be based on the use of compartmental modelling techniques where a separate grid produced based on some aspect of the flow model is created (Gresch et al., 2009; Alvarado et al., 2012; Nauha and Alopaeus, 2012). This new grid contains larger cells to reduce computational time, yet increase accuracy of the biokinetic model by giving a more accurate representation of the local biomass

concentrations in the reactor. There is however still a loss of accuracy as flow features not captured by the compartments will not be considered.

Therefore, in order to reliably predict the growth and decay of biomass in a bioreactor with a non-homogenous mixture, local concentrations of substrates and bacteria need to be known and accounted for in the growth model. For these local concentrations to be known will require the coupling of an accurate flow model – one able to capture the non-homogenous flow fields found in many bioreactors – and a biokinetic growth model that is calculated based upon local biomass and substrate data. These more comprehensive models combining mixing and growth in a more closely linked manner usual will hopefully aid in designing and operating reactors to be more efficient and stable.

1.1 Aims and objectives

A.1 Investigate soluble nutrient based biokinetic modelling methods.

O.1.1 Create a simple generic biokinetic model of the same form as those commonly used in bioreactor research (i.e. Monod kinetics) to evaluate the model methodology and their limitations as tools for predicting growth in bioreactors.

O.1.2 Investigate more complex models to determine if the additional complexity has any benefits.

A.2 Develop a coupled model for photosynthesis and nutrient based biokinetic growth

O.2.1 Investigate photosynthesis models with the aim of determining the effectiveness and accuracy of the modelling methods.

O.2.2 Develop a method of coupling a photosynthesis growth model with a nutrient based biokinetic model.

O.2.3 Investigate the effects the addition of the photosynthetic processes have on the biomass growth in the coupled model.

A.3 Determine whether computational fluid dynamics (CFD) can be used to accurately predict mixing and fluid flow characteristics in bioreactors and what the limitations of these models in relation to bioreactor are.

- O.3.1** Assess limiting factors of computational fluid dynamics model when used to simulate mixing in a typical bioreactor (i.e. gas driven anaerobic digestion reactor).
 - O.3.2** Assess and determine suitable modelling methods for use in predicting mixing in bioreactors (e.g. singlephase/multiphase)
 - O.3.3** Assess and determine suitable modelling methods for use in predicting mixing in bioreactors (e.g. singlephase/multiphase)
 - O.3.4** Assess limitations of available modelling tools and the possible approaches to creating a coupled CFD/biokinetic model.
- A.4** Develop a fully coupled model incorporating nutrient based biomass growth, photosynthetic biomass growth and mixing using CFD.
- O.2.1** Determine a methodology which can be used to coupled biokinetic models with CFD hydrodynamic models.
 - O.2.2** Create a coupled model which can be used for simulating growth of phytoplankton in a bioreactor with complex mixing and under different biokinetic growth conditions.
 - O.2.3** Investigate the effect different factors have on the model results and determine what advantages this new coupled model may have.

Chapter 2

Bioreactors and biological growth

Contents

2.1	Bioreactors and biological processes	7
2.2	Bioreactor Process Modelling	10
2.2.1	Biokinetic modelling strategies	10
2.2.1.1	Monod models	10
2.2.1.2	Cell quota (Droop) models	11
2.2.1.3	Mechanistic models	11
2.2.2	Light limited growth	12
2.2.2.1	Modelling light intensity within bioreactors	15
2.2.2.2	Modelling photosynthesis dependent growth	18
2.2.3	Hydrodynamic mixing	19
2.2.3.1	Modelling hydrodynamic mixing	20
2.3	Summary	22

Nomenclature

Symbols

I_K	Light saturation point
κ	Boltzmann constant
λ	Biomass maintenance coefficient
μ_m	Maximum specific growth rate
σ	Specific absorption coefficient
E_a	Activation energy
I_{av}	Activation intensity
I_{max}	Maximum specific light intensity
I_0	Specific light intensity
P_{max}	Peak photosynthesis rate
X_m	Maximum biomass
l	Distance from incident light intensity point
R	Ideal gas constant
T	Temperature
X	Biomass concentration

Abbreviations

AD	Anaerobic digestion
CFD	Computational fluid dynamics

2.1 Bioreactors and biological processes

Wastewater treatment is a vital part of the modern world; both for environmental and health reasons. Without treatment the huge amount of wastewater produced both domestically and by industry every day in the UK would have a significant detrimental effect on the environment and in particular the UK's waterways. Major impacts that untreated wastewater can include, oxygen depletion in water ways due to biological degradation of organic matter, health risks from waterborne pathogens and imbalance of nutrient content in waterways. These factors can result in significant impacts on the environment and ecology both surrounding as well as within waterways (DEFRA, 2012). In order to maintain this clean environment and treat all the water used, the UK water industry consumes approximately 1% of the UK's electricity (7703GWh/year) (Environmental Knowledge Transfer Network, 2008).

The effects of wastewater treatment methods are not however, limited only to sanitation and the maintenance of environmental balance in waterways. Due to the increased concern

regarding both the global environment and dwindling fossil fuel sources a drive toward finding reliable renewable clean sources of energy is occurring. In 2013 it is estimated that only 8.6% of world energy consumption comes from renewable sources, of that, 6.7% is hydroelectric and the other 1.9% a combination of all other sources of renewable energy. Of the rest nearly 87% of the world's energy consumption comes from fossil fuels (BP, 2013). Of the fossil fuels used in world energy production 33.1% is oil, this amount is continually rising with transport being the main reason for the increase; it is estimated that 116 million barrels a day will be used by 2030 (The Royal Society, 2008). Use of energy for transport is a large contributor to not only energy consumption but of greenhouse gas emissions as well. Although there are many renewable sources of energy around few have become widely used and all have limitations which have yet to be fully resolved.

One renewable source of energy being researched extensively is biofuels. Although biofuels such as biodiesel and bioethanol have been in production since the 1970's in some areas, the methods used in production rely mainly on crops such as sugar cane, sugar beet, soy bean, rapeseed, sunflower and palm oils (Galbe et al., 2007; Mata et al., 2010). Unfortunately the increasing demand for biofuels - which can be easily used as a substitute for petrol and diesel in cars - is pushing the limits of what can be produced through traditional means. As the crops used in biofuel production also form part of other markets there are limits to their availability. Another issue is the space requirement of such crops, as the biofuel crops use the same arable land as food crops there is only limited scope for production dedicated to supplying fuel. As such, research into alternative methods of producing biofuels has become a significant area of research interest with one of the main focus areas being the use of microalgae. As microalgae are not involved in the production of food and have a significant decrease in space requirements when compared to traditional biofuel crops, they are of significant interest. Additionally microalgae can be grown as part of the wastewater treatment processes providing nutrient removal from the wastewater and production of lipids for use as biofuels (Woertz et al., 2009). Although these methods are still being researched the idea of combining wastewater treatment and biofuel production is an enticing one.

Another source of renewable energy related to wastewater treatment processes is anaerobic

digestion (AD). Although forms of anaerobic digestions have been in use for thousands of years it is only in the last century that its use as both a method of treating sewage and of renewable energy production has been developed significantly. AD has found use in many countries, particularly those with large numbers of rural areas where access to more centralised sewage treatment and power supplies are limited. In both India and China significant numbers of small family anaerobic digesters are in use (Abbasi et al., 2012). There is also increased use of AD in the UK, this is mainly as a means of reducing the residual solids that need disposing of; the biogas by-product is generally used to heat the anaerobic digester to improve performance. Some of the larger plant however, are able to export the biogas off site for use in combined heat and power plants (DEFRA, 2012).

Both biofuels and AD are still being heavily researched however, with many areas of these processes requiring significant improvement in order to make their use economically viable as an energy source of the future. Although anaerobic digestion is already in some use as a means of slurry management, reduction of greenhouse gas (GHG) emissions and production of biogas for use in combined heat and power plants (CHP), there are still a number of physical and economic issues limiting its full integration into the UK farming and wastewater treatment industries (Bywater, 2011). Although the majority of the stumbling blocks for farmers adopting AD as part of their slurry management process are economic, there are still some issues with the reliability and efficiency of reactors.

Due to the complex nature of the processes occurring within wastewater treatment reactors the ability to design a reactor that is stable under all loading conditions is difficult. For example the most common cause of reactor instability and failure in anaerobic digesters is imbalance between the two main groups of bacteria. The acidogenic and methanogenic bacteria in an anaerobic reactor have significantly different physiologies, growth kinetics, and nutritional needs and prefer different environmental conditions in which to live (Chen et al., 2008). For these reasons maintaining a stable reactor is a difficult balancing act. These issues are further compounded by the distribution of the reactor contents. Suspended growth reactors contain free floating biological flocs of solid biomass. These flocs need to be suitably distributed throughout the reactor so that their interaction with the wastewater that is their food source is sufficient (Turovskiy and Mathai, 2006). For

this reason mixing and the flow of the fluid within the reactor are important factors to be considered in the design process. Understanding how the flow affects the growth and decay of biomass within the reactor can help with improving the efficiency of the processes.

2.2 Bioreactor Process Modelling

Modelling the processes (both biological and hydrodynamic) occurring within bioreactors is a challenging problem. As such numerous different approaches have been developed and tested, some with more success than others. A number of these modelling strategies are described here.

2.2.1 Biokinetic modelling strategies

There are three main modelling strategies for phytoplankton. These each have differing levels of complexity. The Monod model makes growth rate a direct function of the external nutrient concentration. The cell quota (Droop) modelling method uses the internal concentration of nutrients within the cells as the controlling factor for growth rate with an additional step in the model which accounts for nutrient uptake. More complex mechanistic models are also available where additional internal pools and feedback processes attempt to make the model more closely resemble the actual biological processes (Flynn, 2003).

2.2.1.1 Monod models

Monod models (Monod, 1942, 1949) developed in the 1940s to simulate the steady-state growth of microbes. Monod models although widely used suffer from several issues when compared to other methods. The solutions obtained using Monod equations for growth aren't always as accurate as other methods such as the cell quota model particularly when external nutrients are no longer available (Droop, 1968). This is particularly the case with multi-nutrient models, where, if a single nutrient becomes unavailable growth dependent on internal nutrient reserves is not possible.

2.2.1.2 Cell quota (Droop) models

Droop (1968) found that the specific growth rate of algae (*Monochrysis lutheri*) was not directly dependent on the substrate concentration in the growth medium but on the concentration within the cells (cell quota). For this reason Droop (1968) proposed a model of growth rate (hyperbolic) based on the internal cell quota, rather than the michaelis-menten-monod style of model which relies on the ambient nutrient concentrations. The cell quota model has been tested extensively since its conception comparing favourably to alternatives (Sommer, 1991; Droop, 2003). It has also been used in conjunction with a monod model to determine the nutrient uptake. When used to model co-limitation of nutrients Leibig's law of the minimum - growth is controlled by the scarcest resource - can be used to determine the limiting nutrient. Leibig's law along with the cell quota (growth) and monod (nutrient uptake) models have been used in several cases to model continuous and batch cultures with co-limiting nutrients (Davidson et al., 1999; Legovic and Cruzado, 1997; Klausmeier et al., 2004; Bougaran et al., 2010). When used in conjunction with the cell quota (growth) model the uptake model can require down-regulation through the use of an inhibition function.

2.2.1.3 Mechanistic models

A more complex methods for using in modelling phytoplankton growth is the use of mechanistic models. These models attempt to use the biochemical knowledge to include more biologically meaningful nutrient interactions. Mechanistic models as described here are those which contain active feedback mechanisms. In biochemistry feedback is the process which enables living organisms to control their growth and interact with physico-chemical processes. It is not possible to construct a full mechanistic model for phytoplankton growth due to lack of knowledge on the biochemical processes involved. Even if a full mechanistic model could be created for phytoplankton growth the complexity of the model would result in large computational requirements limiting the models use.

2.2.2 Light limited growth

Photosynthesis is the process through which energy is derived from sunlight on earth. The majority of life found on earth relies on photosynthesis – either directly or indirectly – to obtain the energy required for metabolic processes and growth. The process uses the energy obtained from sunlight in the form of photons to convert inorganic compounds to organic matter.

The term light here, refers to part of the electromagnetic spectrum, it is more accurately described as visible light, being that the term generally refers to electromagnetic wavelengths between 400 and 700 nanometres. This is the range visible to the human eye, hence the name visible light. Electromagnetic radiation including that in the visible spectrum takes the form of wave packets or photons which oscillate at different frequencies. One of the main components of photosynthesis are the pigment molecules (e.g. chlorophyll, carotenoids) which absorb the energy of the photons. The main pigments found in green plants and algae are chlorophyll a and b, which appear green in colour due to the wavelengths of light they are able to absorb. Figure 2.1 shows the absorption spectra for some of the main pigment molecules found in plant life on earth. Chlorophyll a and chlorophyll b pigment molecules (the two main photosynthetic pigments found on earth) are most effective in the ranges of 400nm to 550nm and 640nm to 700nm. This high level of photon absorption in these ranges is shown by the spikes in the graph on the activity spectrum in figure 2.1. The low levels of photon absorption in by these pigments at other wavelengths accounts for the green colour seen in most plant life - the photons at these wavelengths either passing through the or being reflected by the cells.

The term light intensity, as used in the modelling of photosynthesis, is usually described in terms of the incident light intensity and measured in $\mu\text{Molm}^{-2}\text{s}^{-1}$ (or sometimes $\mu\text{Em}^{-2}\text{s}^{-1}$). The $\mu\text{Em}^{-2}\text{s}^{-1}$ unit is defined as one mole of photons when used in studies of photosynthesis, and is equivalent to $\mu\text{Molm}^{-2}\text{s}^{-1}$. However the use of $\mu\text{Em}^{-2}\text{s}^{-1}$ as a unit of measure is ambiguous, as the Einstein unit is also defined as the amount of energy in one mole of Photons. The use of the Einstein unit should therefore be avoided to reduce the possibility of confusion as well as maintaining the use of SI units.

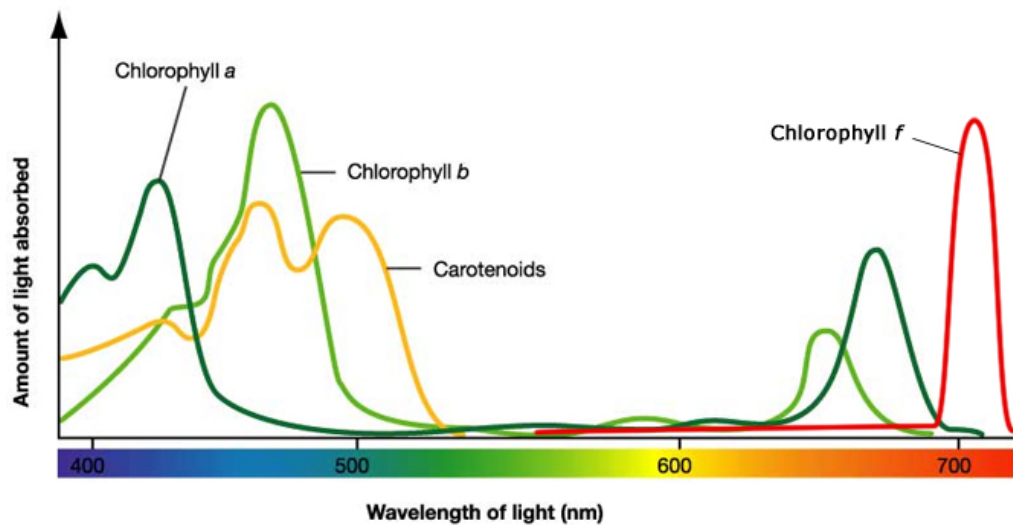


Figure 2.1: Absorption spectra for different photosynthetic pigments, chlorophyll a/b being the most common in plants

Photoautotrophs – organisms capable synthesising their own food with the aid of sunlight – evolved several billion years ago in the then CO_2 rich atmosphere of earth. The majority of photoautotrophic organisms in the modern era perform oxygenic photosynthesis where carbon dioxide and water are converted by sunlight into organic carbon molecules and oxygen. It is as a result of this process that earth has such an oxygen rich atmosphere compared to its younger self.

Oxygenic photosynthesis is generally broken down into two processes, the light dependent reactions and the light independent reactions (sometimes called dark reactions). Both of these processes take place in the light harvesting apparatus of the organism; areas known as chloroplasts in eukaryotic cells and as the photosynthetic membrane in prokaryotes. Plants and algae are eukaryotes (i.e. they contain membrane bound organelles/sub-structures which have specific functions in the same manner as the organs of the human body), whereas cyanobacteria – previously called blue-green algae – are prokaryotes (Allaby, 2012).

Light harvesting organelles, known as chloroplasts, are responsible for most of the processes occurring in photosynthesis in eukaryotic cells. Consisting of a double outer membrane (the envelope), and containing layers of folded membranes (the thylakoid system) surrounded by a protein rich gel (the stroma), chloroplasts form a complex

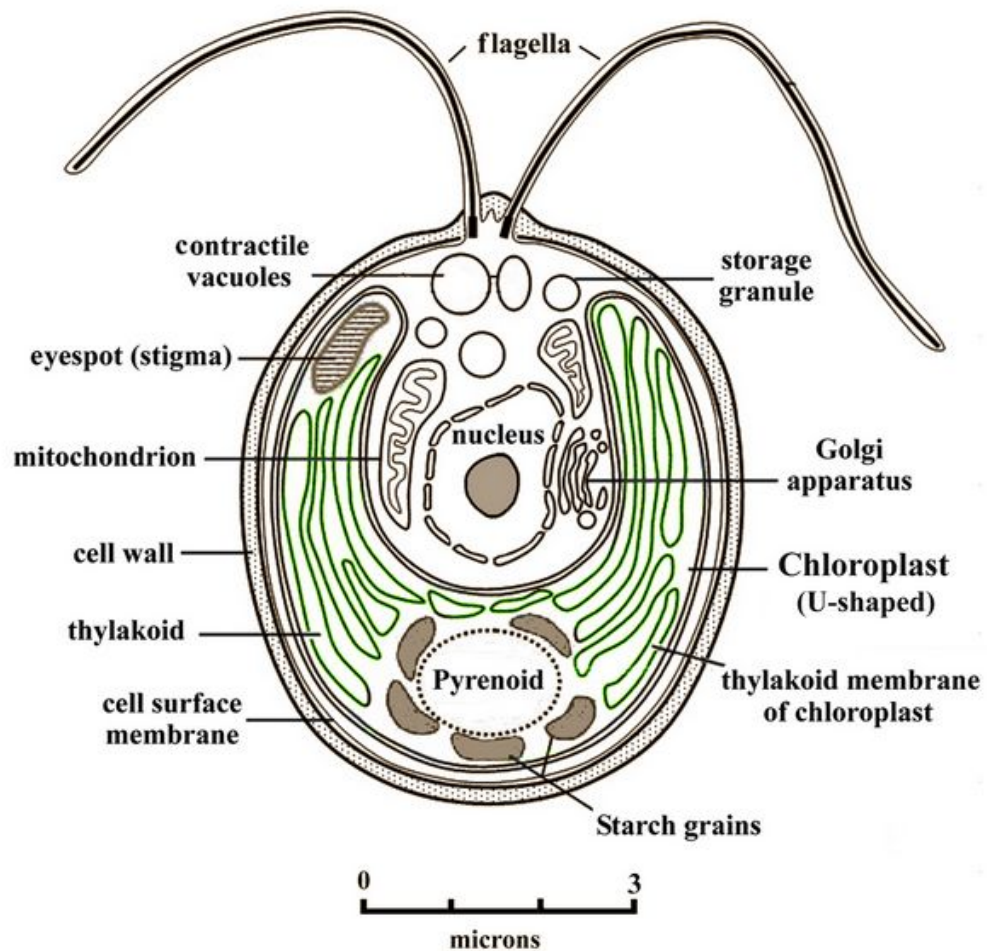


Figure 2.2: Structure of a typical eukaryotic algal cell *Chlamydomonas*; showing the main organelles including the chloroplast, mitochondrion and the thylakoid membrane. (Unknown, 2014)

system which converts inorganic carbon (CO_2) to organic carbon molecules (See figure 2.2. The two phases of photosynthesis take place in different parts of the chloroplast, the light dependent reactions are performed by the thylakoid membranes which results in the production of the enzyme NADPH₂ and adenosine triphosphate (ATP), a molecule often called the "molecular unit of currency" in biological energy transfer (Knowles, 1980). These are then used to drive the light independent reactions (commonly known as the Calvin-Benson cycle) which occur in the stroma (Bassham et al., 1950).

The main driving factor of the light dependent reactions is the absorption of photons of light by chlorophyll pigment molecules. The light dependent reaction can be further divided into two distinct systems commonly referred to as Photosystems I and II.

Photosystems I and II are systems of proteins and molecules which when stimulated by the absorption of light initiate an electron transport chain. The electron transport chain is initiated by the input of energy from photons of light. The energy results in oxidation (loss of an electron) of a pigment molecule which is passed down the electron transport chain to reduce the cofactor NADP to the enzyme NADPH and converting adenosine diphosphate (ADP) to ATP. These molecules are then used in the light independent reactions to convert carbon dioxide and other compounds into glucose and starch for the organism to use in growth and sustenance (Lawlor, 2001; Masojidek et al., 2004).

The processes involved in photosynthesis are highly complex making them difficult to model accurately. As such, most models of photosynthetic processes (which aim to simulate growth) are simple empirical relationships between the incident light intensity and the growth of biomass. There are models which attempt to calculate in detail the many reactions occurring within the cells (Zhu et al., 2013; Pettersson and Ryde-Pettersson, 1988; Laisk et al., 2006) but these all contain extremely complex chemical reaction processes which result in a large set of stiff ordinary differential equations (Zhu et al., 2013). As the models described in this work are designed to be part of a larger system modelling different aspects of the growth of microalgae it is considered unnecessary to include such highly complex models for the sake of a small increase in accuracy in one part of the overall process.

2.2.2.1 Modelling light intensity within bioreactors

There are two main considerations to be taken into account when modelling the growth of phytoplankton under light limiting conditions; the way in which light within a bioreactor is distributed and the biological growth based on the light available to the cells. Although both these points are equally important when constructing an accurate model for light limited growth, each can be considered separately when investigating the effect light has on the growth of biomass.

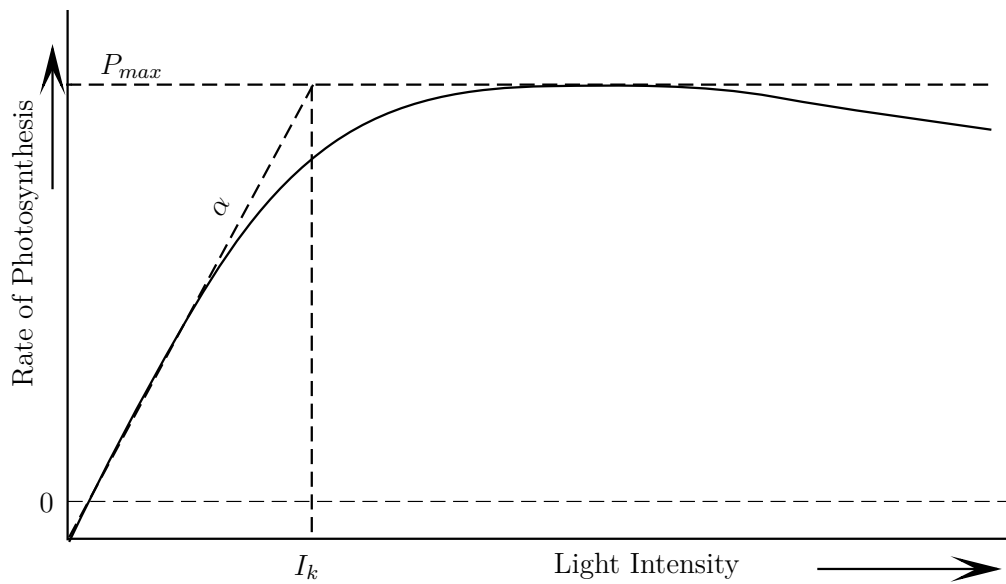


Figure 2.3: A Schematic representation of photosynthetic response to light intensity where α the initial slope of the curve is the maximum efficiency and the point where α meets the line P_{max} is known as I_K the light saturation point. After the peak photosynthesis rate at P_{max} the curve begins to decline, this is generally referred to as photoinhibition. (Figure reproduced from Masojidek et al. (2004))

Homogeneous light intensity models

Carvalho and Malcata (2003) used a Monod type model which considers light as a substrate of the growth process. Although the work described is mostly focused on the effects of varying environmental temperature on the rate of algal reaction rates they do include the effects of light intensity in the growth model in particular the combined effects of temperature and light intensity. The model uses the light intensity at the surface of the system to determine the photosynthetic rate, a simple approach which assumes the light intensity does not vary with distance from the surface of the reactor. The model structure produced from factorial experiments performed by the authors takes the form of a simple logistic growth model (Equation (2.1)). The maximum specific growth rate μ_m and the maximum biomass X_m are determined by the light intensity and temperature (equations (2.2) - (2.4)). K_1 - K_6 are empirical constants determined through the experimental work in Carvalho and Malcata (2003). T is temperature, I_o and I_{max} are the specific light intensity and maximum specific light intensity respectively. R is the ideal gas constant.

$$\frac{dX}{dt} = \mu_m X \left(1 - \frac{X}{X_m} \right) \quad (2.1)$$

$$\mu_m = \frac{K_1 L}{K_2 T + L} e^{-\frac{K_3 L}{RT}} \quad (2.2)$$

$$L = \frac{I_0}{I_m} \quad (2.3)$$

$$X_m = (K_4 + K_5 T) e^{-\frac{K_6 L}{RT}} \quad (2.4)$$

Bordel et al. (2009) used an alternative to the specific light intensity at the surface by using the average light intensity within the broth. This presumes that on average the cells within the culture are on average exposed to the same light intensity if the system is well mixed. The kinetic parameters for these models have however been shown to depend on the operating conditions of the system. Equations 2.5 and 2.6 show the light dependent growth equation and the maximum specific growth rate μ_m respectively. Where $\mu_{m,0}$ is a constant, E_a the activation energy and κ the Boltzmann constant.

$$\frac{dX}{dt} = \mu_m(T) \left(\frac{I_{av}}{K + I_{av}} \right) \quad (2.5)$$

$$\mu_m(T) = \mu_{m,0} e^{-\frac{E_a}{\kappa T}} \quad (2.6)$$

$$I = I_0 e^{-(\lambda_A X_A + \lambda_B X_B)} \quad (2.7)$$

The model developed by Bordel et al. (2009) was shown to fit the available experimental data well. Although this validation of the model is promising the simplicity of the model and low number of fitting parameters limit it to reactors running under similar conditions (e.g. hydraulic mixing conditions, photo-period and number of limiting nutrients). These limitations reduce the flexibility of the models necessitating the development of new models when operating conditions vary significantly from those under which the models were developed.

Intensity gradient models

In Type II models the light gradients within the broth are taken into account and their effect on the photosynthetic rate included. Each of these models consists of a biological growth model and coupled with a light distribution model to determine the local light intensity $I(l)$ at a distance l from the system surface. The most recent formulations of these models tend to use a simple Monod model for the biomass growth with the main variations being in the choice of light distribution model. These models are similar in structure to the incident intensity models with the addition of a function to calculate the light intensity inside the reactor. The types of function commonly used for this are the Beer-Lambert law (equation 2.8) or a two-flux model.

$$I(l) = I_0 \exp(-\sigma Xl) \quad (2.8)$$

2.2.2.2 Modelling photosynthesis dependent growth

Modelling the photosynthetic reactions which take place in algal cultures requires knowledge of a wide variety of influencing parameters. Béchet et al. (2013) divided the models they identified in literature into three categories based on the complexity and perceived accuracy of the model. Type I models were those which predicted the photosynthetic rate of the entire algae culture based upon the intensity of the light at the external surface of the system assuming that the light intensity remained constant throughout the medium. Type II light models account for the light gradients within the a bioreactor. These local rates are then used to calculate a global light intensity which is used to calculate the photosynthetic rate. Finally, type III models take account of the photosynthesis of individual algae cells and the light they receive as they travel through the broth to calculate a total photosynthetic rate for the culture, the most widely used of these are the three population or photosynthetic factory (PSF) models (Béchet et al., 2013). These three types of model are described in the following section. Figure 2.4 shows an outline of difference between the three types of model and how they compare in

complexity and capability.

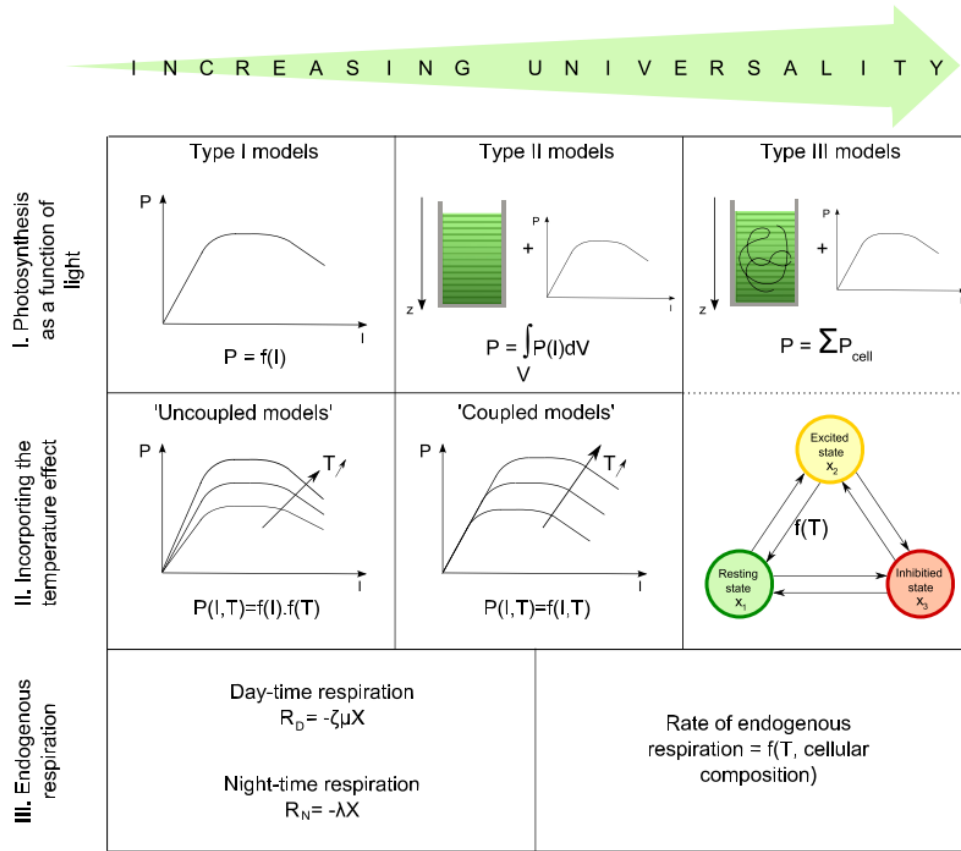


Figure 2.4: Schematic representation of models of algal productivity (P: rate of photosynthesis; I: light intensity; T: temperature; RD:rate of day-time respiration; μ : specific rate of photosynthesis; X: biomass cell concentration; ζ : proportionality constant; RN: night-time maintenance; λ :biomass maintenance coefficient)(Béchet et al., 2013).

2.2.3 Hydrodynamic mixing

The other major area of interest in bioreactor design is the effect of mixing and other hydrodynamic properties on performance and stability. There are a number of different factors which can influence the physical properties of a bioreactors, from the viscosity, which can have a significant effect on the mixing bioreactors (Babaei et al., 2015) to the dimensions of the tank, which significantly effect the light penetration depth in algal photobioreactors (Gupta et al., 2015). In general the mixing processes occurring within bioreactors has been shown to play an important role in the growth of biomass and the overall stability of many bioreactors. How well mixed the digestate in an anaerobic digester is will affect the pH balance throughout the bioreactor; as methane producing bacteria are highly sensitive to pH and even small variations can have a substantial effect careful

control is necessary. Mixing is also useful in preventing settling of suspended biomass and the build-up of a scum layer on the slurry surface which can inhibit the escape of the biogas. As such, a well-mixed homogeneous slurry is necessary for stable, controlled anaerobic digestion (Turovskiy and Mathai, 2006). Due to the nature of the slurries used in the bioreactors and the size of full scale industrial plants, experimental methods of determining the flow characteristics are expensive and complicated. Computational Fluid Dynamics (CFD) provides an excellent method of assessing the flow characteristics and mixing effectiveness under different bioreactor configurations without the time and expense of experimental studies.

2.2.3.1 Modelling hydrodynamic mixing

Over the past 25 years, research work describing numerical modelling of anaerobic bioreactors has been undertaken widely; with CFD being used to assess the mixing in bioreactors of different types.

This includes assessment and development of CFD procedures for use with mechanically mixed bioreactors (Joshi et al., 2011; Bridgeman, 2012). The modelling of mechanically mixed bioreactors has shown that the type of impeller and flow direction effects the mixing efficiency, with up mixing being found to be more efficient than down (Wu, 2010b; Aubin et al., 2004). Yu et al. (2011a) also investigated mechanically mixed bioreactors and showed the potential of helical ribbon impellers in the mixing of high solids content and provided insight into the minimum power requirements. Additionally, high solids bioreactors typically contain slurries of a non-Newtonian nature which have been shown to produce significantly different flow patterns to Newtonian fluids when modelled (Wu and Chen, 2008).

Numerical modelling has also been used to investigate flow and mixing in gas lift bioreactors, using tracers in full scale AD's to monitor mixing time and showing that for internal loop gas lift bioreactors transient oscillatory behaviour can sometimes be found (Terashima et al., 2009). Oey et al. (2003) showed that CFD modelling can be used to predict flow patterns in gas lift bioreactors. Mudde and Van Den Akker (2001) described how such modelling can be used to design and tune gas lift bioreactors and

Karim et al. (2007) used CFD to alter the flow characteristics and reduce the stagnation region, by modifying the geometry of a bench scale anaerobic gas lift digester. Meroney and Sheker (2014) also investigated gas mixing of an anaerobic bioreactor and compared its effectiveness when compared to vertical linear motion mixing with little difference in the quality of the mixing.

There has however been no definitive methodology produced defining the most appropriate models and approach to use in predicting the complex flow in bioreactors. One of the significant factors is that slurry being mixed in many bioreactors, including bench scale reactors from where experimental data is often obtained, has Reynolds numbers indicating flow to be in the transitional turbulent region. This type of flow is known to be difficult to model and many common turbulence models fail to correctly resolve the flow field. This is compounded by the non-Newtonian nature of many slurries which can significantly alter Reynolds numbers throughout the bioreactor where internal shear stresses vary. Published literature has not fully addressed the issue of which turbulence models are appropriate, nor what criteria should be adopted in selecting one for slurries of particular rheology. Failure to simulate turbulence correctly in non-Newtonian, transitional flow regimes may result in an inability to capture the important flow characteristics responsible for mixing reliably. There have been a small number of studies into the effects of turbulence modelling on the CFD results for anaerobic bioreactors (Wu, 2010a, 2011; Joshi et al., 2011; Bridgeman, 2012). The majority of CFD modelling of bioreactors tends to rely on the standard $k-\epsilon$ turbulence model with wall functions (Vesvikar and Dahhan, 2006; Meroney, 2009; Mudde and Van Den Akker, 2001; Oey et al., 2003).

In addition to the problems encountered with the choice of turbulence model and the viscosity of the fluid, many bioreactors are also multiphase in nature and in many cases including solid, liquid and gas phases (Karpinska and Bridgeman, 2016). In order to accurately model these complex fluid systems multiphase modelling is required which can be time consuming and computationally expensive. Wu (2010a) was able to model a gas mixing bioreactor using an Eulerian-Eulerian multiphase approach to model two gas lift bioreactors with different configurations finding that when including non-newtonian fluid properties gas mixing with the inclusion of a draft tube was insensitive to the changes in

fluid properties whereas the opposite occurred when the draft tube was excluded. Further extension of these multiphase models has been made for activated sludge processes by several authors. Lei and Ni (2014) developed an three phase activated sludge model for and oxidation ditch where physical processes for liquid, gas, and solid transport were included as well as biological processes for activated sludge processes. Another method of implementing biokinetic growth with fluid mechanics is through the use of smooth particle hydrodynamics (SPH) which has the advantage that modelling multiple different phases such as liquid and gas is inherently built into the modelling method (Meister et al., 2017).

2.3 Summary

The literature on bioreactor modelling shows that although a great deal of work has been done on the modelling of both the biokinetic processes within bioreactors as well as investigations into the physical aspects of the bioreactor contents, there is little in the way of work coupling these different aspects together. Although some effort has been made to develop models incorporating biokinetics and computational fluid dynamics for activated sludge processes no evidence in literature was found for coupled models incorporating algal biokinetics with both photosynthesis models and mixing performed using computational fluid dynamics. As such it is this area that will be focused on in this work with the aim being to develop a coupled model for algal biokinetics with the inclusion of photosynthesis modelling and coupled in a framework with a CFD model for hydrodynamic mixing.

Chapter 3

Nutrient limited biomass growth modelling

Contents

3.1	Introduction	24
3.2	Numerical methods for ordinary differential equations	25
3.3	Activated sludge treatment models	26
3.3.1	Simple activated sludge biokinetic model	28
3.3.2	Bulk Biokinetic Model Reactor	33
3.3.2.1	Time Dependent Solution	33
3.3.2.2	Steady-State Solution	34
3.4	Anaerobic digestion models	35
3.5	Phytoplankton models	38
3.5.1	Monod Kinetics	38
3.5.2	Cell Quota Modelling	40
3.5.3	Multi-Nutrient modelling	41
3.6	Summary	43

Nomenclature

Symbols

μ	Growth rate
μ_{∞}	Growth rate at infinite quota
μ_m	Maximum growth rate
θ	Hydraulic retention time
C	Nutrient concentration
f_P	Fraction of biomass yielding particulate products
k_H	Maximum specific hydrolysis rate
K_S	Half velocity constant
Q_i	Cell quota of nutrient i
$Q_{min,i}$	Minimum cell quota of nutrient i
R_K	Rate limit for increasing concentrations of C
S_i	Soluble nutrient i
V_{max}	Maximum nutrient uptake rate
V_r	Bioreactor volume
X	Insoluble biomass concentration
X_i	Insoluble biomass concentration of component i
Y_i	Yield of component i
a	Dilution rate
b	Specific decay rate
Q	Flow rate through bioreactor
a_L	Light absorption coefficient
σ_L	Light scattering coefficient

Abbreviations

AD	Anaerobic digestion
ADM	Anaerobic digestion model
ASM	Activated sludge model
CFD	Computational fluid dynamics
IAWPRC	International association on water pollution research and control
IWA	International water association
ODE	Ordinary differential equation
PAO	Phosphorus accumulating organisms
VFA	Volatile fatty acid
WWTP	Wastewater treatment processes

3.1 Introduction

The use of modelling in the prediction of biomass growth has been occurring for many years, the development of models for studying the growth of bacterial cultures by Monod (1949) has provided the basis for many of the biokinetic growth models still used today. In this chapter a number of these models are investigated and discussed in detail.

3.2 Numerical methods for ordinary differential equations

As the majority of the biokinetic models currently in use today take the form of ordinary differential equations (ODEs) it is important to understand how these equations are solved. Described here is one of the most widely used methods of solving systems of ODEs, the Runge-Kutta method. The method is used to solve initial value problems of the form shown in equation 3.1.

$$y' = f(x, y) \quad (3.1)$$

$$y(x_0) = y_0 \quad (3.2)$$

The Runge-Kutta method is what is known as a predictor-corrector method and works in the following way to find solutions to y_{n+1} . For each fixed step h taken by x the calculation for y uses a weighted average of the four values k_{1-4} (equations 3.5 - 3.8). Each of the values of k_i is in fact using a different method of estimating the next value of y by using either Eulers method or by estimating the slope of the solution at some point across the interval. Equations 3.3 - 3.8 describe the numerical method for the 4th order Runge-Kutta method.

$$x_{n+1} = x_n + h \quad (3.3)$$

$$y_{n+1} = y_n + (1/6)(k_1 + 2k_2 + 2k_3 + k_4) \quad (3.4)$$

Where:

$$k_1 = hf(x_n, y_n) \quad (3.5)$$

$$k_2 = hf(x_n + h/2, y_n + k_1/2) \quad (3.6)$$

$$k_3 = hf(x_n + h/2, y_n + k_2/2) \quad (3.7)$$

$$k - 4 = hf(x_n + h, y_n + k_3) \quad (3.8)$$

3.3 Activated sludge treatment models

In 1982 Activated sludge modelling had been undergoing research for about 15 years. It was at this point the International Water Association (IWA) - at the time known as the International Association on Water Pollution Research and Control (IAWPRC) - decided to form a task group to consolidate the currently known information and produce a modelling platform that could be used in future research into nitrogen removal activated sludge treatment processes. The main problems with the models currently available at this time were the lack of trust in the models and the lack of computational power available to run simulations. Additionally there was no standard format used in documenting these models, and the notation used was generally complex due to their complicated nature.

The result of the work of the IWA task group was the formation of the Activated Sludge Model No.1 (ASM1). This model was completed and published in 1987 (Henze et al., 1987, 2000) and has since been the basis of numerous other models used in research into wastewater treatment processes (WWTP), even if it has found little use in its original form. One of the main advantages of the ASM1 was the notation through which it was presented. The task group determined that the best method of easily presenting the large and complex model was to use a matrix form based on the work of Petersen (1965) and using notation from a previous task group in 1982 (Grau et al., 1982). An example of the matrix notation used for the ASM1 and the other wastewater models developed by the IWA task groups since then is shown in Figure 3.1. In line with the recommendations

of Grau et al. (1982), the notations in the matrix represent insoluble (X_i) and soluble (S_i) components, yield (Y), maximum growth rate ($\hat{\mu}$), half-velocity constant (K_S) and specific decay rate (b).

		→ Continuity					
Mass Balance	↓	Component →	i	1	2	3	Process Rate, ρ_j [ML ⁻³ T ⁻¹]
		j Process ↓		X_B	S_S	S_o	
		1 Growth		1	$-\frac{1}{Y}$	$-\frac{1-Y}{Y}$	$\frac{\hat{\mu}S_S}{K_S + S_S}X_B$
		2 Decay		-1		-1	bX_B
		Observed Conversion Rates ML ⁻³ T ⁻¹		$r_i = \sum_j r_{ij} = \sum_j v_{ij}\rho_j$			
			Biomass [M(COD)L ⁻³]	Substrate [M(COD)L ⁻³]	Oxygen (negative COD) [M(-COD)L ⁻³]		

Figure 3.1: Petersen Matrix form developed for ASM1, shows process kinetics and stoichiometry for heterotrophic bacterial growth in an aerobic environment, reproduced from (Henze et al., 2000)

Since the formation of the ASM1 three other IWA ASM models have been published due to advancements in the understanding of activated sludge processes. In 1995 due to better understanding of and the need to be able to model biological phosphorus removal as well as nitrogen removal a second ASM model was published (Henze et al., 2000). ASM2 built upon the knowledge gained through the development and use of ASM1 to include biological phosphorus removal, and to take into account the effects of internal cell structure on biomass growth; it was of the same form as ASM1 using the Petersen matrix format which allowed for publication in a manner with which researchers were already familiar. A further extension to ASM2 was to resolve the denitrification relating to phosphorus accumulating organisms (PAOs) a process that was not fully understood when the ASM2 was published. The ASM2d model which included this was published in 1999 (Henze et al., 2000). After ten years of use and research a number of short comings had become apparent in the IWA ASM1. Such issues as the inability to differentiate between aerobic and anoxic decay rates of nitrifiers which leads to issues predicting the max nitrification rates at

high solid retention times and where there are large anoxic reaction volumes. ASM1 also included the use of certain parameters which were in reality either not measurable or impossible to differentiate from other similar substances making validation of the model unreliable when concerning such parameters. Additionally certain kinetic expressions were either not included or found to have minimal effect on the overall modelling results. This increased understanding resulted in the publication of a revised model, the ASM3, in 1998 (Henze et al., 2000). The ASM3 was a revision of the ASM1 and therefore did not include the processes added to the ASM2d though it did include the internal cell structure modelling found in the ASM2. A few years after its publication an extension to the ASM3 model to include enhanced biological phosphorus removal based around the methods used in the ASM2d was implemented by Rieger et al. (2001). Work from 1994 - 2004 at Delft technical university in the Netherlands paid particular attention to the modelling of biological phosphorus removal. Over the ten years of its development the metabolic BioP model was integrated with the processes of the ASM2d model, validated using a number of experimental setups and found to be capable of modelling COD, Nitrogen and Phosphorus removal for full scale simulations (Meijer, 2004).

As ASM1 is made up of 13 species both soluble and insoluble in order to help understand the structure of the biokinetic models and their limitations a simple model was created by building up in stages the number of reactions being modelled. MATLAB was used as the development platform due to the built in ODE solvers available.

3.3.1 Simple activated sludge biokinetic model

A kinetic reaction model containing substrate limited biomass growth, biomass decay, and substrate utilisation is described. Figure 3.2 shows an over view of the process with cells representing substances (particulates and solutes) and the connecting arrows the processes converting one substance to another. Table 3.1 lists the substances and variables, their notation, units, and typical values obtained from literature (Henze et al., 2000).

The Petersen Matrix for the processes shown in Figure 3.2 is shown in Table 3.2, this format is commonly used for documenting rate equations and models, the Anaerobic Digestion Model 1 (ADM1) and the Activated Sludge Models (ASM's) are often written

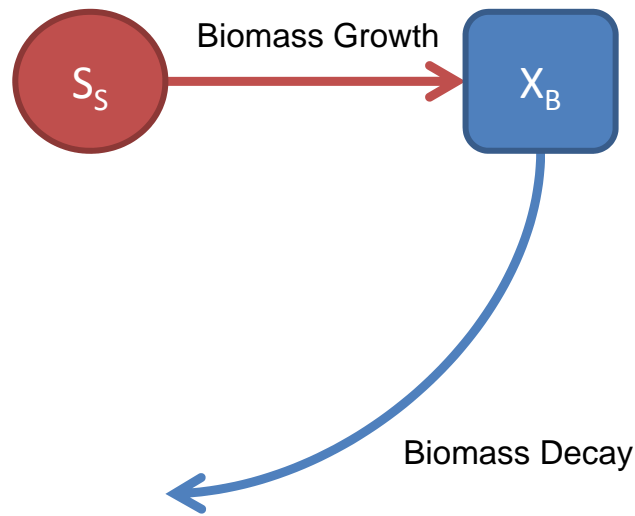


Figure 3.2: Process diagram of reaction model

this way.

Table 3.1: List of variables, units and typical values from literature

Definition	Notation	Units	Value
Readily biodegradable substrate	S_S	$gCODm^{-3}$	-
Active Biomass	X_B	$gCODm^{-3}$	-
Biomass yield	Y_B	$gcellCODformed.(gCODoxidized)^{-1}$	0.67
Max specific growth rate	μ_m	d^{-1}	6
Half saturation coefficient	K_S	$gCODm^{-3}$	20
Biomass decay rate	b_B	d^{-1}	0.62

Table 3.2: Petersen Matrix for processes

	S_S	X_B	ρ_j
1. Biomass Growth	$\frac{1}{Y_B}$	1	$\mu_m \left(\frac{S_S}{K_S + S_S} \right) X_B$
2. Biomass Decay	0	-1	$b_B X_B$

The model was solved using one of MATLABs built in ODE solvers ODE45. ODE45 is a 4th order accurate variable step Runge-Kutta solver for systems of ODEs. The function used to express the ODEs is shown in figure 3.3. To help with understanding the code shown the full ODE's of the processes are shown in equations (3.9) and (3.10). Table 3.1 contains the initial conditions used in the analysis of all models, this data was obtained from the IWA Task Group on Benchmarking of Control Strategies for WWTPs.

$$\frac{dS_S}{dt} = -\frac{1}{Y_B} \mu_m \left(\frac{S_S}{K_S + S_S} \right) X_B \quad (3.9)$$

$$\frac{dX_B}{dt} = \mu_m \left(\frac{S_S}{K_S + S_S} \right) X_B - b_B X_B \quad (3.10)$$

```

1 function dy=hvarfARM(t,y)
2 KS = 20.0; % Half Saturation coefficient
3 global mum %mum = 6.0; % Max specific growth rate
4 bB = 7.17e-6; % Biomass decay rate
5 YB = 0.67; % Biomass yield
6
7 dy = zeros(2,1); % a column vector - (dy(max),1)
8 dy(1) = (-1/YB)*mum*(y(1)/(KS+y(1)))*y(2); % Soluble substrate concentration
9 dy(2) = (1.0*mum*(y(1)/(KS+y(1)))*y(2)) + (-1.0*bB*y(2)); % Biomass concentration

```

Figure 3.3: Function for biokinetic model

Table 3.3: Initial conditions taken from IWA benchmark data set (IWA, 2005).

t	S_S	X_B	X_S
0	63.63455	31.425	224.352

Figure 3.4 shows the growth and decay of the biomass and soluble substrate with the varying line thickness representing different specific growth rate values. As is expected as the specific growth rate is increased the growth of the biomass increases in speed, this results in an increase in the rate of substrate usage but no change in the biomass decay rate. An extension of the previous kinetic reaction model was created consisting of substrate limited biomass growth, biomass decay, and substrate utilisation. Also included is partial hydrolysis of dead biomass. Figure 3.5 shows an over view of the process with cells representing substances (particulates and solutes) and the connecting arrow the processes converting one substance to another. Table 3.4 lists the substances and variables, their notation, units, and typical values obtained from literature.

To help with understanding the code shown in Table 3.5 the full Ordinary Differential Equations (ODE's) of the processes are shown in equations (3.11) - (3.13). Figure 3.6 shows the MATLAB code for the ODE system to be solved using the built in ODE45 (Runge-Kutta Method) solver. As can be seen, the addition of hydrolysis to the model not only adds an additional ODE due to the new slowly biodegradable biomass substance

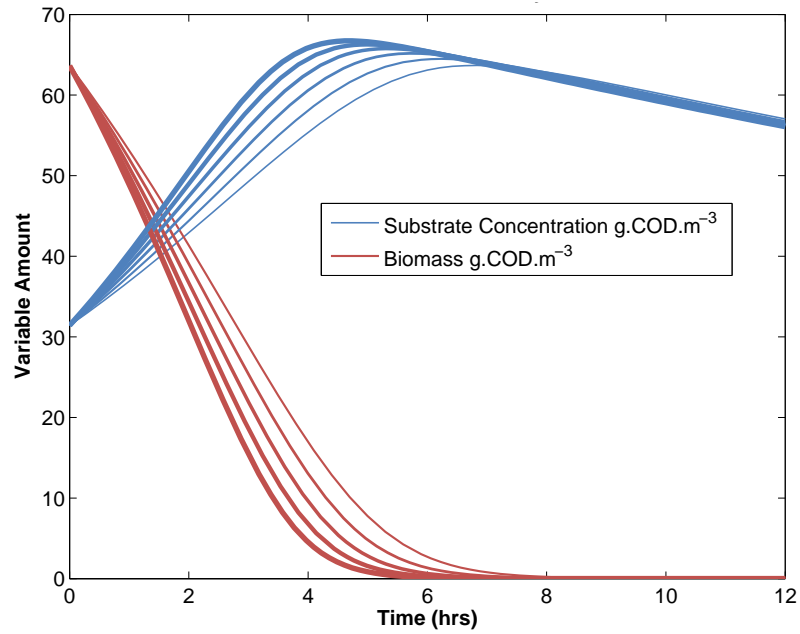


Figure 3.4: Plot of growth and decay of biomass and substrate usage. Line thickness variation based on specific growth rate variable increasing from a value of $\mu_m=6$ in increments of 10% upto $\mu_m=9$ where the thinnest line is the smallest value of μ_m .

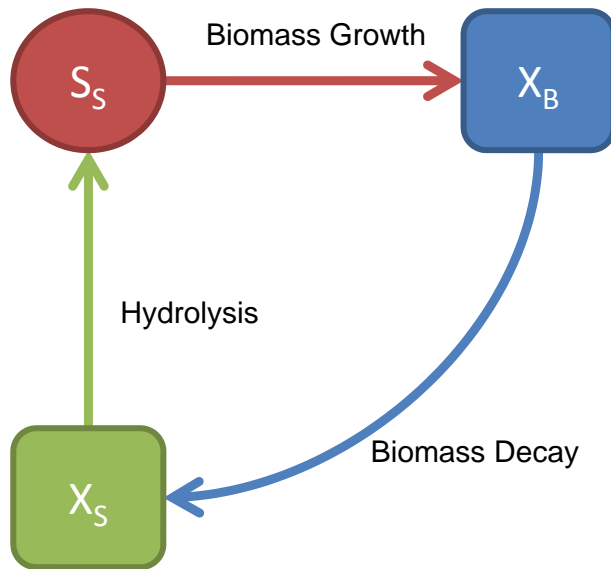


Figure 3.5: Process diagram of extended reaction model, including slowly biodegradable substrate

in the reactor, but increases the number of terms found in the substrate ODE as there is now an increase in the substrate as the slowly biodegradable biomass is hydrolysed.

Table 3.4: List of variables, units and typical values from literature

Definition	Notation	Units	Value
Readily biodegradable substrate	S_S	$gCODm^{-3}$	-
Active Biomass	X_B	$gCODm^{-3}$	-
Slowly biodegradable substrate	X_S	$gCODm^{-3}$	-
Biomass yield	Y_B	$gcellCODformed.(gCODoxidized)^{-1}$	0.67
Max specific growth rate	μ_m	d^{-1}	6
Half saturation coefficient	K_S	$gCODm^{-3}$	20
Biomass decay rate	b_B	d^{-1}	0.62
Fraction of biomass yielding particulate products	f_P	<i>dimensionless</i>	0.08
Max specific hydrolysis rate	k_H	d^{-1}	3
Digester Volume	V_r	m^3	100
Flow rate	Q	m^3s^{-1}	1

Table 3.5: Petersen matrix for extended biokinetic model

	S_S	X_B	X_S	ρ_j
1. Biomass Growth	$\frac{1}{Y_B}$	1		$\mu_m \left(\frac{S_S}{K_S + S_S} \right) X_B$
2. Biomass Decay	0	-1	$1 - f_P$	$b_B X_B$
3. Hydrolysis	1	0	-1	$k_H X_S$

$$\frac{dS_S}{dt} = -\frac{1}{Y_B} \mu_m \left(\frac{S_S}{K_S + S_S} \right) X_B + k_H X_S \quad (3.11)$$

$$\frac{dX_B}{dt} = \mu_m \left(\frac{S_S}{K_S + S_S} \right) X_B - b_B X_B \quad (3.12)$$

$$\frac{dX_S}{dt} = (1 - f_P) (b_B X_B) - k_H X_S \quad (3.13)$$

```

1 function dy=hvarfARM(t,y)
2 KS = 0.02; % Half Saturation coefficient
3 mum = 6.94e-5; % Max specific growth rate
4 bB = 7.17e-6; % Biomass decay rate
5 YB = 0.67; % Biomass yield
6 fP = 0.08; % Fraction of biomass yielding particulate products
7 kH = 3.472e-5; % Max specific hydrolysis rate
8
9 dy = zeros(3,1); % a column vector - (dy(max),1)
10 dy(1) = ((-1.0/YB) * mum * (y(1)/(KS+y(1))) * y(2)) + ((1.0) * (kH*y(3))); % Soluble
    substrate concentration
11 dy(2) = (1.0*mum*(y(1)/(KS+y(1))) * y(2)) + (-1.0*bB*y(2)); % Biomass concentration
12 dy(3) = ((1.0-fP) * (bB*y(2))) + ((-1.0) * (kH*y(3))); % Slowly biodegradable substrate

```

Figure 3.6: Function for extended biokinetic model

Figure 3.7 shows how the changes in the amount of decayed biomass yielding substrate affect the biomass growth and substrate amounts. When compared to previous model the inclusion of the hydrolysis terms shows how the decrease in substrate is slowed and that

a greater maximum value of biomass is achieved.

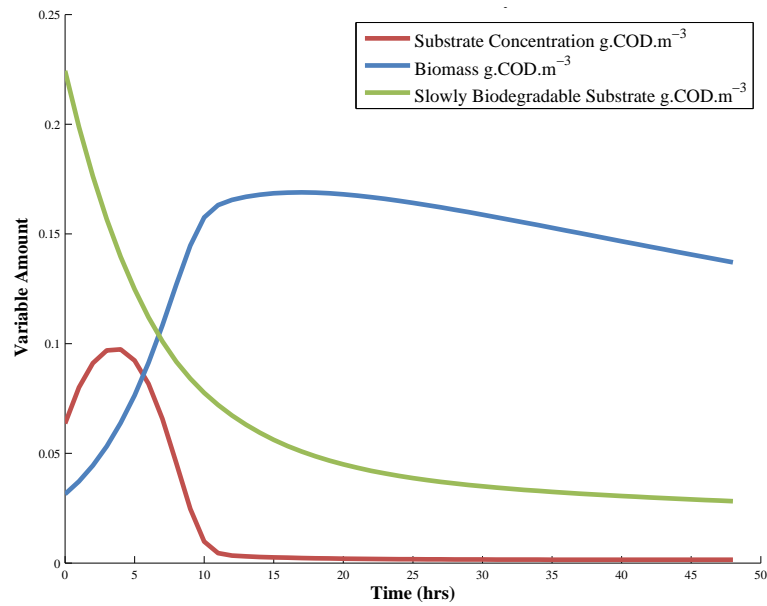


Figure 3.7: Plot of growth and decay of biomass and substrate usage with the addition of hydrolysis of dead biomass

3.3.2 Bulk Biokinetic Model Reactor

An extension of the previous batch model where it was assumed there was no flow in or out of the reactor after start is presented. The new reactor utilises the same kinetic model with substrate limited biomass growth, biomass decay, and substrate utilisation. Also included is partial hydrolysis of dead biomass. This model uses a mass balance approach to simulate a complete-mix reactor with a fixed flow rate.

3.3.2.1 Time Dependent Solution

Figure 3.8 shows an over view of the process with cells representing substances (particulates and solutes) and the connecting arrows the processes converting one substance to another.

The Petersen Matrix for the processes shown in Figure 3.8 is shown in Table 3.5. Figure 3.9 shows the time dependent development of substrate and biomass in the complete mix reactor. The solution reaches a full steady-state after approximately 20 days although it appears steady after 48hrs.

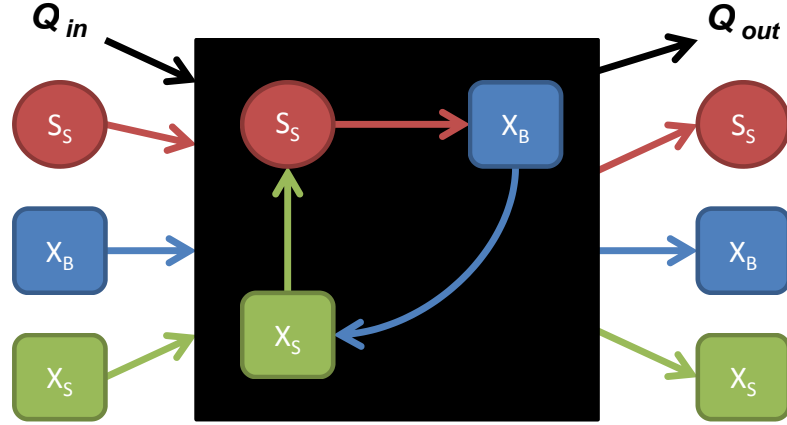


Figure 3.8: Process diagram of bulk reactor model

$$\frac{dS_S}{dt} - \frac{Q}{V_r} S_{S,in} + \frac{Q}{V_r} S_S = -\frac{1}{Y_B} \mu_m \left(\frac{S_S}{K_S + S_S} \right) X_B + k_H X_S \quad (3.14)$$

$$\frac{dX_B}{dt} - \frac{Q}{V_r} X_{B,in} + \frac{Q}{V_r} X_B = \mu_m \left(\frac{S_S}{K_S + S_S} \right) X_B - b_B X_B \quad (3.15)$$

$$\frac{dX_S}{dt} - \frac{Q}{V_r} X_{S,in} + \frac{Q}{V_r} X_S = (1 - f_P) (b_B X_B) - k_H X_S \quad (3.16)$$

The full Ordinary Differential Equations (ODE's) of the processes are shown in equations (3.14) - (3.16). These equations include the flow rate into and out of the domain and the solution to these equations is found using the Runge-Kutta ODE solver in MATLAB.

3.3.2.2 Steady-State Solution

A comparison between the time dependent solution presented above and its hand calculated steady state solution is shown for verification purposes. The mass balances for the microorganism and substrate biomass can be written as equations (3.14) - (3.16). For a steady-state solution $\frac{d\phi}{dt} = 0$, where ϕ is the variable of interest. Additionally, the hydraulic retention time is described by $\frac{V_r}{Q} = \theta$. As such equations (3.17) - (3.19) can be rearranged to:

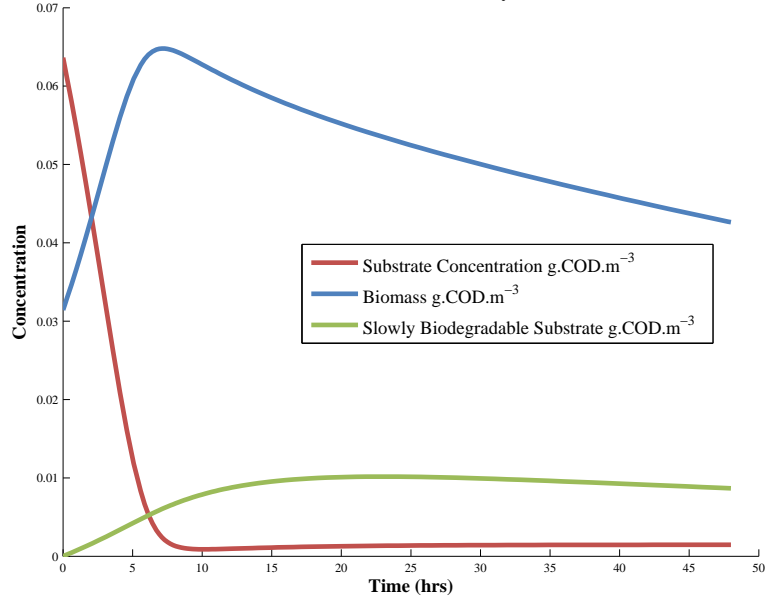


Figure 3.9: Time dependent concentration of variables in complete mix reactor

$$S_{S,in} - S_S - \theta \left(\frac{\mu_m S_S X_B}{Y_B (K_S + S_S)} - k_H X_S \right) = 0 \quad (3.17)$$

$$X_{B,in} - X_B + \theta \left(\frac{\mu_m S_S X_B}{K_S + S_S} - b_B X_B \right) = 0 \quad (3.18)$$

$$X_{S,in} - X_S + \theta ((1 - f_P) (b_B X_B) - K_H X_S) = 0 \quad (3.19)$$

Where the variables are S_S , X_B , and X_S , and all constants are the same as those in table 3.4.

Table 3.6: Steady-state vs transient solution comparison

	S_S (gCODm ⁻³)	X_B (gCODm ⁻³)	X_S (gCODm ⁻³)
Unsteady-State	2.8352	17.5787	4.0086
Steady-State	2.8654	17.5786	4.0086

3.4 Anaerobic digestion models

In 1998 a formal task group was formed by the International Water Association (IWA) to produce a model framework of the processes found in anaerobic digestion. Over the next few years the task group coordinated by Damien Batstone the model structure was

finalised and tested before being presented at the 9th IWA Anaerobic Digestion Conference in 2001. The model was published in 2002 and as expected was received well, mainly due to the success of the IWA ASM models previously published (Batstone et al., 2002b). Work on modelling anaerobic digestion had been done prior to the publication of the ADM1 but had seen limited use. This was possibly due to the large number of models available and the very specific nature of those models. The ADM1 although based upon these previous models was designed to be a general model and a platform upon which future research and model development could be done. The ADM1 is of the same format as the IWA ASM models, being presented using the Petersen matrix notation, making the model easy to understand and familiar to those already aware of the IWA ASM model. Two main types of reaction are included in the model, biochemical and physico-chemical. Biochemical reactions occurring both inside cells as well as enzyme driven extra-cellular reactions are modelled. Physico-chemical reactions such as gas-liquid transfer and ion association and disassociation are also included in the model.

The first stages of the AD process in the model are the extracellular enzyme driven disintegration and hydrolysis stages where the solid waste matter first disintegrates into particulate carbohydrates, proteins and fats before being hydrolysed to form sugars, amino acids and long chain fatty acids. These extracellular steps are followed by three internal cellular biological stages:

Acidogenesis - the degradation of sugars and amino acids to organic acids, hydrogen and carbon dioxide.

Acetogenesis - conversion of volatile fatty acids (VFAs) to acetic acid, hydrogen and carbon dioxide.

Methanogenesis - conversion of acetates to methane and carbon dioxide and the consumption of hydrogen.

These stages are more clearly shown in Figures 3.10 and 3.11.

Also included in the ADM1 model are a number of physico-chemical reactions. These are reactions that are not driven by enzymes. Physico-chemical reactions can generally be separated into three categories; Liquid-liquid reactions which include ion association and

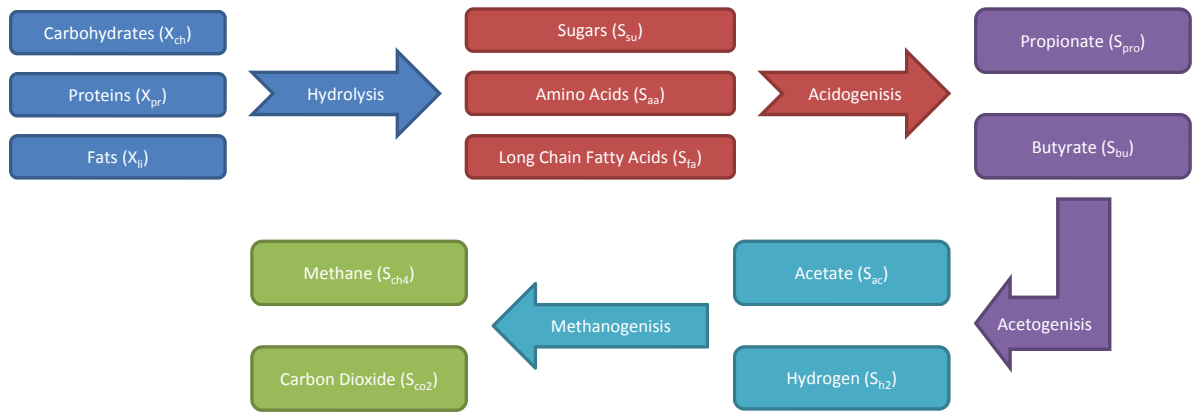


Figure 3.10: ADM1 process flow diagram

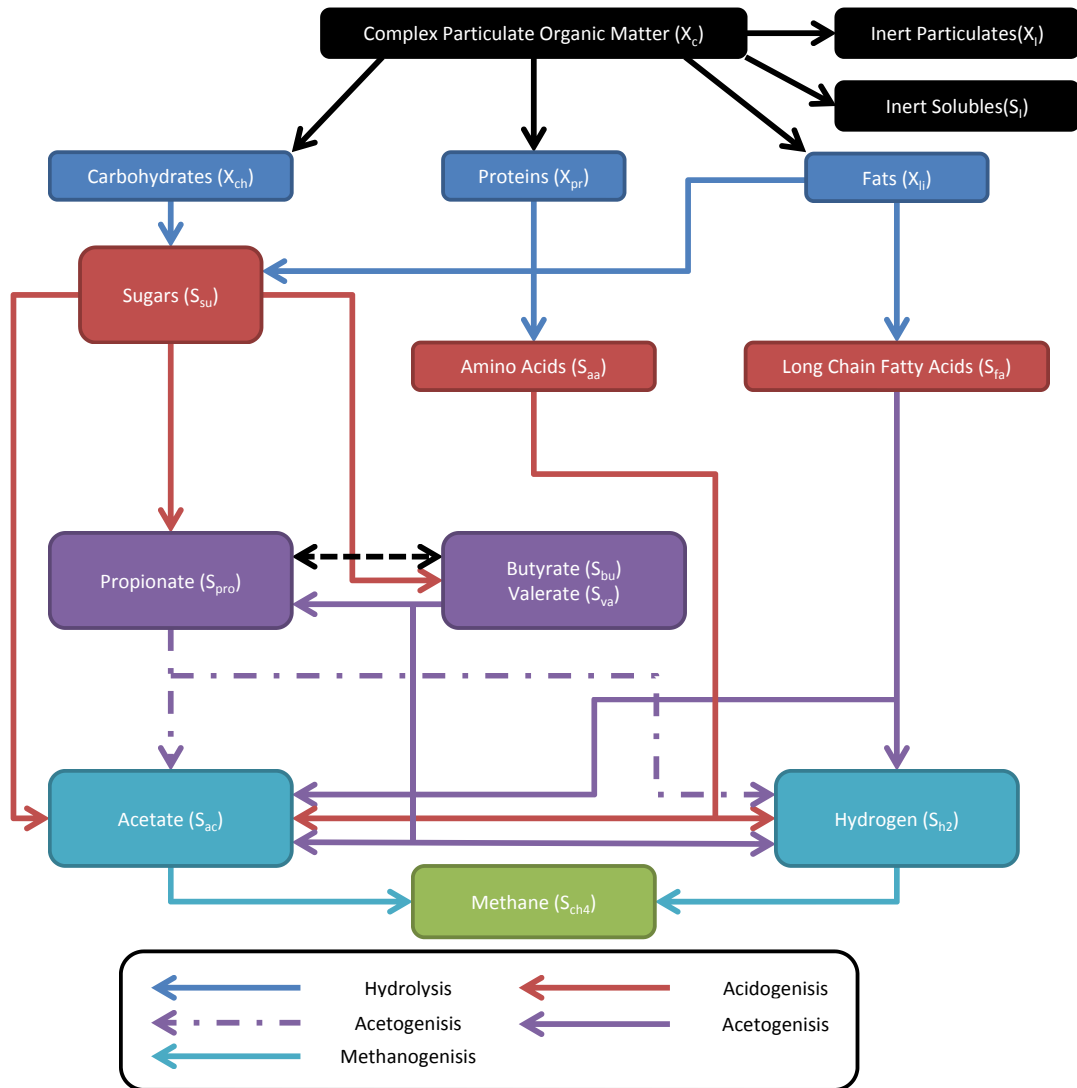


Figure 3.11: ADM1 model flow diagram of reactions (reproduced from Batstone et al. (2002a))

disassociation, solid-liquid transfer such as precipitation and gas-liquid transfer such as dissolving of gas in the solution. Solid-liquid transfer was not implemented in the ADM1 model due to the complex processes and the limited understanding of them at the time the model was created.

A number of extensions to the ADM1 model have been produced since its publication. The ADM1 has been used for improved remote monitoring, control and operation of high-rate anaerobic wastewater treatment plants (the TELEMAC project) (Batstone et al., 2006). A number of extension have been added to ADM1 including an extensive sulphate reduction extension by Fedorovich et al. (2003), this was very complex as it required modification to every part of the ADM1. An extension is also available for CaCO_3 which can be used as a template for other precipitation reactions as well (Batstone and Keller, 2003).

Other than adding extensions to increase the accuracy of the ADM1 extensions such as two-step models have been created to assess things like temperature impact (Elmitwalli et al., 2003) and for use modelling upflow Anaerobic Sludge Blanket reactors (Batstone, 2006). Simplifications to the model have also been made, usually to increase simulation speed, one such case is the implementation in GPS-X by (Copp et al., 2004). This simplification involved lumping together all soluble components more complex than acetate as soluble COD, and separating nitrogen states from COD states. Reduction although useful and valid does reduce specific capabilities of the model. GPS-X does however show an increase in simulation speed of 5x.

3.5 Phytoplankton models

3.5.1 Monod Kinetics

The development of one of the most widely known methods of modelling the growth of microbes was done by a French biologist Jacques Monod in the 1940s. Although he later shared the Nobel prize for medicine with François Jacob and André Lwoff "for their discoveries concerning genetic control of enzyme and virus synthesis" in 1965 (Nobel Media AB 2014, 2014), Monod started his career working on the growth of bacterial cultures for his doctoral degree (Monod, 1942). The result of this work is the Monod

equation; a hyperbolic equation (Equation 3.20) for the steady-state growth of microbes (originally bacterial cultures) where C is the nutrient concentration, R_K is the rate limit for increasing concentrations of C and C_I is the concentration at which the rate is half the maximum.

$$R = R_K \frac{C}{C_I + C} \quad (3.20)$$

The form this equation takes is very similar to that of the Michaelis-Menten kinetics of enzyme growth (Monod, 1949; Michaelis et al., 2011). It can be argued that Jacques Monod did not actually create a new modelling method, rather appropriating the enzyme kinetics model for use in the growth of micro-organisms. As such, review of literature shows both Monod and Michaelis-Menten kinetics as being applied for the growth of bacteria, microalgae and all manner of other plankton species.

The Monod kinetic models used for phytoplankton growth take the form shown in equation 3.21 where S is the limiting substrate, μ_{max} is the maximum growth rate and K_S is the value of S when $\mu/\mu_{max} = 0.5$ also known as the “half-velocity constant”. The value of $S/(S + K_S)$ is always between 0-1 for positive values of K_S . The values of S and K_S are empirical constants, dependent on the environmental conditions and algae species being grown; these constants require experimental data for calibration of the model.

$$\frac{dX}{dt} = \mu_{max} \frac{S_P}{S_P + K_P} \quad (3.21)$$

An important aspect of the Monod type models that must be noted is that they only consider aspects of processes external to the biomass - bacteria, phytoplankton, etc. - being modelled. This means that any storage of nutrients or processes which occur inside the biomass cells is not accounted for directly. In 1968 Droop (1968) found that in studying the growth limitation of vitamin B_{12} in the microalgae *Monochrysis lutheri* growth rate did not directly depend on the external nutrient concentration but upon the concentration

inside the cells, this discovery by Droop resulted in the development of the Cell Quota or Droop model of biokinetic growth.

3.5.2 Cell Quota Modelling

Cell quota model are two stage processes where external nutrients are taken up by the cells into “storage” before being used for biomass growth. This allows for growth to occur when external nutrients are depleted as long as there are available nutrients in the cells quota (storage).

Unlike the Monod kinetic models which calculate the growth of biomass using only a single equation which produces a hyperbolic growth curve dependent on only two empirical constants the cell quota model requires at least two separate equations for nutrient quota and biomass concentration. Both models use an additional equation for the nutrient concentration in the surrounding medium which is usually a Monod style equation. A simple cell quota model is shown in equations 3.22-3.23. The first expression in equation 3.22 - $(V_{max,P}S_P) / (S_P + K_P)$ - dictates the nutrient uptake of the cells using a Monod equation in the same manner as equation 3.21. The difference between the expressions is found in the use of $V_{max,P}$, the maximum nutrient uptake rate, rather than μ_{max} , the maximum algal growth rate.

$$\frac{dQ_P}{dt} = \frac{V_{max,P}S_P}{S_P + K_P} - \mu_{\infty} \left(1 - \frac{Q_{min,P}}{Q_P}\right) Q_P \quad (3.22)$$

$$\frac{dX}{dt} = \mu_{\infty} \left(1 - \frac{Q_{min,P}}{Q_P}\right) X \quad (3.23)$$

A number of different applications of the cell quota model can be found in literature with empirical constants for various different species of algae and environmental conditions. Its use is generally found in models where nitrogen and phosphorus are the nutrients of interest as these are stored internally in the cells and can be used when external availability is limited.

3.5.3 Multi-Nutrient modelling

The cell quota model can also be used for multiple nutrient limited growth. The assumption that the growth rate is determined by the limiting nutrient (i.e. the nutrient with the lowest cell quota). Which of the nutrients is limiting is determined through the use of Liebig's law of the minimum. The equations below show a multi-nutrient cell quota model for phosphorus and nitrogen limited growth. The model below was developed by Klausmeier et al. (2004) based on the experimental work of Rhee (1978). Table 3.7 contains the constants for the model and the initial conditions under nitrogen limited growth.

Parameter	Notation	Value	Units
Dilution rate	a	6.829E-6	s^{-1}
Nitrogen inflow concentration	$S_{in,N}$	1.8E5	$\mu\text{MolN.m}^{-3}$
Phosphorus inflow concentration	$S_{in,P}$	3.0E3	$\mu\text{MolP.m}^{-3}$
Maximum nitrogen uptake rate	$V_{max,N}$	3.947E-12	$\mu\text{MolN.Cell}^{-1}.s^{-1}$
Maximum phosphorus uptake rate	$V_{max,P}$	1.424E-13	$\mu\text{MolP.Cell}^{-1}.s^{-1}$
Nitrogen half saturation constant	K_N	5.6E3	$\mu\text{MolN}.s^{-1}$
Phosphorus half saturation constant	K_P	2.0E2	$\mu\text{MolP}.s^{-1}$
Growth at infinite quota	μ_{∞}	1.563E-5	s^{-1}
Minimum nitrogen cell quota	$Q_{min,N}$	4.54E-8	$\mu\text{MolN.Cell}^{-1}$
Minimum phosphorus cell quota	$Q_{min,P}$	1.640E-9	$\mu\text{MolP.Cell}^{-1}$
<i>Initial Conditions</i>			
Soluble nitrogen	S_N	1.8E5	$\mu\text{MolN.m}^{-3}$
Soluble phosphorus	S_P	3.0E3	$\mu\text{MolP.m}^{-3}$
Nitrogen cell quota	Q_N	4.54E-8	$\mu\text{MolN.cell}^{-1}$
Phosphorus cell quota	Q_P	1.64E-9	$\mu\text{MolP.cell}^{-1}$
Biomass concentration	X	1.0E7	Cells.m^{-3}

Table 3.7: Constants for the multi nutrient cell quota model (Klausmeier et al., 2004)

The multi nutrient cell quota model for nitrogen and phosphorus limited growth is implemented here and solved using the fourth order Runge-Kutta method. Two simulations were run and are compared against each other here, the first was under phosphorus limited growth where it is the phosphorus cell quota which dictates the growth rate of the biomass, the second under nitrogen limited growth. The minimum function which determines the growth of algal cells is found in the equations 3.26, 3.27 and 3.28. The implementation of this model can be found in appendix A.

$$\frac{dS_N}{dt} = a(S_{in,N} - S_N) - \frac{V_{max,N}S_N}{S_N + K_N}X \quad (3.24)$$

$$\frac{dS_P}{dt} = a(S_{in,P} - S_P) - \frac{V_{max,P}S_P}{S_P + K_P}X \quad (3.25)$$

$$\frac{dQ_N}{dt} = \frac{V_{max,N}S_N}{S_N + K_N} - \mu_\infty \min\left(1 - \frac{Q_{min,N}}{Q_N}, 1 - \frac{Q_{min,P}}{Q_P}\right) Q_N \quad (3.26)$$

$$\frac{dQ_P}{dt} = \frac{V_{max,P}S_P}{S_P + K_P} - \mu_\infty \min\left(1 - \frac{Q_{min,N}}{Q_N}, 1 - \frac{Q_{min,P}}{Q_P}\right) Q_P \quad (3.27)$$

$$\frac{dX}{dt} = \mu_\infty \min\left(1 - \frac{Q_{min,N}}{Q_N}, 1 - \frac{Q_{min,P}}{Q_P}\right) X - mX \quad (3.28)$$

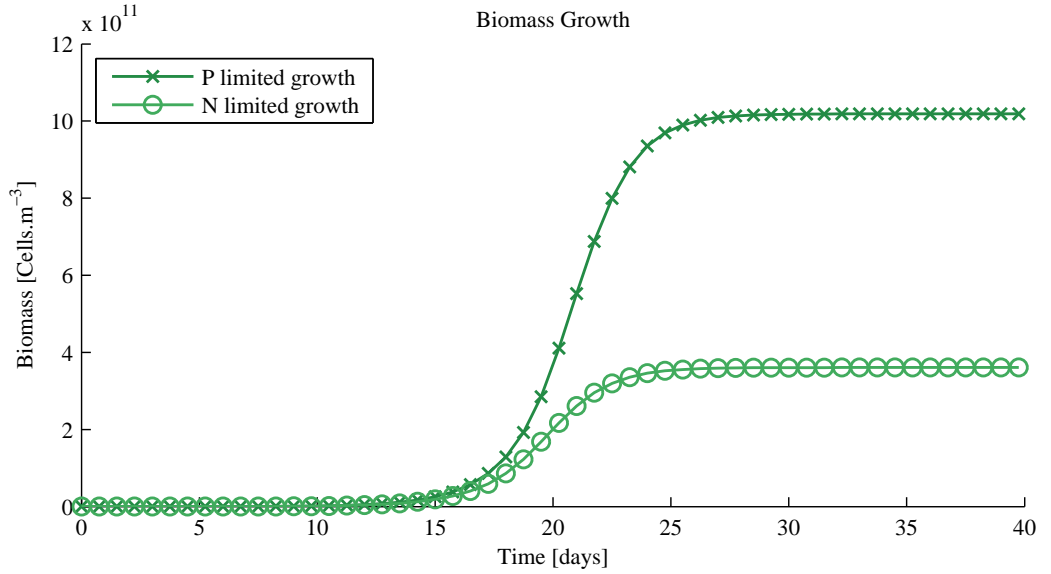


Figure 3.12: Biomass growth under nitrogen and phosphorus limited growth

The results of multi nutrient cell quota model show that nitrogen is a much more limiting substrate than phosphorus in terms of the biomass growth, this can be seen in the fact that the under phosphorus limited growth the biomass concentration at steady state is nearly three times that of the nitrogen under similar conditions.

3.6 Summary

The work in this chapter describes the different soluble nutrient based biokinetic models currently used in modelling bioreactors both in the fields of research and for industrial purposes.

A number of models were implemented to investigate the different aspects of the model. A simple activated sludge model based around monod kinetics was developed to include both growth based on soluble nutrients as well as decay and hydrolysis of biomass. This model was investigated as both a batch bioreactor with no flow in or out as well as continuous flow bioreactor using the mass balance method. Both time-dependent and steady state solutions were calculated and compared with each other to show how the results were in agreement.

A number of different models for soluble nutrient based biokinetic growth of algae were investigated and described. From literature it was determined that the most widely used was the cell-quota or Droop model which has been investigated extensively over many years and shown to provide more accurate results when compared to the simpler monod models.

An implementation of the cell-quota model with a multi-nutrient limiting function was implemented to with variable initial conditions to show how the least abundant nutrient determined the growth rate.

Chapter 4

Photosynthesis Modelling

Contents

4.1	Multiplicative modelling approach	46
4.1.1	Soluble nutrient model methodology	47
4.1.2	Photosynthesis modelling methodology	48
4.1.3	Nutrient uptake limiting model for low light conditions	50
4.1.4	Modelling light distribution within the culture volume	51
4.1.5	Validating the multiplicative model	52
4.2	The photosynthetic factory (PSF) model	58
4.2.1	Effects of light intensity function on the photosynthetic state of biomass	59
4.2.2	The relationship between light intensity and activated biomass in the photosynthetic factory model	63
4.3	Coupling the photosynthetic factory and cell quota models	65
4.3.1	Cell quota model with nutrient uptake limitation	66
4.3.2	Validation of PN coupled model using results from literature	70
4.3.3	Effects of varying the light intensity function on biomass growth	71
4.3.4	Effects on biomass growth of a light intensity function and the average of the function	74
4.4	Summary and conclusions	76

Nomenclature

Symbols

\bar{I}	Average irradiance through culture volume
ξ	Light attenuation rate
λ	Optical depth
μ	Growth rate
μ_∞	Growth rate at infinite quota
μ_m	Maximum growth rate
Ψ_{max}	Chlorophyll:Nitrogen proportional coefficient
ρ	Nutrient uptake rate
ρ_m	Maximum nutrient uptake rate
θ	Hydraulic retention time
$\tilde{\mu}$	Light limited growth rate
A_{Chl}	Chlorophyll light attenuation coefficient
A_B	Biomass attenuation coefficient
C	Nutrient concentration
f_P	Fraction of biomass yielding particulate products
I^*	Photoaddaption intensity of algal cells
K_{il}	Photosynthesis inhibition coefficient
k_H	Maximum specific hydrolysis rate
K_S	Half velocity constant
Q_i	Cell quota of nutrient i
$Q_{min,i}$	Minimum cell quota of nutrient i
R_K	Rate limit for increasing concentrations of C
S_i	Soluble nutrient i
V_r	Bioreactor volume
X	Insoluble biomass concentration
X_i	Insoluble biomass concentration of component i
Y_i	Yield of component i
a	Dilution rate
b	Specific decay rate
Chl	Chlorophyll concentration
Q	Flow rate through bioreactor
R	Baseline respiration rate
I	Light intensity
I_0	Incident light intensity
ϵ	Algal photoacclimation rate
x_1	Resting state for photosynthetic factor model
x_2	Active state for photosynthetic factor model
x_3	Inhibited state for photosynthetic factor model

Abbreviations

AD	Anaerobic digestion
ADM	Anaerobic digestion model
ASM	Activated sludge model
CFD	Computational fluid dynamics
IAWPRC	International association on water pollution research and control
IWA	International water association
ODE	Ordinary differential equation
VFA	Volatile fatty acid
WWTP	Wastewater treatment processes
PN	Photosynthesis nutrient

Incorporating the effects of light on phytoplankton growth into an overall model of the biomass growth can be a complex undertaking; this is especially true when there are several non-independently limiting factors effecting the biomass growth. In this chapter two different methods of including the effects of limited light intensity on the photosynthesis of algal biomass are described, implemented and evaluated against experimental results of phytoplankton growth under different light conditions (e.g. a diurnal light intensity cycle). The first, a multiplicative approach developed by Bernard (2011), considers and includes a number of different factors which can affect the photosynthesis of the phytoplankton (i.e. photoinhibition, light absorption and photoacclimation) along with a single soluble nutrient (Nitrogen) as a limiting factor independent of light. This model is described in some detail and then implemented to reproduce the work of Bernard (2011) comparing the model with experimental results obtained by Flynn et al. (1994); the model is then further validated using the experimental data produced by Davidson et al. (1992).

The second modelling method uses the concept of photosynthetic factories (states) determined by the light intensity to calculate the growth rate of the biomass. This method, first proposed by Eilers and Peeters (1988), considers three possible states for the cells in relation to photosynthetic process. The three states - resting (x_1), active (x_2) and inhibited (x_3) - calculated based on the light intensity, determine the fraction of biomass which is able to grow.

4.1 Multiplicative modelling approach

The multiplicative approach used by Bernard (2011) in the development of an algal growth model including growth limited by both soluble nutrients (Nitrogen) and light,

incorporates a number of photosynthetic processes that have been determined to effect the growth rate of phytoplankton.

4.1.1 Soluble nutrient model methodology

The approach used to model the growth due to Nitrogen concentration is based around that of a single nutrient cell quota model under nitrogen dependent growth (Droop, 1968). The basic structure of the model on which all subsequent functions are built is shown in equations 4.1-4.3 where a is the dilution rate, S_N the soluble Nitrogen, $S_{in,N}$ the inflow concentration of soluble Nitrogen, Q_N the cell nitrogen quota, X the biomass concentration, R the baseline respiration rate, and $\mu(Q_N)$ the growth rate as a function of cell quota; all other constants are defined in table 4.1.

$$\frac{dS_N}{dt} = a(S_{in,N} - S_N) - \rho(S_N)X \quad (4.1)$$

$$\frac{dQ_N}{dt} = \rho(S_N) - \mu(Q_N)Q_N \quad (4.2)$$

$$\frac{dX}{dt} = \mu(Q_N)X - aX - RX \quad (4.3)$$

Where the functions for $\rho_m(S_N)$ and $\mu(Q_N)$ are:

$$\rho(S_N) = \rho_m \left(\frac{S_N}{S_N + K_{s,N}} \right) \quad (4.4)$$

$$\mu(Q_N) = \mu_\infty \left(1 - \frac{Q_{min,N}}{Q_N} \right) \quad (4.5)$$

With $Q_{min,N}$ being the minimum Nitrogen cell quota required for growth to occur and μ_∞ being the growth rate at a theoretical infinite quota.

This basic nutrient dependent growth model was adapted by Bernard (2011) to incorporate cell respiration; this needs to be considered in the case of high density cultures where a fraction of the phytoplankton may be in darkness at any time. The respiration rate, including both baseline respiration (the minimum respiration rate required for basic function) and respiration due to biosynthesis, are included to account for areas (within the bioreactor) and periods where light is so low that the growth rate is lower than the

respiration rate (Geider et al., 1998; Ross and Geider, 2009). The respiration rate due to the baseline function (R) can be considered proportional to biomass while biosynthesis respiration is generally considered to be included in the "net growth rate".

Parameter Name	Symbol	Value	Unit
Light limited growth rate	$\tilde{\mu}$	1.7	day^{-1}
Minimum Nitrogen Cell Quota	$Q_{min,N}$	0.05	$gNgC^{-1}$
Maximum Nitrogen Cell Quota	$Q_{max,N}$	0.25	$gNgC^{-1}$
	K_{sI}^*	1.4	$\mu mol m^{-2} s^{-1}$
Photosynthesis Inhibition Coefficient	K_{il}	295	$\mu mol m^{-2} s^{-1}$
Maximum Nitrogen Uptake Rate	ρ_m	0.073	$gNgC^{-1} day^{-1}$
Half Saturation Constant	K_s	0.0012	gNm^{-1}
Respiration Rate	R	0.0081	day^{-1}
Proportional Coefficient Chl:N	Ψ_{max}	0.57	$gChlgN^{-1}$
	k_I^*	63	$\mu mol m^{-2} s^{-1}$
Chl Light Attenuation Coefficient	A_{Chl}	16.2	$m^2 gChl^{-1}$
Biomass Light Attenuation Coefficient	A_B	0.087	m^{-1}

Table 4.1: Constants for multiplicative photosynthesis model obtained through experimental analysis as described by Bernard (2011)

4.1.2 Photosynthesis modelling methodology

The photosynthetic processes are included in a multiplicative manner as a function of light intensity I within the biomass growth rate term $\mu_{\infty}(I)$ which replaces and includes the previous growth rate at infinite quota term μ_{∞} . The different photosynthetic processes included in the model are described below and include functions for photoinhibition, pigment dynamics, photoacclimation and light distribution within the culture.

Photoinhibition is a process which occurs at high light intensities when surplus energy absorbed by the cells resulting in damage to the photosynthesis centres of the cells (Zonneveld, 1998). Bernard (2011) account for photoinhibition using the kinetic model of Eilers and Peeters (1988, 1993) shown in equation 4.6, where K_{iI} is the inhibition coefficient which when combined with the variable K_{sI} defines $I_{opt} = \sqrt{K_{sI}K_{iI}}$ for which $\mu(I)$ is greatest. Photoacclimation the process by which long term acclimatisation of the phytoplankton to a particular light intensity effects the PI curve (figure 4.1) is also considered and is accounted for through the variable K_{sI} as shown in equation 4.7; where

θ is the initial chlorophyll/biomass ratio ($\theta = Chl/X$).

$$\mu_{\infty}(I) = \tilde{\mu} \frac{I}{I + K_{sI} + I^2/K_{iI}} \quad (4.6)$$

$$K_{sI} = \frac{K_{sI}^*}{\theta} \quad (4.7)$$

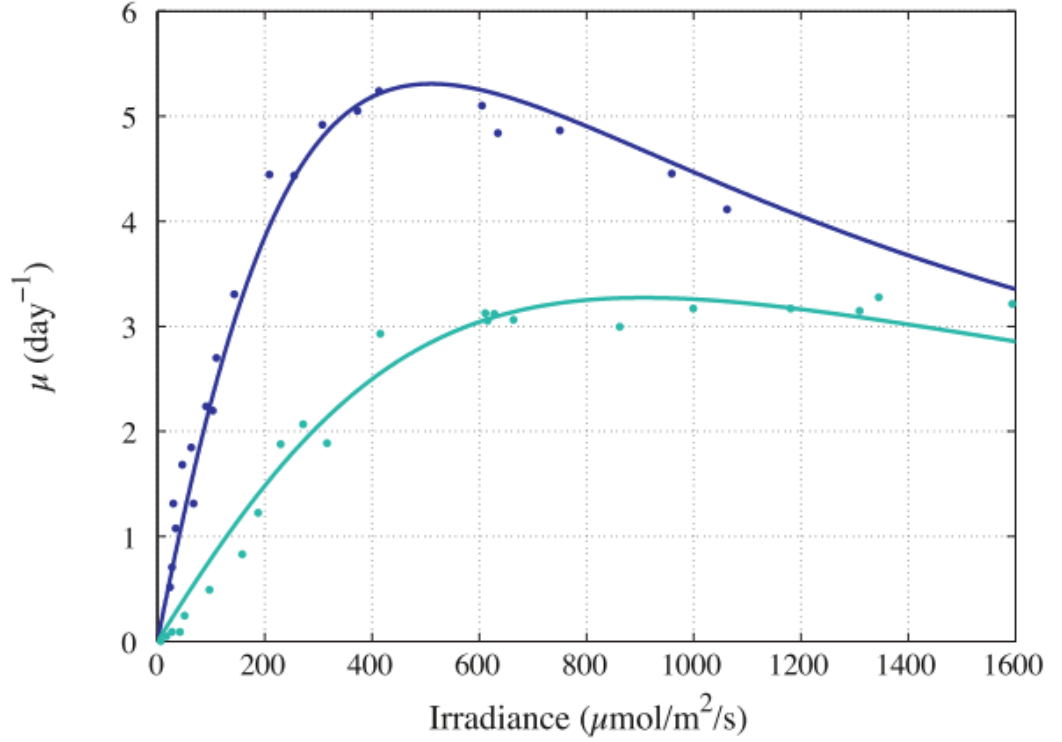


Figure 4.1: Photoacclimation of algae species *Skeletononema costatum* at low light ($I_L = 50 \mu\text{molm}^{-2}\text{s}^{-1}$, dark blue points and lines) and at high irradiance ($I_H = 1200 \mu\text{molm}^{-2}\text{s}^{-1}$, light blue points and lines) reproduced from (Bernard, 2011; Anning et al., 2000)

In order to predict the effect of biomass concentration on the light field within the culture - so as to be able to account for changes in light intensity within the bioreactor - a model of the pigment dynamics is required. The assumption that chlorophyll (Chl) concentration is linearly correlated to particulate nitrogen XQ (Laws and Bannister, 1980) is made, this results in equation 4.8 for Chl concentration of a culture photoacclimated at a light intensity I^* .

$$Chl = \Psi(I^*) XQ \quad (4.8)$$

where:

$$\Psi(I^*) = \Psi_{max} \frac{K_{I^*}}{I^* + K_{I^*}} \quad (4.9)$$

and I^* represents the photoadaptation of the cells to different light intensities described in equation 4.10, where \bar{I} is the average irradiance through the culture volume (i.e. between the surface and the maximum distance from the incident irradiance point) defined in more detail in section 4.1.4 and ϵ is the photoacclimation rate.

$$I^* = \epsilon \mu(Q, I) (\bar{I} - I^*) \quad (4.10)$$

4.1.3 Nutrient uptake limiting model for low light conditions

A further addition to the cell quota nutrient uptake model is required when including light limited growth to account for maximum nutrient cell quota, limiting the uptake rate under conditions of no light where growth can not occur. As the maximum cell quota is defined as:

$$Q_m = Q_{min} + \frac{\rho_m}{\mu_\infty} \quad (4.11)$$

the inclusion of photosynthesis as a limiting factor on the growth rate $\bar{\mu}$ results in the following change to equation 4.11:

$$Q_m(I) = Q_{min} + \frac{\rho_m}{\mu_\infty(I)} \quad (4.12)$$

which under conditions of no light ($I=0$) results in a zero growth rate ($\bar{\mu}(0) = (0)$) and thus an infinite maximum quota, an undesirable and unphysical condition for the model. As such it is necessary to include a limiting factor in the nutrient uptake rate to account for maximum cell quota when growth is reduced to zero in darkness. This limiting factor is included in the function for $\rho(S)$ in equation 4.4 resulting in equation 4.13. This new

addition to the function produces a tail off effect as the cell quota approaches Q_l .

$$\rho(S) = \bar{\rho} \frac{S}{S + K_s} \left(1 - \frac{Q}{Q_l}\right) \quad (4.13)$$

4.1.4 Modelling light distribution within the culture volume

The final problem of interest in the model of Bernard (2011) is the distribution of light within the culture. As the model is based on a mass balance approximation and considers the bioreactor to be homogeneously mixed it is necessary to form an approximation to the change in light intensity over the distance from the incident irradiance point and the maximum distance from that point in the reactor. For this a Beer-Lambert approximation is used. The Beer-Lambert approximation assumes an exponential decrease in the light intensity as distance from the incident location increases with a linear relationship to biomass concentration (equation 4.14).

$$I(z) = I_0 e^{-\xi z} \quad (4.14)$$

The light attenuation rate, ξ , is mainly dependent on the chlorophyll content and the biomass concentration and can be defined as $\xi = A_{Chl}Chl + A_B X + c$ where A_{Chl} and A_B are light attenuation coefficients for chlorophyll and biomass respectively and c is the background turbidity coefficient (the cloudiness of the growth medium on its own). The light attenuation rate is used to calculate the optical depth of the medium $\lambda = \xi L$, which describes how efficiently the light is absorbed. Using this it is possible to calculate an average value for the irradiance of the culture by integrating equation 4.14 from 0 to L (L being the maximum depth) resulting in the following equation:

$$\bar{I} = \frac{I_0}{L} \int_0^L e^{-\xi z} dz = \frac{I_0}{\lambda} [1 - e^{-\lambda}] = \frac{I_0 - I(L)}{\ln(I_0/I(L))} \quad (4.15)$$

where $\bar{\mu}$ contains all the previously described functions for defining the photosynthetic

growth rate in the following form:

$$\bar{\mu} = \tilde{\mu} \frac{2K_{iI}}{\lambda\sqrt{\Delta}} \arctan \left(\frac{I_0 (1 - e^{-\lambda}) \sqrt{\Delta}}{2I_0^2 e^{-\lambda} + I_0 (1 + e^{-\lambda}) K_{iI} + 2I_{opt}^2(\theta)} \right) \quad (4.16)$$

where $\Delta = 4I_{opt}^2(\theta) - K_{iI}^2$.

Finally when all the different parts of the model are combined, the resulting system of equations 4.17-4.20 is obtained.

$$\frac{dS_N}{dt} = a(S_{N,in} - S_N) - \rho_m \frac{S_N}{S_N + K_{s,N}} \left(1 - \frac{Q_N}{Q_{max,N}} \right) X \quad (4.17)$$

$$\frac{dQ_N}{dt} = \rho_m \frac{S_N}{S_N + K_{s,N}} \left(1 - \frac{Q_N}{Q_{max,N}} \right) - \bar{\mu} (Q_N - Q_{min,N}) \quad (4.18)$$

$$\frac{dX}{dt} = \bar{\mu} \left(1 - \frac{Q_{min,N}}{Q_N} \right) X - aX - RX \quad (4.19)$$

$$\frac{dI^*}{dt} = \bar{\mu} \left(1 - \frac{Q_{min,N}}{Q_N} \right) (\bar{I} - I^*) \quad (4.20)$$

4.1.5 Validating the multiplicative model

In order for the model described above to be considered accurate and applicable to real world applications validation of the results must be performed. Therefore, the model is implemented and solved here using numerical methods suitable for the solving of systems of ordinary differential equations (ODEs). These numerical methods are described in more detail in section 3.2; in this case the Runge-Kutta family of methods is used to solve the problems as they provide a good compromise between efficiency and accuracy and are well established numerical methods. The solving of the model was performed using the numerical computing environment MATLAB using the ode23 solver a 3rd order Runge-Kutta method developed by Bogacki and Shampine (1989). The code for the implementation of the model in MATLAB is provided in Appendix B.1.

The results of this implemented model are compared to experimental results from literature - as was done by Bernard (2011), who compared the results produced by the model to

a set of time dependent experimental results produced by ((Flynn et al., 1994)). Figure 4.2 shows the plot comparing the results of the model compared against the experimental result, these results are for the phytoplankton *Isochrysis galbana* Parke, under periodic light and dark conditions at a ratio of 12hrs light:12hrs dark. The model was set up using a set of initial values and boundary conditions (inflow concentrations) obtained from the experimental data to which the results are compared. As the experimental results used for validating the model were performed under batch flow conditions (i.e. no inflow or outflow) only the initial conditions are needed with S_{in} and D being set to 0. Table 4.2 shows the initial conditions used in the implementation of the model for the case described here.

	Ammonium [$\mu g.N.ml^{-1}$]	Cell Nitrogen [$\mu g.N.ml^{-1}$]	Cell Carbon [$\mu g.C.ml^{-1}$]	Light Intensity [$\mu Mol.m^{-2}.s^{-1}$]
Initial Conditions	1.411	0.03	0.6	100

Table 4.2: Initial conditions used for the implementation of the model developed by Bernard (2011) for the periodic light variation simulation

The results of the model show excellent results when compared to the experimental results; the close fit to the experimental data for the external Nitrogen and the cell carbon, in particular the inclusion of the stepping shape of the cell carbon modelling results, shows that the model, even though complex and including a large set of variables, accurately predicts the growth and nutrient consumption processes within the bioreactor. The stepped shape of the cell carbon graph is a result of the periodic light and dark conditions imposed on the bioreactor and can be seen in the experimental results for the cell carbon content. The fact that the model predicts this indicates that the function described in equation 4.6 is properly predicting the effects of limited light on the biomass growth rate. The results for cell chlorophyll and Nitrogen content also show good accuracy particularly in the exponential growth phase in the first half of the growth period. There is however a slight loss of accuracy for both of these variables after the point where external nitrogen is depleted. Both of these plots fail to reach the peak values shown in the experimental data indicating the model functions fail to account for continued activity in Chl production and possibly uptake of Nitrogen from an alternative source other than the Ammonium shown

in the external Nitrogen plot. Additionally, the model prediction between 10 and 25 days for the chlorophyll concentration has a lower gradient than is shown by the experimental results. This may be due to experimental errors as there is some visible fluctuation in the experimental data in that period. However, without further experimental data for a longer experimental run it is not possible to tell whether the model predictions would diverge from the experimental data.

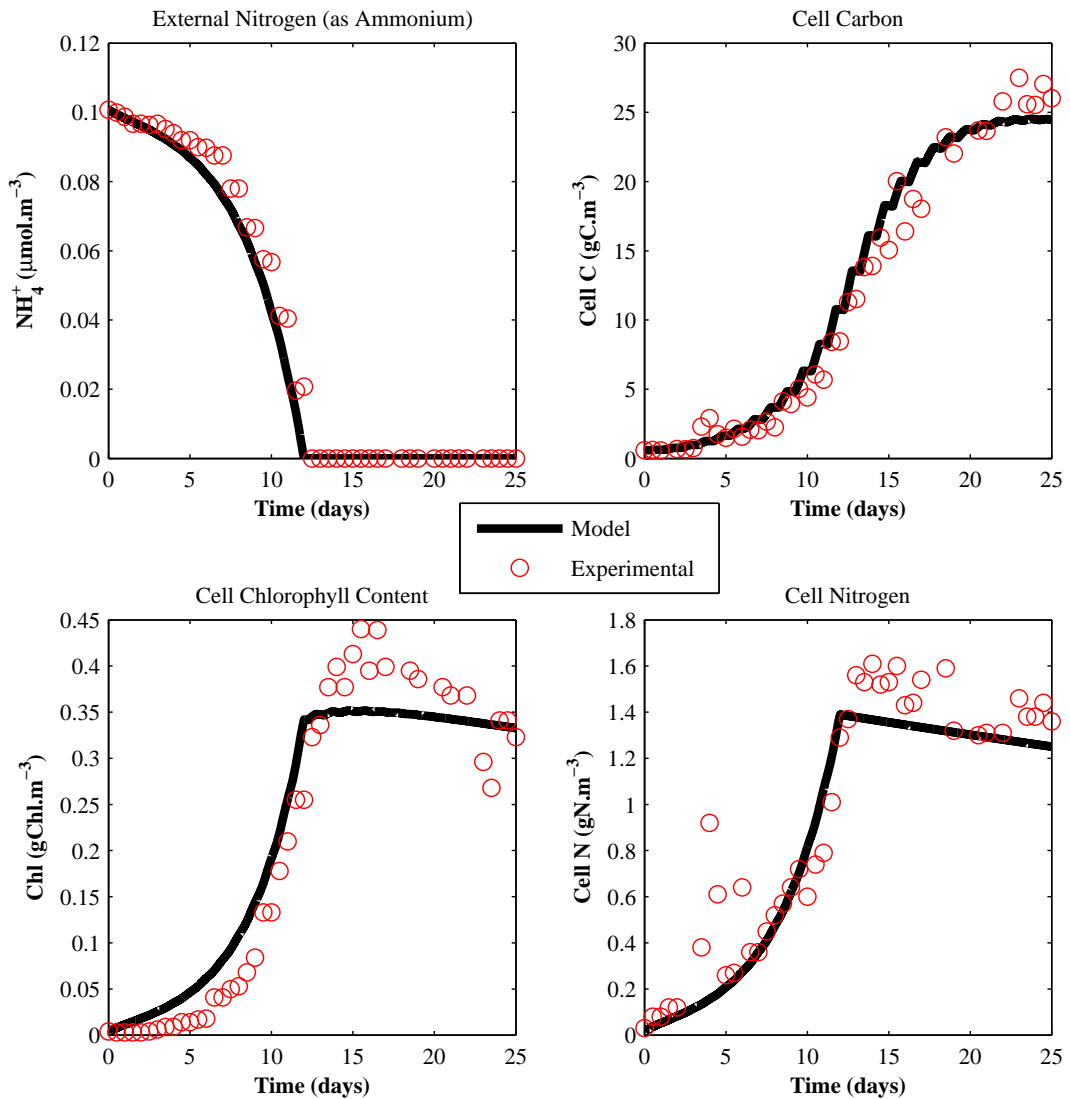


Figure 4.2: Comparison performed between the model of Bernard (2011), implemented here, and the dynamic experimental data of Flynn et al. (1994) for a light:dark periodic light source.

Although the results produced by Bernard (2011) indicate that the model is able to accurately predict the growth and decay of biomass as well as the concentrations of internal

and external nutrients and Chl the model is only compared to results under a single set of experimental conditions. To this end a second set of data for the same species of algae was obtained from literature and compared with results produced by the model implemented. As the algal species is the same as that used in the previous case, the model constants should still be appropriate and are thus kept the same as described in table 4.1. The initial conditions for this simulation are the same as the initial conditions of the experimental work to which it is to be compared; these initial values are shown in table 4.3.

	Ammonium [$\mu g.N.ml^{-1}$]	Cell Nitrogen [$\mu g.N.ml^{-1}$]	Cell Carbon [$\mu g.C.ml^{-1}$]	Light Intensity [$\mu Mol.m^{-2}.s^{-1}$]
Initial Conditions	1.4	0.05	1.29	100

Table 4.3: Initial conditions obtained from the experimental work of Davidson et al. (1992) for use with the Bernard (2011) algal growth model implemented here as part of validating the model accuracy.

As the only significant difference (other than slight variations in initial conditions) between the model set-up described previously and the one shown here is the lighting conditions, the results should show a number of similarities and the results of the model predictions should be comparable to those found by Bernard (2011) for the periodic lighting condition. Figure 4.3 shows the results of the simulation performed here with the experimental results for dynamic growth of the phytoplankton species *Isochrysis galbana* Parke under constant light intensity growth conditions, the experimental results were obtained from the work of Davidson et al. (1992). Although the accuracy of the model is not as great as when compared that of the original experimental data set - from which some of the model parameters were tuned - there is still reasonably good agreement between the experimental and model results. In this second case the model has a tendency to overshoot the experimental results even though it maintains the same basic shape for the different plots. On the whole the results of the comparison with a second set of experimental data show that although the model fails to reproduce the accuracy shown from the original validation it does show itself capable of predicting the main features of the second data set. Again the chlorophyll calculation shows the most inaccuracies of the results plotted with peak values being $0.05g.Chl.m^{-3}$ greater than the experimental result and maintaining that difference for the remaining 9 days of simulation time. This shows that, although the model is

providing good predictions of the biomass and cell nutrient contents, the difference in the peak simulated chlorophyll vs experimental results indicates that some part of the model requires further investigation. Whether the calculated chlorophyll concentration has a significant effect on the overall result is unknown considering the number of different factors which have been included in the model. This is particularly the case as a number of the controlling processes were 'tuned' using the initial set of experimental data from Flynn et al. (1994). Additionally, although the model accounts for quite a few factors which may have an effect on the results it doesn't account for any form of mixing which may have a much greater effect on the availability of light for individual algal cells. This would make it difficult to use the model for any bioreactors with complex geometries or lighting conditions without significant changes and enhancements.

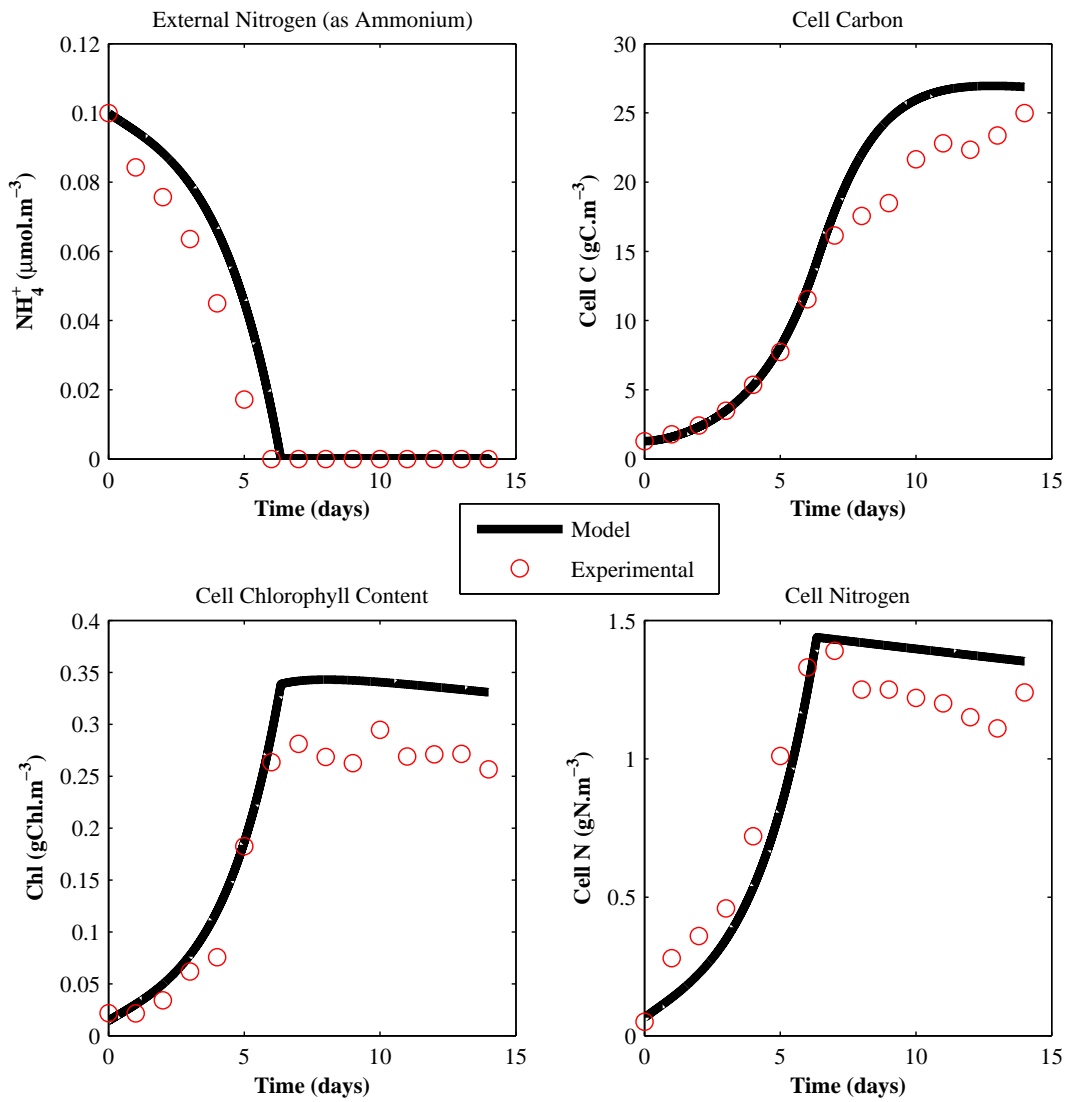


Figure 4.3: Comparison between solutions from the model of Bernard (2011) implemented here and the experimental results of Davidson et al. (1992) for a constant light intensity

4.2 The photosynthetic factory (PSF) model

The photosynthetic factory (PSF) model for light limited phytoplankton growth described here was originally created and published by Eilers and Peeters (1988) and further developed by Wu and Merchuk (2002) and Nauha and Alopaeus (2012). The model describes the photosynthetic processes through the use of the concept of photosynthetic factories or states. This approach, although not accounting for the full complexity of the photosynthesis process, does consider the effect light can have on photosynthetic cells when at extreme low and high concentrations as well as at the optimum intensity. There are three possible states for the PSFs, (1) the resting state (x_1), (2) the activated state (x_2) and (3) the inhibited state (x_3). The transition from one state to another is dictated by rate constants where change from the resting to the activated state and from the activated to the inhibited state is proportional to the light intensity (figure 4.4). The recovery from the activated and inhibited states to the resting state is controlled by enzymatic processes which are not dependent on the light intensity, this is reflected in the model equations. Equations 4.21 to 4.23 show the linear coupled ODEs which represent the changes in state of the PSF model shown in figure 4.4. The diagram describes the connections between the PSF states, where α , β , γ and δ are constants describing the behaviour of the photosynthetic process and I is the incident light intensity. The values for the model constants are provided in table 4.4.

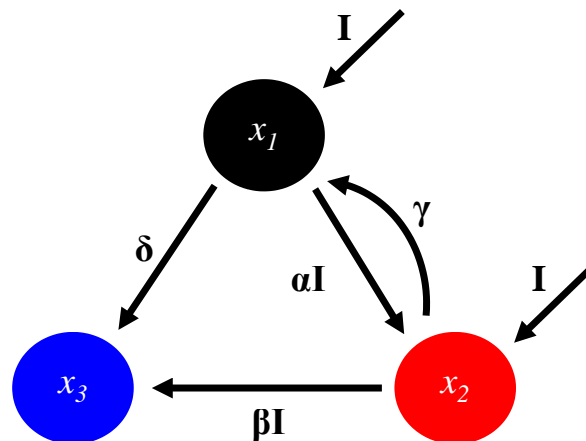


Figure 4.4: Photosynthetic factory model states diagram

$$\frac{dx_1}{dt} = -\alpha I x_1 + \gamma x_2 + \delta x_3 \quad (4.21)$$

$$\frac{dx_2}{dt} = \alpha I x_1 - \gamma x_2 - \beta I x_2 \quad (4.22)$$

$$\frac{dx_3}{dt} = \beta I x_2 - \delta x_3 \quad (4.23)$$

Parameter Name	Symbol	Value	Unit
alpha	α	0.001935	$(\mu\text{Mol.m}^{-2})^{-1}$
beta	β	5.7848e-7	$(\mu\text{Mol.m}^{-2})^{-1}$
gamma	γ	0.1460	s^{-1}
delta	δ	0.0004796	s^{-1}

Table 4.4: Constants for the photosynthetic factory model (Wu and Merchuk, 2001)

This section details a series simulations using the photosynthetic factory model for growth of phytoplankton under limited light conditions; variable functions are imposed for the light intensity to demonstrate the effects of changing light levels on the photosynthetic state of the biomass. The initial conditions used for the PSF model are for all biomass to be in the resting state (i.e. $x_1 = 1, x_2 = 0$ and $x_3 = 0$) this condition is analogous to conditions where the algae has been kept in darkness for a considerable period of time. The code used to implement each of the simulations described here is found in Appendix B.

4.2.1 Effects of light intensity function on the photosynthetic state of biomass

In order to understand how the PSF model works, a series of functions describing the light intensity applied to the biomass were implemented for the model. Four different functions were tested to determine the response under different theoretical lighting situations. Although the light intensity in a bioreactor can vary based on a number of factors (e.g. time of day, location within the reactor, global latitude), due to the one-dimensional nature of the ODE systems implemented here, the functions are considered as variations in time rather than in space with the bioreactor being considered as homogeneously

mixed and with the incident light intensity applied to all depths within the reactor. The implementation for these different lighting conditions can be found in Appendix B.

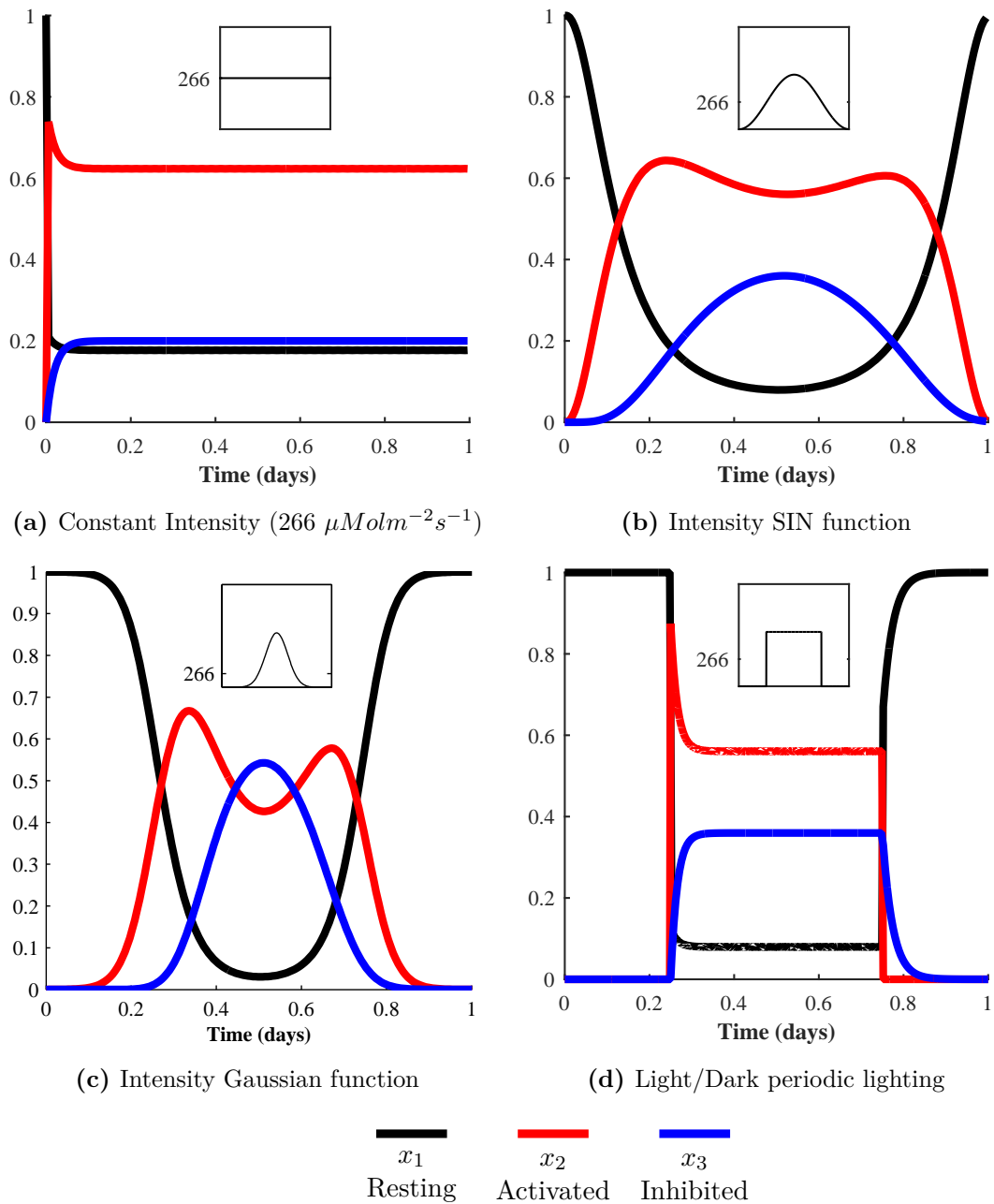


Figure 4.5: Difference in photosynthetic states for differing light intensity functions, where the subplot is the light intensity function shape. Each function has the same average value over a one day period ($266\mu\text{Mol.m}^{-2}\text{s}^{-1}$), also depicted within the subplots.

The four functions implemented were a constant fixed value of $266\mu\text{Mol.m}^{-2}\text{s}^{-1}$ (as used in the experimental work of Rhee (1973)), a periodic step function to represent a lamp being turned on after a period of time and then later switched off, a SIN function with

a frequency of $1d^{-1}$ and a Gaussian function also applied over a period of 1 day. In cases where results are shown over multiple days the functions for light intensity repeat at a frequency of one cycle per day. All of these functions were set-up to have the same average light intensity ($266\mu Mol.m^{-2}.s^{-1}$) when calculated over one 24 hour day. The average value was chosen to represent the light intensity provided by the lamps used in the experimental work of Rhee (1974, 1978) which are later used for validation purposes. Plots of all these functions are shown as sub figures in figure 4.5 alongside their resulting PSF states. In order to clearly show the photosynthetic states using the different light intensity functions, the plots are over a period of only a single day. Each of the functions would repeat if the plots were extended over a longer period of time.

Each of the light intensity functions and their resultant photosynthetic states represents different lighting conditions under which phytoplankton might be grown. The constant light intensity in figure 4.5a represents the response when under lighting conditions which could only be found in an artificial environment such as a laboratory. Figure 4.5d also describes laboratory type conditions where the lamps providing the light are switched off and on periodically; this function may also be used with a much shorter period to represent a strobe effect. The final two light intensity functions, the SIN function, figure 4.5b, and the Gaussian function, figure 4.5c, both display behaviour similar to that of the day/night cycle of sunlight showing a smooth transition from light to dark. However it should be noted that, although the light intensity of daylight is significantly higher than the values shown here and when implemented with a more realistic daylight intensity the effect of photoinhibition is more readily apparent (Figure 4.7).

Figure 4.6 shows mean values of the three photosynthetic states for the different light functions as fractions of the total biomass, this gives a more obvious visual description of the living conditions of the biomass in relation to available light. The obvious conclusions which can be drawn from the chart are that the constant intensity function produces the highest ratio of active-inactive biomass with nearly 2/3 in the active state (x_2). The SIN function produces the next highest active-inactive ratio with the Gaussian and step functions having active-inactive ratios less than half that of the constant intensity. This shows that although the average light intensities are the same it is just as important

to reduce the range over which the light intensity varies and the time spent under light intensities which may inhibit the photosynthesis process greatly. This is shown by the fact that both the Gaussian and step functions spend the majority of the cycle at values much greater and less than the average.

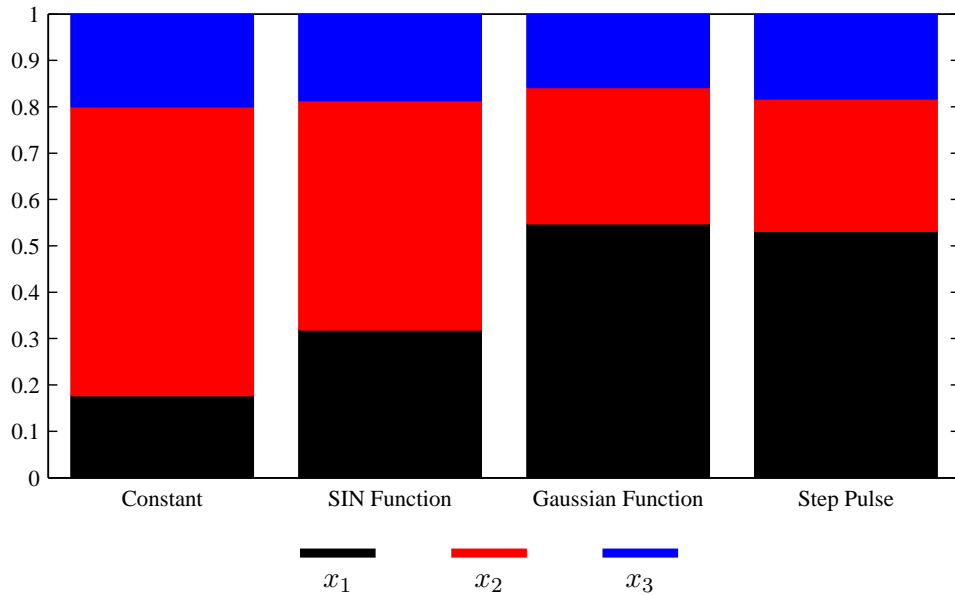


Figure 4.6: The the average ratios for the different photosynthetic states under the different light intensity functions

Figure 4.7 is a comparison between the photosynthetic states of biomass for two different Gaussian functions. Figure 4.7b shows the result for a Gaussian function with an average light intensity of $500\mu\text{molm}^{-2}\text{s}^{-1}$ and a maximum value of $2000\mu\text{molm}^{-2}\text{s}^{-1}$ which is typically regarded as maximum bright direct sunlight, this is compared with the results for the Gaussian function with an average value of $266\mu\text{molm}^{-2}\text{s}^{-1}$. The result of increasing the light intensity effects the photosynthetic states increasing the time the biomass spends inhibited (x_3) particularly at peak light intensity which in turn slightly increases the time the biomass is dormant or in the resting state (x_1). Additionally, and in correspondence with the increase in time spent in the resting and inhibited states, the fraction of biomass which is active at peak light intensity (i.e. midday) has decreased. These results are as expected when considering the typical light response curve of phytoplankton (figure 2.3).

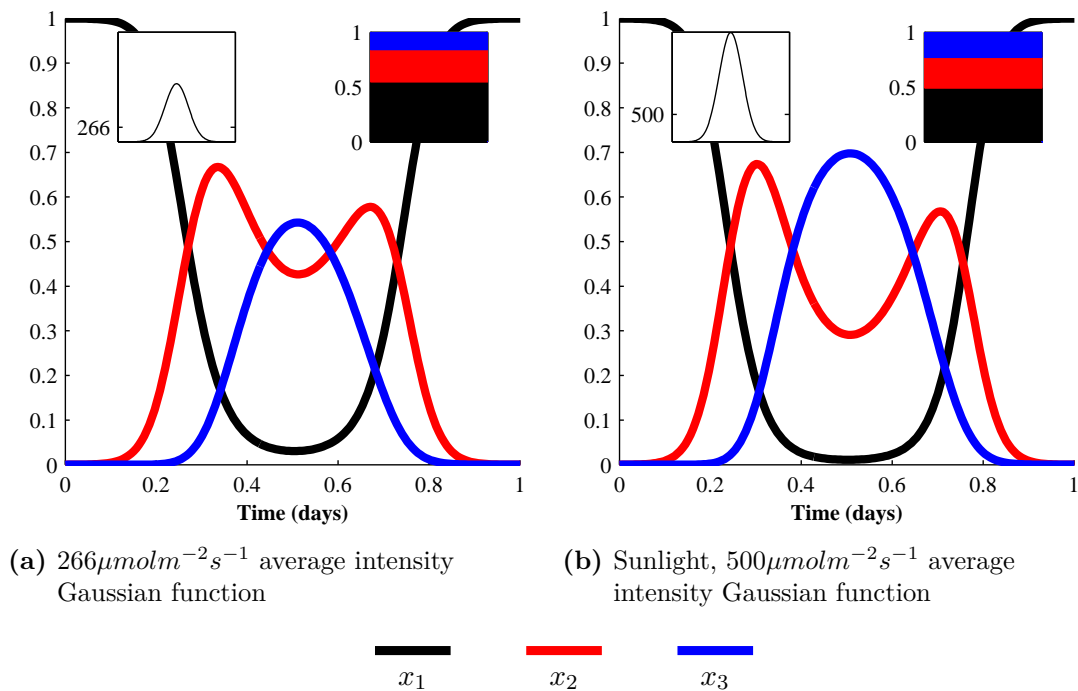


Figure 4.7: A comparison between the photosynthetic states for Gaussian light functions with average values of $266 \mu\text{molm}^{-2}\text{s}^{-1}$ and $500 \mu\text{molm}^{-2}\text{s}^{-1}$ representing sunlight (maximum value of $2000 \mu\text{molm}^{-2}\text{s}^{-1}$ representing sunlight intensity at midday.) along with a plot of diurnal light intensity and a bar chart of average biomass state

4.2.2 The relationship between light intensity and activated biomass in the photosynthetic factory model

It is important to understand how the amount of light received by the algae affects its ability to photosynthesise. It is well known that the photosynthetic response of photoautotrophs follows a curve with a peak photosynthetic rate preceded by a steep incline and followed by a shallower decline as shown in figures 2.3 and 4.8. For a photosynthesis model to include inhibition it must be able to produce results of this nature.

In order to determine how the PSF model responds under different light intensities in terms of the fraction of activated biomass, a comparison between x_2 (the activated portion of biomass) and a range of light intensities was produced. This comparison includes results for three different light intensity functions all with the same average value for each of the light intensities. Figure 4.8 shows how the mean light intensity affects the amount of biomass in the active state when using the PSF model. Figure 4.8 shows that as expected

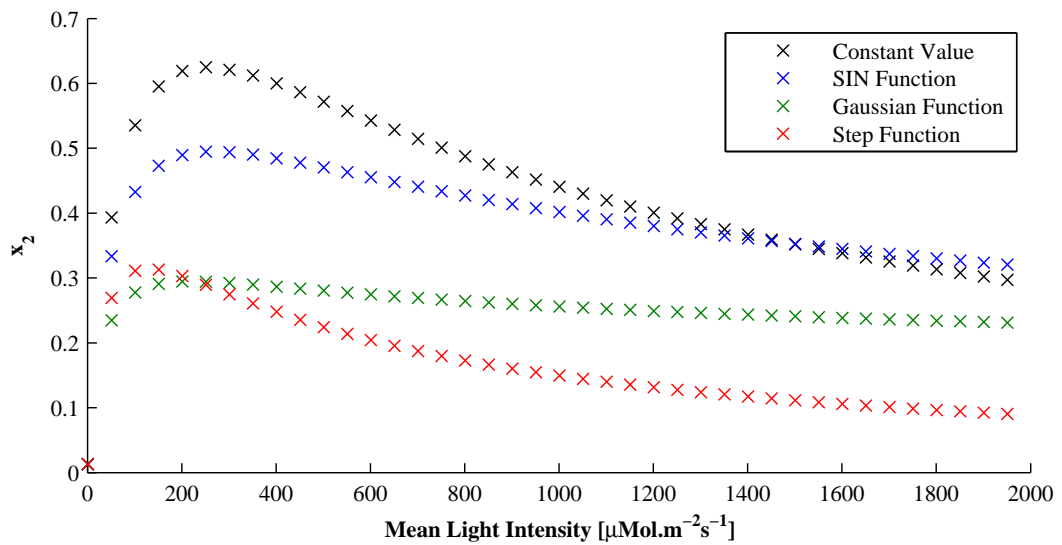


Figure 4.8: Comparison of light intensity functions (constant, SIN function, Gaussian function and a step function) for activated biomass vs. average light intensity ranging from 0 to $2000 \mu\text{Mol.m}^{-2}\text{s}^{-1}$ (Peak direct sunlight). Figure shows the mean activated biomass fraction per day vs the mean light intensity

the constant light intensity function produces the highest mean biomass fraction when compared to the other light functions. The general trend shows that the functions which have a greater proportion of time spent at very low and very high light intensities where inhibition of the cells and lack of light reduce photosynthesis significantly (Table 4.5). An interesting point to note, which to the best of the authors knowledge has not been shown before, is that the peak average x_2 value varies for the different functions indicating that it is important to aware of both the range of light intensities the algal will be subjected to as well as the average value. Additionally the time spent at the at different light intensities will also have a role in determining the average light intensity at which the peak activated state occurs.

	$I \mu\text{Mol.m}^{-2}\text{s}^{-1}$
Constant	252
SIN	267
Gaussian	218
Step Function	128

Table 4.5: Light intensity at peak x_2 for four different functions (See figure 4.8)

4.3 Coupling the photosynthetic factory and cell quota models

On their own both the cell quota (section 3.5.2) and PSF models are limited in their application to where the effects of only a single controlling parameter are considered (e.g. only light limited growth with infinite soluble nutrients). In order for light dependent limitation to be included in a nutrient model, some way of coupling the light dependent and cell quota models is needed.

Here, a method of coupling the photosynthetic factory model with the multi-nutrient cell quota model described in section 3.5.3 is proposed. The coupling method proposed for this photosynthesis-nutrient (PN) model is to use the output of equation 4.22 from the PSF model as an additional variable (x_2) in equations 3.26 - 3.28; by replacing μ_∞ with a proposed new variable $\mu_I(x_2)$ (equation 4.24), which is a function of x_2 , the modified biomass growth and cell nutrient quota equations 4.25 - 4.27 are obtained. The variable μ_I takes the value $2.5084\text{E-}5\text{s}^{-1}$ in equation 4.24.

$$\mu_I = x_2\mu_l \quad (4.24)$$

$$\frac{dQ_N}{dt} = \frac{V_{max,N}S_N}{S_N + K_N} - \mu_I \min\left(1 - \frac{Q_{min,N}}{Q_N}, 1 - \frac{Q_{min,P}}{Q_P}\right) Q_N \quad (4.25)$$

$$\frac{dQ_P}{dt} = \frac{V_{max,P}S_P}{S_P + K_P} - \mu_I \min\left(1 - \frac{Q_{min,N}}{Q_N}, 1 - \frac{Q_{min,P}}{Q_P}\right) Q_P \quad (4.26)$$

$$\frac{dX}{dt} = \mu_I \min\left(1 - \frac{Q_{min,N}}{Q_N}, 1 - \frac{Q_{min,P}}{Q_P}\right) X - mX \quad (4.27)$$

The addition of x_2 to the cell quota model works by effectively scaling the growth rate at infinite quota (μ_∞) by the amount of photosynthetically active biomass as determined by the PSF model. As the work of Klausmeier et al. (2004) was based on experimental

data collected by Rhee (1978) it is possible to determine a corrected value for μ_∞ when under light limitation. Rhee (1978) stated that a "Continuous illumination of about 0.082 $lymin^{-1}$ was provided by white fluorescent lamps" for the experimental work. This value can be converted using the formula and data tables in Thimijan and Heins (1983), resulting in a light intensity value of $266\mu Mol.m^{-2}.s^{-1}$. At this constant light intensity value the PSF model produces a constant x_2 value of 0.6231. This allows the value of μ_l to replace μ_∞ when the light intensity is included.

4.3.1 Cell quota model with nutrient uptake limitation

As with the multiplicative model described in section 4.1 the inclusion of light limited growth in the cell quota model necessitates the inclusion of an uptake limiting function to prevent infinite uptake of nutrient under low light conditions. To limit the nutrient uptake, a function which which tapers off as the cell quota reaches a maximum value is added to the equations for calculating soluble Nitrogen and Phosphorus and the Nitrogen and Phosphorus cell quotas. The inclusion of the function described by Lehman et al. (1975) in equation 4.13 results in the following equations for soluble substrate and cell quotas (equations 4.28 - 4.31), where the limiting part of the function is highlighted in red.

$$\frac{dS_N}{dt} = a(S_{in,N} - S_N) - \left(1 - \frac{Q_N}{Q_{max,N}}\right) \frac{V_{max,N}S_N}{S_N + K_N} X \quad (4.28)$$

$$\frac{dS_P}{dt} = a(S_{in,P} - S_P) - \left(1 - \frac{Q_P}{Q_{max,P}}\right) \frac{V_{max,P}S_P}{S_P + K_P} X \quad (4.29)$$

$$\frac{dQ_N}{dt} = \left(1 - \frac{Q_N}{Q_{max,N}}\right) \frac{V_{max,N}S_N}{S_N + K_N} - \mu_I \min\left(1 - \frac{Q_{min,N}}{Q_N}, 1 - \frac{Q_{min,P}}{Q_P}\right) Q_N \quad (4.30)$$

$$\frac{dQ_P}{dt} = \left(1 - \frac{Q_P}{Q_{max,P}}\right) \frac{V_{max,P}S_P}{S_P + K_P} - \mu_I \min\left(1 - \frac{Q_{min,N}}{Q_N}, 1 - \frac{Q_{min,P}}{Q_P}\right) Q_P \quad (4.31)$$

Several papers describe a maximum cell quota as a ratio of the minimum quota. Lehman et al. (1975) describes a ratio of maximum:minimum of 8:1 for the Nitrogen max cell quota

and 16:1 for the Phosphorus cell quota, these values are collated from a number of sources from different sets of experimental data and for different species of algae. Bernard (2011) used a ratio of 10:1 for the maximum:minimum ratio for the Nitrogen cell quota but did not model Phosphorus uptake. For the work done here ratios of 8:1 for Nitrogen and 16:1 for Phosphorus were used with the resulting values quoted in table 4.6.

Parameter	Symbol	Value $\mu\text{Mol.m}^{-3}$
Max Nitrogen cell quota	$Q_{max,N}$	3.632e-13
Max Nitrogen cell quota	$Q_{max,P}$	2.624e-14

Table 4.6: Maximum cell quota values for Nitrogen and Phosphorus

To determine the effect the use of this quota limit has on the growth of algae under light limiting conditions a comparison between the model both with and without the limit was performed. The Gaussian function was used to describe the light intensity as, of the functions described in section 4.2.1, it is the one which most closely describes lighting conditions under which phytoplankton might be grown (i.e. the natural night/day cycle) whilst still having significant periods of both low and high light intensity with a gradual change between the extremes. Figure 4.9 illustrates the difference in soluble nutrient concentration between the two models; these results show that with the quota limit, the nutrient concentration has a slower decline than when modelled without the limit as would be expected with the inclusion of periods of no growth in low light where the cell quota maximum could be reached. This result is confirmed by the results in figures 4.9a and 4.9b, which show that the cell quota limit function imposes a hard maximum on the nutrients within the algal cells which is surpassed when modelled without the limiting function. The effect this cell quota limit has on the growth of the biomass itself can be seen in figure 4.10c where the result of including the quota limit is an increase in the time taken to reach the steady-state solution. This is understandable given that the available cell nutrients for growth is limited at any given time but globally soluble nutrients remain the same in the system; this result in a delay in growth but has no effect on the maximum biomass concentration achievable.

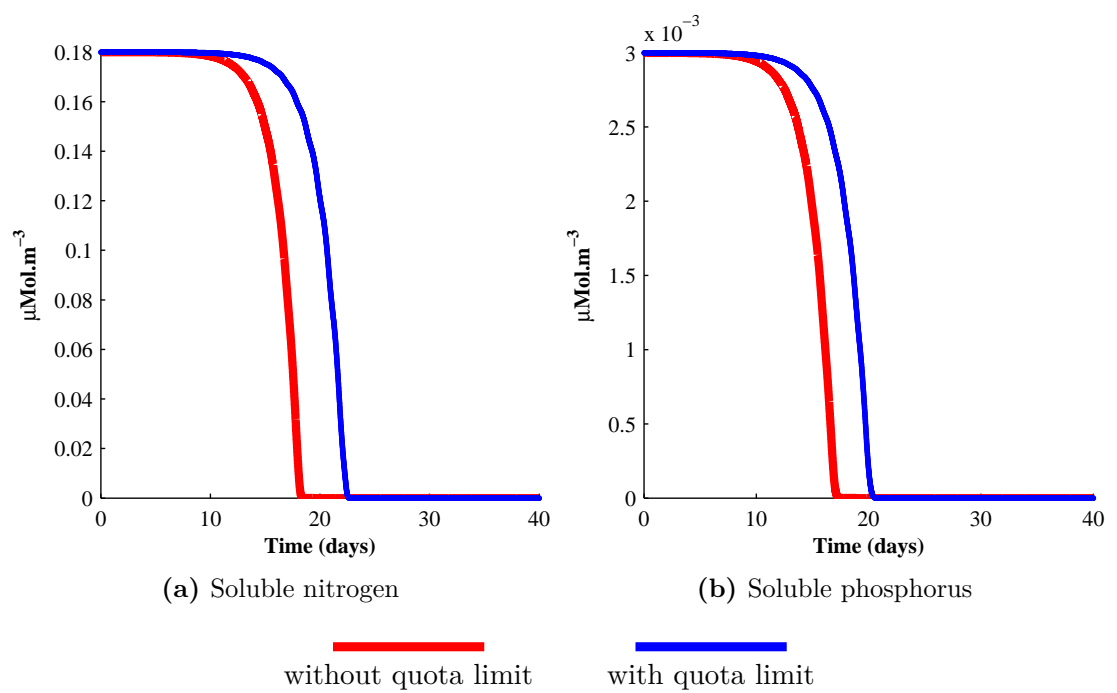


Figure 4.9: Soluble nutrient concentration under cell quota limited nutrient uptake

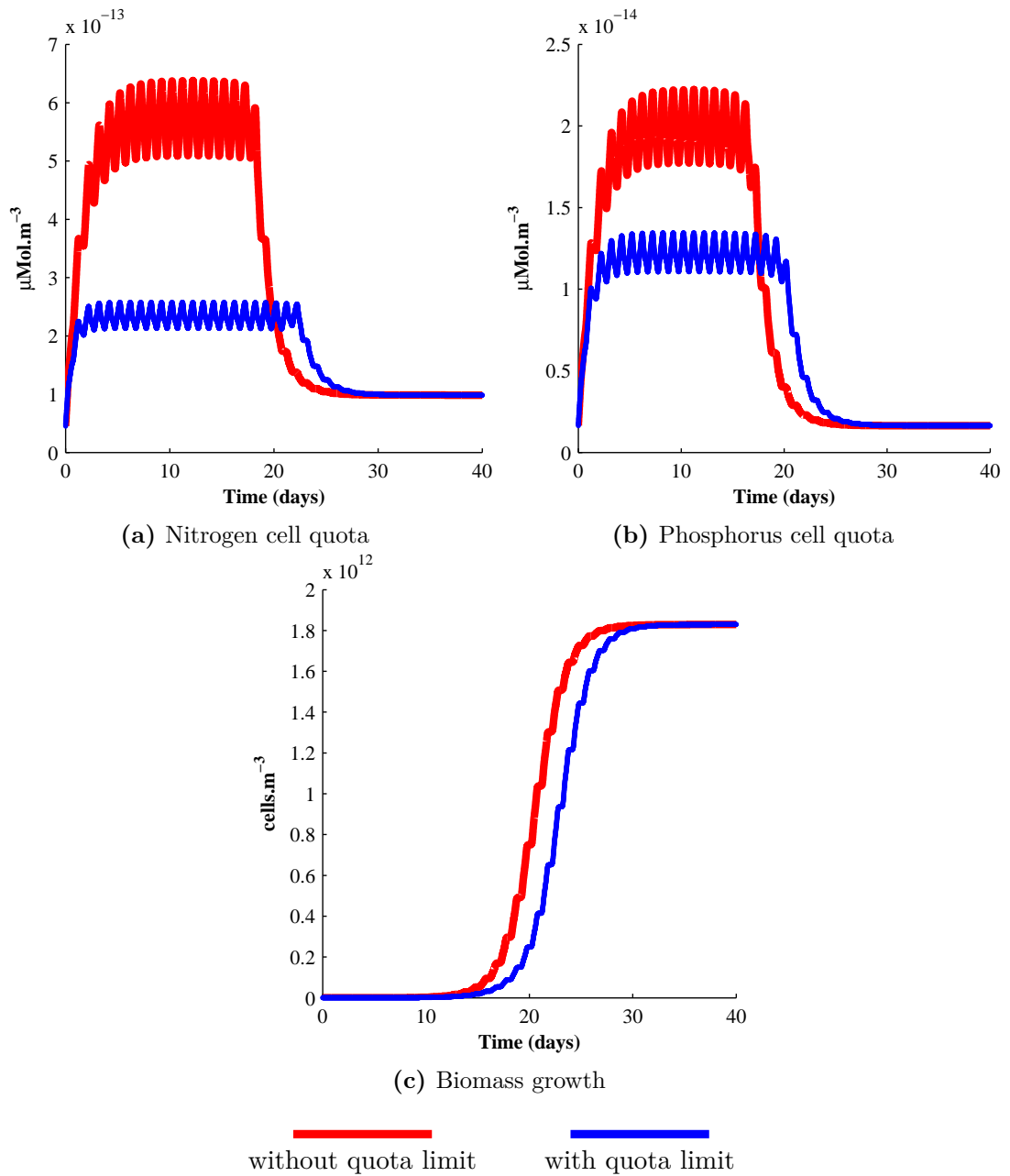


Figure 4.10: Cell quota nutrient concentration and biomass for model with and without quota limited uptake

4.3.2 Validation of PN coupled model using results from literature

The coupled model was compared with the work of Rhee (1978) as shown in figure 4.11 along with the results from a simulation using a much smaller value of constant light intensity to show the effect on the growth of algal cells. The graph shows a set of experimental results obtained under constant light conditions at an intensity of $266\mu\text{Mol.m}^{-2}.\text{s}^{-1}$. Each point on the graph represents the final values of biomass under different ratios of Nitrogen to Phosphorus. Two sets of simulation results are shown, one at $266\mu\text{Mol.m}^{-2}.\text{s}^{-1}$ and a second at a much lower light intensity of $60\mu\text{Mol.m}^{-2}.\text{s}^{-1}$. The results of the simulations performed at a light intensity of $266\mu\text{Mol.m}^{-2}.\text{s}^{-1}$ compare favourably to the experimental results. The plot shows how the change in the light intensity effects the maximum amount of biomass obtained with the lower light intensity producing significantly less biomass. If $266\mu\text{Mol.m}^{-2}.\text{s}^{-1}$ is considered to be the intensity at peak algal growth the maximum cell number at $60\mu\text{Mol.m}^{-2}.\text{s}^{-1}$ is as expected less than two thirds that of the higher intensity value. A similar but shallower fall off in the peak cell number would be expected for light intensities higher than $266\mu\text{Mol.m}^{-2}.\text{s}^{-1}$ in line with effect on the activated state at different light intensities shown in figure 4.8.

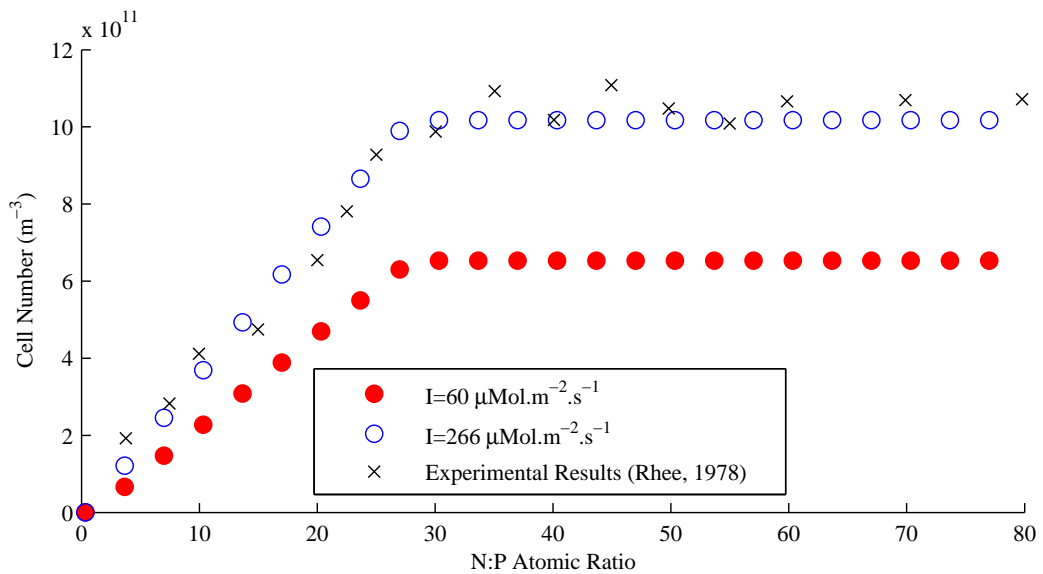
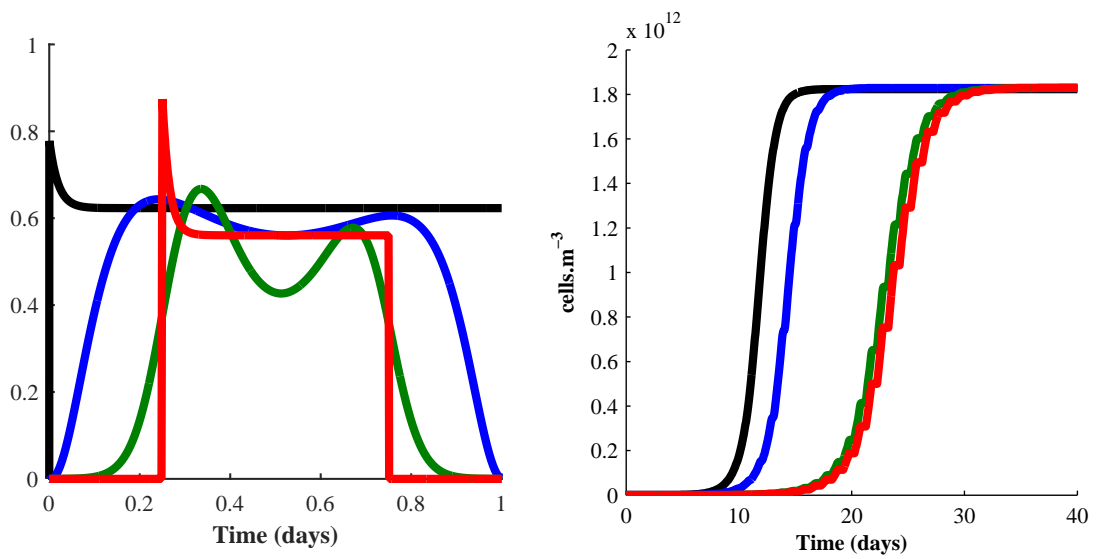


Figure 4.11: Biomass growth at different N:P cell ratios for two different light intensities compared to experimental work done by Rhee (1978)

4.3.3 Effects of varying the light intensity function on biomass growth

Figure 4.12 is a comparison between the different light intensity functions. Figure 4.12a shows the changes in activated photosynthetic state x_2 over a period of one day for the four different models studied above. This shows that although the maximum values of x_2 for the functions are similar, both the time spent at that maximum value and the mean values vary more greatly. Figure 4.12b shows the growth of the biomass over a period of forty days using equation 4.27. This plot shows that the growth rate is highly dependent on the average light intensity. The four functions used show growth which correlates with the results for the activated state for the different light intensity functions as shown in figure 4.6 with the greatest biomass growth occurring with the constant light intensity function due to the greatest value of activated biomass.

As can be seen in figures 4.12b, 4.13c and 4.13d there is a periodic fluctuation in the biomass growth over each day, this corresponds to the periodic behaviour of the light intensity function used. The plateaus in the gradients of the growth curve correspond to the times when the biomass in the activated state is at a minimum (Figure 4.12a), this occurs shortly after the light intensity function is at a minimum indicating a delay in changes of state.



(a) Percentage activated state (x_2) for each intensity function

(b) Biomass growth over a period of 40 days.

Constant
 SIN
 Gaussian
 Step function

Figure 4.12: Growth comparison between different light intensity functions

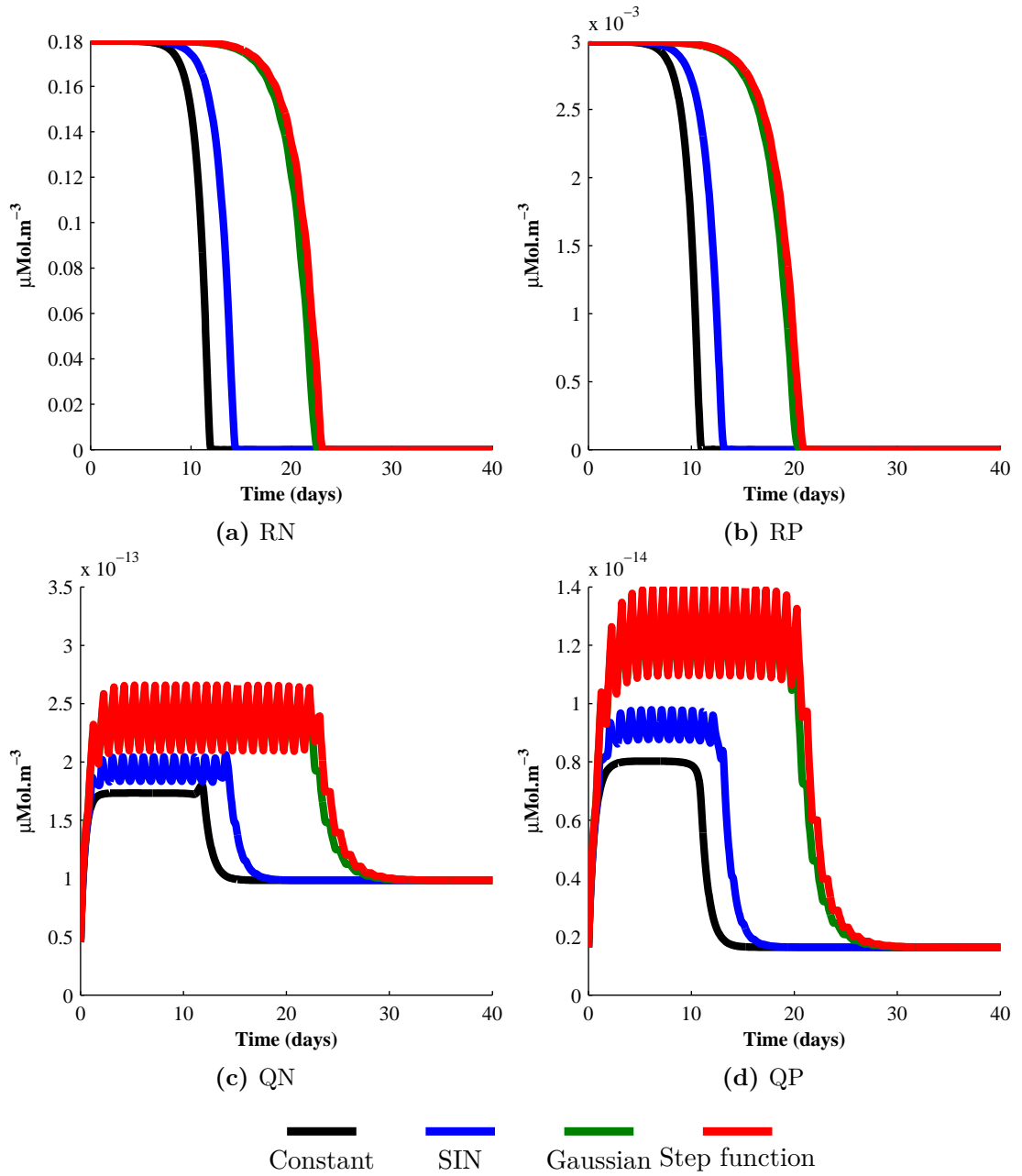


Figure 4.13: Growth comparison between different light intensity functions, showing plots for soluble nutrients nitrogen and phosphorus as well as their respective cell quotas.

4.3.4 Effects on biomass growth of a light intensity function and the average of the function

In order to determine the effect of variable light intensity on the PSF a comparison between a light intensity function and the average of that function. The reason being to determine whether the use of a complex function for light intensity is necessary or whether the use of the average of the function is sufficient to determine the effect of light on the biomass growth and thus provide a reduction in the computational cost of any simulations. To this end, a comparison of the biomass growth results for the function and its average is shown in figure 4.15. The Gaussian function and its average were modelled to show how the results from the average light intensity compares to the results produced by the full light intensity function.

As can be seen in figure 4.14, the difference in amount of activated biomass between the Gaussian function and the average of that function is significant, although the peak values are similar the average value over time is noticeably greater with the function average. The effect this disparity in the activated biomass fraction has on the biomass growth is clearly illustrated in figure 4.15 where the difference in the solutions over a period of forty days is plotted.

The immediately obvious difference is in the time taken to reach the maximum value of biomass at the end of the simulation where the Gaussian function problem takes more than twice the time of the average of the function. As expected from the results shown in figure 4.12b the growth with a constant value of light intensity has a smooth slope with no obvious short term variation, conversely, the solution with light intensity based on a Gaussian function shows an obvious stepping period in biomass growth when compared to the function average.

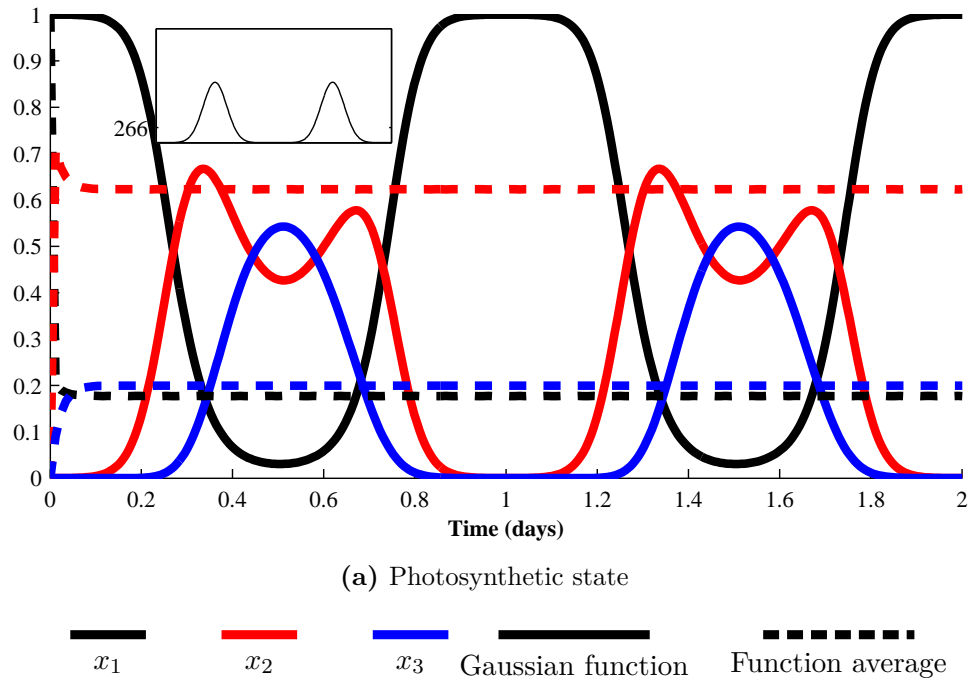


Figure 4.14: Comparison between the photosynthetic states of biomass for a Gaussian light intensity function and the average intensity of the function.

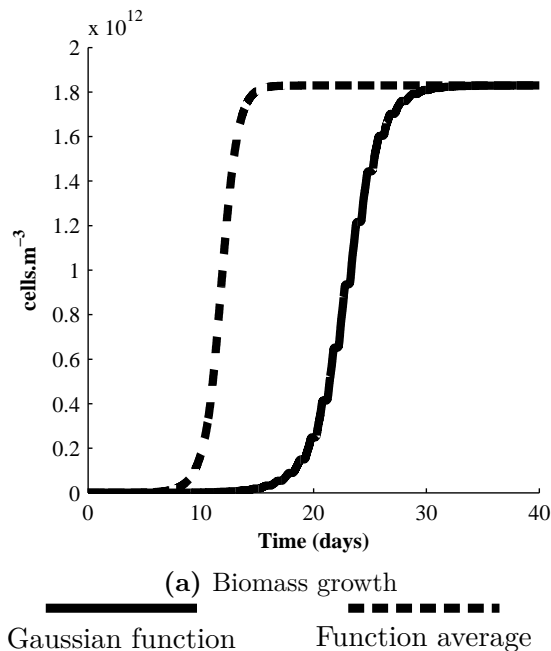


Figure 4.15: Comparison of biomass growth for a Gaussian light intensity function and the average of that function

4.4 Summary and conclusions

The work in this chapter describes the implementation of two of the different methods of modelling photosynthesis in algae, some of the characteristics and behaviours of these models and methods by which they can be coupled to the soluble nutrient dependent growth models described in chapter 3. The two different modelling methodologies implemented in this chapter were a multiplicative approach, which describes the various mechanisms controlling photosynthesis dependent growth as terms in the overall growth rate function, and the photosynthetic factories method, in which the biomass can be in one of three states with the transition between them controlled through a set of coupled ODEs.

The multiplicative model described was implemented and compared to experimental data obtained from literature and shown to produce good results for biomass concentration and cell nutrient content. Some differences were noted in the results for cell chlorophyll content where higher than expected peak values indicate the model is compensating elsewhere for calculating biomass growth or that the cell chlorophyll content is not a significant factor influencing biomass growth. The model also does not account for mixing and would require some changes to the growth rate functions to be usable with bioreactors including complex mixing or bioreactor geometries.

The second photosynthesis model implemented was the photosynthetic factories model. This model includes several of the same processes as the multiplicative model in a different manner. The effect of different light intensity values and functions on the photosynthetic state of the biomass was investigated and showed that large variation in the light intensity has a detrimental effect on the amount of active biomass. It was also shown that the variation in light intensity has an impact on the average light intensity at which maximum average active biomass is obtained with lower variation in light intensity range producing both high peak average active biomass and a higher average light intensity at which this occurs.

Finally a method was proposed to couple the photosynthetic factory model with a multi-nutrient cell quota model. This coupling necessitated the inclusion of a function in the

soluble nutrient and cell nutrient quota equations to limit the uptake of nutrients under limited light conditions. This was to represent cell activity when no light for growth is available and only nutrient uptake occurs, without the function cells would continue to absorb nutrient beyond their actual capacity to do so. This model was then run under the different lighting conditions to determine the effect these had on the biomass growth rate. The results showed that although the maximum biomass concentration did not vary based on the light function the time taken to achieve that maximum did. The results for the model were validated against experimental data from literature showing good correlation with the experimental work.

The results described in this chapter show that the inclusion of photosynthetic processes in models of algal biomass growth is important. This is especially the case where large variations in the light intensity occur either in the bioreactor itself or as a product of time variations (e.g. day/night cycle).

Chapter 5

Hydrodynamic Modelling

Contents

5.1	Introduction	79
5.2	Computational fluid dynamics modelling	80
5.2.1	The Navier-Stokes equations	80
5.2.2	Reynolds averaged Navier-Stokes (RANS) turbulence models . . .	83
5.2.2.1	Two equation turbulence models	84
5.2.3	Euler-Lagrange multiphase modelling	85
5.3	CFD modelling of a gas-lift bioreactor, assessing turbulence model selection and flow control	86
5.3.1	Mesh independence testing of CFD simulations	91
5.3.2	RANS turbulence model assessment	94
5.3.3	CFD solver comparison (ANSYS Fluent vs. OpenFOAM)	100
5.3.4	A comparison of different approaches for modelling the velocity induced by bubble flow in the bioreactor draft tube	102
5.4	Summary and conclusions	107

Nomenclature**Symbols**

ϵ	Turbulent dissipation rate
λ	Second coefficient of viscosity
∇	Gradient operator
ν_G	Superficial gas velocity
ω	Turbulent specific frequency
ρ	Fluid density
ρ_b	Density of bubbles
σ	Fluid stress tensor
\mathbf{F}	Body force vector
\mathbf{U}	Velocity vector
C_D	Drag coefficient
D_D^i	Draft tube inner diameter
D_D^o	Draft tube outer diameter
D_T	Tank diameter
μ	Coefficient of fluid viscosity
Re	Reynolds number
Y^+	A non-dimensional wall distance for wall bounded flow
H	Distance from tank base to bottom of draft tube
L	Draft tube length

Abbreviations

CARPT	Computer automated radioactive particle tracking
CFD	Computational fluid dynamics
CT	Computed tomography
GCI	Grid convergence index
MUSCL	Monotonic upstream-centered scheme for conservation laws
RANS	Reynolds averaged Navier Stokes
RSM	Reynolds stress model
SST	Shear stress transport
VSM	Viscous sublayer model
PN	Photosynthesis nutrient

5.1 Introduction

Mixing is an important factor when considering design and operation of bioreactors. The effects of poor mixing can range from inefficiencies to operational instability in the bioreactor resulting in short circuiting and forced shutdown.

As discussed in chapter 2, modelling of bioreactors has mainly focused on the biokinetic growth of biomass within the reactor, using the assumption that biomass concentrations are homogeneously distributed throughout the bioreactor at all times. Some mixing studies

have been undertaken but rarely in conjunction with biokinetics; this is particularly the case when considering algae. As such, the inclusion of mixing in models designed to accurately predict the growth of biomass in bioreactors is of considerable interest. In this chapter detail on computational fluid dynamics as a method of modelling bioreactor mixing is given along with details of a number of simulations which were performed of mixing in a typical bioreactor. These simulations aim to give insight into some of the considerations required when modelling mixing of complex flows in bioreactors, including turbulence model selection and overall modelling approach.

5.2 Computational fluid dynamics modelling

Computational fluid dynamics (CFD) is the broad term used to describe the discrete numerical modelling methods used in fluid mechanics to predict the dynamics of fluid flow under a wide variety of conditions. It has found use in a wide variety of fields from aerodynamics and river modelling (Bernardini et al., 2015; Fischer-Antze et al., 2008) to aerosol transport and blood flow (King et al., 2013; Doost et al., 2015). CFD is concerned with the solving of the partial differential equations used to describe various different aspects of fluid dynamics, from conservation of mass and momentum, to scalar transport and heat transfer. Due to the complexity and non-linearity of the equations involved, the solving of these equations is not a trivial matter. To be able to apply these equations to all but the simplest of problems requires the use of discretisation methods, such as the finite volume and finite difference approximations (Ferziger and Perić, 2002; S. V. Patankar, 1980).

5.2.1 The Navier-Stokes equations

The system of equations governing the flow of viscous fluids are the well known Navier-Stokes equations which can be solved to find a velocity field for the fluid. The equations are the culmination of work by a number of people who discovered the equations in various different forms from various physical hypotheses. This work by Navier, Poisson, Saint-Venant and Stokes was summarised by Stokes (1847) who also presented a derivation of the equations (Drazin and Riley, 2006). The equations for conservation of momentum and

mass of a Newtonian fluid are described below in vector form where equation 5.1 is the result of Stokes (1847) work.

$$\rho \frac{D\mathbf{U}}{Dt} = \rho \mathbf{F} + \nabla \cdot \sigma \quad (5.1)$$

where $\rho(\mathbf{x}, t)$ is the fluid density as a function of the position vector (\mathbf{x}) and time (t), $\mathbf{U}(\mathbf{x}, t)$ the velocity vector, $\mathbf{F}(\mathbf{x}, t)$ the body-force vector per unit mass and σ the stress tensor of the fluid. Applying the material derivative as defined in equation 5.2 to equation 5.1 results in temporal and convective terms of the momentum equation 5.2.

$$\frac{D}{Dt} \equiv \frac{\partial}{\partial t} + \mathbf{U} \cdot \nabla \quad (5.2)$$

The stress tensor, σ , for a Newtonian fluid is a linear function of the rate of strain and can be expanded out into the components shown in equation 5.3 where λ is the second coefficient of viscosity and μ the coefficient of viscosity of the fluid. These values may vary in time in non-Newtonian or other variable fluid conditions, it is common however to assume they are constant in both space and time for most fluids and systems.

$$\sigma_{ij} = -p\delta_{ij} + \lambda \frac{\partial U_k}{\partial x_k} \delta_{ij} + \mu \left(\frac{\partial U_i}{\partial x_j} + \frac{\partial U_j}{\partial x_i} \right) \quad (5.3)$$

Additionally an equation for the conservation of mass is required, the equation of continuity (equation 5.4) describes the idea that a material volume must contain a proportionally constant amount of fluid at all times.

$$\frac{1}{\rho} \frac{D\rho}{Dt} + \nabla \cdot \mathbf{U} = 0 \quad (5.4)$$

Equation 5.4 under constant density in incompressible flow simplifies to 5.6 this also implies that the stress is independent of λ , the volume viscosity, and can be ignored for incompressible fluids. The final result of the above equations when substituted into one another where appropriate are the Navier-Stokes equations (equation 5.5) for incompressible Newtonian fluid flow and the mass continuity equation 5.6.

$$\rho \left(\frac{\partial \mathbf{U}}{\partial t} + \mathbf{U} \cdot \nabla \mathbf{U} \right) = -\nabla p + \mu \nabla^2 \mathbf{U} + f \quad (5.5)$$

$$\nabla \cdot \mathbf{U} = 0 \quad (5.6)$$

These equations contain highly non-linear convective terms which make solving them impossible by analytical means for the majority of flows. CFD focuses on the solving of the continuity and momentum equations through various numerical techniques such as finite element and finite volume methods, in which the equations are discretised over a large number of small cells connected over the whole flow area. With a sufficient number of cells these equations can be used to obtain flow scales down to microscopic turbulent fluctuations, which significantly impact the larger flow features and are thus important to resolve. This level of simulation is known as Direct Numerical Simulation (DNS); unfortunately this is prohibitively expensive for all but the simplest of cases (e.g. low Reynolds number channel flow). As such it is necessary and common to make some assumptions that simplify the equations. For low speed flows ($\text{Mach} < 0.3$), where compressibility effects can be ignored, the density can be considered constant and the full continuity and momentum equations simplify for Newtonian fluids to the incompressible momentum and Navier-Stokes equations (equations 5.5 and 5.6).

Additionally, in order to resolve the effect of turbulence fluctuations at the very small scales without incurring prohibitive computational expense, time averaging of the equations can be performed, resulting in the Reynolds Averaged Navier-Stokes (RANS) equations (Blazek, 2005).

5.2.2 Reynolds averaged Navier-Stokes (RANS) turbulence models

The RANS equations contain additional Reynolds stress terms which mean the equations are not fully closed (there are more unknowns than equations), requiring a turbulence model to provide the additional necessary transport equations (Menter, 2011). These turbulence models are generally only useful for Reynolds numbers in the turbulent region (above 4000), below this the flow is either laminar where no turbulence model is required or transitionally turbulent where turbulence modelling is more complex. There are several methods that can be used to perform the closure of the equations, such as the Boussinesq approximation and Prandtl's mixing length hypothesis. It is the use of the Boussinesq approximation relating the Reynolds stresses to the mean flow that results in the commonly used two equation eddy viscosity models such as $k-\epsilon$ and $k-\omega$. These eddy viscosity models have become the industry standard in solving turbulent flow and, provided the correct model is chosen for the particular flow being simulated, produce a good compromise between accuracy and computational expense.

The prediction of flow separation and Laminar-Turbulent transition has for a long time been difficult to capture using turbulence models as they have a tendency to over or under predict these points in the majority of situations. The standard $k-\epsilon$ model has been consistently found unsuitable for use in accurately modelling low-Re turbulent flows or the separation of turbulent boundary layers effectively; this resulted in attempts to develop more accurate formulations such as the $k-\omega$ SST model (Menter et al., 2003a).

These RANS turbulence models are particularly sensitive when close to walls and the effect of the approach taken when modelling near these boundaries can be significant. The no-slip condition used on solid walls creates a boundary layer that has a significant effect on the flow characteristics close by. Within the boundary layer both molecular and kinematic forces have an effect on the turbulence production and dissipation. There are several methods that can be used to take this effect into account; the simplest and cheapest in terms of computational expense is the use of wall functions. Wall functions use empirical formulations to model the near wall flow where the $k-\epsilon$ model is known to fail. They are however only valid for mesh densities where the Y^+ - a dimensionless wall

distance dependent on the distance to and friction velocity at the nearest wall and the local kinematic viscosity - falls within certain values (between 30 and 300). As such it is desirable to use a near wall treatment that is independent of the Y^+ value. The SST $k-\omega$ model uses a near wall treatment that shifts between a viscous sublayer model (VSM) at small Y^+ values and wall functions at Y^+ values where the VSM is invalid (Menter et al., 2003a). A variation on this blended near wall treatment is also available for epsilon based two-equation turbulence models in the form of the enhanced wall treatment in Fluent 13.0sp2. This Y^+ independent wall treatment is more attractive in terms of mesh refinement studies, posing no restrictions on the refinement near walls.

5.2.2.1 Two equation turbulence models

5.2.2.1.1 RNG $k - \epsilon$ model

The RNG $k - \epsilon$ model is an extension of the original $k - \epsilon$ model developed by Jones and Launder (1972). The $k - \epsilon$ model has been the most widely used of the RANS turbulence models over the last 40 years. Originally designed to improve the mixing length model, two additional transport equations for turbulent kinetic energy (k) and turbulent dissipation rate (ϵ) are solved. The model has been shown to give reasonably good results for external aerodynamic flows with small pressure gradients. Similarly, the results for wall bounded flows with small pressure gradients compare well with experimental results. The model has however shown to be less well suited to flows with large pressure gradients (Bardina et al., 1997). The RNG $k - \epsilon$ model was developed by Yakhot et al. (1992) using re-normalisation group methods in order to account for the effects of smaller scales of motion. These improvements to the $k - \epsilon$ model improve the accuracy in predicting secondary turbulent flows as well allowing the model to account for low Reynolds number effects with the use of appropriate wall treatments.

5.2.2.1.2 $k - \omega$ SST model

The original idea behind the $k - \omega$ SST (shear stress transport) turbulence model was to develop a model which was able to accurately predict aeronautical flows with strong

adverse pressure gradients. Although many turbulence models had had been developed of the decades previous none had succeeded in producing accurate predictions for such flows. The idea behind the $k - \omega$ SST model was to use the $k - \epsilon$ model which produced good predictions in the free stream flow away from boundary layers but which failed capture the behaviour of turbulent boundary layers along with the $k - \omega$ model developed by Wilcox which although giving good results in the boundary layer was unable to predict pressure induced boundary layer separation, additionally, the model suffered from high sensitivity of ω in the freestream. Using a zonal approach which used the $k - \omega$ formulation near walls in the boundary layer and the $k - \epsilon$ model reformulated in terms of ω in the freestream allowed for the model to provide accurate predictions for pressure-induced boundary layer separation as well as in the freestream flow (Menter et al., 2003b).

5.2.3 Euler-Lagrange multiphase modelling

Euler-Lagrange multiphase modelling assumes one fluid phase to be dominant (by volume), usually consisting of more than 90% of the domain, which is treated as a continuum, modelled in the Eulerian reference frame and solved using the Navier-Stokes equations. Additional dispersed phases (e.g. sand particles, bubbles, etc.) are modelled as particle packets. These dispersed particles are modelled by integrating the force balance on the particles in the Lagrangian reference frame (Brebba and Mammol, 2011). Equation 5.7 is the force balance equation for the Cartesian X coordinate, where the drag force (FD) is described by equation 5.8.

$$\frac{du_b}{dt} = F_D \left(u - u_b \right) + \frac{g_x (\rho_b - \rho)}{\rho_b} + F_{vm} + F_p \quad (5.7)$$

$$F_D = \frac{18\mu C_D Re}{\rho_b d_b^2} \frac{1}{24} \quad (5.8)$$

The last two terms in equation 5.7, F_{vm} and F_p , are additional force terms specific to bubble driven flow. Equation 5.9 is a virtual mass force which accelerates the fluid surrounding the particles, applicable where $\rho \gg \rho_b$ equation 5.10 is included to account for the effect of pressure gradients.

$$F_{vm} = \frac{1}{2} \frac{\rho}{\rho_b} \frac{d}{dt} (u - u_b) \quad (5.9)$$

$$F_p = \left(\frac{\rho}{\rho_b} \right) u_{b_i} \frac{\partial u}{\partial x_i} \quad (5.10)$$

5.3 CFD modelling of a gas-lift bioreactor, assessing turbulence model selection and flow control

Mixing the fluid within a bioreactor to create a homogeneous solution can be performed in a number of different ways, including mechanical impellers, recirculation pumps, bubble induced mixing as well as combinations of these methods as described in detail in section 2.2.3. Although all these methods have advantages in disadvantages in themselves they also incur differing numerical cost when attempting to perform CFD analysis of a bioreactor. A number of approximations and simplifications have been developed which are of use in these situations but they themselves incur costs in terms of accuracy and must be properly validated to be used appropriately (Aubin et al., 2004). In order to develop a coupled model which includes both biokinetic and CFD mixing a suitable bioreactor model is required. One of the commonly used methods of mixing in bioreactors (and introducing oxygen in the case of aerobic reactions) is the use of gas (e.g. air, nitrogen, etc.) injected at some point near the bottom of the bioreactor. Additionally, the use of draft tubes to create a recirculating flow within the bioreactor and improve mixing of biomass vertically is sometimes seen (Luo and Al-Dahhan, 2011; Kojima et al., 1999; Karim et al., 2004; Meroney and Sheker, 2014). An example of a bubble mixed bioreactor is described here and further investigated under a number of different modelling conditions to determine the sensitivity of the model and show the importance of careful consideration when setting up the model.

Karim et al. (2007) performed CFD analysis on a bench-scale gas-lift anaerobic bioreactor with a central draft-tube (figure 5.1a), this modelling work was an extension of previous work by the authors ((Karim et al., 2004)) investigating the mixing within the bioreactor

using experimental methods. Both velocity profiles and velocity vectors for the bioreactor were obtained using a combination of computer automated radioactive particle tracking (CARPT) and computed tomography (CT). The geometry (figure 5.1a) and layout of the computational domain (figure 5.1b) for this gas-lift bioreactor consist of a small cylindrical glass tank with a draft tube suspended within the fluid below the surface and not touching the base. The gas was pumped through a tube which extended from the top of the tank to the bottom edge of the draft tube with the gas being pumped in at several different flow rates. Karim et al. (2007) made the assumption that the gas holdup (amount of gas) in the annular section of the bioreactor was negligible allowing them to reduce their model to a singlephase approximation of the experimental bioreactor. This simplification although reducing the complexity and computational expense of the model wouldn't take into account any of the more localised effects of the bubbles, particularly, directly above and below the draft tube where any effects would be most prominent.

The assumption reducing the model to a single-phase problem with the gas phase neglected requires a method to approximate the velocity induced by the rising bubbles within the draft tube, to this end an inlet boundary condition was assumed at the top of the draft tube with the corresponding outlet condition at the bottom of the draft tube. In order to apply an appropriate inlet boundary condition which would imitate the velocity at the top of the draft tube in the real bioreactor Karim et al. (2007) used a simplified version of an equation (equation 5.11) developed by Kojima et al. (1999) for flow velocity at the top of a draft tube. The resulting formula modified by Karim et al. (2007) to equation 5.12, where ν_G is the superficial gas velocity, D_T is the tank diameter, D_D^i the tube inner diameter, D_D^o the tube outer diameter, L the draft tube length and H the distance from the draft tube bottom to the bioreactor base. Using equation 5.12 a constant value of velocity at the top of the draft tube was calculated based on the experimental gas flow rate was obtained.

$$U = 0.401 \left[\nu_G \left(\frac{D_T}{D_D^i} \right)^2 \right]^{0.564} \left[\frac{D_T^2 - D_D^{o2}}{D_D^{i2}} \right]^{-0.182} L^{0.283} H^{0.0688} \quad (5.11)$$

$$U = 0.401 \left[\nu_G \left(\frac{D_T}{D_D^i} \right)^2 \right]^{0.564} \left[\frac{D_T^2 - D_D^{o2}}{D_D^{i2}} \right]^{-0.182} \quad (5.12)$$

Additionally, as the bioreactor is cylindrical in shape and assuming the gas flowed out of the inlet tube in all radial directions the model can be further reduced to an axisymmetric problem decreasing the number of degrees of freedom being modelled, allowing for a much smaller mesh (lower cell count) and lowering the computational cost. As the bioreactor is being modelled as a singlephase system the freesurface of the liquid becomes a boundary condition rather than being considered as an interface between liquid and gas. The most appropriate boundary approximation in this case is a zero shear boundary (as opposed to the standard no-slip boundary used at walls) allowing for free flow of the fluid along the boundary. All other walls have a no slip boundary applied as is standard for approximating the effects fluids on smooth walls. The inlet at the top of the draft tube has a constant velocity inlet using the values calculated from equation 5.12 and the outlet is a zero pressure outlet.

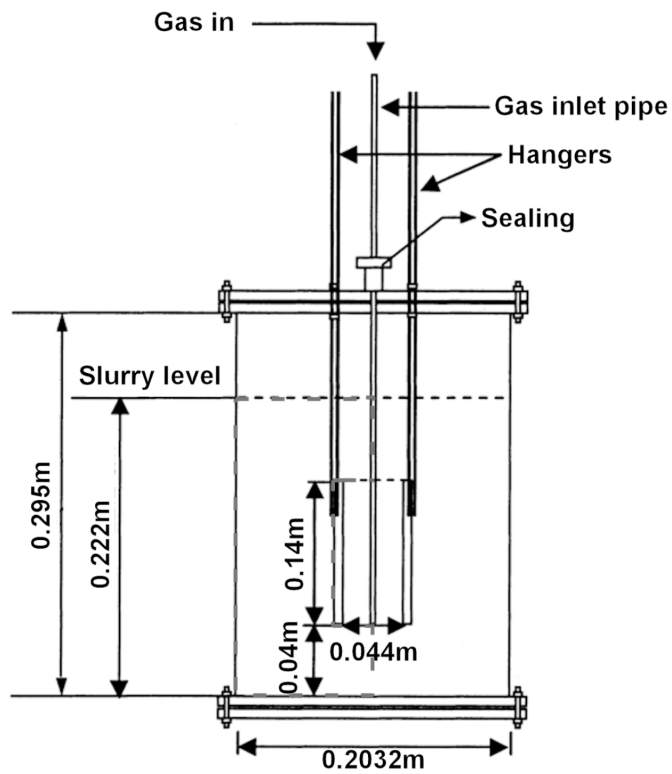
A calculation of the Reynolds number of the bioreactor under conditions described by Karim et al. (2004) of $\nu_G = 56.64l.h^{-1}$ produces a value in the transitional turbulent region making the use of a turbulence model advisable. The addition of flow separation shown in the experimental work makes the choice of turbulence model an important question and one that will be analysed in some depth here. The specific solver settings used for the modelling are described in table 5.1, any additional settings or changes to settings for specific simulations are described in the appropriate sections.

The remainder of this chapter is dedicated to describing the CFD simulations performed assessing the different approaches to modelling the gas-lift bioreactor described above. Mesh independence testing, CFD solver comparison, turbulence model selection and singlephase vs. multiphase approximations are all discussed in detail. All modelling shown here, unless otherwise stated, was performed using the ANSYS Fluent 13.0sp2

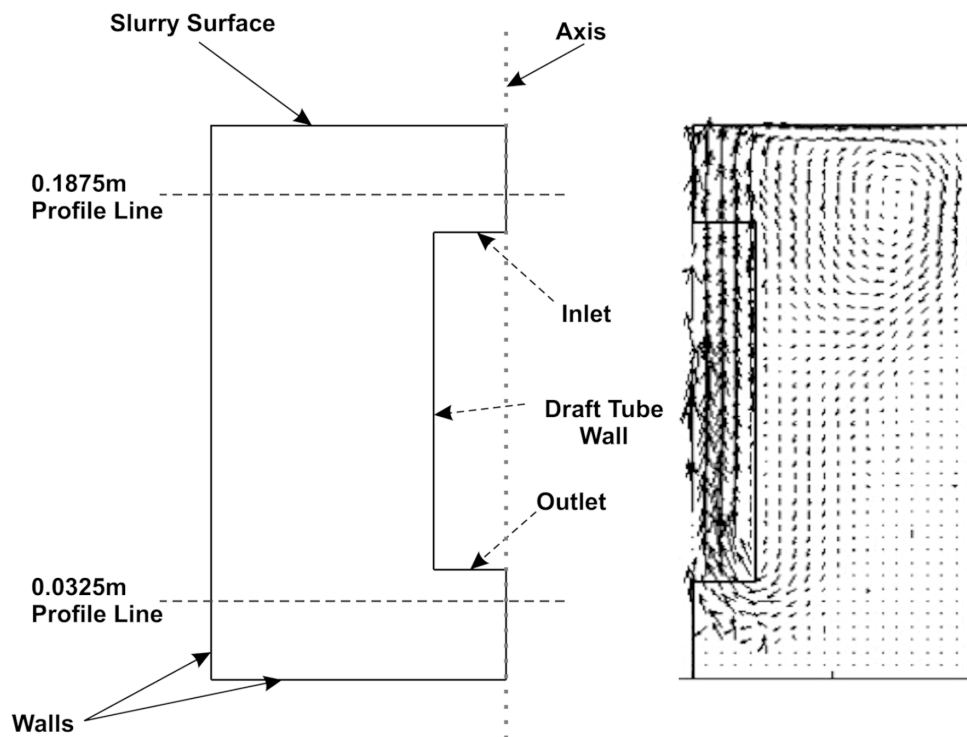
	Solver Setting (Fluent)
Solver	Coupled
Turbulence model	$k - \omega$ SST
Wall treatment	Blended VSM
<i>Boundary conditions</i>	
Inlet	Velocity normal inlet 0.09804 m.s^{-1}
Outlet	0 Pa gauge pressure
Walls	No slip
Surface	Zero shear
<i>Discretisation Schemes</i>	
Gradient Scheme	Least squares cell based
Pressure	Second order
Momentum	Third order MUSCL
Turbulent kinetic energy (k)	Third order MUSCL
Specific dissipation rate (ω)	Third order MUSCL

Table 5.1: Solver settings for CFD simulations performed here. Any changes to these setting are described where appropriate.

CFD package.



(a) Bench scale bioreactor geometry (adapted from (Karim et al., 2004)).



(b) Computational geometry for singlephase model and experimental results of Karim et al. (2004).

Figure 5.1: Gas-lift bioreactor geometry and experimental results as used by Karim et al. (2004) and 2-D computational geometry for CFD analysis.

5.3.1 Mesh independence testing of CFD simulations

Mesh independence testing is an important part of all CFD modelling, it allows for the determination of the accuracy of the solution in terms of the numerical errors produced by the mesh discretisation and the numerical order of the equation discretisation schemes. Described here are the mesh independence test results for the bioreactor using the settings described in table 5.1. Figure 5.3 shows the mesh independence of the solutions where ' m ' and ' n ' are the horizontal and vertical cell counts as described in table 5.2. Also included in table 5.2 are the average Y^+ values for the mesh with the $k - \omega$ SST turbulence model. Four different mesh densities were used, scaling based on the ' m ' and ' n ' values.

Mesh number	m	n	No. of elements	Average Y^+
N_4	80	160	4450	2.07
N_3	160	320	17800	1.07
N_2	320	640	71200	0.55
N_1	480	960	160200	0.37

Table 5.2: Mesh independence densities and Y^+ values

When using the $k - \omega$ turbulence models a $Y^+ \approx 1$ is desirable to keep the node of the first element as close to the wall as possible; this keeps the node within the laminar layer and thus allows the solution to be integrated to the wall. Figure 5.2 shows the velocity contour with velocity vectors for the mesh independence solution for a mesh of 71200 elements. The figure shows the boundary layer separation at the outer wall an reattachment on the draft tube, points which are also shown in figure 5.4 where their significance is more apparent.

To determine whether the velocity fields calculated in the simulations are independent of the mesh density a method known as the grid convergence index (GCI) is used (Celik et al., 2008). The GCI reports the discretisation error and apparent order p of a numerical solution method. The apparent order p of the solution method was calculated as 2.304. Three GCI values were determined for the four meshes, $GCI_{fine}^{21} = 0.19\%$, $GCI_{medium}^{32} = 0.49\%$, and $GCI_{coarse}^{43} = 0.83\%$. The small value of GCI shown for the 160200, 71200 and 17800 element meshes indicates that mesh independence is achieved with the 17800 element mesh. Figure 5.3 shows axial velocity profiles at locations just

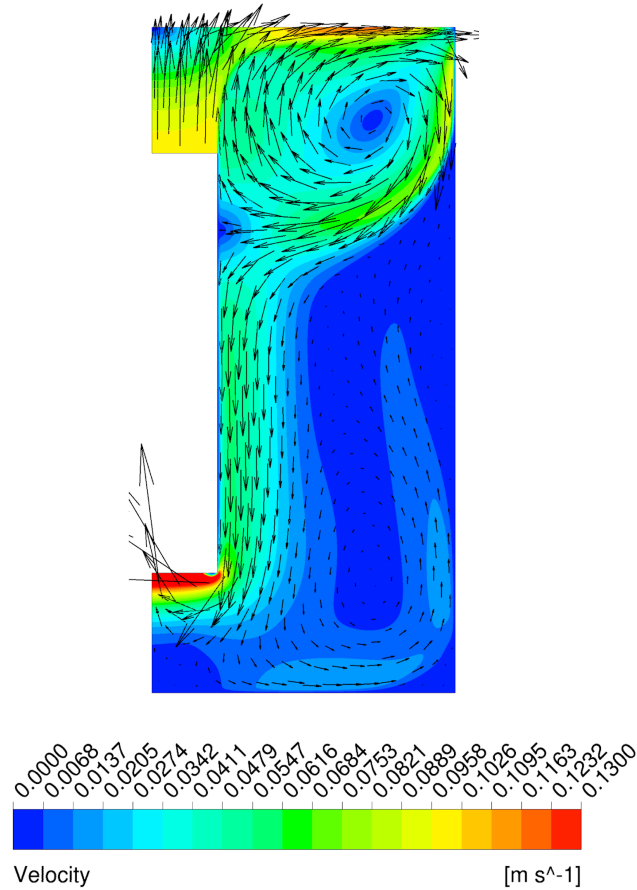
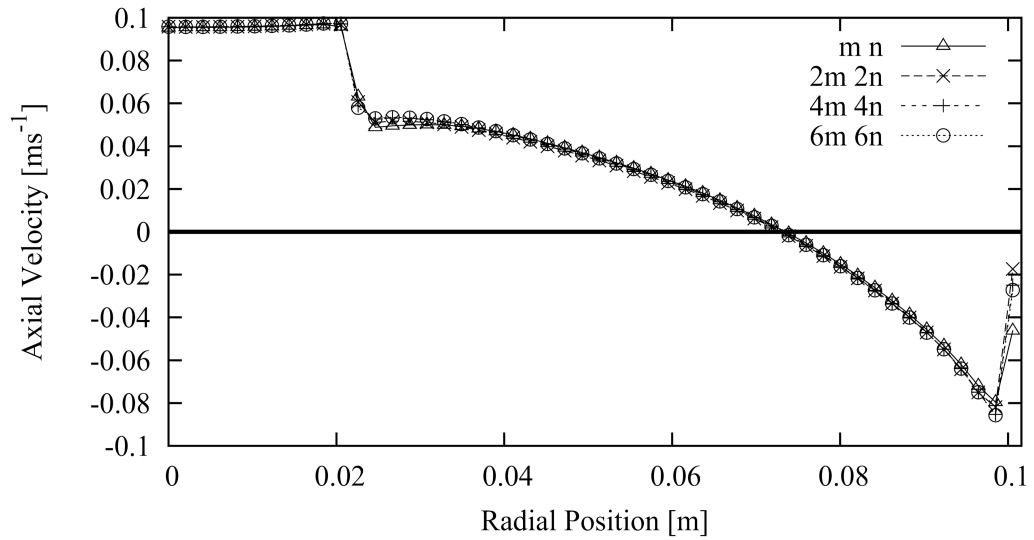


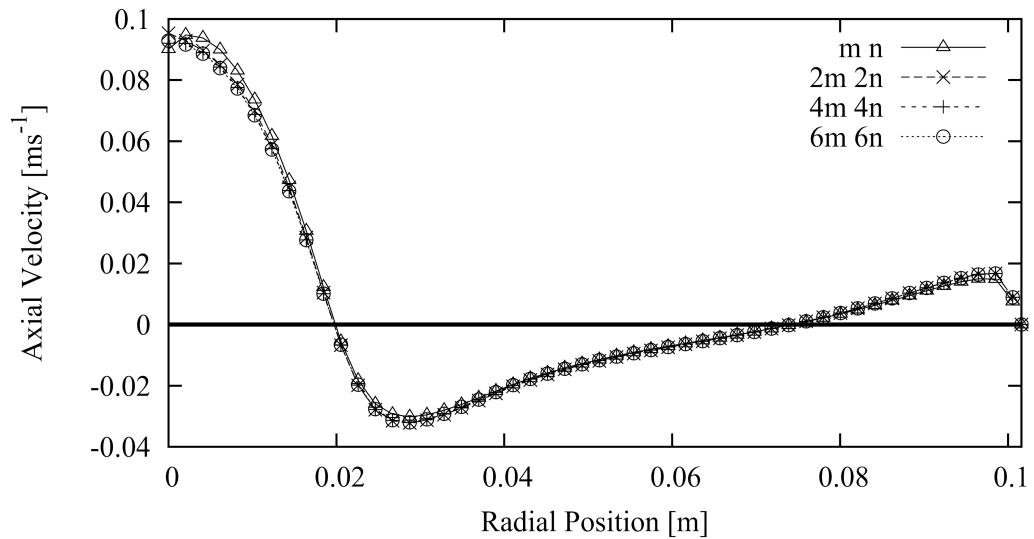
Figure 5.2: Velocity contour and vector for mesh independence testing

above the inlet (figure 5.3a) and just below the outlet (figure 5.3b) (in a similar way to Karim et al. (2007)).

These plots show agreement with the GCI indicating that the solution may be deemed mesh independent for the 17800 element mesh. However, the point where the solution separates from the outer wall and reattaches at the draft tube wall, as shown in the plots of figure 5.4a and 5.4b, that the solution is more sensitive at the wall and independence can only be reasonably assumed with a mesh of 71200 elements. This increase in mesh density also has the advantageous effect of reducing the average Y^+ value to less than 1, a preferable value for maintaining accuracy near the wall. As it is not possible in this case to obtain a Y^+ value of 30 (without significantly compromising mesh independence) as would be recommended when using wall functions, it is more appropriate to aim for unity where the VSM is most applicable. This may not however be the case in a full scale bioreactor where Re numbers can be significantly higher and computations on a mesh fine enough to



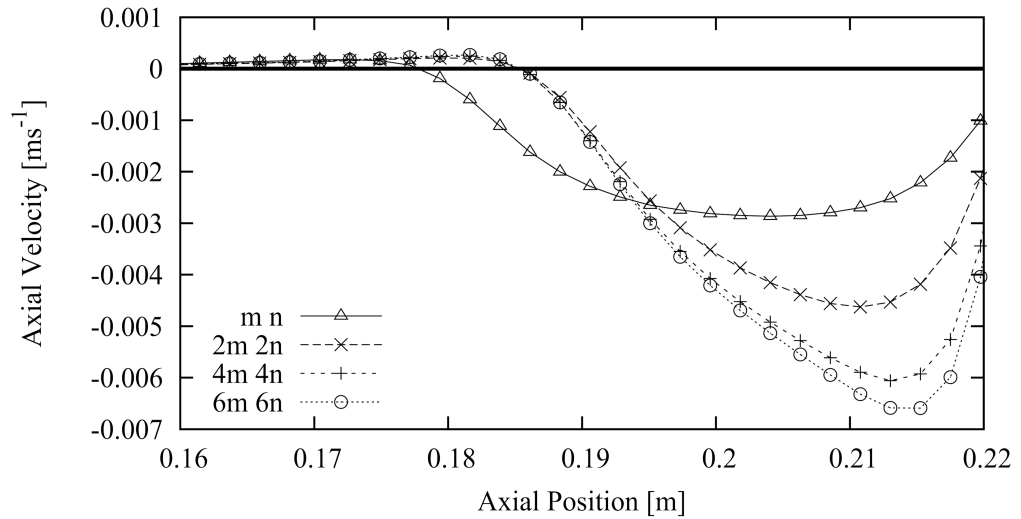
(a) Velocity profiles at 0.1875m above the base of the bioreactor for different mesh densities



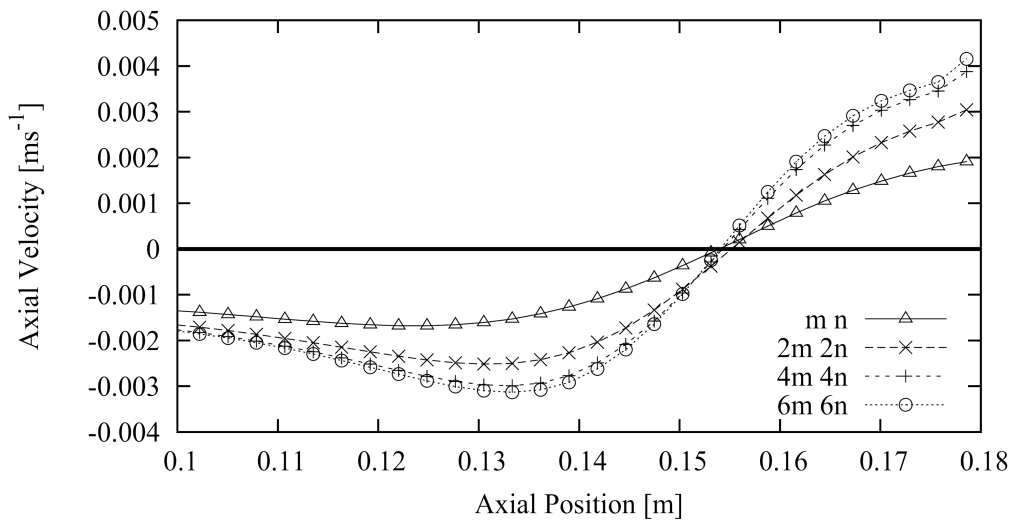
(b) Velocity profiles at 0.0325m above the base of the bioreactor for different mesh densities

Figure 5.3: Velocity profiles for mesh independence testing where the different mesh densities displayed in the plot are defined in table 5.2

achieve a $Y^+ \approx 1$ are expensive. Taking all these factors into account it was decided that the 71200 cell mesh was most suitable for use in all subsequent calculations.



(a) Separation point



(b) Reattachment point

Figure 5.4: Separation and reattachment points for mesh independence testing

5.3.2 RANS turbulence model assessment

When modelling turbulent flow, in particular flow with boundary layer separation, it is important to choose the most appropriate turbulence model for the problem at hand. To determine the most appropriate turbulence model for flow in the bench-scale gas-lift bioreactor, an assessment of some common turbulence models and their capabilities in resolving the flow field was performed. As was previously stated in section the fact that flow separation is an important factor in the mixing within this bioreactor it is essential to choose a turbulence model which accurately predicts the points at which flow separation

occurs. For this reason the turbulence models assessed here were chosen because of their ability to capture such flow features. The turbulence models which fit the requisite criteria are listed in table 5.3 along with the most appropriate wall treatment for the mesh used here (as described in section 5.3.1).

Turbulence model	Wall treatment
RNG $k - \epsilon$	Enhanced wall treatment
$k - \omega$ SST	Omega blended wall treatment
Linear RSM	Enhanced wall treatment
SST Transition	Omega blended wall treatment

Table 5.3: Turbulence models and their respective wall treatments

Using the same geometry and model setup as for the mesh independence test, velocity vector and contour plots for each of the chosen turbulence models are shown in 5.5. Additionally the axial velocity profiles for locations 0.1875m and 0.0325m above the bioreactor base are shown (figure 5.6) along with the plots of flow separation and reattachment points (figure 5.7). Experimental results collected by Karim et al. (2004) are also shown on the velocity profile, separation and reattachment plots as a validation of the effectiveness of each turbulence model. As can be seen in the contour plots each of the turbulence models gives significantly different results to its fellows, this further illustrates the importance of choosing the correct one and not just relying on industry standards.

As can be seen in figure 5.6a when comparing the results of the different turbulence models to the experimental results of Karim et al. (2004) the model predict the velocity profile quite well with the Transition-SST model being the most consistent over the width of the bioreactor. The turbulence model with the least accurate result when considering flow on this profile is the RNG $k - \epsilon$ model. The results for the velocity profile near the outlet (0.0325m from bioreactor base) in figure 5.6b are less accurate when compared to the experimental results were all the turbulence models over predict the velocity at the base of the draft tube. This is most likely due to the lack of any downward velocity provided by the inflow of gas into the bioreactor.

Figure 5.7a shows the separation point of the boundary layer on the outer wall of the

bioreactor, this plot show that the RNG $k - \epsilon$ over predicts the location of the separation point while the $k - \omega$ SST under predicts it (a known problem with this model). Both the Transition SST and Linear RSM model do a good job of predicting the separation point accurately when compared to the experimental results. The obvious differences in the separation point locations can also be clearly seen in 5.5. The results for the reattachment point (figure 5.7b) mimic those of the separation point with the Transition SST and Linear RSM both performing well.

The results of the turbulence model comparison shown here indicates that the best choice of turbulence model for this bioractor is the Transition SST model which provides accurate results for the velocity profiles and in terms of the predicting the stagnation zones in the bioreactor.

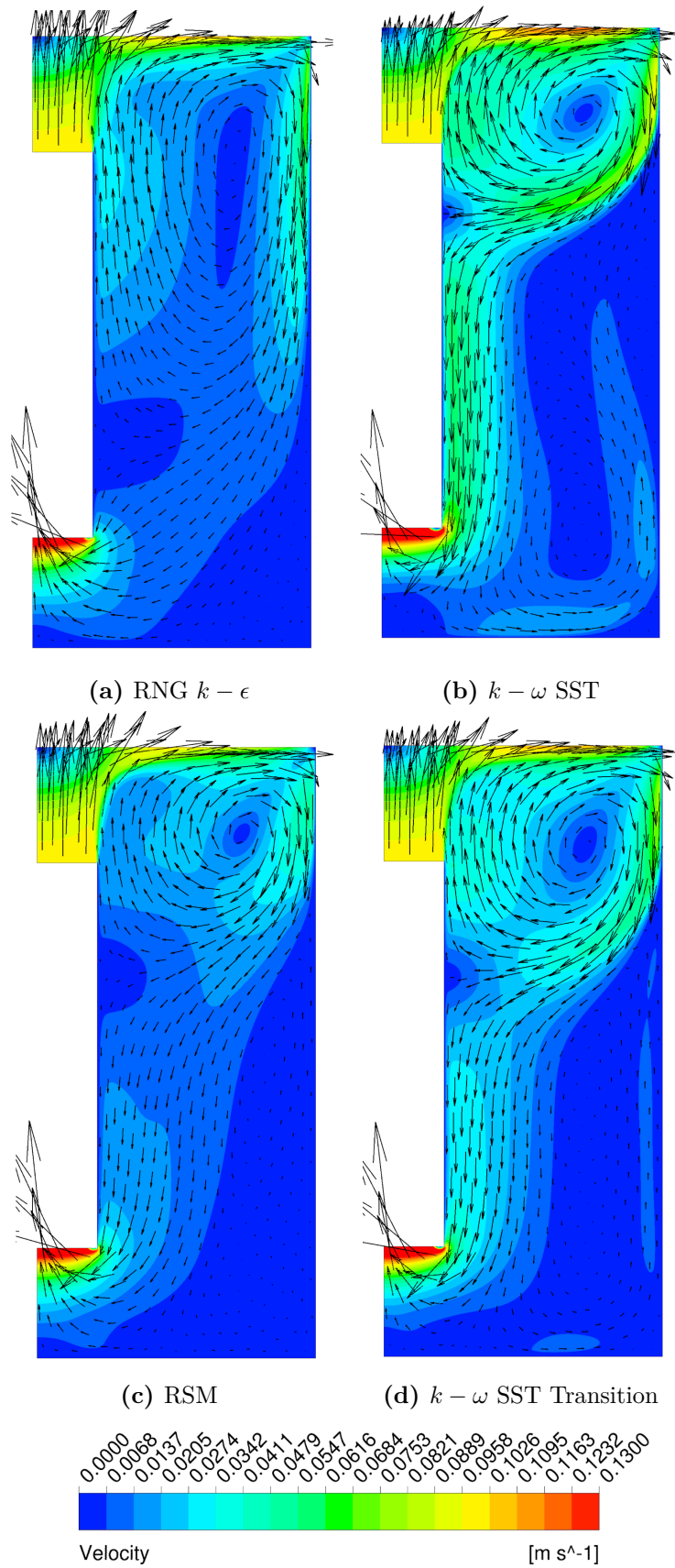
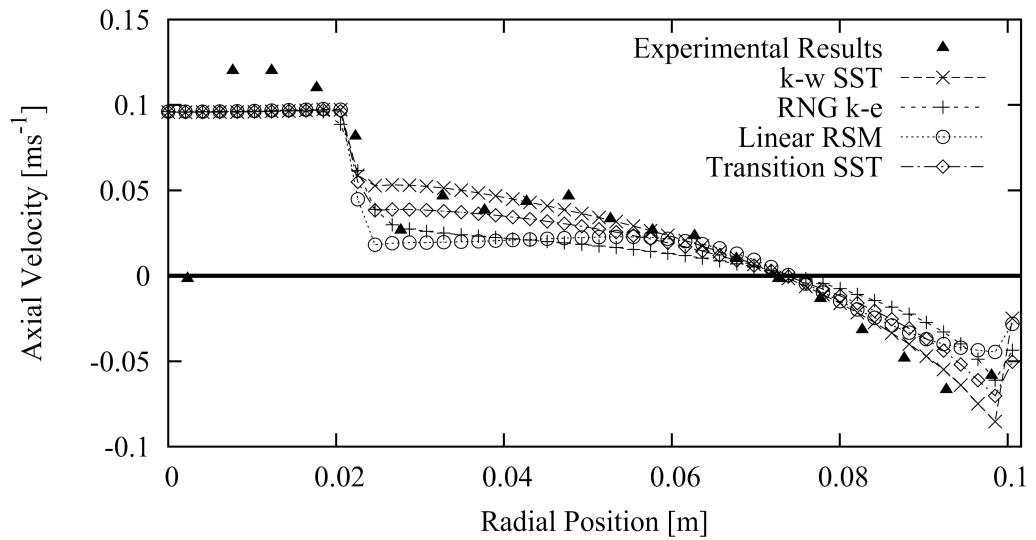
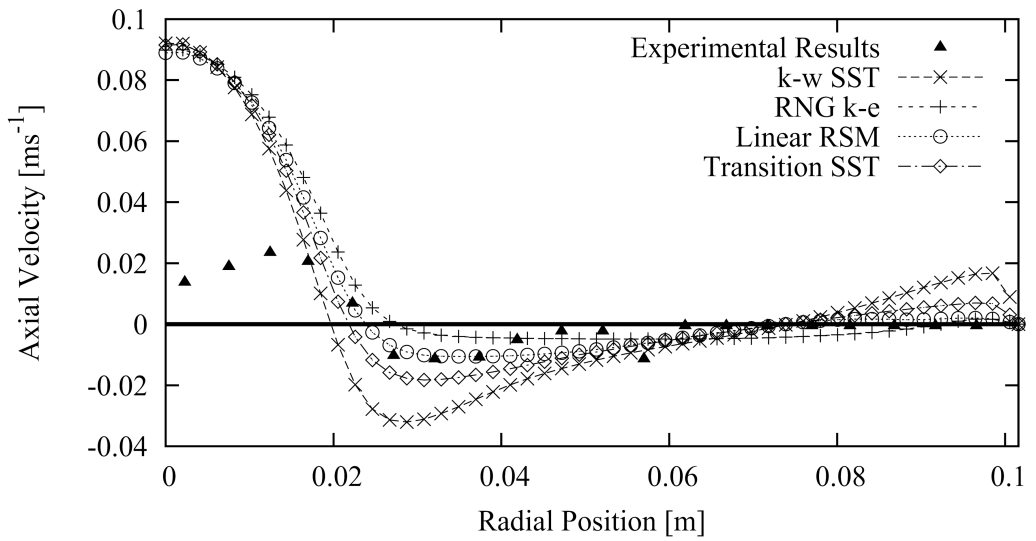


Figure 5.5: Velocity contour and vector plots for different turbulence models for flow in a bench-scale bioreactor.

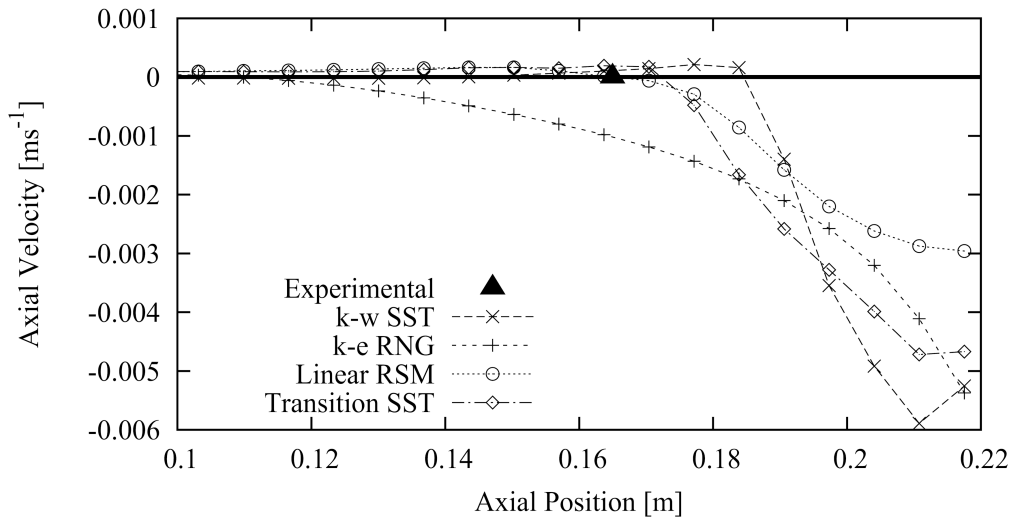


(a) Axial velocity profiles at 0.1875m from bioreactor base

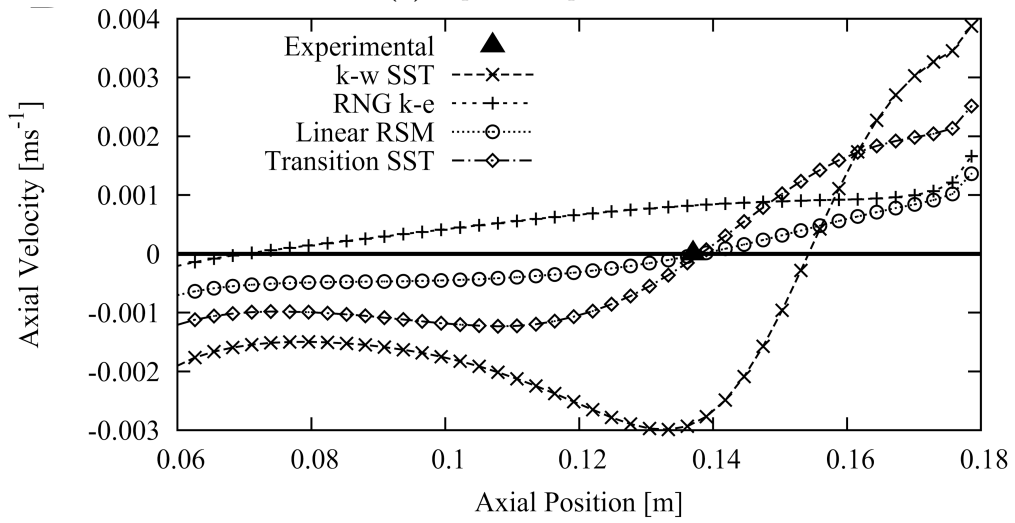


(b) Axial velocity profiles at 0.0325m from bioreactor base

Figure 5.6: Axial velocity profiles at 0.1875m and 0.0325m from base of bioreactor for different turbulence models compared with experimental results obtained by Karim et al. (2004)



(a) Separation points



(b) Reattachment points

Figure 5.7: Axial velocity profile plots for the separation point at the outer wall of the bioreactor and the reattachment point on the drafttube wall for the different turbulence models

5.3.3 CFD solver comparison (ANSYS Fluent vs. OpenFOAM)

In order to be assured the results being obtained were solver independent a comparison between results from Fluent 13.0sp2 and OpenFOAM 3.0.0 was made. Table 5.4 shows the settings used in both the solvers including boundary conditions and discretization schemes.

Setting	Fluent	OpenFOAM
Solver	Coupled	Simple
Turbulence model	$k - \omega$ SST	$k - \omega$ SST
Wall treatment	Blended VSM	Blended VSM
<i>Boundary conditions</i>		
Inlet	Velocity normal inlet 0.09804 m.s^{-1}	Velocity normal inlet 0.09804 m.s^{-1}
Outlet	0 Pa gauge pressure	0 Pa fixed value
Walls	No slip	No slip
Surface	Zero shear	Zero shear
<i>Discretisation Schemes</i>		
Gradient Scheme	Least squares cell based	Least squares
Pressure	Second order	Least squares
Momentum	Third order MUSCL	∇ :Gauss MUSCL, ∇^2 :Gauss linear corrected
Turbulent kinetic energy (k)	Third order MUSCL	∇ :Gauss MUSCL, ∇^2 :Gauss linear corrected
Specific dissipation rate (ω)	Third order MUSCL	∇ :Gauss MUSCL, ∇^2 :Gauss linear corrected

Table 5.4: Fluent and OpenFOAM settings comparison

OpenFOAM is an open source CFD code and like Fluent it is Finite Volume based. It would be expected that both solvers should produce very similar results when using the same (in principal) settings. The $k-\omega$ SST turbulence model was used as its application and the near wall treatment available in OpenFOAM is produced from the work of Menter and Esch (2001) as in Fluent. The availability of the VSM for near wall treatment when using the $k-\omega$ SST in OpenFOAM allows the solver settings to be kept as similar as possible to those used in Fluent. Figure 5.8 shows contours of velocity magnitude for the two solvers, as can be seen there is qualitatively little difference in the solutions in regards to the general flow field. However, the velocity profiles shown in Figure 5.9 do highlight some very minor differences. The profiles at 0.1875m show little difference, whereas the

solution at 0.0325m shows a slight divergence between the results below the outlet. This is likely due to the formulation of the pressure outlet boundary condition being different in the two solvers. This strong agreement of the two solvers confirms that the study results are solver independent.

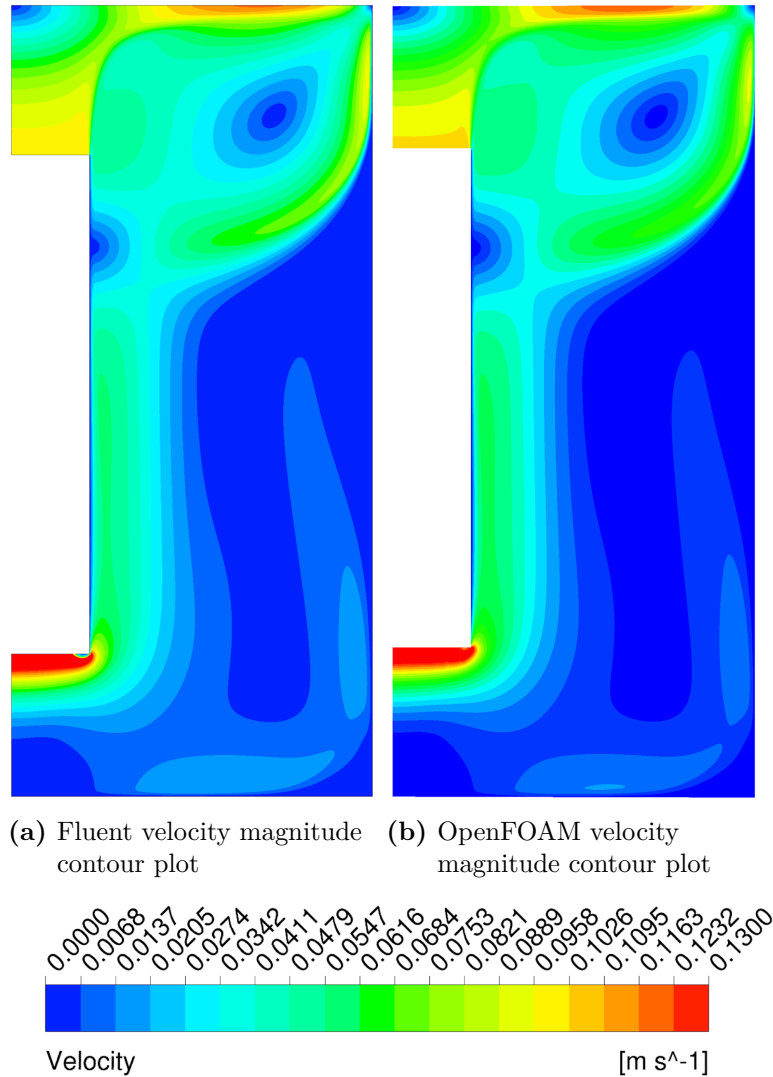
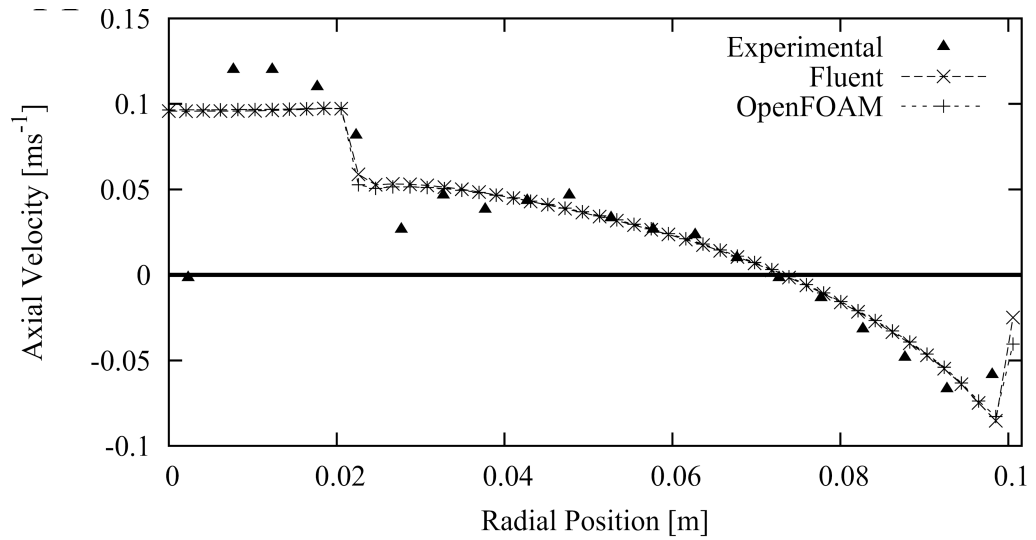
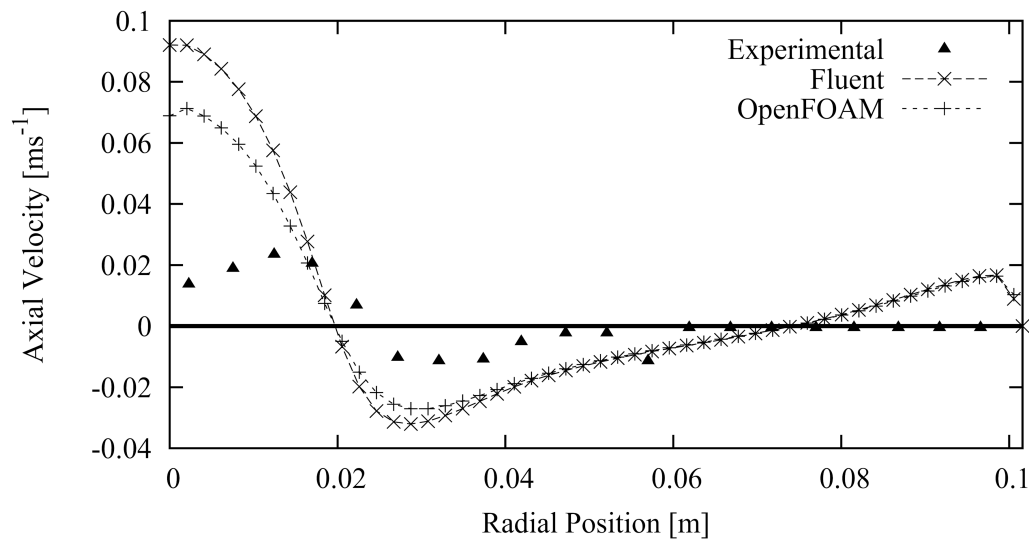


Figure 5.8: Comparison between Fluent and OpenFOAM velocity contours



(a) Inlet profile



(b) Outlet profile

Figure 5.9: Comparison between Fluent and OpenFOAM velocity profiles

5.3.4 A comparison of different approaches for modelling the velocity induced by bubble flow in the bioreactor draft tube

Here a comparison between three different methods of approximating the effect of the rising bubbles which are used to drive the flow inside the bioreactor are described and evaluated. The solver settings for the modelling described in this section use the same values as those described in table 5.4 for the appropriate solver unless otherwise stated. Two of the methods use a singlephase approach while the last uses Euler-Lagrange multiphase modelling to mimic bubble flow in the draft tube as described in section 5.2.3. The first

singlephase approximation was that previously described in sections 5.3.1 - 5.3.3 where the velocity as calculated in equation 5.12 is applied as an inlet condition at the top of the draft tube and a zero pressure outlet condition is applied at the bottom of the outlet. The second singlephase method implemented was a model using a mean average velocity force at the top of the draft tube to drive the flow in the bioreactor. This negates the need for an inlet and outlet condition reducing the problem to a closed loop system (figure 5.10). The same value for velocity was used as with the inlet/outlet singlephase model even though the implementation averaged the velocity across the width of the draft tube. This momentum source term model was implemented in the software OpenFOAM-3.0.0; the method works by calculating and applying the force necessary to maintain the desired average velocity in the area specified. The lack of availability of the Transition-SST model in OpenFOAM-3.0.0 means that an alternative turbulence model is required; as such the $k - \omega$ SST model was used instead.

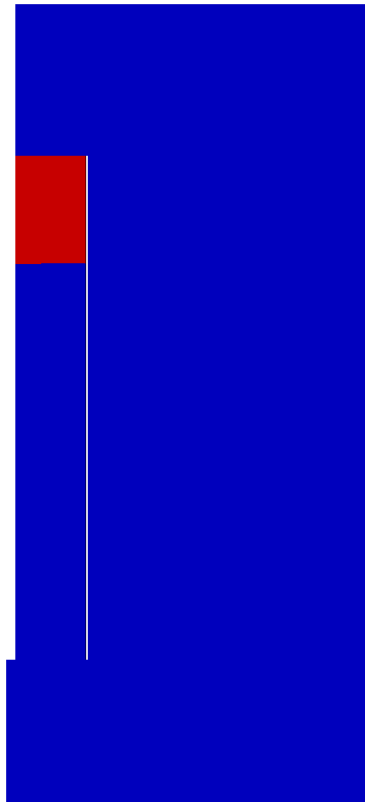


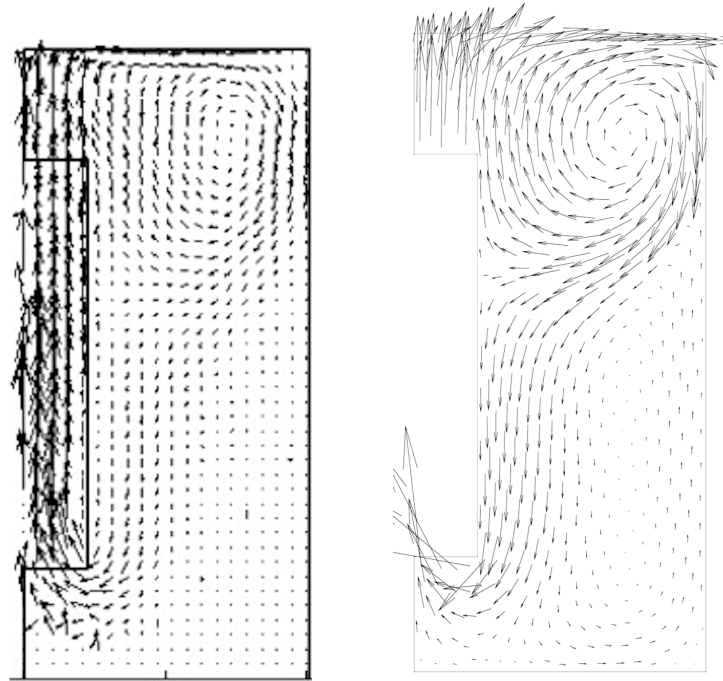
Figure 5.10: Closed loop singlephase bioreactor with momentum source. Zone in which the mean average velocity force was applied in the draft tube shown in red

The final method of approximating the bubble driven flow was through the use of

a Lagrangian particle tracking multiphase method in the Fluent solver. Use of the multiphase approach allows for the assessment of the velocity approximation used at the top of the draft tube by the singlephase models. Of particular interest were the effects the use of the multiphase method would have on the velocity just above and below the draft tube where the singlephase models shown in figure 5.6 struggle to accurately predict. For the multiphase model several assumptions were made to reduce the complexity of the model. The first assumption was to release the bubble half way between the draft tube wall and the gas inlet pipe (location 0.011, 0.04). This allows the bubble to rise unhindered by the walls which would not be the case if the bubbles were released from the bottom of the gas inlet pipe. By injecting the bubbles in this way the inclusion of thin film models for the walls is unnecessary as the bubbles rise without coming into contact with the walls. Axisymmetry was also assumed as with the singlephase model, which for the Lagrangian phase results in a continuous bubble ring.

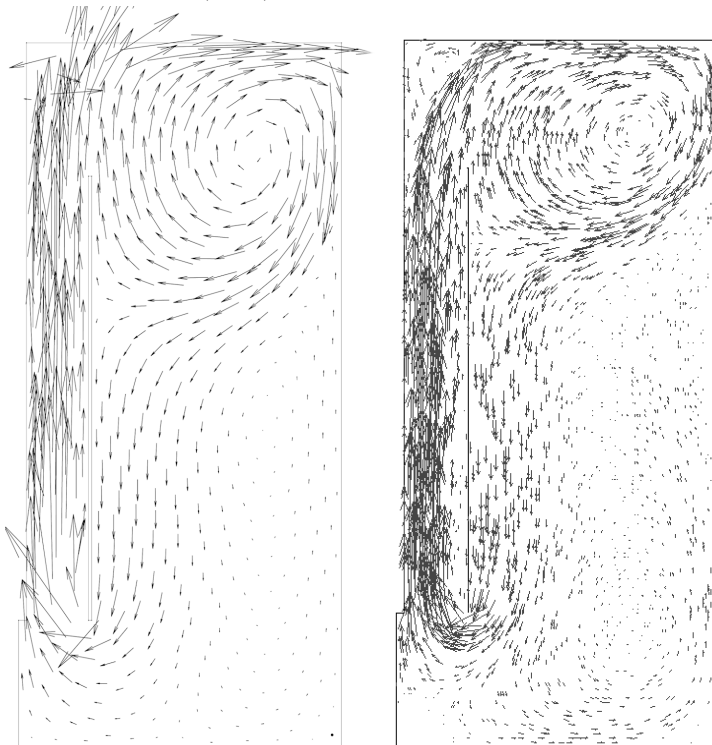
The velocity vector plots of these three different methods of implementing the velocity in the bioreactor are shown in figure 5.11 along with the experimental velocity vector plot obtained by Karim et al. (2004) in their experimental analysis of the bioreactor. As is to be expected all three methods show similar vector profiles with the appropriate flow separation and reattachment as well as the stagnation zone in the outside bottom corner of the bioreactor. The only differences between the results shown occur in figure 5.11d showing the results for the momentum source model where flow separates from the outer wall higher up than in the other plots. This difference however is more likely to be due to the use of the $k - \omega$ SST turbulence model in lieu of the transition SST model which is unavailable in OpenFOAM. This can be confirmed when comparing the result with those in figure 5.8.

Further analysis of the results using velocity profiles plots above and below the draft tube shows good agreement for all the models when compared to the experimental results of Karim et al. (2004). The profile plots above the draft tube (figure 5.12a) show good agreement for all the flow control methods used, directly above the draft tube itself (Radial position 0 - 0.022m) shows that the momentum source term modelling method provides the most accurate results showing a velocity profile consistent with wall bounded flow as



(a) Experimental results of Karim et al. (2004)

(b) Inlet/outlet singlephase model



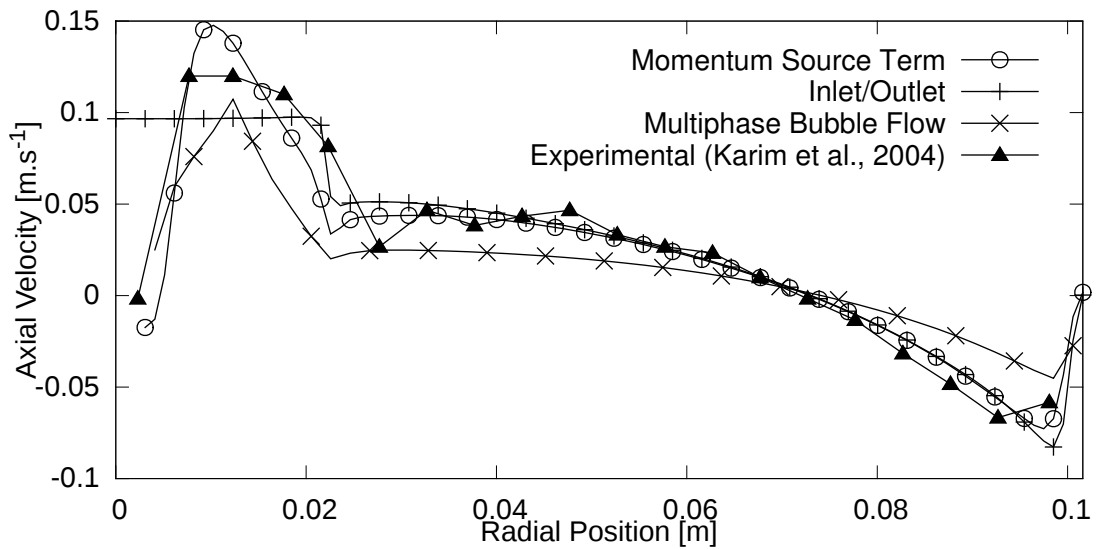
(c) Euler-Lagrange multiphase model

(d) Momentum source term singlephase model

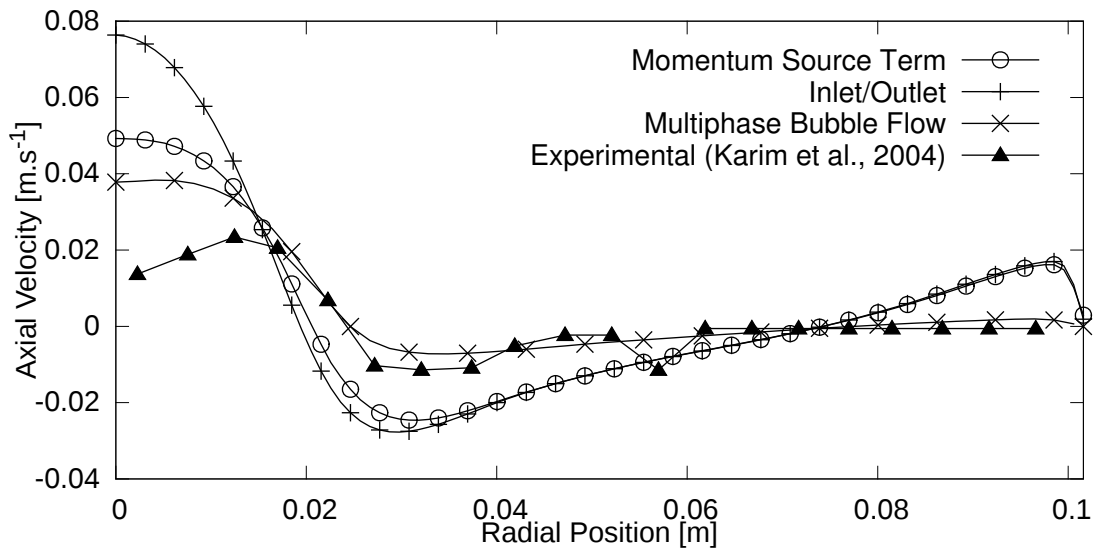
Figure 5.11: Velocity vector plots for the different methods of controlling the flow in the gas-lift bioreactor

would be expected. A similar profile is shown for the multiphase model with a slightly higher peak velocity when compared to both the experimental and momentum source results. The inlet outlet method shows the least correlation with the experimental results with a flat velocity profile due to the constant velocity at the top of the draft tube. This trend in the accuracy of the results is reversed however when looking at the results near the outer wall of the bioreactor with the multiphase model producing the less accurate velocity profile and the inlet/outlet model being more accurate. The momentum source model again shows a good approximation to the experimental results however making it the most accurate of the three when looking at the velocity profile above the draft tube. When considering the results for the velocity profiles below the bioreactor however the results are in favour of the multiphase model in all areas of the bioreactor. In the main annular section (0.022 - 0.1016m) the multiphase results are almost identical to the experimental data with both the singlephase models both under and over predicting the velocities. Directly below the draft tube again the multiphase model predicts the velocity more accurately than the singlephase models, though not with the same accuracy as in the main reactor.

Overall the multiphase model predicts the velocities and flow pattern in the bioreactor the most accurately. The additional computational expense and complexity however makes this model less desirable than those using a singlephase approximation. Although the singlephase approximations are less accurate than the multiphase model they can still be of use in modelling the bioreactor particularly in cases where additional equations need to be solved on top of the CFD model as would be the case with a coupled biokinetic-hydrodynamic model. In the case of a coupled model the inlet/outlet singlephase model would be the least use as it neglects part of the domain where biokinetic growth and decay may be occurring, this makes the momentum source model the more desirable of the two in this case.



(a) Axial velocity profile at 0.1875m from bioreactor base



(b) Axial velocity profile at 0.0325m from bioreactor base

Figure 5.12: Velocity vectors for the different methods of controlling the flow in the gas-lift bioreactor

5.4 Summary and conclusions

This chapter contains details of computational fluid dynamics modelling as well as a numerical study of the effects of different model assumptions and settings on the prediction of flow within a gas-lift bioreactor. Turbulence model selection, CFD solver comparison and single vs. multiphase approximations are all discussed in detail showing the effects these assumptions make on the results which can be obtained for a gas-lift bioreactor.

It was stated that the choice of turbulence model is an important consideration when modelling complex turbulent flows; in particular those which have boundary layer separation due to adverse pressure gradients. This was proved through an assessment of a number of RANS turbulence models when applied to a bench-scale cylindrical gas-lift bioreactor with internal draft tube. The flow had been shown to have boundary layer separation by experimental work obtained from literature and therefore required careful choice of turbulence model. It was found that the Transition-SST turbulence model provided the most accurate predictions for velocity, separation/reattachment and overall flow-field. The RNG $k - \epsilon$ model was shown to be unsuitable for modelling the low-Re number flows found in the model bioreactor and significantly under predicted the separation and reattachment points as well as the size of stagnation regions. The $k - \omega$ SST and RSM models provided more accurate results; however they exhibited some inaccuracies with velocity and separation and reattachment prediction.

A comparison between the results obtained from two different CFD solver packages was used to show what if any effect the choice of solver may have on the results obtained. As the two solvers (ANSYS Fluent 13.0sp2 and OpenFOAM 3.0.0) are well developed and benchmarked as well as using the same finite volume methodology little difference was shown as is expected. With well developed CFD software, little difference in solutions of well established model types should be seen due to thorough testing of the underlying methods as was demonstrated here.

Further analysis was provided comparing different methods of implementing the bubble driven velocity field within the bioreactor. Two singlephase models, one with an inlet and outlet with a fixed inlet velocity and the other using a momentum source enforcing the appropriate velocity within the draft tube, were compared with a multiphase model using a Lagrangian particle tracking method to approximate bubble flow in the draft tube. The solution using the momentum source was found to be more accurate than both the single and multiphase models when predicting the velocity profile at 0.1875m above the bioreactor base but suffered from the same shortcomings as the inlet/outlet singlephase model when predicting flow near the bottom of the draft tube.

Chapter 6

Coupling hydrodynamics and biokinetic growth

Contents

6.1	Coupled model methodology	111
6.1.1	Coupling biokinetic growth models with hydrodynamics	111
6.1.2	Modelling light distribution within a bioreactor	115
6.1.3	Steady-state CFD and mesh mapping	118
6.2	Implementation and assessment of the coupled photosynthesis-nutrient- hydrodynamic model	119
6.2.1	Solver set up	120
6.2.2	Implementation verification	122
6.2.3	Mesh mapping independence testing	123
6.2.4	Light absorption and scattering affect on biomass growth	129
6.2.5	Reynolds number scaling of a bioreactor	134
6.2.6	Effect of increasing incident light intensity on the active biomass and biomass growth	140
6.3	Summary and conclusions	142

Nomenclature**Symbols**

∇	Gradient operator
\mathbf{U}	Velocity vector
Γ	Diffusion coefficient
x_1	Resting state for photosynthetic factor model
x_2	Active state for photosynthetic factor model
x_3	Inhibited state for photosynthetic factor model
I	Light intensity
I_0	Incident light intensity
μ_I	Light intensity dependent growth rate
Q_i	Cell quota of nutrient i
$Q_{min,i}$	Minimum cell quota of nutrient i
V_{max}	Maximum nutrient uptake rate
X	Insoluble biomass concentration
S_i	Soluble nutrient i
Chl	Chlorophyll concentration

Abbreviations

CARPT	Computer automated radioactive particle tracking
CFD	Computational fluid dynamics
CT	Computed tomography
PN	Photosynthesis nutrient
PNH	Photosynthesis nutrient hydrodynamic
TIS	Tanks in series

As was described in the introduction (chapter 1), one of the main aims of this work is the development and implementation of a coupled model framework for use in modelling and investigation of bioreactors, including under conditions such as complex mixing regimens, large scale bioreactors, and with the inclusion of multiple possible controlling factors. In previous chapters, models describing nutrient dependent biomass growth, photosynthetic processes and hydrodynamic mixing were described and implemented, additionally, a method of coupling the nutrient biomass growth and photosynthesis models together (the PN model) was proposed and investigated. The next step in the development of a comprehensive coupled model of biokinetic growth of phytoplankton in bioreactors is the inclusion of hydrodynamic mixing, as described in chapter 5, to produce a coupled framework of biokinetic growth in bioreactors with complex mixing. A method of constructing this photosynthesis-nutrient-hydrodynamic (PNH) model is proposed here, this model is then investigated using some of the scenarios under which it may be beneficial

to include complex mixing flows, including bioreactor scale-up and variations in lighting conditions.

6.1 Coupled model methodology

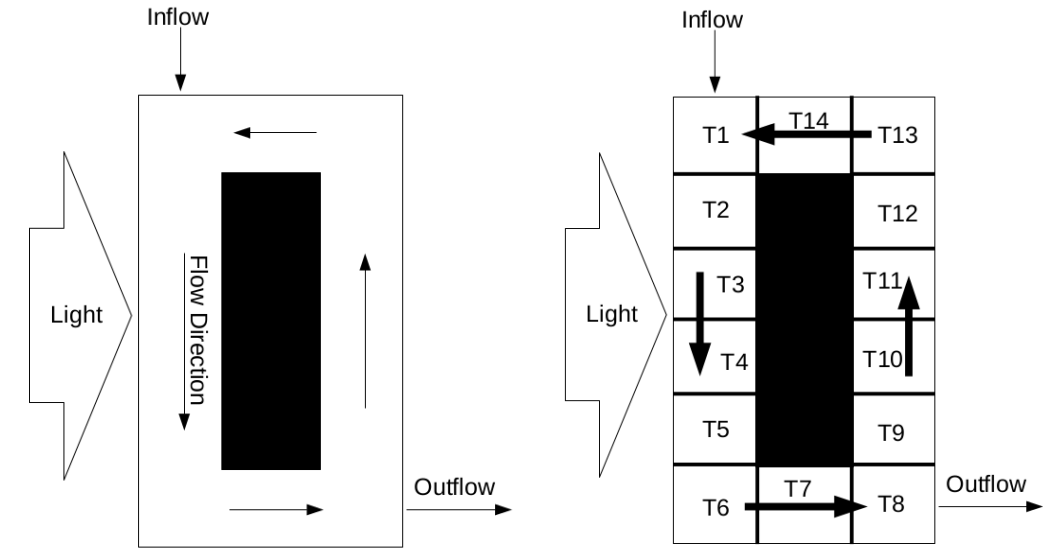
In order to create a model combining fluid flow with biokinetic growth, a suitable framework around which to base the model it is required. Proposed here is a new coupled model, combining both the photosynthetic and soluble nutrient based biokinetic growth models of phytoplankton, as well as the hydrodynamic mixing found within non-homogeneously mixed bioreactors. In addition to the coupling between the biokinetic and hydrodynamic models, a model to describe light distribution within the bioreactor is proposed to account for the absorption and scattering of light by the biomass.

6.1.1 Coupling biokinetic growth models with hydrodynamics

Coupling biokinetic growth and hydrodynamic models together to form a model which can account for the effects of mixing on growth of biomass within a bioreactor can be achieved in a couple of different ways. The method used however, depends on the complexity of the hydrodynamic mixing within the bioreactor.

In the case of a simple circulating flow bioreactor, such as that shown in figure 6.1a, where the flow simply circulates around in one direction a tanks in series (TIS) approach can be used. This approach, diagrammed in figure 6.1b, uses the mass balance equations normally used in biokinetic modelling in a series with the biomass concentrations being passed from one tank to the next based on the flow-rate around the bioreactor. In simple cases, where flow-rate is constant and passes in a single direction, like the one shown in figure 6.1 the modelling is relatively easy in that it only requires an increase in the number of times the model equations are solved with the concentrations being transferred through the tanks successively.

A slightly more complex version of this method uses TIS connected in a more complex manner with flow from and to multiple tanks. In this case, the calculation for the flow rates between tanks is more complex and usually requires greater understanding of the flow field itself through either experimental analysis or CFD modelling as was done by



(a) Simple loop bioreactor geometry where flow is transported in a single direction around the loop (b) Division of loop bioreactor as a series of tanks in which biokinetic growth models are applied

Figure 6.1: Tanks in series model method diagram for simple loop bioreactor

Alvarado et al. (2011). This method of using TIS to model flow with biokinetic growth it does not produce a truly coupled model since there is significant separation between the calculation of the flow field and the biokinetic modelling, additionally, the model relies on user interaction to determine the position and size of the tanks to be used as well as calculate the flow-rates between them. This makes applying the modelling method very problem specific with no method of easily generalising the set-up of different bioreactor scenarios.

To couple the flow-field and biokinetic growth in a more general way, where the solution method is the same for a wide variety of bioreactor problems, a different approach is required. Although the use of TIS with the ODE mass balance models can produce good results when cases are set up with care (Alvarado et al., 2012), the lack of efficient coupling between the flow field and biokinetics makes this limited to simpler mixing problems. A more efficient method of coupling the flow-field and biokinetics is to approach the problem from the CFD side of the modelling methodology. CFD models are already well established in regards to transporting various properties around a domain, including pollutants (Tominaga and Stathopoulos, 2013; Lateb et al., 2016), thermal energy (Yadav and Bhagoria, 2013) and chemical reactants in combustion (Hilbert et al., 2004) and

so provides a good basis upon which to build a coupled model for biokinetic growth in bioreactors.

In order for the biokinetic models described in chapters 3 and 4 to be coupled with computational fluid dynamics (CFD) flow-field, a method of transporting the different components in relation to the flow velocity is required. The ordinary differential equations (ODEs) that govern the growth and decay of biomass within the bioreactor are one dimensional in nature, are solved based on mass conservation (Equation 3.15) and as such are incompatible with the multi-dimensional nature of the partial differential equations (PDEs) used in CFD. One method of incorporating the biokinetic growth is the use a scalar transport equations for each of the components being modelled. The scalar transport equation is the underlying basis for many of the transport equations used in CFD, the equation takes the form of a time dependent advection-diffusion equation usually with source terms for additional sources and sinks for the field being transported. Equation 6.1 describes the general advection-diffusion equation for scalar transport in CFD, where C is the variable of interest \mathbf{U} is the velocity vector field obtained from the Navier-Stokes equations (5.5), D is the diffusion coefficient and S_C is the combined term representing the sources and sinks.

$$\underbrace{\frac{\partial C}{\partial t}}_{\text{Time dependent term}} + \underbrace{\nabla \cdot (\mathbf{U}C)}_{\text{Advection term}} - \underbrace{\nabla \cdot (D\nabla C)}_{\text{Diffusion term}} = \underbrace{S_C}_{\text{Source terms}} \quad (6.1)$$

Using the advection-diffusion equation as the basis of the biokinetic transport in the coupled model produces a set of equations with coupled source and sink terms representing the growth and decay of the various species used in the PN model described in section 4.3. Equations 6.2 -6.4 represent the photosynthetic states of the biomass described in detail in section 4.2, the source terms from the ODEs used in the mass balance equations of the bulk model.

$$\frac{\partial x_1}{\partial t} + \nabla \cdot (Ux_1) - \nabla \cdot \Gamma \nabla x_1 = -\alpha Ix_1 + \gamma x_2 + \delta x_3 \quad (6.2)$$

$$\frac{\partial x_2}{\partial t} + \nabla \cdot (Ux_2) - \nabla \cdot \Gamma \nabla x_2 = \alpha Ix_1 - \gamma x_2 - \beta Ix_2 \quad (6.3)$$

$$\frac{\partial x_3}{\partial t} + \nabla \cdot (Ux_3) - \nabla \cdot \Gamma \nabla x_3 = \beta Ix_2 - \delta x_3 \quad (6.4)$$

As with the PSF model equations described above the nutrient based biokinetic growth model described in section 3.5.3 has been reformulated in equations 6.5 - 6.9, again with the source terms from the mass balance equation being used as the source terms on the advection-diffusion equations.

$$\frac{\partial S_N}{\partial t} + \nabla \cdot (US_N) - \nabla \cdot \Gamma \nabla S_N = a(S_{in,N} - S_N) - \left(1 - \frac{Q_N}{Q_{max,N}}\right) \frac{V_{max,N} S_N}{S_N + K_N} X \quad (6.5)$$

$$\frac{\partial S_P}{\partial t} + \nabla \cdot (US_P) - \nabla \cdot \Gamma \nabla S_P = a(S_{in,P} - S_P) - \left(1 - \frac{Q_P}{Q_{max,P}}\right) \frac{V_{max,P} S_P}{S_P + K_P} X \quad (6.6)$$

$$\begin{aligned} \frac{\partial Q_N}{\partial t} + \nabla \cdot (UQ_N) - \nabla \cdot \Gamma \nabla Q_N &= \left(1 - \frac{Q_N}{Q_{max,N}}\right) \frac{V_{max,N} S_N}{S_N + K_N} \\ &\quad - \mu_I \min\left(1 - \frac{Q_{min,N}}{Q_N}, 1 - \frac{Q_{min,P}}{Q_P}\right) Q_N \end{aligned} \quad (6.7)$$

$$\begin{aligned} \frac{\partial Q_P}{\partial t} + \nabla \cdot (UQ_P) - \nabla \cdot \Gamma \nabla Q_P &= \left(1 - \frac{Q_P}{Q_{max,P}}\right) \frac{V_{max,P} S_P}{S_P + K_P} \\ &\quad - \mu_I \min\left(1 - \frac{Q_{min,N}}{Q_N}, 1 - \frac{Q_{min,P}}{Q_P}\right) Q_P \end{aligned} \quad (6.8)$$

$$\frac{\partial X}{\partial t} + \nabla \cdot (UX) - \nabla \cdot \Gamma \nabla X = \mu_I \min\left(1 - \frac{Q_{min,N}}{Q_N}, 1 - \frac{Q_{min,P}}{Q_P}\right) X - mX \quad (6.9)$$

6.1.2 Modelling light distribution within a bioreactor

Although the model described in equations 6.2 - 6.9 can be run using a constant value of light intensity I this would provide little additional benefit to the bulk model with regard to light dependent biomass growth. In order to have a non-homogeneous light gradient within the bioreactor domain which will have an affect on the biomass growth through the amount of photosynthetically active biomass an equation solving for the diffusion of light within the domain is required. As such, a model is proposed here for the distribution of light within a bioreactor to be coupled with the biokinetic and hydrodynamic models.

The main concepts which govern the radiation intensity at any point within a medium are the initial incoming intensity, absorption and scattering which reduce the intensity and emission and scattering from other directions which increase the intensity (figure 6.2).

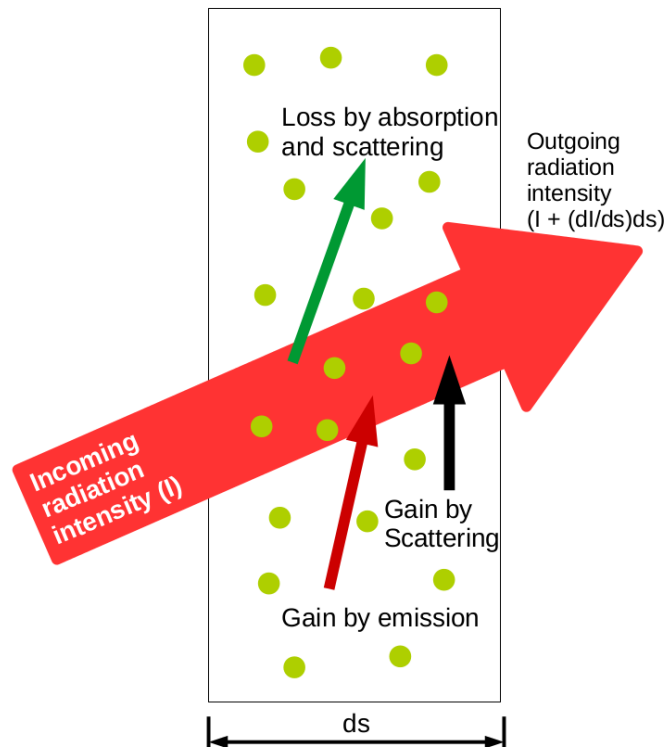


Figure 6.2: Diagram of radiative transfer equation processes over a small distance ds

These functions are described by the integrodifferential equation shown in equation 6.10, which describes the propagation of radiation along a path through the medium (Siegel and

Robinson, 1992). Where I'_λ is the directional radiation intensity at a specific wavelength, s is the radiation path direction, a_λ and $\sigma_{s\lambda}$ the absorption and scattering coefficients, ω the scattering angle and Φ the scattering phase function. The equation for I'_λ describes the radiation intensity at position \mathbf{r} along direction s , this requires that the equation be discretised in both space and the direction of radiation propagation. There are a number of different ways in which the direction can be discretised and the application of these methods has resulted in a number of radiation transfer models; none of these models have been universally accepted as appropriate for all radiation transfer problems (Sazhin et al., 1996).

$$\frac{\partial I'_\lambda}{\partial s} = \underbrace{-(a_\lambda + \sigma_{s\lambda}) I'_\lambda(s)}_{\text{Loss by absorption and scattering}} + \underbrace{a_\lambda I'_{\lambda b}(s)}_{\text{Gain by emission}} + \underbrace{\frac{\sigma_{s\lambda}}{4\pi} \int_{\omega_I=0}^{4\pi} I'_\lambda(s, \omega) \Phi(\lambda, \omega, \omega_I)}_{\text{Gain by scattering into s direction}} \quad (6.10)$$

The radiation transfer models which have been developed range in complexity from the simple Rosseland diffusion approximation model, to the discrete ordinates model which solves the radiative transfer model for a set of n different directions (Habibi et al., 2007). One the simpler models is the P1 approximation, the model is the simplest formulation of the general P-N model which expands the radiation intensity into a series of orthogonal spherical harmonics resulting in a series of partial differential equations. The P1 model uses only the first two terms in the series resulting in equation 6.11 for the radiative flux where I is the incident radiation intensity, a_L is the absorption coefficient, σ_L is the scattering coefficient and C_s is the linear-anisotropic phase function coefficient, a property of the fluid which in all cases here is taken to be zero, this assumes that scattering is isotropic. (Siegel and Robinson, 1992).

$$q_r = -\frac{1}{3(a_L + \sigma_L) - C_s \sigma_L} \nabla I \quad (6.11)$$

At this point it is only necessary to find a solution for the incident intensity rather than the

directional dependent intensity described in equation 6.10. If the terms for the absorption and scattering in equation 6.11 are combined into the diffusion coefficient Γ (equation 6.12) the equation simplifies to equation 6.13.

$$\Gamma = \frac{1}{3(a_L + \sigma_L) - C_s \sigma_L} \quad (6.12)$$

$$q_r = -\Gamma \nabla I \quad (6.13)$$

The equation for solving the transport of I is the diffusion equation, as the speed of light determines that the time dependent term of the advection-diffusion equation can be neglected assuming propagation of light is infinitely fast and reducing the equation to 6.14. Where σ_b is the Stefan-Boltzmann constant and S_I is the total intensity source and sink terms. This can be further reduced in this case by neglecting the temperature component under the assumption that radiation emitted by the algae due is negligible at the temperatures in which they can survive.

$$\nabla \cdot (\Gamma \nabla I) - a_L I + 4a_L \sigma_b T^4 = S_I \quad (6.14)$$

This results in the final equation for transport of light intensity which is described in equation 6.15.

$$\nabla \cdot (\Gamma \nabla I) - a_L I = S_I \quad (6.15)$$

6.1.3 Steady-state CFD and mesh mapping

One of the main obstacles to be overcome when coupling CFD models of hydrodynamics and biokinetic growth models is the computational resources required. By combining CFD, which requires small time-steps and large computational grids, with biokinetic growth models, which are run over long periods of simulated time, it is easily possible to end up with models which are prohibitively expensive to run, both in terms of required resources and time. In order to reduce these requirements there are several steps which can be taken, which while increasing model efficiency, should have little impact on the overall accuracy.

To reduce the computational expense of including CFD in modelling the bioreactor hydrodynamics, it is possible to produce a steady-state flow field for the biomass transport in the bioreactor; this is only possible however in cases where mixing is kept in a constant stable state. The benefit of this is in the reduction in the number of equations being solved over the long simulation period the biokinetic models require, whilst also allowing for the time-step to be increased improving the overall simulation run time. This method works by first solving for the flow field, before starting the biokinetic simulation using the results from that initial CFD simulation. However, this method of separating the models somewhat is not applicable in all cases. Simulations where the start-up of the bioreactor from an unmixed or settled state is of interest would not benefit from this loosely coupled method and would require the solving of the fluid flow equations at every time-step. Additionally, this loosely coupled method does not account for any changes to the fluid properties, such as increases in viscosity; to include such two directional coupling would require the inclusion of a model of viscosity dependent on biomass concentration. This method of solving for a steady-state velocity field also doesn't allow for changes in flow rates of influent, as in cases of activated sludge wastewater treatment bioreactors; changes in influent concentration are still possible however. Even given the limitation described above, reducing the computational cost of the model by using a steady-state flow field applied to time dependent biokinetic equations has many benefits. Given the difference in time-scales between the biokinetic processes and the fluid velocity in phytoplankton growth the difference in the flow field in the start-up phase of a bioreactor can be neglected.

Another method of reducing the computational cost of the coupled simulations is to solve the CFD and biokinetic models on two different grids. This method, which works well with the method of producing a steady-state CFD solution for use by the biokinetic model described above, maps the velocity vector values from the fine mesh used to calculate the flow field in the bioreactor onto a coarser mesh for solving the biokinetic model. This allows the solution for the biokinetic models to be solved faster due to the reduced number of linear equations being solved at each time-step whilst still obtaining a non-homogeneous flow-field within the bioreactor based on well established numerical modelling techniques.

6.2 Implementation and assessment of the coupled photosynthesis-nutrient-hydrodynamic model

Documented here are a number simulations which assess potential of the new PNH coupled model which has been developed. The simulations describe some different scenarios in which show the differences between the bulk PN model and the PNH model which includes hydrodynamic mixing. Also investigated is the effect the mesh mapping discussed above has on the results produced by the model. The implementation of the models here was done using the OpenFOAM CFD software package and all the code for the model is provided in appendix C. OpenFOAM was chosen for the model implementation due to its open-source nature, this allows a user to alter the underlying code of the programme and adapt it their needs making the PNH model more closely integrated with the CFD and able to use many of the features built into OpenFOAM. Furthermore, the code itself can then be easily provided for others to further improve upon the model in the future, while still having access to all current and new features of the OpenFOAM platform. This makes it easier to produce a more generalised model for growth of phytoplankton in bioreactors and in future generalising the code to work with other biokinetic models such as the ASM and ADM models.

6.2.1 Solver set up

All the simulations in this section are set-up based around the cases described in sections 4.3 and 5.3 in order for comparison between the increasingly complex models to be made. The exact solver set-up for the PNH coupled simulations are discussed here along with any alterations which were necessary when compared to the simulations performed in previous chapters.

Model constants

As the model has been implemented in OpenFOAM it must conform to the code structures used by the software, this includes the dimensional units which OpenFOAM attaches to all field data (e.g. velocity, temperature, etc.) and physical properties. As such, it is advisable to convert all units to the OpenFOAM dimension set to avoid any later confusion as to the units being portrayed. The OpenFOAM dimension set uses SI units by default and contains units for the properties described in table 6.1; only the properties for Mass, Length, Time and Quantity are used in the models described here.

No.	Property	SI unit
1	Mass	kilogram (kg)
2	Length	metre (m)
3	Time	second (s)
4	Temperature	Kelvin (K)
5	Quantity	mole (mol)
6	Current	ampere (A)
7	Luminous Intensity	candela (cd)

Table 6.1: OpenFOAM dimension system and units

The constants for the PNH model are listed below in table 6.2, the units of $Cell^{-1}$ are not included in the OpenFOAM dimension set and as such do not appear in the model code. However as this is kept consistent throughout the model it has no effect on the results obtained and the unit labels are adjusted during post processing.

Geometry and meshing

The geometry and mesh chosen for the simulations using the PNH model are those that have been described and evaluated in section 5.3; this set-up was chosen due to the validation already performed on the mixing results as well as the inhomogeneous nature

Parameter	Notation	Value	Units
<i>PSF parameters</i>			
alpha	α	1935	$m^2.s^{-1}$
beta	β	0.57848	$m^2.s^{-1}$
gamma	γ	0.1460	s^{-1}
delta	δ	4.796E-4	s^{-1}
<i>Nutrient model parameters</i>			
Dilution rate	a	6.829E-6	s^{-1}
Nitrogen inflow concentration	$S_{in,N}$	1.8E-1	$MolN.m^{-3}$
Phosphorus inflow concentration	$S_{in,P}$	3.0E-3	$MolP.m^{-3}$
Maximum nitrogen uptake rate	$V_{max,N}$	3.947E-18	$MolN.Cell^{-1}.s^{-1}$
Maximum phosphorus uptake rate	$V_{max,P}$	1.424E-19	$MolP.Cell^{-1}.s^{-1}$
Nitrogen half saturation constant	K_N	5.6E-3	$MolN.s^{-1}$
Phosphorus half saturation constant	K_P	2.0E-4	$MolP.s^{-1}$
Growth at infinite quota	μ_l	2.5084E-5	s^{-1}
Minimum nitrogen cell quota	$Q_{min,N}$	4.54E-14	$MolN.Cell^{-1}$
Minimum phosphorus cell quota	$Q_{min,P}$	1.640E-15	$MolP.Cell^{-1}$
Maximum nitrogen cell quota	$Q_{max,N}$	3.632E-13	$MolN.Cell^{-1}$
Maximum phosphorus cell quota	$Q_{max,P}$	2.624E-14	$MolP.Cell^{-1}$

Table 6.2: Constants for PNH model in OpenFOAM

of the internal flow field. This incomplete mixing of the bioreactor is big step away from the homogeneous mixing assumed by the PN model and so makes for a good point of comparison. Additionally, in order to implement the PNH model properly is necessary to use a geometry which covers the whole bioreactor (i.e. contains the draft tube and annular section), as this is not the case with the original CFD model geometry used (figure 5.1a) the geometry for the momentum source driven flow in section 5.3.4 is used instead. This allow the biokinetic model to calculate the growth in the draft tube as well as the annular section of the bioreactor.

Boundary conditions and solver settings

Boundary conditions for the velocity field calculations are as those described in section 5.3.4 for the momentum source term driven flow unless otherwise stated. The flow rate for the bioreactors of different sizes is defined in the appropriate sections of this chapter due to the changes in flow rate when scaling bioreactors up based on Reynolds number. The light intensity at the surface of the bioreactor is the same value of $266\mu Mol.m^{-2}.s^{-1}$ as that used in the validation of the PN model in section 4.3.2 and is kept at a constant rate in all the simulations described here.

Additionally, as there is not inlet or outlet in the momentum source driven bioreactor the biomass inflow and outflow are defined as global source and sink terms. This allows the the model to be tested for the effects of the photosynthetic growth on the biomass independently of local variations in nutrient concentration and allowing for comparison with the PN model. Although this condition is not strictly physical in how a real bioreactor with inflow and outflow would behave it is important to assess the different aspects of the model coupling as independently as possible. The solver settings for the biokinetic equations are described in table 6.3.

Setting	Value	Units
Time step Δt	1	s
Run time	45	days
<i>Discretisation Schemes</i>		
Time	First order implicit Euler	
Gradient ∇	Gauss linear	
Divergence	bounded Gauss upwind	
Laplacian	Gauss linear corrected	

Table 6.3: Solver settings for PNH model in OpenFOAM

6.2.2 Implementation verification

Described here is a simulation designed to verify that the code implemented for the PNH model performs as would be expected and can reproduce the same results as the bulk model under the same conditions. As such the simulation set-up conditions include a fully homogeneously mixed bioreactor with light intensity maintained constant over the whole domain. As the results of this simulation as shown in figure 6.3 are identical to that of the PN bulk model it can be assumed that the equations implemented in the source code are equivalent to those of the PN model. Although this does not validate the accuracy of the model in terms of the physics it is portraying, the verification is still an important step in developing a working and usable model.

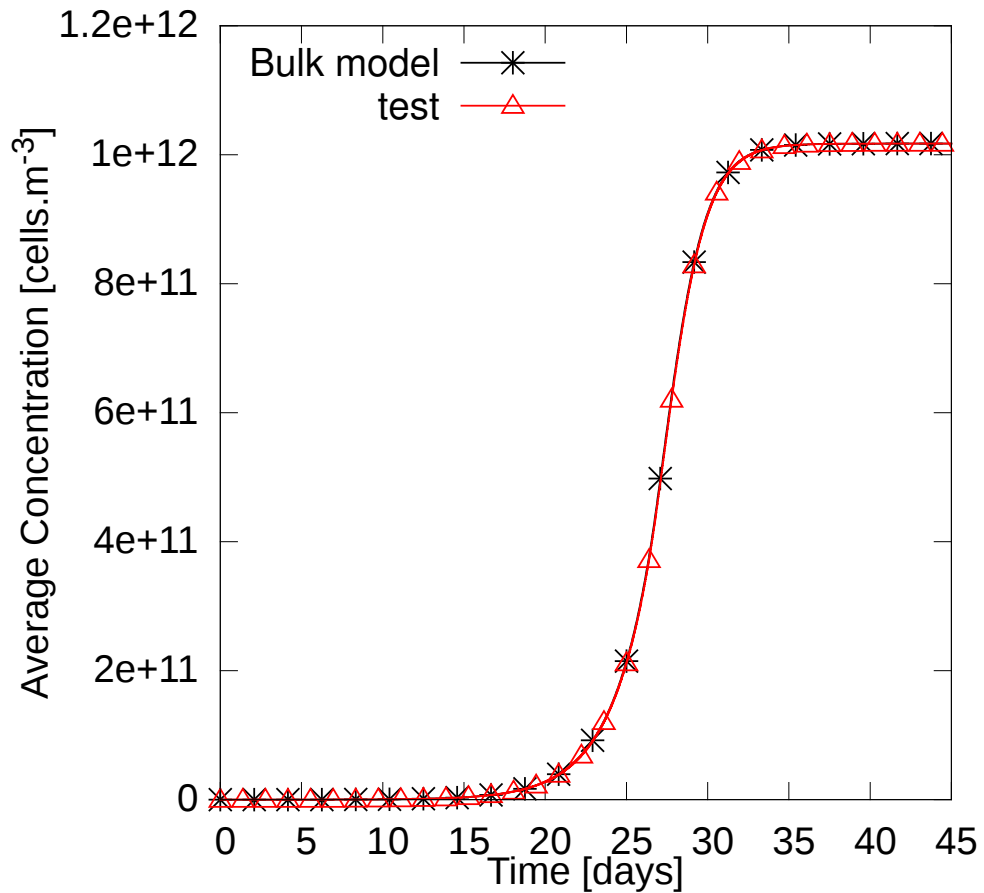


Figure 6.3: Biomass growth plot for a simple case where light intensity is set to a constant value of $266\mu\text{Mol.m}^{-2}.\text{s}^{-1}$ and the fluid velocity is at 0m.s^{-1}

6.2.3 Mesh mapping independence testing

The second test case shown here describes the response of the model results when using the mesh mapping to reduce the number of elements in the mesh and thus reduce the solution clock time (i.e. the real world time taken to run the simulations). In all the models for the different mesh sizes here the velocity field used is that produced on the largest mesh and validated in chapter 5.

The process used was to first solve for the velocity field in the fine mesh and then use the OpenFOAM mapFields utility to interpolate the calculated velocity field onto the coarser mesh. As the mesh used become coarser it is easy to see the loss of accuracy in the flow field at a local level with finer flow features becoming steadily less visible in the velocity contour plots (figure 6.4). However, the overall flow-field shape is still visible including

the areas of relatively high velocity and the stagnation region. Additionally the velocities appear to be consistent with the areas from which they were mapped.

Further evidence that the mapping of the velocity field onto the coarser meshes provides little loss in the overall accuracy in terms of the flow rate can be seen in figures 6.5a and 6.5b where the velocity profiles 0.1875m and 0.0325m above the base of the bioreactor show good correlation with both the results of the original velocity field and the experimental velocity profiles of Karim et al. (2007). The only obvious discrepancy in the velocity profile plots in on figure 6.5b in the location corresponding to a position directly below the draft tube in the bioreactor. There the variation in the velocities is at its greatest when compared to the original velocity field, this is likely due to the greater velocity gradient in that area, this is likely to have been smeared out considerably as can be seen in figure 6.4 on the coarser meshes.

The second variable of interest when mapping the mesh is the light intensity profile across the bioreactor. Figure 6.6a shows the contour of the light intensity across the bioreactor domain for the mesh with 348 elements while figure 6.6b shows the light profile just above the bioreactor draft tube. Little difference is shown in the results for the light intensity between the different meshes.

Finally, a comparison between the biomass growth concentrations is shown in figure 6.7 for the different mesh sizes. Again there is no indication that there is any difference between the solutions for the coarsest vs the finest mesh with the results also being comparable to those of the bulk PN model.

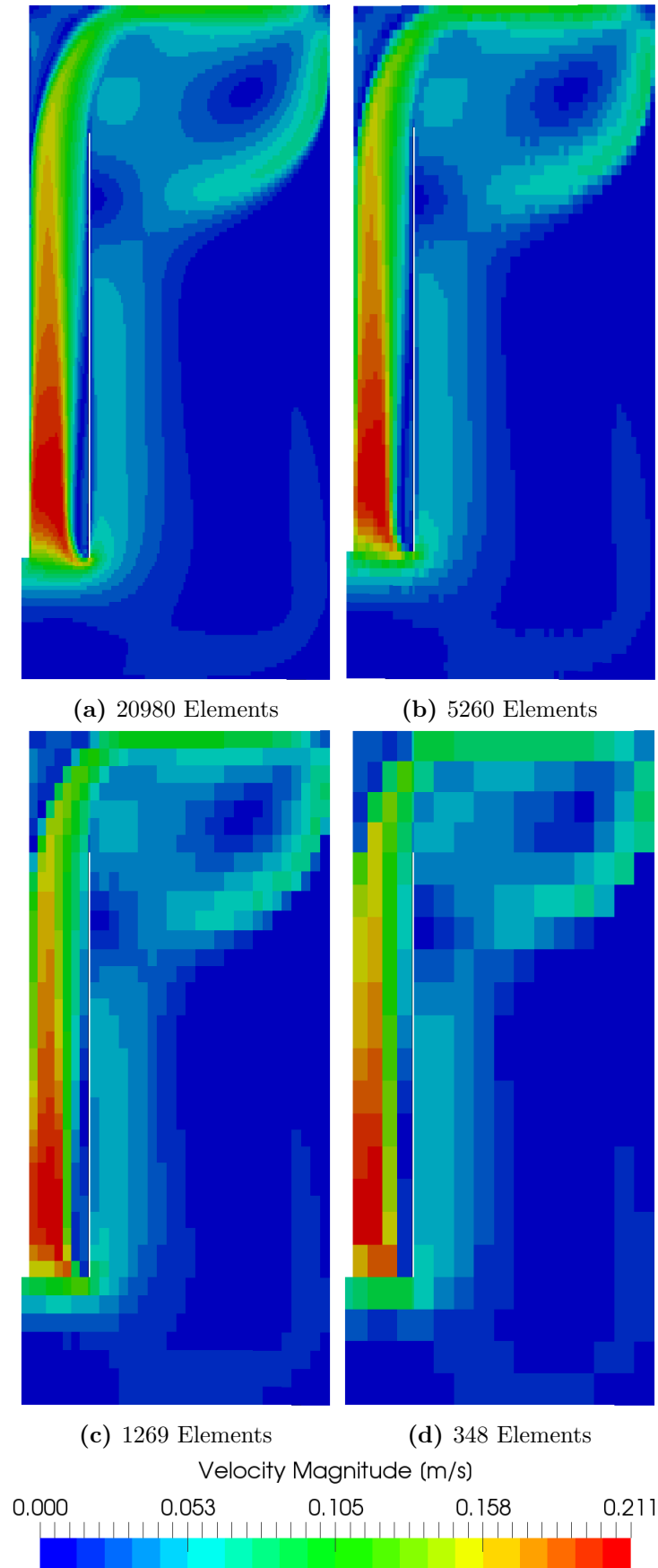
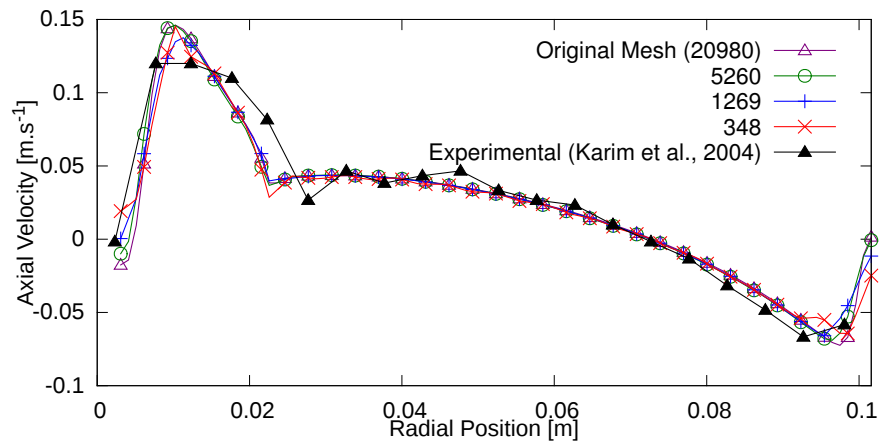
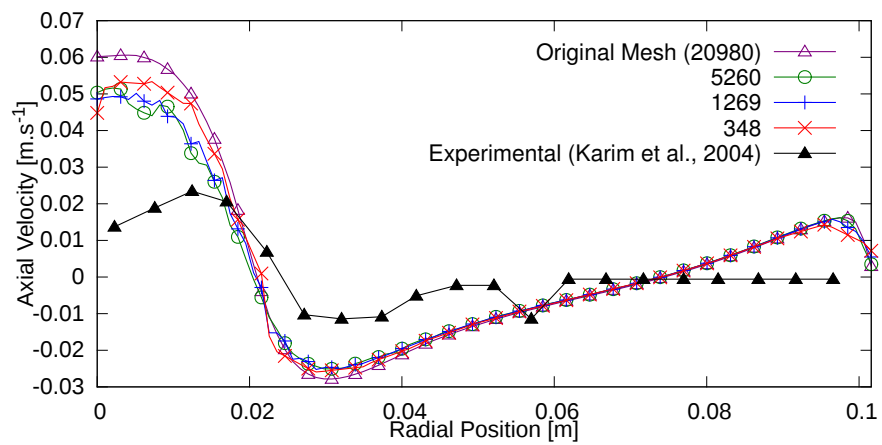


Figure 6.4: Velocity contour plots for the velocity field when mapped from the original mesh onto coarser meshes for biokinetic growth modelling.



(a) Velocity profile plot at 0.1875m from base of bioreactor



(b) Velocity profile plot at 0.0325m from base of bioreactor

Figure 6.5: Velocity profile plots for CFD solutions mapped onto coarser meshes

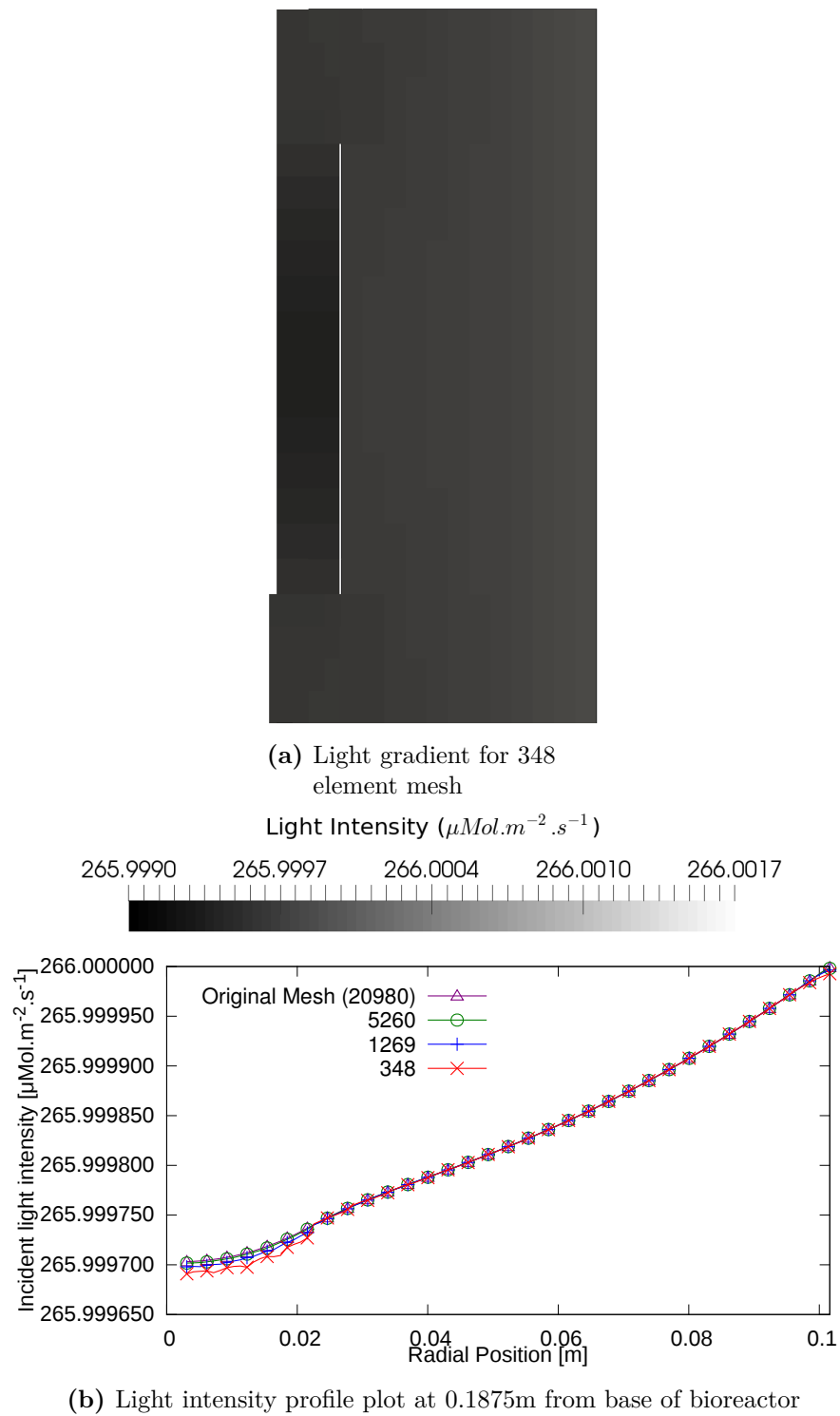


Figure 6.6: Light gradient within bioreactor (a) and light intensity profile across width of bioreactor (b)

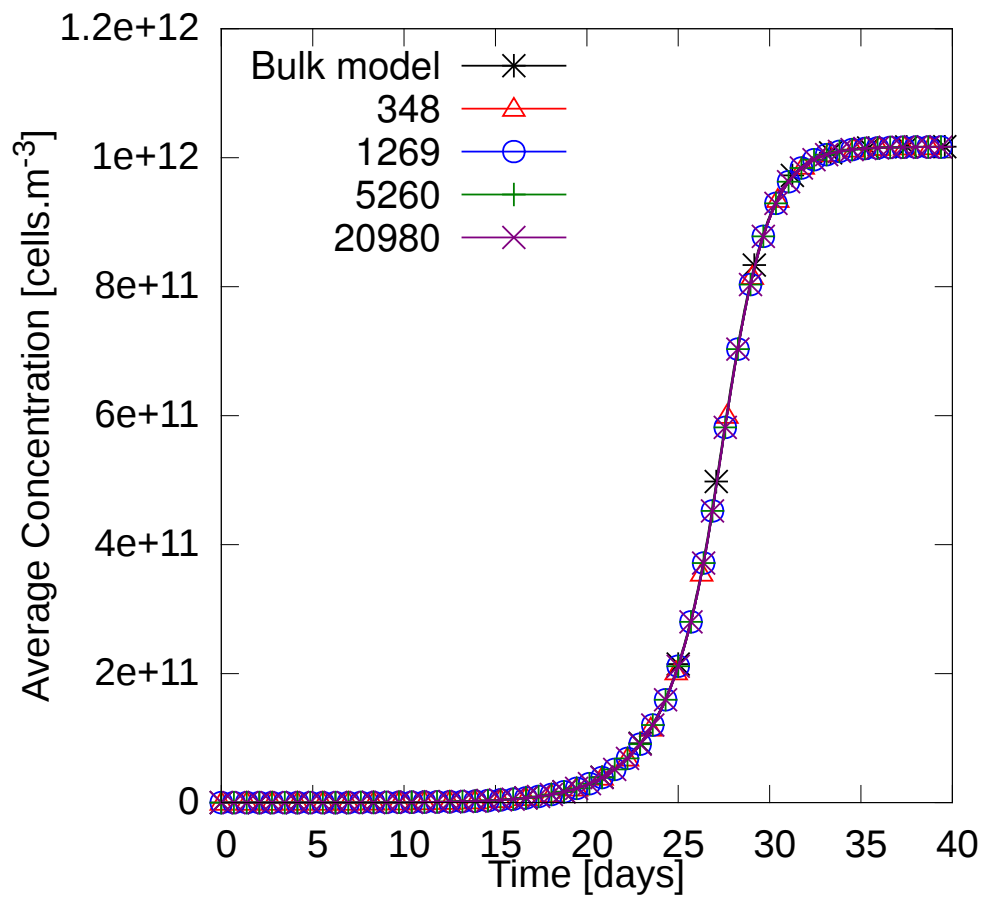


Figure 6.7: Comparison of mesh independence for biomass growth in simulations using different mesh sizes with mapped velocity fields

6.2.4 Light absorption and scattering affect on biomass growth

Light absorption and scattering in the bioreactor can have a significant effect on the light intensity at even small distances from the incident location, particularly when biomass concentration is high. This is the reason why many photobioreactors have large surface area to volume ratios allowing them to have higher light intensities over a greater fraction of the bioreactor interior. These large surface area to volume ratios require more material in the bioreactor structure, which, in the case of photobioreactors is required to be transparent (e.g. glass) in order to admit light and are therefore expensive to produce. It is therefore important to gain a better understanding of the relationship between the light within a bioreactor, the flow-field and the biomass growth.

As such a series of simulations at different light absorption and scattering coefficients are described. The absorption and scattering coefficients used were determined through the use of functions obtained from literature developed from experimental results. Bricaud et al. (1995) developed a function for the absorption coefficient of phytoplankton at different wavelengths and biomass concentrations (equation 6.16).

$$a_L = 0.0403 < Chl(440nm) >^{0.668} \quad (6.16)$$

As the most common chlorophyll type is chlorophyll 'a', which provides the green pigment in plants and phytoplankton, and which absorbs electromagnetic radiation most effectively at wavelengths of 440nm (figure 2.1), it is at this wave length the calculated absorption rates were obtained for. To calculate absorption coefficient values appropriate to the biomass concentrations typical of the biokinetic model being investigated three values of biomass concentration calculated by the PN bulk model were used. These concentrations are shown in table 6.4 and are for the initial biomass concentration, a typical result calculated when the biomass concentration reached a steady-state and a value half of that. The value of chlorophyll per cell was taken to be $2pg.cell^{-1}$ based on the work of Pirastru et al. (2012). A similar function for the scattering coefficient, equation 6.17, was

found in literature (Voss, 1992; Loisel and Morel, 1998).

$$\sigma_L = 0.39 < Chl(440nm) >^{0.57} \quad (6.17)$$

Simulations were run for the benchscale gas-lift bioreactor with the absorption and scattering coefficients for each of the three biomass concentrations and for absorption and scattering coefficients typical of fresh water (table 6.4). All other settings for the bioreactor were maintained as described above with the validated velocity field and the initial conditions and constants from the PN bulk model.

Case ID	@Biomass Concentration [Cells.m ⁻³]	Absorption Coefficient [m ⁻¹]	Scattering Coefficient [m ⁻¹]
Water	-	0.01	0.005
<i>a</i> ₁	1e7	0.0129	0.0469
<i>a</i> ₂	5e11	4.077	20.006
<i>a</i> ₃	1e12	6.472	29.697

Table 6.4: Absorption and scattering coefficients for different test cases with their corresponding biomass concentrations

As the values for the absorption and scattering in the bioreactor were kept constant over the simulation duration the light intensity gradient also remained constant. The light intensity gradients for the different absorption and scattering coefficients are shown in figure 6.8. The first point of interest is in the comparison between the results for the cases for *a*₁ and water, it is not unexpected that the results for light distribution between the two are so similar as the absorption coefficients are of the same order of magnitude. Although the scattering coefficients are significantly different they are both low enough that over the short distance between the outer wall and the centre of the bioreactor little difference in their results is likely to be seen. Cases *a*₂ and *a*₃ show a much greater degree of change in the light intensity over the width of the bioreactor and also show a more significant difference between their results. This is further confirmed in figure 6.9 where the light profile for case *a*₃ drops significantly further and faster than the others resulting in a much lower light intensity at the centre of the bioreactor.

These results confirm that the absorption and scattering coefficients at different biomass concentrations can have a great effect on the light intensity within the bioreactor. The biomass concentration results for these difference cases, shown in figure 6.10, do not however show any significant difference in growth rate or final concentration. Although some small difference in the results can be seen in the sub figure for case a_3 the difference is not great. This lack of difference in the biomass concentration for the different absorption and scattering coefficients is most likely to be due to the small size of bioreactor and the relatively high velocity of the flow within where the biomass circulates around up to 10 times per minute. As a result of this high rate of recirculation the growth rate is not overly affected as the resulting biomass concentration shows, however, this is unlikely to be the case in larger scale bioreactor which would be of greater use in industrial growth of phytoplankton rather than the 7.2L bench-scale bioreactor. To show that this is the likely case simulations in scaled up bioreactors are shown in section 6.2.5.

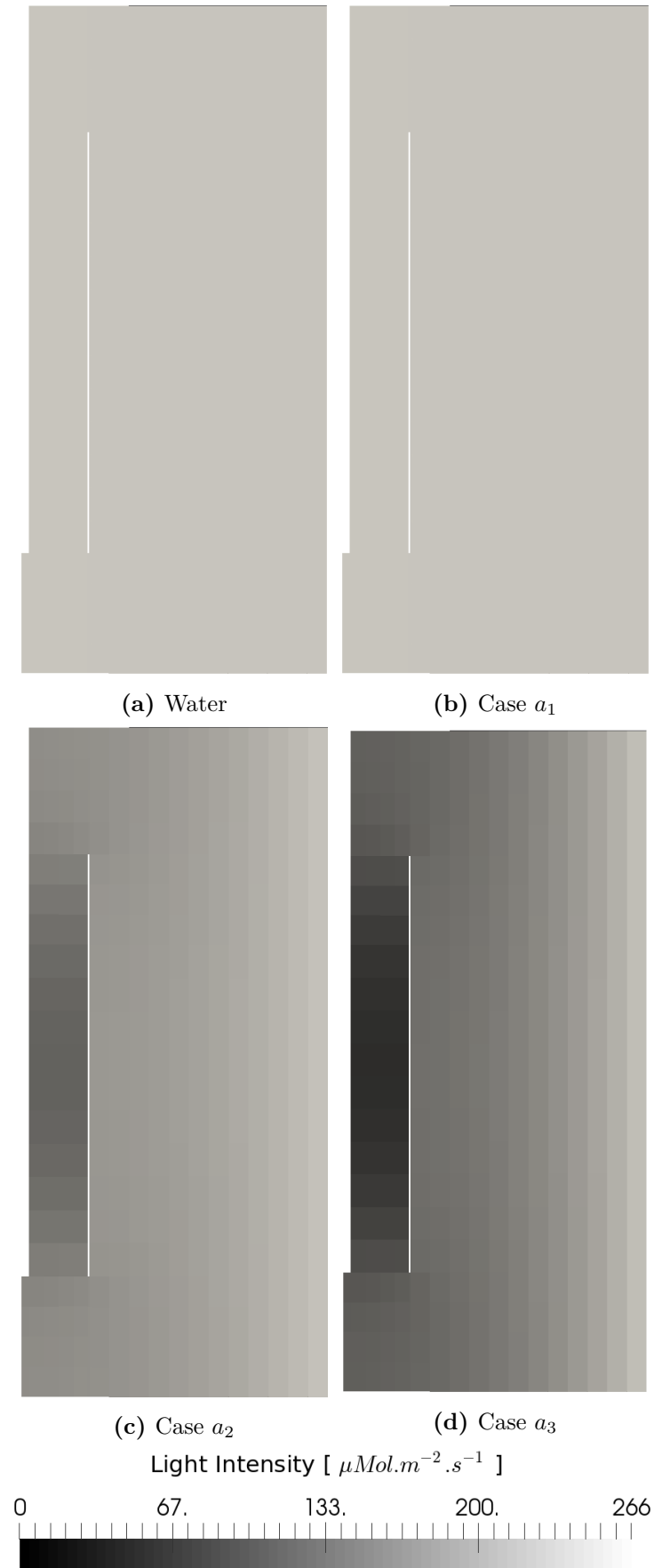


Figure 6.8: Light intensity contour plots for the cases in table 6.4 under different absorption and scattering coefficients

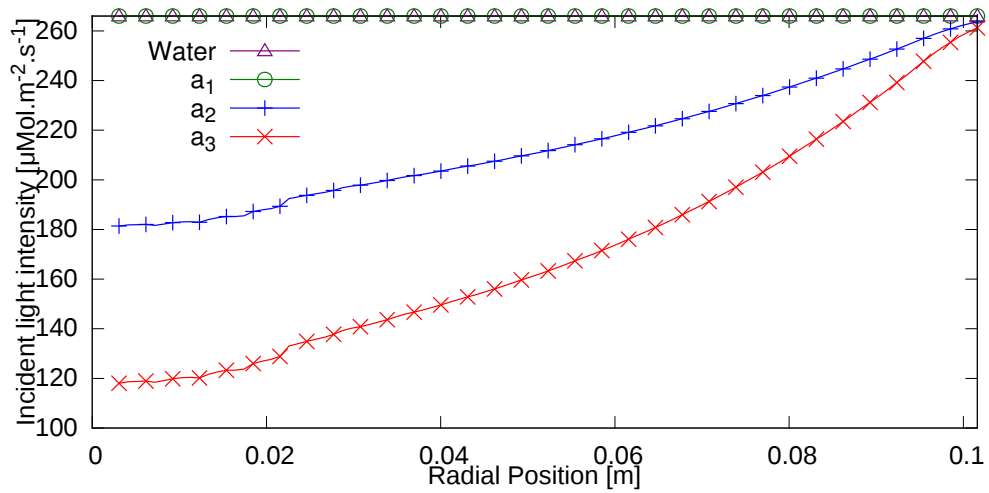


Figure 6.9: Comparison of light intensity distribution along profile line 0.1875m from base of bioreactor at the different light absorption and scattering coefficients described in table 6.4.

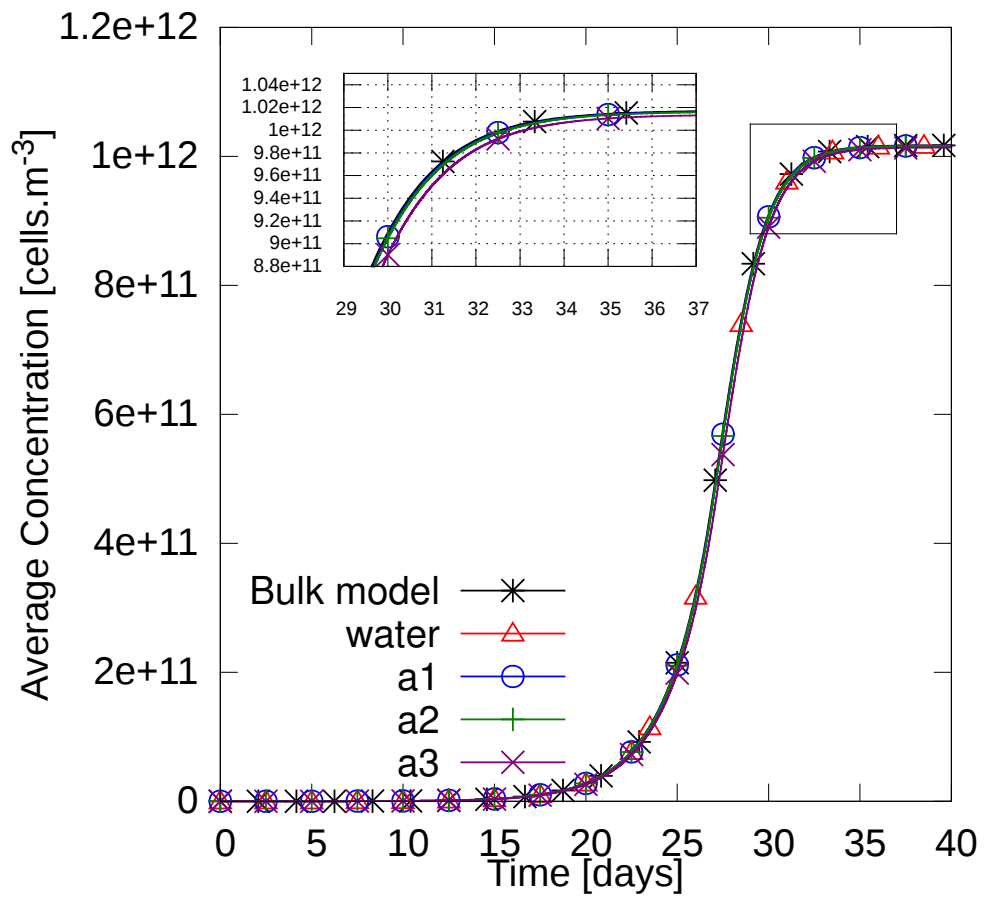


Figure 6.10: Biomass growth plot comparing biomass concentration for the different absorption and scattering coefficient cases.

6.2.5 Reynolds number scaling of a bioreactor

As the previous studies in this chapter have focused on the bench-scale bioreactor and have shown that there is little difference in the biomass growth even under high absorption and scattering conditions a series of simulations on different sized bioreactors of the same configuration are shown here.

In order to maintain the same flow-field as in the bench-scale bioreactor the scaling up here is done based on the Reynolds number of the bioreactor. This scale up based on Reynolds number results in a decrease in the velocities within the bioreactors whilst still maintaining the same flow field. Three additional sizes of bioreactor were modelled for a single set of absorption and scattering coefficients from case a_2 in section 6.2.4, ranging up to on thousand times the volume of the bench-scale bioreactor. Table 6.5 describes the differences in the bioreactor scales and figure 6.11 shows a visual comparison of the differences in the dimensions of the bioreactors.

Volume [L]	Radius [m]	Height [m]
7.2	0.1016	0.222
150	0.28	0.61
900	0.51	1.11
7200	1.02	2.22

Table 6.5: Dimensions and volumes for different scaled bioreactors

The results of modelling the flow field for the different scale bioreactors, seen in figure 6.12, show that the increase in size whilst maintaining the Reynolds number reduces the velocities significantly. This reduction in flow rate coupled with the increase in dimensions results in much lower recirculation rates within the bioreactors with times of around 5 minutes for a single circuit in the 7200L bioreactor. Even so the shape of the flow-field itself has not changed in any noticeable way with the stagnation region remaining and the highest velocities within the draft-tube. Even as the slower circulation time will affect the biomass growth rate the likely greater influence will come from the decrease in light intensity in larger fractions of the bioreactor due to increased distance from the incident location. Figure 6.13 shows how the increase in bioreactor size affects the diffusion of light in the bioreactor, as was shown previously the 7.2L bench-scale bioreactor (figure 6.13a) is

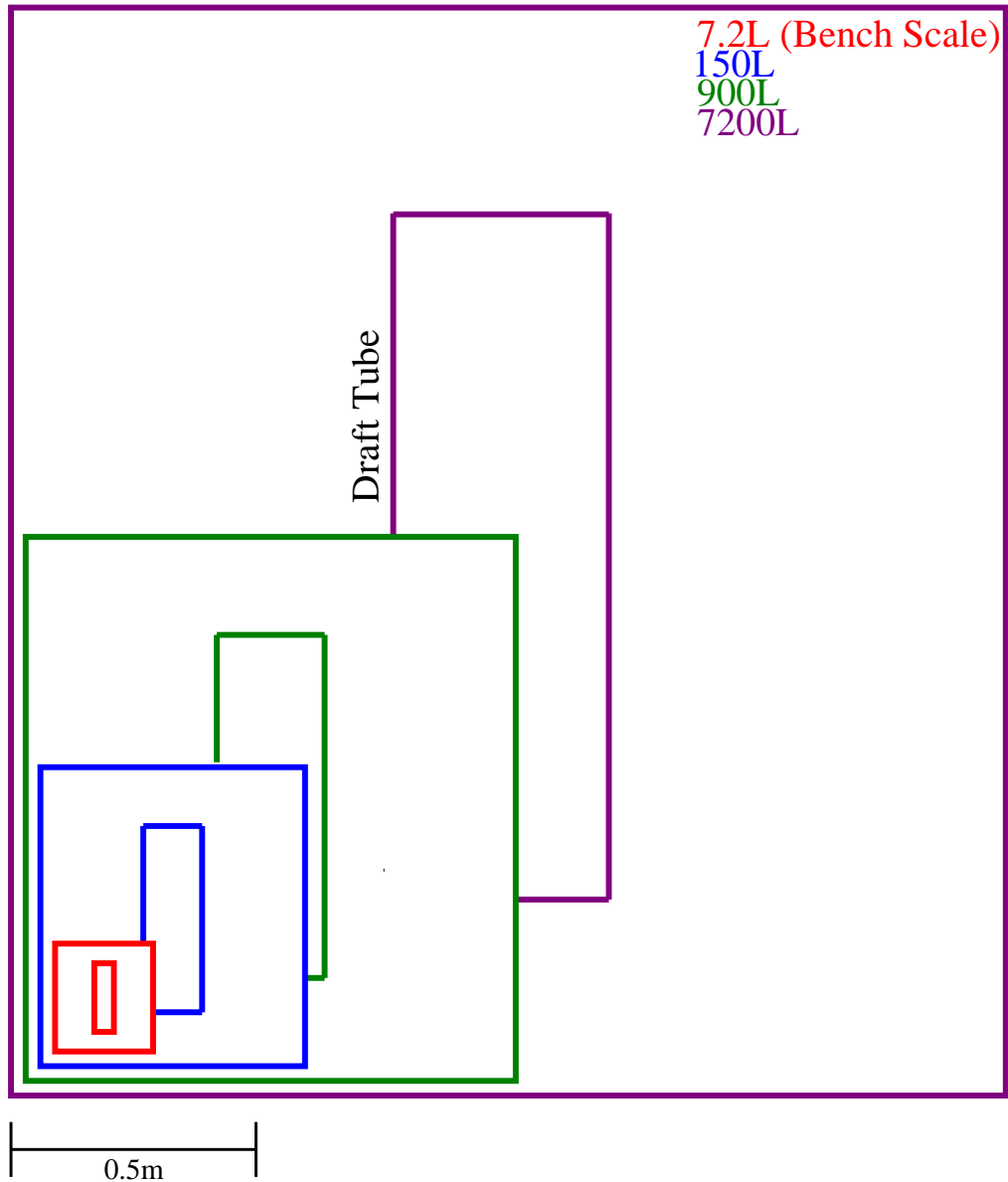


Figure 6.11: Visual comparison between different scaled bioreactors based on scaling up using Reynolds number from the bench-scale bioreactor of Karim et al. (2004).

well lit with little variation in the light intensity between the outer wall and the centreline, the only obvious variation in the light intensity is within the draft-tube where the light is inhibited by the draft-tube wall. Upon increasing the bioreactor volume to 150L the light distribution changes significantly. Figure 6.13b shows much greater diffusion from the outer wall to the centre of the bioreactor, this large decrease in the internal light intensity is further demonstrated by the plot in figure 6.14 which shows a drop of $150\mu\text{Mol.m}^{-2}.\text{s}^{-1}$ in the light intensity between the 7.2L and 150L bioreactors at the centreline.

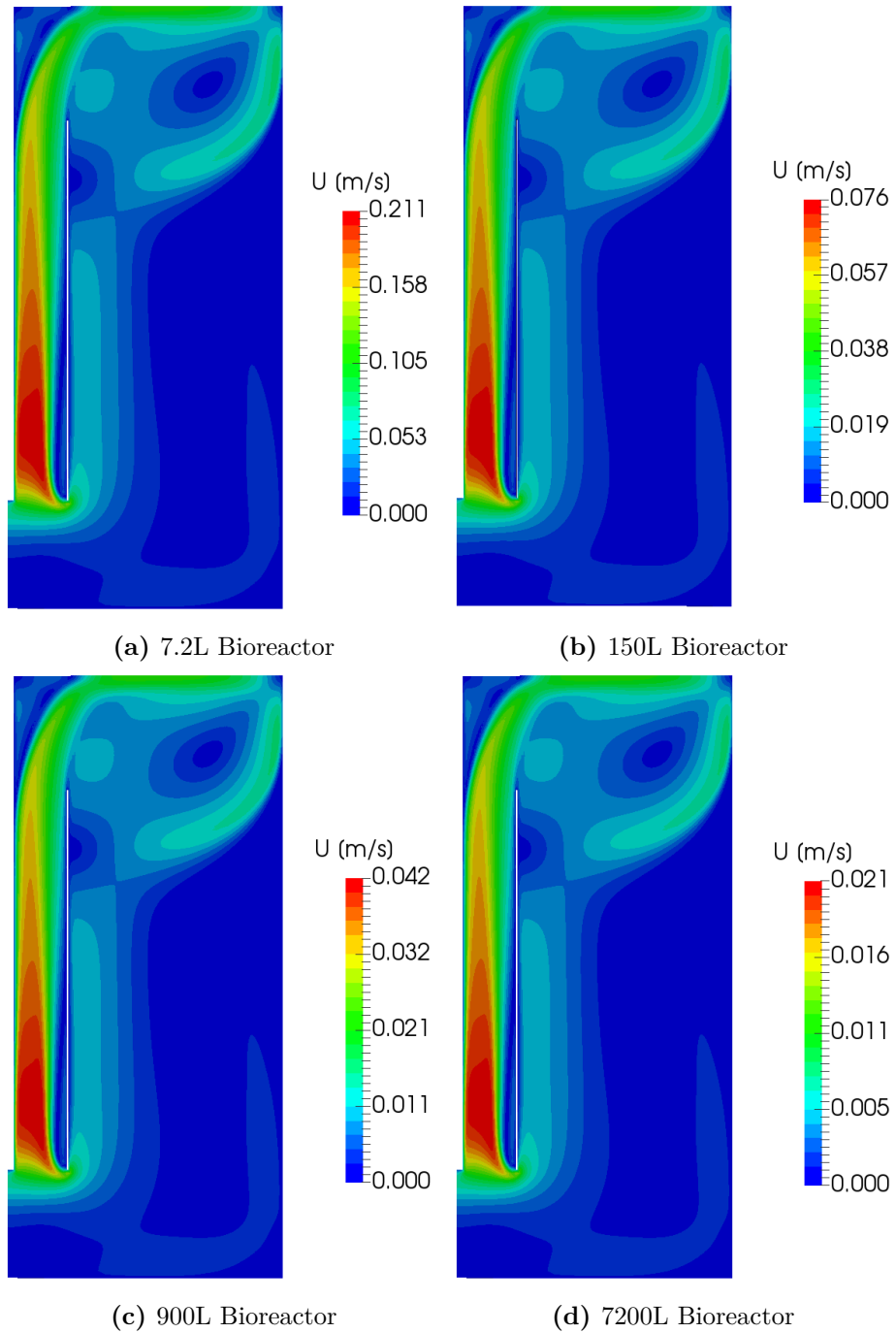


Figure 6.12: Contour plots of velocity magnitude for different scale bioreactors

The light intensity gradients for the two largest bioreactors (900L and 7200L) show the most significant difference in the bioreactor fraction that is in darkness with the 7200L bioreactor having nearly 80% of its width at light intensities below $25\mu Mp.m^{-2}.s^{-1}$ (figure 6.14). This significant fraction of the bioreactor being in relative darkness has a major effect on the fraction of the biomass which is in the active state as shown by figure 6.15

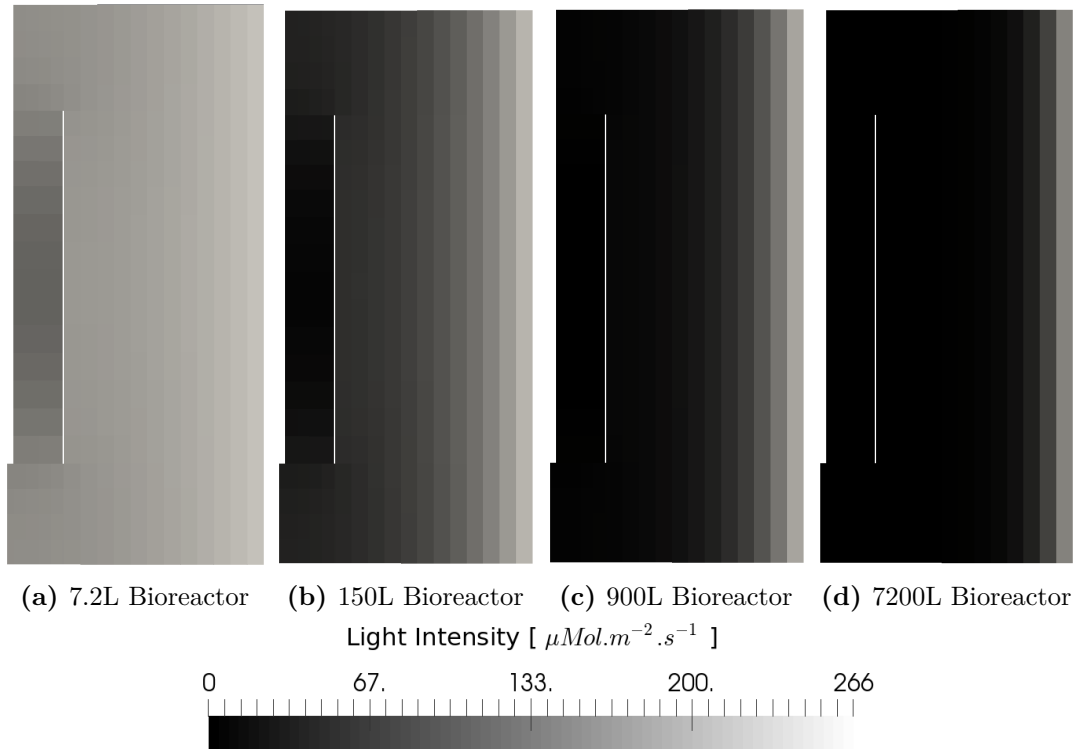


Figure 6.13: Contour plots of light intensity for different bioreactor sizes

where it is easy to see that photosynthetically active biomass fraction (x_2) in the 7200L bioreactor is significantly lower than in the smaller bioreactors.

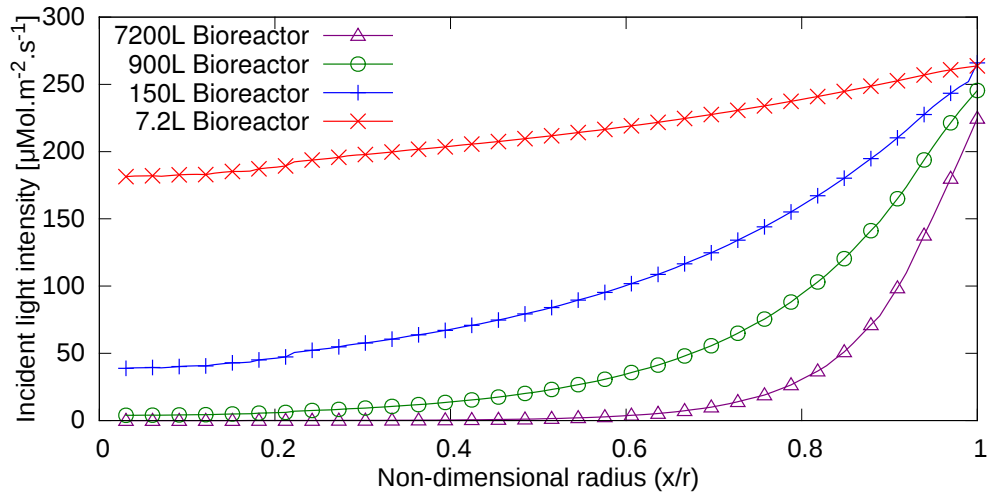


Figure 6.14: Comparison of light intensity distribution within bioreactors at different scales using the same light absorption and scattering coefficients

It is also possible to see the effects the flow-field has on the active biomass fraction in the bioreactor in particular in the 900L and 7200L bioreactors. The area around where the recirculation region is at top of the annular section of the bioreactor show a higher

fraction of active biomass at a greater distance from the outer wall. This indicates that the mixing in that recirculation zone is having a positive affect on the biomass growth rate. This gives a good indication that the mixing within the bioreactor has an important role to play in obtaining the optimal biomass growth rate for larger scale bioreactor with low light penetration depth. This also show that the couple PNH model proposed here can be used to help in the design of bioreactors with complex mixing used to aid in biomass growth.

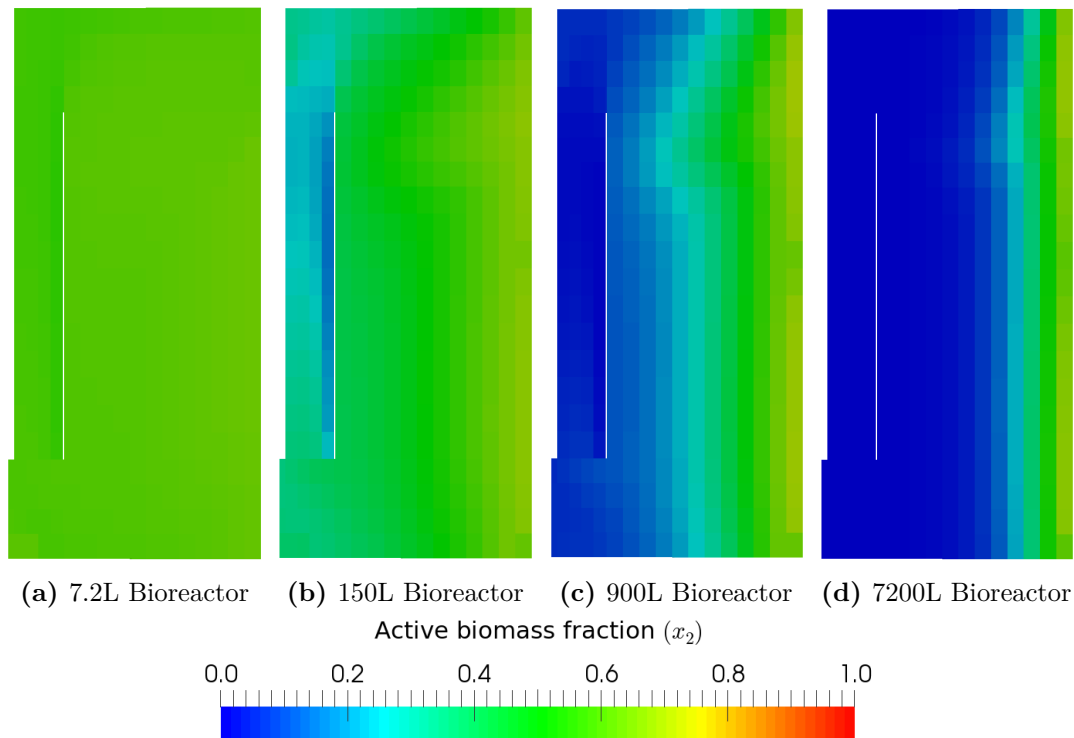


Figure 6.15: Contour plots of photosynthetically active biomass (x_2) for different bioreactor sizes

As is expected the active biomass fraction in the bioreactors has an affect on the growth of the biomass itself. Figure 6.16 shows how the biomass concentration varies in the different scale bioreactors after 40 days. All of the different size bioreactors show different values for the biomass concentration with the 7.2L bioreactor having the highest concentration of the four, this is as expected due to the near homogeneous light intensity over the whole bioreactor domain. The 7.2L bioreactor also shows no local variations in the biomass concentration. In contrast the three larger bioreactors produced lower biomass concentrations with increase in bioreactor size corresponding to a decrease in the biomass concentration. The 7200L bioreactor once again showed the most significant difference

between itself and the others with a much larger decrease in biomass concentration. It can also be seen in figures 6.16b - 6.16d that there is some local variation in the biomass concentration within the bioreactor. In the 150L bioreactor this local variation is confined to the point directly below the gas inlet tube, a location where a small stagnation region can be found, as this area is also one of the furthest points from the outer wall where the light is shining, it stands to reason that the biomass growth rate would be very low. This region of low biomass concentration can also be seen in the two larger bioreactors as well. Additionally, the 7200L bioreactor shows an increase in the biomass concentration in the main stagnation zone near the lower outer edge of the annular section, this is most likely due to the biomass in that region spending a greater amount of time in the higher light concentration than the biomass which is constantly circulating around the bioreactor.

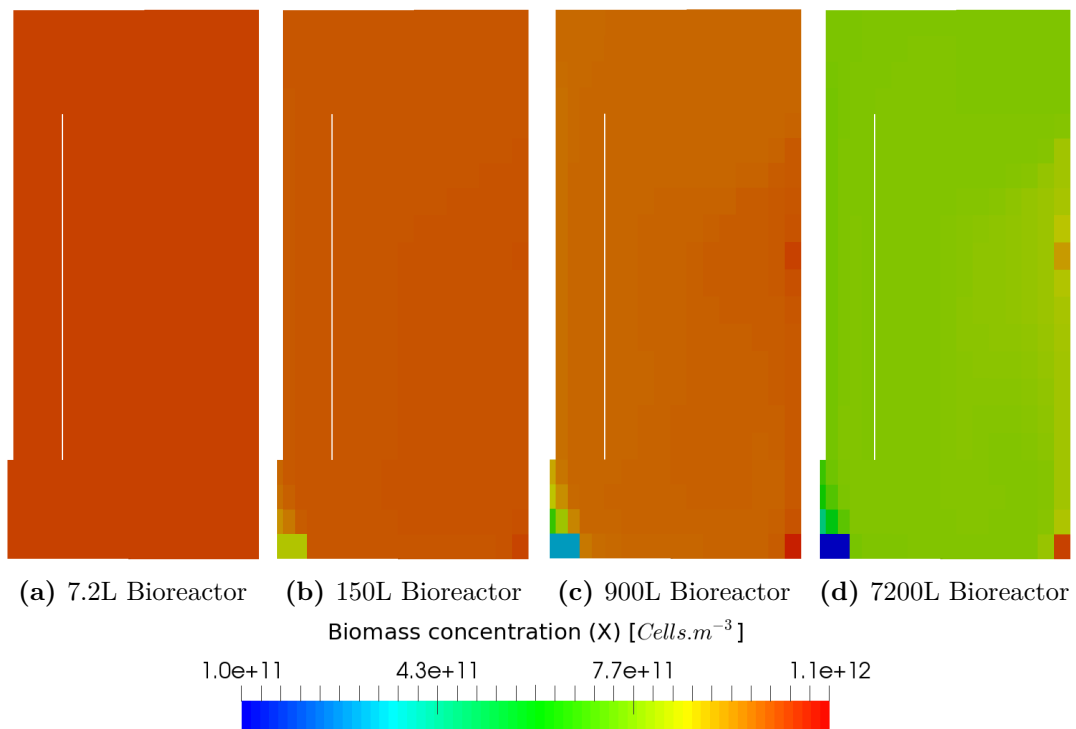


Figure 6.16: Contour plots of biomass concentration for the different bioreactor sizes after 40 days of growth

Finally the difference scaling up the bioreactors while maintaining the same Reynolds number and flow-field has on the biomass growth can be seen from the results in figure 6.17 where the differences in the final biomass concentrations between the bioreactors is easy to see. Additionally, although there is some difference between the results for

the 150L and 900L bioreactors when compared to the PN bulk model and the bench-scale bioreactor the differences are not as great as expected. This implies that the mixing within this gas-lift bioreactor is homogeneous enough to compensate for the lower penetration depth of the light. However, the largest of the scaled bioreactors shows a much greater drop in the final biomass concentration indicating that mixing is not able to overcome the much lower light penetration depth of such a large bioreactor.

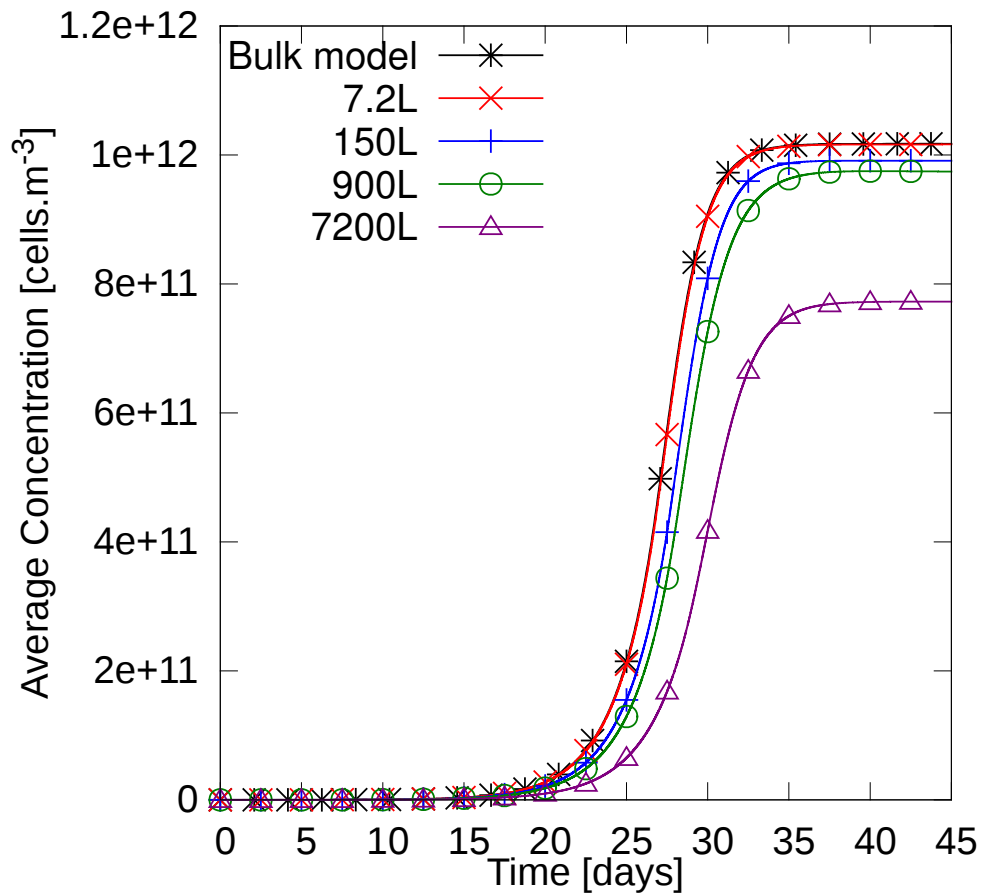


Figure 6.17: Average concentration of biomass in the different sized bioreactors

6.2.6 Effect of increasing incident light intensity on the active biomass and biomass growth

The case tested here is to see what affect varying the incident light intensity value at the outer wall has on the biomass growth within the bioreactor. The case was set-up in the same manner as the 900L bioreactor from section 6.2.5 with the only change being an increase in incident light intensity from $266\mu\text{Mol.m}^{-2}.\text{s}^{-1}$ to $500\mu\text{Mol.m}^{-2}.\text{s}^{-1}$. Figure

6.18 shows the light intensity gradient for the two incident intensities as well as the active biomass fractions within the bioreactors. Although the higher incident intensity appears to produce the greater values for active biomass, the results shown in figure 6.19 show that the final biomass concentration and the biomass growth rate are both lower for the higher incident intensity, this indicates that the higher incident intensity causes inhibition of the photosynthetic processes.

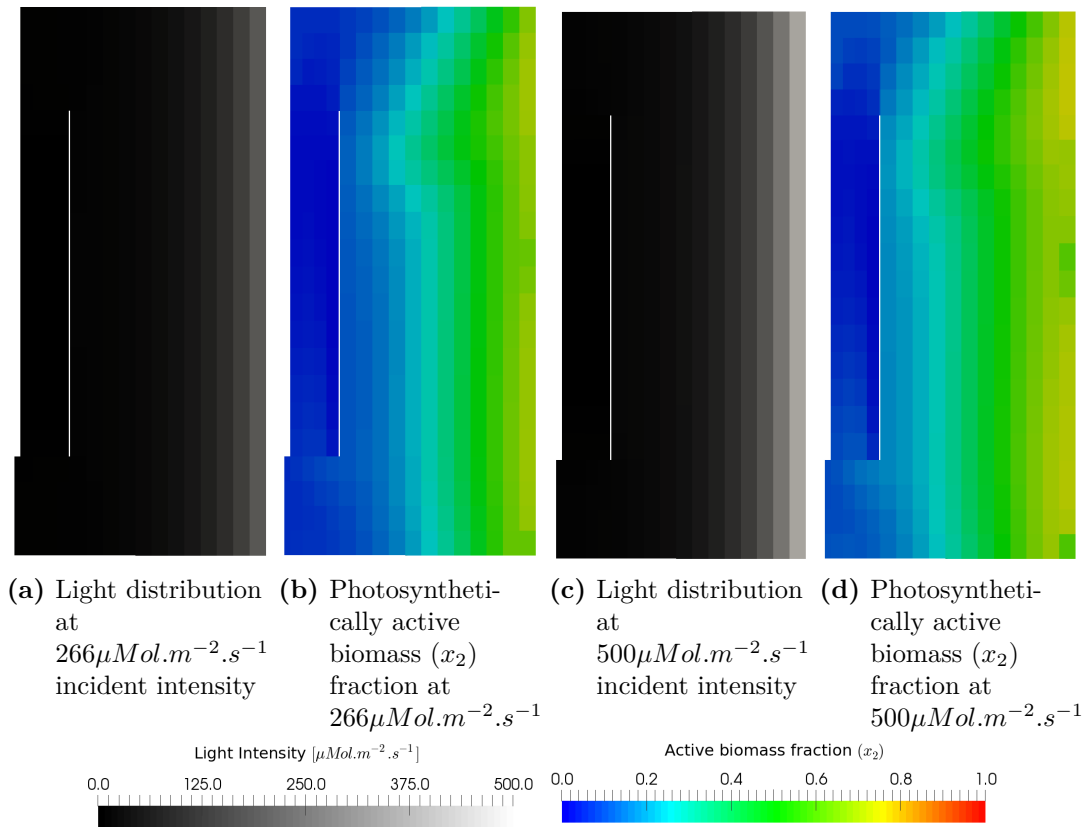


Figure 6.18: Contour plots of different light intensities and their respective active biomass fractions

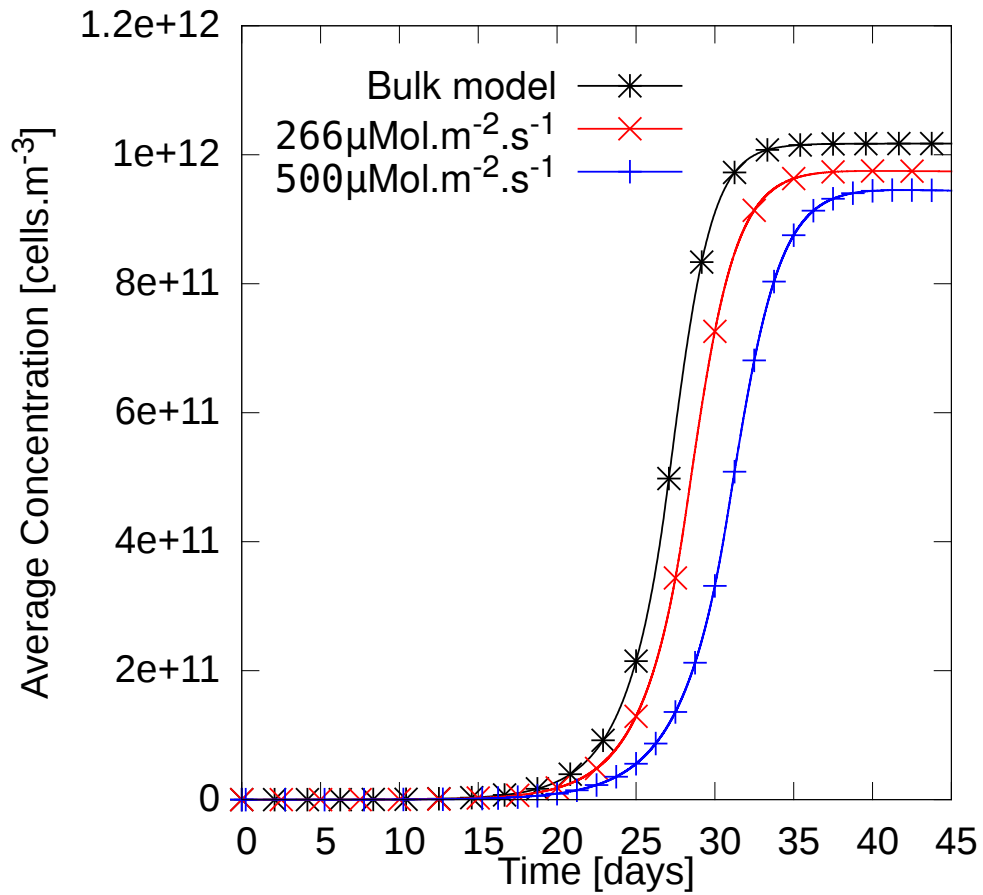


Figure 6.19: Average concentration of biomass for two different incident light intensities at the outer wall of the bioreactor; comparison with the results of the PN model.

6.3 Summary and conclusions

This chapter contains details of a proposed coupled model which combines photosynthetic and nutrient based biokinetic models with a CFD based hydrodynamic mixing model. The model takes the PN bulk coupled model proposed in chapter 4 and couples it to CFD based hydrodynamic mixing using a series of scalar advection-diffusion equations with coupled source terms. This approach was chosen as it allows for a more general model structure than other methods which use a tanks in series approximation.

The model implemented here uses a steady-state velocity field calculated using CFD modelling to transport the biokinetic species around the bioreactor domain. In addition to the biokinetic coupling a model for the diffusion of light within the domain was proposed which uses absorption and scattering coefficients to determine the light intensity as the

radiation passes through the fluid.

This new PNH model was then tested in a series of simulations designed to assess its capabilities in modelling growth of phytoplankton within a bioreactor. In order to reduce the computational time for solving the biokinetic model, which are run of long periods of simulated time, a method of mapping the the velocity field calculated on the fine CFD mesh onto a coarser mesh for the biokinetic modelling. This method was assessed and the resulting velocities, light distribution fields and biomass concentrations were found to not be significantly effected by the reduction in the flow field accuracy. The model was then assessed to determine the effects different absorption and scattering coefficients have on the biomass growth. Although the biomass growth was not significantly effected when varying the absorption and scattering coefficients, this was due to the small size of the bioreactor being investigated. Further simulations on larger scale bioreactors showed that absorption and scattering of the light within the bioreactor could have a significant affect on the final biomass concentration. These simulations on scaled up bioreactors also showed that the mixing within the bioreactor could overcome the low light penetration to a certain extent reducing its affect on biomass growth rate by continually circulating the biomass through the areas of higher light intensity. Finally the model was tested to determine the effect increasing the light intensity had on the biomass growth, as was expected although increasing the incident light intensity increased the depth to which light was able to diffuse at usable intensities into the bioreactor the inhibition which occurred near due to the higher intensities reduced the photosynthetically active biomass fraction.

The results this new coupled PNH model produced for the test simulations described are very promising with regard to the future applicability of the model in investigating and designing bioreactors for efficient growth of phytoplankton.

Chapter 7

Conclusions and further work

Contents

7.1	Conclusions	144
7.2	Implications of results	147
7.3	Further work	148

7.1 Conclusions

The main aim of the research presented in this thesis was to develop a framework combining biokinetic models for both nutrient based biokinetic growth and photosynthesis based growth of phytoplankton with a hydrodynamic model. Coupling these models together is of great interest with regard to modelling bioreactors of all types, as the current widely used model focus on biokinetic growth whilst neglecting the hydrodynamic flow within a bioreactor. As complex mixing can have a significant affect on the interactions within a bioreactor neglecting the flow outright is not an ideal solution. To this end a coupled model has been developed here which incorporates both biokinetic growth and hydrodynamic mixing.

As the chosen biological process for the coupled model involved photosynthetic growth as well as nutrient based biokinetic modelling it was important to investigate the modelling processes for both these area. As such, an investigation into nutrient based biokinetic growth models was performed looking at the processes involved in activated sludge models

as well as phytoplankton models for microalgae. From this investigation it was determined that the most attractive modelling method for microalgal growth was the cell quota model which accounts for both external nutrient uptake and internal storage of nutrient by the cells. This is an important factor when modelling microalgae as they are able to continue surviving for a time even when not external nutrient supply is available.

The next step in the development of the coupled model was an investigation into photosynthesis based growth modelling. When modelling a photosynthetic organism such as microalgae it is equally important to determine the growth based on light as it is the soluble nutrients such as nitrogen and phosphorous. Chapter 4 of this thesis describes an investigation into two different methods of modelling photosynthetic growth of phytoplankton along with some of the characteristics of the models, their behaviour and methods of coupling them to the soluble nutrient dependent models in chapter 3. The two different modelling methodologies, a multiplicative approach which describes the various processes involved in photosynthesis in terms of multiplicative functions in the overall growth rate term and a method using photosynthetic factories (PSF) which calculates the photosynthetic state of the biomass depending on the light intensity with the transition between the three different states controlled by a set of coupled ODEs. The multiplicative model was implemented and compared to experimental data obtained from literature. The model was shown to produce good results for the biomass concentration and cell nutrient content. The PSF model was also implemented and the effect different time dependent light intensity function had on the photosynthetic state of the biomass was investigated. The results of these simulations showed that large variations in the light intensity values had a detrimental effect on the amount of active biomass. Following these investigations a proposal was made for a method of coupling the PSF model with a multi nutrient cell quota model. In order for this coupling to be possible a change to the cell quota model structure was required. A limiting function related to a maximum cell quota was added to the nutrient uptake so as to prevent infinite uptake of nutrient in low light conditions where no growth could occur. The method used to couple the PSF and cell quota models involved incorporating the active biomass term into the equations for biomass growth and cell quota in the nutrient model. Following this the photosynthesis-nutrient (PN)

model was validated against experimental data from literature and an investigation into the effects of light on biomass growth was performed for the model. The results showed that time taken to reach maximum biomass concentration increased in low light conditions although there was no effect on the maximum value of concentration itself. This showed that the model was able to predict variation in biomass growth rate in conditions where the cell quota model alone would not.

The next stage in the work was to investigate the use of computational fluid dynamics (CFD) in modelling the flow within a typical bioreactor. A number of different model assumptions were investigated and their effects on the flow within the bioreactor assessed. Turbulence modelling, solver comparison and single vs. multiphase flow were all investigated with regard to a bench-scale gas-lift bioreactor. It was stated that the choice of turbulence model can have a significant effect on the results produced by the model, in particular when there is flow separation.

This was found to be one of the main influencing factors with regard to predicting the flow field in the gas-lift bioreactor with the Transition SST model providing the best results with regard to the flow separation location and velocity profiles. Several different methods of modelling the bubble driven flow were also investigated, the most accurate of these was the Lagrangian multiphase method followed closely by a method which uses a momentum source term in the draft tube to drive the flow.

Finally, a method of coupling the PN and CFD models was proposed and investigated. This new photosynthesis-nutrient-hydrodynamic (PNH) model also included the addition of a model for diffusion of light within a bioreactor. This allows for investigations into the effects of light absorption and scattering within the bioreactor and how mixing affects the active biomass. Further investigation was then performed using this new PNH model, simulations regarding the effects of different light absorption and scattering coefficients on the distribution of light and active biomass within the bioreactor were performed. The results showed that although there was some small variation in the biomass concentration with high absorption and scattering values the bioreactor was on too small a scale to be affected. Further investigation when scaling up the bioreactor showed that the results became more definitive at larger scales with the largest bioreactor with a radius of 1m

providing significant loss of biomass growth due to low light penetration. It was also determined that the coupling of the biokinetics and flow field provided some insight into the ability of a well-mixed bioreactor to counter low light penetration to an extent, the low loss of biomass growth in a bioreactor with a radius of 0.5m when compared to smaller reactors along with the affect the flow field had on the active biomass showed that the mixing is of importance and can be advantageous in larger scale bioreactor.

7.2 Implications of results

The work presented here has shown that by modifying existing biokinetic growth models for bioreactors to include computational fluid dynamics models which are able to predict the flow characteristic a framework for more extensive investigation of bioreactor physics can be created.

Current state-of-the-art bioreactor design is based on general empirical guidelines and the experience of the designers rather than comprehensive design strategies using well validated models. As such there is a need to quantify the processes occurring within these bioreactors to enable improvements to be made to their efficiency and reliability. The coupled model developed in this work provides a method by which these improvements can be made.

One of the issues with full-scale bioreactors is the designs are based on bench-scale and pilot-scale bioreactor data. This can often be misleading when used for full-scale bioreactors as the methods used to scale them do not account for all the physical and biological components of the bioreactor (Valentín-Vargas et al., 2012). The coupled PNH model developed in this work by including both biokinetic growth models and fluid models allows for a more comprehensive study on the differences in bioreactor conditions at different scales. This should also allow for improvements to the design of full-scale bioreactors as greater understanding of the effects mixing has on the biomass growth are determined.

Furthermore as the model can be expanded to include other physical and biochemical phenomena, the uses to which the model framework can be put are extensive and should

provide a valuable tool for both bioreactor research and design.

7.3 Further work

There are a number of different areas that could be investigated to improve the PNH model presented.

The inclusion of a dynamic model for absorption and scattering of light within the bioreactor domain would allow for a better understanding of the effect mixing has on the photosynthesis growth of biomass. The ability to determine whether local increases in biomass concentration become a significant factor in the growth rates in localised areas of the bioreactor would be beneficial to determining the improvements to mixing methods within the bioreactor that may be needed.

Additionally the an investigation into the effect of continuous flow bioreactors with flow both into and out of the domain from a local point would provide insight into the development of long term biomass growth reactors.

In its current form the model framework is only coupled in one direction, where the effects of mixing on the biomass growth are considered. There is currently no inclusion of the effect changes in biomass concentration would have on the fluid properties which at high biomass concentrations would be a necessary due to increases in the viscosity. Whether or not the fluid would be considered non-Newtonian is also a factor worth considering and investigating. However by including a model in which the viscosity of the fluid changed based solely on the increase in biomass concentration (neglecting any changed due to shear stress), a more accurate representation of the mixing and growth within the bioreactor at high solids concentrations would be possible.

Finally, a comprehensive experimental investigation would be needed to fully validate the model proposed as at this current time there is no experimental investigation available as far as the author knows which contains data for all the variables required to ascertain if the model it accurate.

Bibliography

Abbasi, T., Tauseef, S.M. and Abbasi, S.A. 2012. A Brief History of Anaerobic Digestion and “Biogas”. In *Biogas Energy* chapter 2, pp.11–24. Springer New York. New York, NY.

Allaby, M. 2012. *A Dictionary of Plant Sciences*. 3rd ed. Oxford University Press.

Alvarado, A., Amerlinck, Y., Vedantam, S., Goethals, P. and Nopens, I. 2011. Biokinetic modelling of a WSP in combination with a rigorous, yet simple mixing model.

Alvarado, A., Vedantam, S., Goethals, P. and Nopens, I. 2012. A compartmental model to describe hydraulics in a full-scale waste stabilization pond. *Water research*. **46**(2), pp.521–530.

Anning, T., MacIntyre, H.L., Pratt, S.M., Sammes, P.J., Gibb, S. and Geider, R.J. 2000. Photoacclimation in the marine diatom *Skeletonema costatum*. *Limnology and Oceanography*. **45**(8), pp.1807–1817.

Aubin, J., Fletcher, D.F. and Xuereb, C. 2004. Modeling turbulent flow in stirred tanks with CFD: the influence of the modeling approach, turbulence model and numerical scheme. *Experimental, Thermal and Fluid Science*. **28** pp.431–445.

Babaei, R., Bonakdarpour, B. and Ein-Mozaffari, F. 2015. Analysis of gas phase characteristics and mixing performance in an activated sludge bioreactor using electrical resistance tomography. *Chemical Engineering Journal*. **279** pp.874–884.

Bardina, J.E., Huang, P.G. and Coakley, T.J. 1997. Turbulence Modeling Validation, Testing, and Development. Technical Report 110446.

- Bassham, J., Benson, A. and Calvin, M. 1950. The path of carbon in photosynthesis - VIII the role of malic acid. *Journal of Biological Chemistry*. (2),.
- Batstone, D. 2006. Mathematical Modelling of Anaerobic Reactors Treating Domestic Wastewater: Rational Criteria for Model Use. *Reviews in Environmental Science and Bio/Technology*. **5**(1), pp.57–71.
- Batstone, D., Keller, J., Angelidaki, R., Kalyuzhnyi, S., Pavlostathis, S., Rozzi, A., Sanders, W., Siegrist, H. and Vavilin, V. 2002a. The IWA Anaerobic Digestion Model No 1 (ADM1). *Water Science & Technology*. **45**(10), pp.65–73.
- Batstone, D.D., Picioreanu, C. and van Loosdrecht, M.M. 2006. Multidimensional modelling to investigate interspecies hydrogen transfer in anaerobic biofilms. *Water Research*. **40**(16), pp.3099–3108.
- Batstone, D.J. and Keller, J. 2003. Industrial applications of the IWA anaerobic digestion model No.1 (ADM1). *Water Science and Technology*. **47**(12), pp.199–206.
- Batstone, D.J., Keller, J., Angelidaki, I., Kalyuzhnyi, S.V., Pavlostathis, S.G., Rozzi, A., Sanders, W.T.M., Siegrist, H. and Vavilin, V.a. 2002b. Anaerobic Digestion Model No.1 (ADM1). Technical report. IWA Task Group for Mathematical Modelling of Anaerobic Digestion Processes.
- Béchet, Q., Shilton, A. and Guieysse, B. 2013. Modeling the effects of light and temperature on algae growth : State of the art and critical assessment for productivity prediction during outdoor cultivation. *Biotechnology Advances*.
- Bernard, O. 2011. Hurdles and challenges for modelling and control of microalgae for CO₂ mitigation and biofuel production. *Journal of Process Control*. **21**(10), pp.1378–1389.
- Bernardini, E., Spence, S.M., Wei, D. and Kareem, A. 2015. Aerodynamic shape optimization of civil structures: A CFD-enabled Kriging-based approach. *Journal of Wind Engineering and Industrial Aerodynamics*. **144** pp.154–164.
- Blazek, J. 2005. *Computational Fluid Dynamics: Principles and Applications*. 2nd ed. Elsevier.

- Bogacki, P. and Shampine, L. 1989. A 3(2) Pair of Runge-Kutta Formulas. *Appl Math Lett.* **2**(4), pp.321–325.
- Bordel, S., Guieysse, B. and Munoz, R. 2009. Mechanistic model for the reclamation of industrial wastewaters using algal-bacterial photobioreactors. *Environmental science & technology.* **43**(9), pp.3200–7.
- Bougaran, G., Bernard, O. and Sciandra, A. 2010. Modeling continuous cultures of microalgae colimited by nitrogen and phosphorus. *Journal of theoretical biology.* **265**(3), pp.443–54.
- BP, 2013. BP Statistical Review of World Energy June 2013. Technical Report June. BP.
- Brebbia, C.A. and Mammol, A.A. 2011. *Computational Methods in Multiphase Flow VI.*
- Bricaud, A., Babin, M., Morel, A. and Claustre, H. 1995. Variability in the chlorophyll-specific absorption coefficients of natural phytoplankton : Analysis and parameterization phytoplankton $a \cdot h(A)$ was analyzed using a data set including 815 spectra determined chlorophyll concentration range ph values wer. *Journal of Geophysical Research.* **100**(C7), pp.13321–13332.
- Bridgeman, J. 2012. Computational fluid dynamics modelling of sewage sludge mixing in an anaerobic digester. *Advances in Engineering Software.* **44**(1), pp.54–62.
- Bywater, A. 2011. Anaerobic digesters can play a key role in slurry management on UK livestock farms. Technical report. Royal Agricultural Society of England.
- Carvalho, A.P. and Malcata, F.X. 2003. Kinetic modeling of the autotrophic growth of *Pavlova lutheri*: study of the combined influence of light and temperature. *Biotechnology progress.* **19**(4), pp.1128–35.
- Celik, I.B., Ghia, U., Roache, P.J., Freitas, C.J., Coleman, H. and Raad, P.E. 2008. Procedure for Estimation and Reporting of Uncertainty Due to Discretization in CFD Applications. *Journal of Fluids Engineering.* **130**.
- Chen, Y., Cheng, J.J. and Creamer, K.S. 2008. Inhibition of anaerobic digestion process: a review. *Bioresource technology.* **99**(10), pp.4044–64.

- Copp, J.B., Peerbolte, A., Snowling, S., Schraa, O., Froehlich, D. and Belia, E. 2004. Integrating anaerobic digestion into plant-wide wastewater treatment modeling.
- Coughtrie, A., Borman, D. and Sleigh, P. 2013. Effects of turbulence modelling on prediction of flow characteristics in a bench-scale anaerobic gas-lift digester. *Bioresource Technology*. **138** pp.297–306.
- Davidson, K., Flynn, K.J. and Cunningham, A. 1992. Non-steady state ammonium-limited growth of the marine phytoflagellate, *Isochrysis galbana* Parke. *New Phytologist*. **122**(3), pp.433–438.
- Davidson, K., Wood, G., John, E.H., Flynn, K.J. and Pa, O. 1999. An investigation of non-steady-state algal growth . I . An experimental model ecosystem. *Journal of Plankton Research*. **21**(5), pp.811–837.
- DEFRA, 2012. Waste water treatment in the United Kingdom – 2012. Technical report. DEFRA.
- Doost, S.N., Zhong, L., Su, B. and Morsi, Y.S. 2015. The numerical analysis of non-Newtonian blood flow in human patient-specific left ventricle. *Computer Methods and Programs in Biomedicine*. **127** pp.232–247.
- Drazin, P.G. and Riley, N. 2006. *The Navier-Stokes Equations: A Classification of Flows and Exact Solutions, Volume 13*. Cambridge University Press.
- Droop, M.R. 1968. Vitamin B12 and Marine Ecology. IV. The Kinetics of Uptake, Growth and Inhibition in *Monochrysis Lutheri*. *Journal of the Marine Biological Association of the United Kingdom*. **48** pp.689–733.
- Droop, M.R. 2003. In defence of the Cell Quota model of micro-algal growth. *Journal of Plankton Research*. **25**(1), pp.103–107.
- Eilers, P.H.C. and Peeters, J.C.H. 1988. A model for the relationship between light intensity and the rate of photosynthesis in phytoplankton. *Ecological Modelling*. **42** pp.199–215.
- Eilers, P.H.C. and Peeters, J.C.H. 1993. Dynamic behaviour of a model for photosynthesis and photoinhibition. *Ecological Modelling*. **69** pp.113–133.

- Elmitwalli, T.a., Sayed, S., Groendijk, L., van Lier, J., Zeeman, G. and Lettinga, G. 2003. Decentralised treatment of concentrated sewage at low temperature in a two-step anaerobic system: two upflow-hybrid septic tanks. *Water science and technology : a journal of the International Association on Water Pollution Research*. **48**(6), pp.219–26.
- Environmental Knowledge Transfer Network, 2008. Energy Efficient Water and Wastewater. Technical report.
- Fedorovich, V., Lens, P. and Kalyuzhnyi, S. 2003. Extension of Anaerobic Digestion Model No. 1 with processes of sulfate reduction. *Applied Biochemistry and Biotechnology*. **109**(1-3), pp.33–45.
- Ferziger, J.H. and Perić, M. 2002. *Computational Methods for Fluid Dynamics*. 3rd ed. Springer.
- Fischer-Antze, T., Olsen, N.R.B. and Gutknecht, D. 2008. Three-dimensional CFD modeling of morphological bed changes in the Danube River. *Water Resources Research*. **44**(9), pp.1–15.
- Flynn, K., Davidson, K. and Leftley, J. 1994. Carbon-nitrogen relations at whole-cell and free-amino-acid levels during batch growth of *Isochrysis galbana* (Prymnesiophyceae) under conditions of alternating light and dark. *Marine Biology*. **118** pp.229–237.
- Flynn, K.J. 2003. Modelling multi-nutrient interactions in phytoplankton; balancing simplicity and realism. *Progress in Oceanography*. **56**(2), pp.249–279.
- Fricke, J., Pohlmann, K., Jonescheit, N.A., Ellert, A., Joksch, B. and Luttmann, R. 2013. Designing a fully automated multi-bioreactor plant for fast DoE optimization of pharmaceutical protein production. *Biotechnology Journal*. **8**(6), pp.738–747.
- Galbe, M., Sassner, P., Wingren, A. and Zacchi, G. 2007. Process Engineering Economics of Bioethanol Production. In Olsson, L., ed, *Biofuels SE - 63*. volume 108 of *Advances in Biochemical Engineering/Biotechnology* pp.303–327. Springer Berlin Heidelberg.
- Geider, R., MacIntyre, H. and Kana, T. 1998. A dynamic regulatory model of phytoplanktonic acclimation to light, nutrients. *Limnology and Oceanography*. **43**(4), pp.679–694.

Grau, P., Sutton, P.M., Henze, M., Elmaleh, S., Grady, C.P., Gujer, W. and Koller, J. 1982. Recommended Notation for Use in the Description of Biological Wastewater Treatment Processes. *Water Research*. **16** pp.1501 – 1505.

Gresch, M., Brügger, R., Meyer, A. and Gujer, W. 2009. Compartmental models for continuous flow reactors derived from CFD simulations. *Environmental science & technology*. **43**(7), pp.2381–2387.

Gupta, P.L., Lee, S.M. and Choi, H.J. 2015. A mini review: photobioreactors for large scale algal cultivation. *World Journal of Microbiology and Biotechnology*. **31**(9), pp.1409–1417.

Habibi, A., Merci, B. and Heynderickx, G.J. 2007. Impact of radiation models in CFD simulations of steam cracking furnaces. *Computers and Chemical Engineering*. **31**(11), pp.1389–1406.

Henze, M., Grady, C.P.L., Gujer, W., Marais, G.v.R., Matsuo, T., Mino, T., Wentzel, M.C. and van Loosdrecht, M. 2000. *Activated Sludge Models ASM1, ASM2, ASM2D and ASM3*. IWA Publishing.

Henze, M., Jr, C.P.L.G., Gujer, W., Marais, G.V.R. and Matsuo, T. 1987. A General Model for Single-Sludge Wastewater Treatment Systems. *Water research*. **21**(5), pp.505–515.

Hilbert, R., Tap, F., El-Rabii, H. and Th??venin, D. 2004. Impact of detailed chemistry and transport models on turbulent combustion simulations. *Progress in Energy and Combustion Science*. **30**(1), pp.61–117.

IWA, 2005. Iwa activated sludge benchmark data. <http://www.benchmarkwwtp.org/>. [Accessed December, 2016].

Jones, W.P. and Launder, B.E. 1972. The prediction of laminarization with a two-equation model of turbulence. *International Journal of Heat Mass Transfer*. **15** pp.301–314.

Joshi, J.B., Nere, N.K., Rane, C.V., Murthy, B.N., Mathpati, C.S., Patwardhan, A.W. and Ranade, V.V. 2011. CFD simulation of stirred tanks: Comparison of turbulence models. Part I: Radial flow impellers. *The Canadian Journal of Chemical Engineering*. **89**(1), pp.23–82.

- Karim, K., Thoma, G.J. and Al-Dahhan, M. 2007. Gas-lift digester configuration effects on mixing effectiveness. *Water research*. **41**(14), pp.3051–3060.
- Karim, K., Varma, R., Vesvikar, M. and Al-Dahhan, M. 2004. Flow pattern visualization of a simulated digester. *Water research*. **38**(17), pp.3659–3670.
- Karpinska, A.M. and Bridgeman, J. 2016. CFD-aided modelling of activated sludge systems – A critical review. *Water Research*. **88** pp.861–879.
- King, M.F., Noakes, C.J., Sleight, P.A. and Camargo-Valero, M.A. 2013. Bioaerosol deposition in single and two-bed hospital rooms: A numerical and experimental study. *Building and Environment*. **59** pp.436–447.
- Klausmeier, C.A., Litchman, E. and Levin, S.A. 2004. Phytoplankton growth and stoichiometry under multiple nutrient limitation. *Limnology and Oceanography*. **49**(1), pp.1463–1470.
- Knowles, J.R. 1980. Enzyme-Catalyzed Phosphoryl Transfer Reactions. *Annual Review of Biochemistry*. **49**(1), pp.877–919.
- Kojima, H., Sawai, J., Uchino, H. and Ichige, T. 1999. Liquid circulation and critical gas velocity in slurry bubble column with short size draft tube. *Chemical Engineering Science*. **54**(21), pp.5181–5185.
- Laisk, A., Eichelmann, H. and Oja, V. 2006. C3 photosynthesis in silico. *Photosynthesis research*. **90**(1), pp.45–66.
- Langner, J.M. 2009. *Investigation of Non-Newtonian Flow in Anaerobic Digesters*. Ph.d thesis. University of Manitoba.
- Lateb, M., Meroney, R., Yataghene, M., Fellouah, H., Saleh, F. and Boufadel, M. 2016. On the use of numerical modelling for near-field pollutant dispersion in urban environments - A review. *Environmental Pollution*. **208** pp.271–283.
- Latha, S., Borman, D. and Sleight, P.A. 2010. CFD multiphase modelling for evaluation of gas mixing in an anaerobic digester. In *14th European Biosolids and Organic Resources Conference and Exhibition*. volume 2010 pp.1–16.

- Lawlor, D.W. 2001. *Photosynthesis*. 3rd ed. BIOS Scientific Publishers Ltd. Oxford.
- Laws, E.A. and Bannister, T.T. 1980. Nutrient- and light-limited growth of *Thalassiosira fluviatilis* in continuous culture, with implications for phytoplankton growth in the ocean. *Limnology and Oceanography*. **25**(3), pp.457–473.
- Legovic, T. and Cruzado, A. 1997. A model of phytoplankton growth on multiple nutrients based on the Michaelis-Menten-Monod uptake, Droop's growth and Liebig's law. *Ecological Modelling*. **99** pp.19–31.
- Lehman, J.T., Botkin, D.B. and Likens, G.E. 1975. The assumptions and rationales of a computer model of phytoplankton population dynamics. *Limnology and Oceanography*. **20**(3), pp.343–364.
- Lei, L. and Ni, J. 2014. Three-dimensional three-phase model for simulation of hydrodynamics, oxygen mass transfer, carbon oxidation, nitrification and denitrification in an oxidation ditch. *Water Research*. **53** pp.200–214.
- Loisel, H. and Morel, A. 1998. Light scattering and chlorophyll concentration in case 1 waters: A reexamination. *Limnology and Oceanography*. **43**(5), pp.847–858.
- Luo, H.P. and Al-Dahhan, M. 2011. Verification and validation of CFD simulations for local flow dynamics in a draft tube airlift bioreactor. *Chemical Engineering Science*. **66**(5), pp.907–923.
- Masojidek, J., Koblizek, M. and Torzillo, G. 2004. Photosynthesis in microalgae. In Richmond, A., ed, *Handbook of microalgal culture: Biotechnology and applied phycology* pp.20–39. Blackwell Publishing Company.
- Mata, T.M., Martins, A.a. and Caetano, N.S. 2010. Microalgae for biodiesel production and other applications: A review. *Renewable and Sustainable Energy Reviews*. **14**(1), pp.217–232.
- Meijer, S.C.F. 2004. Theoretical and practical aspects of modelling activated sludge processes. Technical report. Delft University of Technology, The Netherlands. Delft.
- Meister, M., Winkler, D., Rezavand, M. and Rauch, W. 2017. Integrating

hydrodynamics and biokinetics in wastewater treatment modelling by using smoothed particle hydrodynamics. *Computers & Chemical Engineering*. **99** pp.1–12.

Menter, F.R. 2011. Turbulence Modeling for Engineering Flows. *ANSYS Inc. Technical Paper* p.25.

Menter, F.R. and Esch, T. 2001. Elements of industrial heat transfer predictions. In *16th Brazilian Congress of Mechanical Engineering (COBEM)* pp.117–127.

Menter, F.R., Kuntz, M. and Langtry, R. 2003a. Ten Years of Industrial Experience with the SST Turbulence Model. In Hanjalic, K., Nagano, Y. and Tummers, M., eds, *Turbulence, Heat and Mass Transfer 4*. Begell House, Inc.

Menter, F.R., Kuntz, M. and Langtry, R. 2003b. Ten Years of Industrial Experience with the SST Turbulence Model. In Hanjalic, K., Nagano, Y. and Tummers, M., eds, *Proceedings of the Fourth International Symposium on Turbulence, Heat and Mass Transfer*. Antalya, Turkey.

Merchuk, J.C. 2003. Airlift Bioreactors : Review of Recent Advances. *The Canadian Journal of Chemical Engineering*. **81**(August), pp.324–337.

Meroney, R.N. 2009. CFD simulation of mechanical draft tube mixing in anaerobic digester tanks. *Water research*. **43**(4), pp.1040–50.

Meroney, R.N. and Sheker, R.E. 2014. CFD Simulation of Vertical Linear Motion Mixing in Anaerobic Digester Tanks. *Water Environment Research*. **86**(9), pp.816–827.

Michaelis, L., Menten, M.L., Johnson, K.A. and Goody, R.S. 2011. The original Michaelis constant: translation of the 1913 Michaelis-Menten paper. *Biochemistry*. **50**(39), pp.8264–9.

Monod, J. 1942. *Recherches sur la croissance des cultures bacteriennes*. 2nd ed. Paris, Hermann & cie.

Monod, J. 1949. The growth of bacterial cultures. *Annual Review of Microbiology*. **3**(XI), pp.371–394.

Mudde, R.F. and Van Den Akker, H.E.A. 2001. 2D and 3D simulations of an internal

airlift loop reactor on the basis of a two-uid model. *Chemical Engineering Science*. **56** pp.6351–6358.

Nauha, E.K. and Alopaeus, V. 2012. Modeling algal cultivation in a bubble column photobioreactor. In *14th European Conference on Mixing*, number September pp.335–340. Warszawa.

Nobel Media AB 2014, 2014. The nobel prize in physiology or medicine 1965. http://www.nobelprize.org/nobel_prizes/medicine/laureates/1965/index.html. [Accessed October 13th, 2014].

Oey, R.S., Mudde, R.F. and Van Den Akker, H.E.A. 2003. Numerical Simulations of an Oscillating Internal-loop Airlift Reactor. *The Canadian Journal of Chemical Engineering*. **81**(August), pp.684–691.

Petersen, E.E. 1965. *Chemical Reaction Analysis*. Englewood Cliffs : Prentice-Hall.

Pettersson, G. and Ryde-Pettersson, U. 1988. A mathematical model of the Calvin photosynthesis cycle. *European Journal of Biochemistry*. **175** pp.661–672.

Pirastru, L., Perreault, F., Chu, F.L., Oukarroum, A., Sleno, L., Popovic, R. and Dewez, D. 2012. Long-term stress induced by nitrate deficiency, sodium chloride, and high light on photosystem II activity and carotenogenesis of green alga *Scenedesmus* sp. *Botany*. **90**(10), pp.1007–1014.

Rhee, G.Y. 1973. A continuous culture study of phosphate uptake, growth rate, and polyphosphate in *Scenedesmus* sp.

Rhee, G.Y. 1974. Phosphate uptake under nitrate limitation by *Scenedesmus* sp. and its ecological implications. *Journal of Phycology*. **10** pp.470–475.

Rhee, G.Y. 1978. Effects of N:P atomic ratios and nitrate limitation on algal growth, cell composition, and nitrate uptake. *Limnology and Oceanography*. **23**(1), pp.10–25.

Richmond, A. 2004. Principles for attaining maximal microalgal productivity in photobioreactors: an overview. In Ang Jr., P., ed, *Asian Pacific Phycology in the 21st Century: Prospects and Challenges SE - 5*. volume 173 of *Developments in Hydrobiology* pp.33–37. Springer Netherlands.

- Rieger, L., Koch, G., Kühni, M., Gujer, W. and Siegrist, H. 2001. The EAWAG Bio-P module for activated sludge model No. 3. *Water research*. **35**(16), pp.3887–903.
- Ross, O.N. and Geider, R.J. 2009. New cell-based model of photosynthesis and photo-acclimation: accumulation and mobilisation of energy reserves in phytoplankton. *Marine Ecology Progress Series*. **383** pp.53–71.
- S. V. Patankar, 1980. *Numerical Heat Transfer and Fluid Flow*. Hemisphere Publishing Corporation.
- Sazhin, S., Sazhina, E., Faltsi-Saravelou, O. and Wild, P. 1996. The P-1 model for thermal radiation transfer: advantages and limitations. *Fuel*. **75**(3), pp.289–294.
- Siegel, M.H. and Robinson, C.W. 1992. Applications of Airlift Gas-Liquid-Solid Reactors in Biotechnology. *Chemical Engineering Science*. **47**(13/14), pp.3215–3229.
- Sommer, U. 1991. A comparison of the Droop and the Monod models of nutrient limited growth applied to natural populations of phytoplankton. *Functional Ecology*. **5**(4), pp.535–544.
- Stokes, G.G. 1847. Report on Recent Reserches In Hydrodynamics. Technical report. British Association for the Advancement of Science.
- Stroot, P.G., McMahon, K.D., Mackie, R.I. and Raskin, L. 2001. Anaerobic codigestion of municipal solid waste and biosolids under various mixing conditions - I: Digester performance. *Water research*. **35**(7), pp.1804–1816.
- Terashima, M., Goel, R., Komatsu, K., Yasui, H., Takahashi, H., Li, Y. and Noike, T. 2009. CFD simulation of mixing in anaerobic digesters. *Bioresource Technology*. **100**(7), pp.2228–2233.
- The Royal Society, 2008. Sustainable biofuels : prospects and challenges. Technical Report January. The Royal Society.
- Thimijan, R.W. and Heins, R.D. 1983. Photometric, radiometric, and quantum light units of measure: a review of procedures for interconversion.
- Tominaga, Y. and Stathopoulos, T. 2013. CFD simulation of near-field pollutant dispersion

- in the urban environment: A review of current modeling techniques. *Atmospheric Environment*. **79** pp.716–730.
- Turovskiy, I.S. and Mathai, P.K. 2006. *Wastewater Sludge Processing*. John Wiley & Sons, Inc.. New Jersey.
- Unknown, 2014. Section 6 - Precambrian Life. In *Athena Review Vol. 5*.
- Valentín-Vargas, A., Toro-Labrador, G. and Massol-Deyá, A.A. 2012. Bacterial community dynamics in full-scale activated sludge bioreactors: Operational and ecological factors driving community assembly and performance. *PLoS ONE*. **7**(8),.
- Vavilin, V.A. and Angelidaki, I. 2005. Anaerobic degradation of solid material: importance of initiation centers for methanogenesis, mixing intensity, and 2D distributed model. *Biotechnology and bioengineering*. **89**(1), pp.113–22.
- Vesvikar, M. and Dahhan, M.A. 2006. Effect of Mixing and Scale on the Performance and Hydrodynamics of Anaerobic Digesters.
- Voss, K.J. 1992. A spectral model of the beam attenuation ocean and coastal areas. *Limnol. Oceanogr.* **37**(3), pp.501–509.
- Woertz, I., Feffer, A., Lundquist, T. and Nelson, Y. 2009. Algae Grown on Dairy and Municipal Wastewater for Biofuel Feedstock. *Journal of Environmental Engineering*. **135**(11), pp.1115–1122.
- Wu, B. 2010a. CFD simulation of mixing in egg-shaped anaerobic digesters. *Water Research*. **44**(5), pp.1507–1519.
- Wu, B. 2010b. CFD simulation of mixing in egg-shaped anaerobic digesters. *Water research*. **44**(5), pp.1507–19.
- Wu, B. 2011. CFD investigation of turbulence models for mechanical agitation of non-Newtonian fluids in anaerobic digesters. *Water research*. **45**(5), pp.2082–94.
- Wu, B. and Chen, S. 2008. CFD Simulation of Non-Newtonian Fluid Flow in Anaerobic Digesters. *Biotechnology and Bioengineering*. **99**(3), pp.700–711.

- Wu, X. and Merchuk, J.C. 2001. A model integrating fluid dynamics in photosynthesis and photoinhibition processes. *Chemical Engineering Science*. **56** pp.3527–3538.
- Wu, X. and Merchuk, J.C. 2002. Simulation of algae growth in a bench-scale bubble column reactor. *Biotechnology and bioengineering*. **80**(2), pp.156–68.
- Yadav, A.S. and Bhagoria, J.L. 2013. Heat transfer and fluid flow analysis of solar air heater: A review of CFD approach. *Renewable and Sustainable Energy Reviews*. **23** pp.60–79.
- Yakhot, V., Orszag, S.a., Thangam, S., Gatski, T.B. and Speziale, C.G. 1992. Development of turbulence models for shear flows by a double expansion technique. *Physics of Fluids*. **4**(7), pp.1510–1520.
- Yamauchi, Y., Okamoto, T., Murayama, H., Nagara, A., Kashihara, T. and Nakanishi, K. 1994. Beer brewing using an immobilized yeast bioreactor design of an immobilized yeast bioreactor for rapid beer brewing system. *Journal of Fermentation and Bioengineering*. **78**(6), pp.443–449.
- Yu, L., Ma, J. and Chen, S. 2011a. Numerical simulation of mechanical mixing in high solid anaerobic digester. *Bioresource Technology*. **102**(2), pp.1012–1018.
- Yu, L., Zhao, Q., Jiang, A. and Chen, S. 2011b. Analysis and optimization of ammonia stripping using multi-fluid model. *Water Science & Technology*. **63**(6), pp.1143–1152.
- Zhu, X.G., Wang, Y., Ort, D.R. and Long, S.P. 2013. e-Photosynthesis: a comprehensive dynamic mechanistic model of C3 photosynthesis: from light capture to sucrose synthesis. *Plant, cell & environment*. **36**(9), pp.1711–27.
- Zonneveld, C. 1998. Photoinhibition as affected by photoacclimation in phytoplankton: a model approach. *Journal of Theoretical Biology*. **193** pp.115–123.

Appendices

Appendix A

Biokinetic model code

MATLAB code A.1: Multi nutrient cell quota model

```
1 function klausmeierMicroMol
2 set(0,'DefaultFigureWindowStyle','docked')
3 clear all;
4 clc;
5 close all;
6 Greens=cbrewer('seq','Greens',9);
7 Reds=cbrewer('seq','Reds',9);
8 Blues=cbrewer('seq','Blues',9);
9
10 filename = 'D:\pm10arc\Research\PhDWork\Data Manipulation\Algae CFD Models\
    klausmeierModel.xlsx';
11 sheet = 4;
12 xlRange = 'B11:B15';
13
14 initial = xlsread(filename, sheet, xlRange)
15
16 xlRange = 'B19:B30';
17
18 constants = xlsread(filename, sheet, xlRange);
19
20 global a RinN RinP VmaxN VmaxP KN KP muinf m QminN QminP
21
22 a = constants(1);
23 RinN = constants(2);
24 RinP = constants(3);
25 VmaxN = constants(4);
26 VmaxP = constants(5);
27 KN = constants(6);
28 KP = constants(7);
29 muinf = constants(8);
30 m = constants(9);
31 QminN = constants(10);
32 QminP = constants(11);
33
34
35
36 initial(1) = 180000;
37 initial(2) = 3000;
38 RinN = initial(1);
39 RinP = initial(2);
40 [t,y]=ode45(@model,[0:3600:3456000],initial);
41
42 initial(1) = 30000;
43 initial(2) = 3000;
```

```

44 RinN = initial(1);
45 RinP = initial(2);
46 [t2,y2]=ode45(@model,[0:3600:3456000],initial);
47
48 h(1)=figure(1);
49 th=t(:)/86400;
50 th2=t2(:)/86400;
51 hold on;
52 QNQP = y(:,3)./y(:,4);
53 subplot(3,1,1); plot(th,y(:,5),'-','Color',[155/255,187/255,89/255],'linewidth'
,3);
54 title('Biomass Growth');
55 xlabel('Time [days]')
56 ylabel('Biomass [Cells.m^{-3}]')
57 subplot(3,1,2); plot(y(:,2),y(:,1),'-','Color',[192/255,80/255,77/255],'
linewidth',3);
58 title('Available Phosphorus and Nitrate');
59 xlabel('R_P [mol P m^{-3}]')
60 ylabel('R_N [mol N m^{-3}]')
61 subplot(3,1,3); plot(th,QNQP,'-','Color',[192/255,80/255,77/255],'linewidth',3)
;
62 title('N:P Stiochiometry vs. Time');
63 xlabel('Time [days]')
64 ylabel('N:P, Q_N/Q_P [mol N /mol P]')
65 hold off
66
67
68 h(2)=figure(2);
69 hold on;
70 subplot(2,1,1); plot(th,y(:,1)*512,'.','Color',[155/255,187/255,89/255],'
linewidth',1);
71 title('Nitrate');
72 xlabel('Time [days]')
73 ylabel('R_N [mol N m^{-3}]')
74 subplot(2,1,2); plot(th,y(:,2)*512,'-','Color',[192/255,80/255,77/255],'
linewidth',3);
75 title('Phosphorus');
76 xlabel('Time [days]')
77 ylabel('R_P [mol P m^{-3}]')
78
79 h(3)=figure(3);
80 hold on;
81 subplot(2,1,1); plot(th,y(:,3),'-','Color',[192/255,80/255,77/255],'linewidth'
,3);
82 title('Q_N vs. Time');
83 xlabel('Time [days]')
84 ylabel('Q_N [mol N]')
85 subplot(2,1,2); plot(th,y(:,4),'-','Color',[192/255,80/255,77/255],'linewidth'
,3);
86 title('Q_P vs. Time');
87 xlabel('Time [days]')
88 ylabel('Q_P [mol P]')
89 hold off
90
91 lp = 18;
92
93 h(4)=figure(4);
94 hold on;
95 plot(th(1:lp:end),y(1:lp:end,5),'-x','Color',Greens(7,:), 'linewidth',1);
96 plot(th2(1:lp:end),y2(1:lp:end,5),'-o','Color',Greens(6,:), 'linewidth',1);
97 title('Biomass Growth');
98 xlabel('Time [days]')
99 ylabel('Biomass [Cells.m^{-3}]')
100 pleg=legend('P limited growth','N limited growth','location','northwest');
101 set(figure(4),'PaperSize',[14 7]);
102 set(figure(4),'PaperPosition',[-0.5 0 15 7]);
103
104 h(5)=figure(5);
105 hold on;
106 plot(th(1:lp:end),y(1:lp:end,1),'-x','Color',Blues(7,:), 'linewidth',1);
107 plot(th2(1:lp:end),y2(1:lp:end,1),'-o','Color',Blues(6,:), 'linewidth',1);
108 title('Available Nitrogen');
109 xlabel('Time [days]')
110 ylabel('S_N [\mumol N m^{-3}]')
111 pleg=legend('P limited growth','N limited growth','location','northwest');
112 set(figure(5),'PaperSize',[14 7]);

```

```

113 set(figure(5), 'PaperPosition', [-0.5 0 15 7]);
114
115 h(6)=figure(6);
116 hold on;
117 plot(th(1:lp:end), y(1:lp:end,2), '-x', 'Color', Reds(7,:), 'linewidth', 1);
118 plot(th2(1:lp:end), y2(1:lp:end,2), '-o', 'Color', Reds(6,:), 'linewidth', 1);
119 title('Available Phosphorus');
120 xlabel('Time [days]');
121 ylabel('S_P [\mumol P m^{-3}]');
122 pleg=legend('P limited growth', 'N limited growth', 'location', 'northwest');
123 set(figure(6), 'PaperSize', [14 7]);
124 set(figure(6), 'PaperPosition', [-0.5 0 15 7]);
125
126 h(7)=figure(7);
127 hold on;
128 plot(th(1:lp:end), y(1:lp:end,3), '-x', 'Color', Blues(7,:), 'linewidth', 1);
129 plot(th2(1:lp:end), y2(1:lp:end,3), '-o', 'Color', Blues(6,:), 'linewidth', 1);
130 title('Nitrogen Cell Quota');
131 xlabel('Time [days]');
132 ylabel('Q_N [\mumol N Cell^{-1}]');
133 pleg=legend('P limited growth', 'N limited growth', 'location', 'best');
134 set(figure(7), 'PaperSize', [14 7]);
135 set(figure(7), 'PaperPosition', [-0.5 0 15 7]);
136
137 h(8)=figure(8);
138 hold on;
139 plot(th(1:lp:end), y(1:lp:end,4), '-x', 'Color', Reds(7,:), 'linewidth', 1);
140 plot(th2(1:lp:end), y2(1:lp:end,4), '-o', 'Color', Reds(6,:), 'linewidth', 1);
141 title('Phosphorus Cell Quota');
142 xlabel('Time [days]');
143 ylabel('Q_P [\mumol N Cell^{-1}]');
144 pleg=legend('P limited growth', 'N limited growth', 'location', 'best');
145 set(figure(8), 'PaperSize', [14 7]);
146 set(figure(8), 'PaperPosition', [-0.5 0 15 7]);
147
148 print (h(1), '-dpdf', 'bio+QNQP+NP.pdf');
149 print (h(2), '-dpdf', 'RN+RP.pdf');
150 print (h(3), '-dpdf', 'QN+QP.pdf');
151 print (h(4), '-dpdf', 'algalBiomass.pdf');
152 print (h(5), '-dpdf', 'availableN.pdf');
153 print (h(6), '-dpdf', 'availableP.pdf');
154 print (h(7), '-dpdf', 'QN.pdf');
155 print (h(8), '-dpdf', 'QP.pdf');
156
157 output=[th(:), y(:,1)*512, y(:,2)*512, y(:,3)*512, y(:,4)*512, y(:,5)*512];
158 dlmwrite('matlabDataReactor', output, 'delimiter', '\t', 'precision', 6);
159 dlmwrite('constants', constants, 'delimiter', '\t', 'precision', 6);
160
161 end
162
163 function dy=model(t,y)
164
165 global a RinN RinP VmaxN VmaxP KN KP muinf m QminN QminP
166
167 dy=zeros(5,1);
168 dy(1) = a*(RinN - y(1)) - (VmaxN * y(1) * y(5))/(y(1) + KN); % Nitrate
169 % concentration
170 dy(2) = a*(RinP - y(2)) - (VmaxP * y(2) * y(5))/(y(2) + KP); % Phosphorus
171 % concentration
172 dy(3) = ((VmaxN * y(1))/(y(1) + KN)) - muinf * min(1 - (QminN/y(3)), 1 - (QminP
173 /y(4))) * y(3); % Nitrate cell quota
174 dy(4) = ((VmaxP * y(2))/(y(2) + KP)) - muinf * min(1 - (QminN/y(3)), 1 - (QminP
175 /y(4))) * y(4); % Phosphorus cell quota
176 dy(5) = (muinf * min(1 - (QminN/y(3)), 1 - (QminP/y(4))) * y(5)) - (m * y(5));
177 % Biomass
178 end

```

Appendix B

Photosynthetic model code

MATLAB code B.1: Implementation of multiplicative photosynthesis algal growth model developed by Bernard (2011). Code includes the main function with the call to ODE23 and all plotting of results, a subfunction called hvarfAlgal (line 124) which includes the ODEs to be solved and is called by the ODE23 function as well as a function to calculate the light intensity based on a step pulse on line 171.

```
1 function Bernard2011
2 tic
3 clf;
4 close all;
5 clear;
6 clc;
7
8 days = 25;
9 hrs = 12; % hours for width of pulse
10 w = hrs/24; % width of peak
11 td = w; % width of gap
12 lw = 3;
13
14 const = [
15     days; % (1)
16     w; % (2) width of peak
17     td; % (3) width of gap
18 ];
19
20 init=[1.411 0.03 0.6 100];
21
22 odeOptions = odeset('RelTol',1e-12);
23 [t,y]=ode23(@t,y) hvarfAlgal(t,y,const), [0:0.01:25],init,odeOptions);
24
25 gammaMax = 0.57;
26 KIStar = 63;
27
28
29 load('Y:\Matlab\rateEquations\algae\Experimental\Flynn1994.mat')
30 %convert
31 A(:,4) = A(:,4)*0.0713944041066;
32 y(:,1) = y(:,1)*0.0713944041066;
33 h(1)=figure(1);
```

```

34 th=t(:);
35 plot(th,y(:,1),'-k','linewidth',lw)
36 hold on
37 plot(A(:,1),A(:,4),'or')
38 pleg=legend('Model','Experimental');
39 set(pleg,'fontsize',12)
40 xlabel('Time (days)','fontsize',12,'fontweight','b')
41 ylabel('NH4+ (\mumol.m-3)','fontsize',12,'fontweight','b')
42 %title('Nutrient','fontsize',12,'fontweight','b')
43 hold off
44
45
46 h(2)=figure(2);
47
48 %convert
49 xqA(:,1) = (A(:,2).*A(:,5))/0.0713944041066;
50 xqy(:,1) = (y(:,2).*y(:,3));
51 plot(th,xqy(:,1),'-k','linewidth',lw)
52 hold on
53 plot(A(:,1),A(:,6),'or')
54 pleg=legend('Model','Experimental');
55 set(pleg,'fontsize',12,'location','southEast')
56 xlabel('Time (days)','fontsize',12,'fontweight','b')
57 ylabel('Cell N (gN.m-3)','fontsize',12,'fontweight','b')
58 title('Cell Nitrogen Content','fontsize',12,'fontweight','b')
59 hold off
60
61 h(3)=figure(3);
62 plot(th,y(:,3),'-k','linewidth',lw)
63 hold on
64 plot(A(:,1),A(:,5),'or')
65 pleg=legend('Model','Experimental');
66 set(pleg,'fontsize',12,'location','southEast')
67 xlabel('Time (days)','fontsize',12,'fontweight','b')
68 ylabel('Cell C (g.m-3)','fontsize',12,'fontweight','b')
69 title('Cell Carbon Content','fontsize',12,'fontweight','b')
70 hold off
71
72 xq(:,1) = (y(:,2).*y(:,3));
73 Chl(:,1)=(gammaMax.*(KIStar./(y(:,4)+KIStar)).*xq(:,1));
74 h(5)=figure(5);
75 %convert
76 A(:,8) = A(:,8)/1000;
77 plot(th,Chl,'-k','linewidth',lw)
78 hold on
79 plot(A(:,1),A(:,8),'or')
80 pleg=legend('Model','Experimental');
81 set(pleg,'fontsize',12,'location','southEast')
82 xlabel('Time (days)','fontsize',12,'fontweight','b')
83 ylabel('Chl (gChl.m-3)','fontsize',12,'fontweight','b')
84 title('Chlorophyll','fontsize',12,'fontweight','b')
85 hold off
86
87 pAf = 8;
88 axA = [0 25];
89 h(6)=figure(6);
90 subplot(2,2,1), line1=plot(th,y(:,1),'-k','linewidth',lw),
91     hold on, line2=plot(A(:,1),A(:,4),'or'), axis([axA 0 0.12]),
92     xlabel('Time (days)','fontsize',pAf,'fontweight','b'),
93     ylabel('NH4+ (\mumol.m-3)','fontsize',pAf,'fontweight','b'),
94     title('External Nitrogen (as Ammonium)')
95 subplot(2,2,2), plot(th,y(:,3),'-k','linewidth',lw), axis([axA 0 30]),
96     hold on, plot(A(:,1),A(:,5),'or'),
97     xlabel('Time (days)','fontsize',pAf,'fontweight','b'),
98     ylabel('Cell C (gC.m-3)','fontsize',pAf,'fontweight','b'),
99     title('Cell Carbon')
100 subplot(2,2,3), plot(th,Chl,'-k','linewidth',lw), axis([axA 0 0.45]),
101     hold on, plot(A(:,1),A(:,8),'or'),
102     xlabel('Time (days)','fontsize',pAf,'fontweight','b'),
103     ylabel('Chl (gChl.m-3)','fontsize',pAf,'fontweight','b'),
104     title('Cell Chlorophyll Content')
105 subplot(2,2,4), plot(th,xqy(:,1),'-k','linewidth',lw), axis([axA 0 1.8]),
106     hold on, plot(A(:,1),A(:,6),'or'),
107     xlabel('Time (days)','fontsize',pAf,'fontweight','b'),
108     ylabel('Cell N (gN.m-3)','fontsize',pAf,'fontweight','b'),
109     title('Cell Nitrogen')

```

```

110 hL = legend([line1,line2],{'Model','Experimental'});
111 newPosition = [0.45 0.46 0.15 0.1];
112 newUnits = 'normalized';
113 set(hL,'Position', newPosition, 'Units', newUnits);
114
115 % export images
116 set(figure(6),'PaperSize', [14 14]);
117 set(figure(6),'PaperPosition',[-0.5 -0.5 15 15]);
118 print (h(6),'-dpdf', 'AllPeriodicLight.pdf');
119
120 %end
121 toc
122 end
123
124 function dx=hvarfAlgal(t,x,C)
125 muTilda = 1.7;
126 Q0 = 0.050;
127 QI = 0.25;
128 KSIStar = 1.4;
129 Kil = 295;
130 rhoBar = 0.073;
131 Ks = 0.0012;
132 R = 0.0081;
133 gammaMax = 0.57;
134 KIStar = 63;
135 a = 16.2;
136 b = 0.087;
137 c = 0.5;
138 I0 = 100;
139 Chl0 = 0.004;
140 x0 = 0.6;
141 L = 0.13;
142
143 %Function for creating a rectangular pulse
144 ts = C(2);
145 te = C(1);
146 d = [ts:C(2)+C(3):te]; % width of gap between centre of peaks
147 y = pulstran(t,d,'rectpuls',C(2));
148 I0 = I0 * y;
149
150 %calculated
151 Chl=(gammaMax*(KIStar/(x(4)+KIStar))*x(3)*x(2));
152 Theta0C = Chl/x(3);
153 Ksi = KSIStar/Theta0C;
154 Iopt = sqrt(Ksi * Kil);
155 Delta = (4 * (Iopt^2)) - (Kil^2);
156 zeta = (a*Chl)+(b*x(3));
157 lambda = zeta * L;
158 muBar = (muTilda * ((2 * Kil)/(lambda * sqrt(Delta))))...
159 * atan((I0*(1-exp(-lambda))*sqrt(Delta))/...
160 ((2*(I0^2)*exp(-lambda))+(I0*(1 + exp(-lambda))*Kil)+(2*(Iopt^2))));
161 Ibar = ((I0/lambda)*(1-exp(-lambda)));
162
163 dx = zeros(4,1);
164 dx(1)=((-rhoBar * (x(1)/(x(1)+Ks))) * (1-(x(2)/QI)) * x(3));
165 dx(2)=(rhoBar * (x(1)/(x(1)+Ks))) * (1-(x(2)/QI)) - (muBar * (x(2)-Q0));
166 dx(3)= muBar * (1-(Q0/x(2))) * x(3) - (R * x(3));
167 dx(4)= muBar * (1-(Q0/x(2))) * (Ibar - x(4));
168
169 end
170
171 function [th,S,SA]=StepPulse(days, wh, tdh, l)
172 %Function for creating a rectangular pulse
173 w = wh * 3600; % width of peak
174 td = tdh * 3600;
175 ts = (wh * 3600)/2;
176 te = days * 86400;
177 t = 0:60:te; % time steps and range, small steps equal sharp continuity
178 d = [ts:w+td:te]; % width of gap between centre of peaks
179 y = pulstran(t,d,'rectpuls',w);
180 th=t(:)/3600;
181 S = l * y;
182 SA = mean(S);
183 end

```

MATLAB code B.2: PSF Coupled model

```

1 function lightModelComp
2 set(0,'DefaultFigureWindowState','docked')
3 set(0,'DefaultAxesFontSize',8)
4 set(0,'DefaultAxesFontname','Times New Roman')
5 set(0,'DefaultTextFontname','Times New Roman')
6 %set(0,'defaultTextInterpreter','latex');
7 set(gca,'box','off')
8 clear all;
9 clc;
10 close all;
11
12
13 filename = 'D:/matlab/klausmeierModel.xlsx';
14 sheet = 4;
15 xlRange = 'K11:K15';
16
17 iR = xlsread(filename, sheet, xlRange);
18
19 xlRange = 'K19:K30';
20
21 constants = xlsread(filename, sheet, xlRange);
22
23 global a RinN RinP VmaxN VmaxP KN KP muinf m QminN QminP n QmaxN QmaxP
24
25 a = constants(1);
26 RinN = constants(2);
27 RinP = constants(3);
28 VmaxN = constants(4);
29 VmaxP = constants(5);
30 KN = constants(6);
31 KP = constants(7);
32 muinf = 2.5084e-5; %constants(8);
33 m = constants(9);
34 QminN = constants(10);
35 QminP = constants(11);
36 QmaxN = 8*4.540E-14;% (19) Qmax,N
37 QmaxP = 16*1.640E-15;% (20) Qmax,P
38
39 %Colour maps
40 Blues=cbrewer('seq','Blues',9);
41 Greens=cbrewer('seq','Greens',9);
42 Reds=cbrewer('seq','Reds',9);
43
44 lw=3;
45 %for i=0.1:0.1:0.5
46 init=[1,0,0,iR(1),iR(2),iR(3),iR(4),iR(5)];
47 %init=[0,1,0];
48 % [t,y]=ode45(@hvarfAlgal,[0,1036800],init);
49 options = odeset('RelTol',1e-3);
50 days =60;
51 for i=1:4
52 n=i;
53 [ti,yi]=ode15s(@PSF,[0:3600:days*86400],init,options);
54 t(:,i)=ti(:)';
55 y1(:,i)=yi(:,1)';
56 y2(:,i)=yi(:,2)';
57 y3(:,i)=yi(:,3)';
58 y4(:,i)=yi(:,4)';
59 y5(:,i)=yi(:,5)';
60 y6(:,i)=yi(:,6)';
61 y7(:,i)=yi(:,7)';
62 y8(:,i)=yi(:,8)';
63 Check = [num2str(i), ' is complete'];
64 disp(Check)
65 end
66
67 fw(:,1)=t(:,1);
68 fw(:,2)=y8(:,1);
69 dlmwrite('bulkData.dat',fw,'delimiter',' ')
70
71 i=1;
72 for i=1:4
73 meanVals(i,1)=mean(y1(:,i)); %constant
74 meanVals(i,2)=mean(y2(:,i)); %constant

```

```

75 meanVals(i,3)=mean(y3(:,i)); %constant
76 end
77 meanVals
78 bH(1)=figure('name','BarChart');
79 b = bar(meanVals,'stacked');
80 ylim([0 1]);
81 xlabel={'Constant','SIN Function','Gaussian Function','Step Pulse'};
82 set(gca, 'xticklabel',xlabels);
83 set(b(1), 'FaceColor','k','EdgeColor','k');
84 set(b(2), 'FaceColor','r','EdgeColor','r');
85 set(b(3), 'FaceColor','b','EdgeColor','b');
86 set(bH(1), 'PaperSize', [14 7]);
87 set(bH(1), 'PaperPosition', [-0.25 0.1 14.5 7]);
88 print (bH(1), '-dpdf', 'meanBars.pdf');
89
90
91 th=t(:,1)/3600/24;
92
93 h(2)=figure('name','X');
94 hold on
95 plot(th,y8(:,1),'-k','linewidth',lw)
96 plot(th,y8(:,2),'-b','linewidth',lw)
97 plot(th,y8(:,3),'color',[0 0.5 0],'linewidth',lw)
98 plot(th,y8(:,4),'-r','linewidth',lw)
99 xlabel('Time (days)','fontweight','b')
100 ylabel('cells.m^{-3}','fontweight','b')
101 set(h(2), 'PaperSize', [7 7]);
102 set(h(2), 'PaperPosition', [0 0 7.5 7]);
103 print (h(2), '-dpdf', 'X.pdf');
104
105 h(3)=figure('name','RN');
106 hold on
107 plot(th,y4(:,1),'-k','linewidth',lw)
108 plot(th,y4(:,2),'-b','linewidth',lw)
109 plot(th,y4(:,3),'color',[0 0.5 0],'linewidth',lw)
110 plot(th,y4(:,4),'-r','linewidth',lw)
111 ylim([0 0.18])
112
113 xlabel('Time (days)','fontweight','b')
114 ylabel('\muMol.m^{-3}','fontweight','b')
115 set(h(3), 'PaperSize', [7 7]);
116 set(h(3), 'PaperPosition', [0 0 7.5 7]);
117 print (h(3), '-dpdf', 'RN.pdf');
118
119 h(4)=figure('name','RP');
120 hold on
121 plot(th,y5(:,1),'-k','linewidth',lw)
122 plot(th,y5(:,2),'-b','linewidth',lw)
123 plot(th,y5(:,3),'color',[0 0.5 0],'linewidth',lw)
124 plot(th,y5(:,4),'-r','linewidth',lw)
125 ylim([0 3e-3])
126 xlabel('Time (days)','fontweight','b')
127 ylabel('\muMol.m^{-3}','fontweight','b')
128 set(h(4), 'PaperSize', [7 7]);
129 set(h(4), 'PaperPosition', [0 0 7.5 7]);
130 print (h(4), '-dpdf', 'RP.pdf');
131
132 h(5)=figure('name','QN');
133 hold on
134 plot(th,y6(:,1),'-k','linewidth',lw)
135 plot(th,y6(:,2),'-b','linewidth',lw)
136 plot(th,y6(:,3),'color',[0 0.5 0],'linewidth',lw)
137 plot(th,y6(:,4),'-r','linewidth',lw)
138 xlabel('Time (days)','fontweight','b')
139 ylabel('\muMol.m^{-3}','fontweight','b')
140 set(h(5), 'PaperSize', [7 7]);
141 set(h(5), 'PaperPosition', [0 0 7.5 7]);
142 print (h(5), '-dpdf', 'QN.pdf');
143
144 h(6)=figure('name','QP');
145 hold on
146 plot(th,y7(:,1),'-k','linewidth',lw)
147 plot(th,y7(:,2),'-b','linewidth',lw)
148 plot(th,y7(:,3),'color',[0 0.5 0],'linewidth',lw)
149 plot(th,y7(:,4),'-r','linewidth',lw)
150 xlabel('Time (days)','fontweight','b')

```

```

151 ylabel('\muMol.m^{-3}','fontweight','b')
152 set(h(6),'PaperSize',[7 7]);
153 set(h(6),'PaperPosition',[0 0 7.5 7]);
154 print(h(6),'-dpdf','QP.pdf');
155 hold on
156 end
157
158 function dx=PSF(t,x)
159 alpha = 0.001935; % per micro einsteins per metre square (\muE m^{-2})^{-1}
160 beta = 5.7848e-7; % per micro einsteins per metre square (\muE m^{-2})^{-1}
161 gamma = 0.1460; % per second s^{-1}
162 Δ = 0.0004796; % per second s^{-1}
163
164 global a RinN RinP VmaxN VmaxP KN KP muinf m QminN QminP n QmaxN QmaxP
165 switch n
166 case 1
167     l = 266;
168 case 2
169     l=267+267*sin((0.728e-4*t)+21600);
170 case 3
171     sigma = 8640;
172     mu = 43200;
173     ga = 61094/(sigma*sqrt(pi));
174     ti=rem(t,86400);
175     l= 266*ga*exp(-((ti-mu)^2)/(2*sigma^2));
176 case 4
177     l=2*266;
178     %Function for creating a rectangular pulse
179     totLength = 86400; %total pulse length seconds (on+off)
180     onPulse = 1/2; %fraction of total length pulse is on
181     ts = onPulse * totLength;
182     te = totLength;
183     d = [ts:ts+ts:te]; % width of gap between centre of peaks
184     ti=rem(t,totLength);
185     y = pulstran(ti,d,'rectpuls',ts);
186     l = l * y;
187 end
188
189 dx = zeros(8,1);
190 dx(1) = (-alpha*l*x(1)) + (gamma*x(2)) + Δ*(1 - x(1) - x(2));
191 dx(2) = (alpha*l*x(1)) - (gamma*x(2)) - (beta*l*x(2));
192 dx(3) = (beta*l*x(2)) - Δ*x(3);
193 dx(4) = a*(RinN - x(4)) - (1-(x(6)/QmaxN)) * (VmaxN * x(4) * x(8))/(x(4) + KN);
194 % Nitrate concentration
195 dx(5) = a*(RinP - x(5)) - (1-(x(7)/QmaxP)) * (VmaxP * x(5) * x(8))/(x(5) + KP);
196 % Phosphorus concentration
197 dx(6) = (1-(x(6)/QmaxN)) * ((VmaxN * x(4))/(x(4) + KN)) - muinf * x(2) * min(1
198 - (QminN/x(6)), 1 - (QminP/x(7))) * x(6); % Nitrate cell quota
199 dx(7) = (1-(x(7)/QmaxP)) * ((VmaxP * x(5))/(x(5) + KP)) - muinf * x(2) * min(1
200 - (QminN/x(6)), 1 - (QminP/x(7))) * x(7); % Phosphorus cell quota
201 dx(8) = (muinf * min(1 - (QminN/x(6)), 1 - (QminP/x(7))) * x(2) * x(8)) - (m *
202 x(8)); % Biomass
203 end
204
205 function [th,S,SA]=StepPulse(days, wh, tdh, l)
206 %Function for creating a rectangular pulse
207 w = wh * 3600; % width of peak
208 td = tdh * 3600;
209 ts = (wh * 3600)/2;
210 te = days * 86400;
211 t = 0:60:te; % time steps and range, small steps equal sharp continuity
212 d = [ts:w+td:te]; % width of gap between centre of peaks
213 y = pulstran(t,d,'rectpuls',w);
214 th=t(:)/3600;
215 S = l * y;
216 SA = mean(S);
217 end
218
219 function S=funcEval(li)
220 %integrate gaussian function
221 syms tgauss
222 sigma = 8640;
223 mu = 43200;
224 ga = 61094/(sigma*sqrt(pi));
225 R=int(li*ga*exp(-((tgauss-mu)^2)/(2*sigma^2)), 0,86400)/(86400);
226 S=double(R);

```

222 | [end](#)

Appendix C

Coupled model source code

The source code displayed here is for the PNH coupled model. All the files required for compiling the model are provided here, to compile the model copy the source code into separate files named based on the captions and place them in a folder called PNHFoam. The code can be compiled for and standard build of OpenFOAM 3.0.0 using the 'wmake' command.

OpenFOAM source code C.1: PNHFoam.C

```
1 #include "fvCFD.H"
2 #include "fvIOoptionList.H"
3 #include "simpleControl.H"
4
5 // * * * * *
6
7 int main(int argc, char *argv[])
8 {
9     #include "setRootCase.H"
10    #include "createTime.H"
11    #include "createMesh.H"
12
13    simpleControl simple(mesh);
14
15    #include "createScalarFields.H"
16    #include "createPSFFields.H"
17    #include "createFvOptions.H"
18
19    // * * * * *
20
21    Info<< "\nCalculating scalar transport\n" << endl;
22
23    #include "CourantNo.H"
24
25    while (simple.loop())
26    {
27        Info<< nl << "Time = " << runTime.timeName() << "s" << nl
28            << "ClockTime = " << runTime.elapsedClockTime() << "s"
29            << nl << endl;
30    }
```

```

31     while (simple.correctNonOrthogonal())
32     {
33         #include "PSF.H"
34         #include "cellQuota.H"
35     }
36
37     runTime.write();
38 }
39
40 Info<< "End\n" << endl;
41
42 return 0;
43 }

```

OpenFOAM source code C.2: PSF.H

```

1  fvScalarMatrix IEqn
2  (
3  (
4      fvm::laplacian(DI, I)
5      - fvm::Sp(aL, I)
6  )
7  );
8  IEqn.solve();
9
10 fvScalarMatrix xL1Eqn
11 (
12     fvm::ddt(xL1)
13     + fvm::div(phi, xL1)
14     - fvm::laplacian(DX, xL1)
15     ==
16     (gamma*xL2) - (alpha*I*xL1) + (delta*xL3)
17 );
18
19 fvScalarMatrix xL2Eqn
20 (
21     fvm::ddt(xL2)
22     + fvm::div(phi, xL2)
23     - fvm::laplacian(DX, xL2)
24     ==
25     (alpha*I*xL1) - (gamma*xL2) - (beta*I*xL2)
26 );
27
28 fvScalarMatrix xL3Eqn
29 (
30     fvm::ddt(xL3)
31     + fvm::div(phi, xL3)
32     - fvm::laplacian(DX, xL3)
33     ==
34     (beta*I*xL2) - (delta*xL3)
35 );
36
37     xL1Eqn.relax();
38     xL2Eqn.relax();
39     xL3Eqn.relax();
40
41 for (int coup=0; coup<=1; coup++)
42 {
43     xL1Eqn.solve();
44     xL2Eqn.solve();
45     xL3Eqn.solve();
46 }

```

OpenFOAM source code C.3: cellQuota.H

```

1  fvScalarMatrix nNEqn

```

```

2 (
3     fvm::ddt(nN)
4     + fvm::div(phi, nN)
5     - fvm::laplacian(Dn, nN)
6     == a*(ninN - nN) - (scalar(1.0) - (QN/QmaxN)) * (VmaxN*nN*X)/(nN + KN)
7 );
8
9 fvScalarMatrix nPEqn
10 (
11     fvm::ddt(nP)
12     + fvm::div(phi, nP)
13     - fvm::laplacian(Dn, nP)
14     == a*(ninP - nP) - (scalar(1.0) - (QP/QmaxP)) * (VmaxP*nP*X)/(nP + KP)
15 );
16
17 fvScalarMatrix QNEqn
18 (
19     fvm::ddt(QN)
20     + fvm::div(phi, QN)
21     - fvm::laplacian(DX, QN)
22     == (scalar(1.0) - (QN/QmaxN)) * ((VmaxN*nN)/(nN + KN)) - muinf*xL2*min(scalar
23     (1.0) - (QminN/QN), scalar(1.0) - (QminP/QP)) * QN
24 );
25 fvScalarMatrix QPEqn
26 (
27     fvm::ddt(QP)
28     + fvm::div(phi, QP)
29     - fvm::laplacian(DX, QP)
30     == (scalar(1.0) - (QP/QmaxP)) * ((VmaxP*nP)/(nP + KP)) - muinf*xL2*min(scalar
31     (1.0) - (QminN/QN), scalar(1.0) - (QminP/QP)) * QP
32 );
33 fvScalarMatrix XEqn
34 (
35     fvm::ddt(X)
36     + fvm::div(phi, X)
37     - fvm::laplacian(DX, X)
38     == (muinf*xL2*min(scalar(1.0) - (QminN/QN), scalar(1.0) - (QminP/QP)) * X) -
39     (a*X)
40 );
41 for (int coup=0; coup<=1; coup++)
42 {
43     nNEqn.solve();
44     nPEqn.solve();
45     QNEqn.solve();
46     QPEqn.solve();
47     XEqn.solve();
48 }

```

OpenFOAM source code C.4: createScalarFields.H

```

1     Info<< "Reading field U\n" << endl;
2
3     volVectorField U
4     (
5         IOobject
6         (
7             "U",
8             runTime.timeName(),
9             mesh,
10            IOobject::MUST_READ,
11            IOobject::AUTO_WRITE
12        ),
13        mesh
14    );
15
16    Info<< "Reading field nN\n" << endl;
17
18    volScalarField nN

```

```

19  (
20      IOobject
21      (
22          "nN",
23          runTime.timeName(),
24          mesh,
25          IOobject::MUST_READ,
26          IOobject::AUTO_WRITE
27      ),
28      mesh
29  );
30
31  Info<< "Reading field nP\n" << endl;
32
33  volScalarField nP
34  (
35      IOobject
36      (
37          "nP",
38          runTime.timeName(),
39          mesh,
40          IOobject::MUST_READ,
41          IOobject::AUTO_WRITE
42      ),
43      mesh
44  );
45
46  Info<< "Reading field QN\n" << endl;
47
48  volScalarField QN
49  (
50      IOobject
51      (
52          "QN",
53          runTime.timeName(),
54          mesh,
55          IOobject::MUST_READ,
56          IOobject::AUTO_WRITE
57      ),
58      mesh
59  );
60
61  Info<< "Reading field QP\n" << endl;
62
63  volScalarField QP
64  (
65      IOobject
66      (
67          "QP",
68          runTime.timeName(),
69          mesh,
70          IOobject::MUST_READ,
71          IOobject::AUTO_WRITE
72      ),
73      mesh
74  );
75
76  Info<< "Reading field X\n" << endl;
77
78  volScalarField X
79  (
80      IOobject
81      (
82          "X",
83          runTime.timeName(),
84          mesh,
85          IOobject::MUST_READ,
86          IOobject::AUTO_WRITE
87      ),
88      mesh
89  );
90
91  Info<< "Reading biokineticProperties\n" << endl;
92
93  IOdictionary biokineticProperties
94  (

```

```

95     IObject
96     (
97         "biokineticProperties",
98         runTime.constant(),
99         mesh,
100        IObject::MUST_READ_IF_MODIFIED,
101        IObject::NO_WRITE
102    )
103 );
104
105 dimensionedScalar a
106 (
107     biokineticProperties.lookup("a")
108 );
109
110 dimensionedScalar ninN
111 (
112     biokineticProperties.lookup("ninN")
113 );
114
115 dimensionedScalar ninP
116 (
117     biokineticProperties.lookup("ninP")
118 );
119
120 dimensionedScalar VmaxN
121 (
122     biokineticProperties.lookup("VmaxN")
123 );
124
125 dimensionedScalar VmaxP
126 (
127     biokineticProperties.lookup("VmaxP")
128 );
129
130 dimensionedScalar KN
131 (
132     biokineticProperties.lookup("KN")
133 );
134
135 dimensionedScalar KP
136 (
137     biokineticProperties.lookup("KP")
138 );
139
140 dimensionedScalar muinf
141 (
142     biokineticProperties.lookup("muinf")
143 );
144
145 dimensionedScalar QminN
146 (
147     biokineticProperties.lookup("QminN")
148 );
149
150 dimensionedScalar QminP
151 (
152     biokineticProperties.lookup("QminP")
153 );
154
155 dimensionedScalar QmaxN
156 (
157     biokineticProperties.lookup("QmaxN")
158 );
159
160 dimensionedScalar QmaxP
161 (
162     biokineticProperties.lookup("QmaxP")
163 );
164
165 Info<< "Reading transportProperties\n" << endl;
166
167 IOdictionary transportProperties
168 (
169     IObject
170     (

```

```

171         "transportProperties",
172         runTime.constant(),
173         mesh,
174         IOobject::MUST_READ_IF_MODIFIED,
175         IOobject::NO_WRITE
176     )
177 );
178
179 Info<< "Reading diffusivity DX\n" << endl;
180
181 dimensionedScalar DX
182 (
183     transportProperties.lookup("DX")
184 );
185
186 Info<< "Reading diffusivity Dn\n" << endl;
187
188 dimensionedScalar Dn
189 (
190     transportProperties.lookup("Dn")
191 );
192
193
194 # include "createPhi.H"

```

OpenFOAM source code C.5: createPSFFields.H

```

1     Info<< "Reading field I\n" << endl;
2
3     volScalarField I
4     (
5         IOobject
6         (
7             "I",
8             runTime.timeName(),
9             mesh,
10            IOobject::MUST_READ,
11            IOobject::AUTO_WRITE
12        ),
13        mesh
14    );
15
16     Info<< "Reading field xL1\n" << endl;
17
18     volScalarField xL1
19     (
20         IOobject
21         (
22             "xL1",
23             runTime.timeName(),
24             mesh,
25            IOobject::MUST_READ,
26            IOobject::AUTO_WRITE
27        ),
28        mesh
29    );
30
31     Info<< "Reading field xL2\n" << endl;
32
33     volScalarField xL2
34     (
35         IOobject
36         (
37             "xL2",
38             runTime.timeName(),
39             mesh,
40            IOobject::MUST_READ,
41            IOobject::AUTO_WRITE
42        ),
43        mesh
44    );

```

```

45
46     Info<< "Reading field xL3\n" << endl;
47
48     volScalarField xL3
49     (
50         IOobject
51         (
52             "xL3",
53             runTime.timeName(),
54             mesh,
55             IOobject::MUST_READ,
56             IOobject::AUTO_WRITE
57         ),
58         mesh
59     );
60
61     Info<< "Reading PSFProperties\n" << endl;
62
63     IOdictionary PSFProperties
64     (
65         IOobject
66         (
67             "PSFProperties",
68             runTime.constant(),
69             mesh,
70             IOobject::MUST_READ_IF_MODIFIED,
71             IOobject::NO_WRITE
72         )
73     );
74
75     dimensionedScalar alpha
76     (
77         PSFProperties.lookup("alpha")
78     );
79
80     dimensionedScalar beta
81     (
82         PSFProperties.lookup("beta")
83     );
84
85     dimensionedScalar gamma
86     (
87         PSFProperties.lookup("gamma")
88     );
89
90     dimensionedScalar delta
91     (
92         PSFProperties.lookup("delta")
93     );
94
95     dimensionedScalar aL
96     (
97         transportProperties.lookup("aL")
98     );
99
100    dimensionedScalar sigma
101    (
102        transportProperties.lookup("sigma")
103    );
104
105    dimensionedScalar DI
106    (
107        1.0/(3.0*aL + sigma)
108    );

```

OpenFOAM source code C.6: Make/files

```

1 PNHFoam.C
2
3 EXE = $(FOAM_USER_APPBIN)/PNHFoam

```

OpenFOAM source code C.7: Make/options

```
1 EXE_INC = \  
2   -I$(LIB_SRC)/finiteVolume/lnInclude \  
3   -I$(LIB_SRC)/fvOptions/lnInclude \  
4   -I$(LIB_SRC)/meshTools/lnInclude \  
5   -I$(LIB_SRC)/sampling/lnInclude  
6  
7 EXE_LIBS = \  
8   -lfiniteVolume \  
9   -lfvOptions \  
10  -lmeshTools \  
11  -lsampling
```